



Provided by the author(s) and University of Galway in accordance with publisher policies. Please cite the published version when available.

Title	A thermodynamically motivated investigation of cell and tissue remodelling
Author(s)	McEvoy, Eóin
Publication Date	2018-08-24
Publisher	NUI Galway
Item record	http://hdl.handle.net/10379/14844

Downloaded 2024-04-19T20:02:59Z

Some rights reserved. For more information, please see the item record link above.



A THERMODYNAMICALLY MOTIVATED INVESTIGATION OF CELL AND TISSUE REMODELLING

Eóin McEvoy, B.E. (2014)



A thesis submitted to the National University of Ireland as fulfilment
of the requirements for the Degree of Doctor of Philosophy

August 2018

Discipline of Biomedical Engineering
College of Engineering and Informatics
National University of Ireland Galway

Supervisor of Research: Dr. J. Patrick McGarry

For my mother, Sharon, who I don't thank often enough for everything she's done

And for Maud, who patiently supports me every time I stumble.

“Mathematics is much more than a language for dealing with the physical world.

It is a source of models and abstractions which will enable us to obtain amazing new insights into the way in which nature operates.

Indeed, the beauty and elegance of the physical laws themselves are only apparent when expressed in the appropriate mathematical framework.”

Melvin Schwartz (In *Principles of Electrodynamics*, 1972)

“Even if I should be right in this, I do not know whether my way of approach is really the best and simplest. But, in short, it was mine.”

Erwin Schrödinger (In *What is Life?*, 1944)

ABSTRACT

The overall objective of this thesis is to provide a new understanding of the mechanisms that drive cell spreading and remodelling, and to extend this understanding to remodelling at a tissue and organ level.

A steady-state adaptation of the thermodynamically motivated stress fibre (SF) model of Vigliotti *et al.* (2015) is implemented in a non-local finite element setting, where global conservation of cytoskeletal proteins and binding integrins is considered. We present a number of simulations of cell spreading in which we consider a limited subset of the possible deformed spread-states assumed by the cell, to examine the hypothesis that free energy minimization drives the process of cell spreading. Simulations suggest that cell spreading can be viewed as a competition between (i) decreasing cytoskeletal free energy due to strain induced assembly of cytoskeletal proteins into contractile SFs, and (ii) increasing elastic free energy due to stretching of the mechanically passive components of the cell. The computed minimum free energy spread area is shown to be lower for a cell on a compliant substrate than on a rigid substrate. Furthermore, a low substrate ligand density is found to limit cell spreading. The predicted dependence of cell spread area on substrate stiffness and ligand density is in agreement with the experimental measurements. Experiments of cells adhering to “V-shaped” and “Y-shaped” ligand patches are also simulated, and analysis reveals that deformed configurations with the lowest free energy exhibit a SF distribution that corresponds to experimental observations.

The equilibrium statistical mechanics framework developed by Shishvan *et al.* (2018) allows for the simulation of the homeostatic ensemble for cells on an elastic substrate. This framework is expanded to describe the free energy associated with formation of focal adhesions between the cell and substrate. The extended model is shown to predict the effects of substrate stiffness and surface collagen density on the response of spread cells, as reported experimentally by Engler *et al.* (2003). Alteration of the surface collagen density directly affects formation of adhesion complexes and the associated free energy. At a low collagen density there is a high probability cells will assume rounded morphologies with low spread areas. With increasing collagen densities, the probability of cells becoming highly spread with irregular morphologies increases. The influence of substrate stiffness is shown to be highly coupled with surface collagen density. Elastic free energy associated with substrate deformation lowers the probability of observing a highly spread cell, thereby altering the tractions that influence assembly of adhesion complexes. The homeostatic ensemble for cells, expanded to include focal adhesion formation, provides new insight into observed cell behaviour on deformable collagen coated substrates.

The active cytoskeleton is known to play an important mechanistic role in cellular structure, spreading, and contractility. Contractility is actively generated by SFs, which continuously remodel in response to physiological dynamic loading conditions. The influence of actin-myosin cross-bridge cycling on SF remodelling under dynamic loading

conditions has not previously been uncovered. A novel SF cross-bridge cycling model is developed to predict transient active force generation in cells subjected to dynamic loading. Rates of formation of cross-bridges within SFs are governed by the chemical potentials of attached and unattached myosin heads. This transient cross-bridge cycling model is coupled with a thermodynamically motivated framework for SF remodelling to analyse the influence of transient force generation on cytoskeletal evolution. The model is shown to correctly predict complex patterns of active cell force generation under a range of dynamic loading conditions, as reported in previous experimental studies.

In order to bridge the gap between cell and organ level remodeling, a thorough understanding of the passive tissue mechanics is required. While the anisotropic behaviour of the complex composite myocardial tissue has been well characterized in recent years, the compressibility of the tissue has not been rigorously investigated to date. Experimental evidence is presented that passive excised porcine myocardium exhibits volume change under tensile and confined compression loading conditions. To simulate the multi-axial passive behaviour of the myocardium a nonlinear volumetric hyperelastic component is combined with the well-established Holzapfel-Ogden anisotropic hyperelastic component for myocardium fibres. This framework is shown to describe the experimentally observed behaviour of porcine and human tissues under shear and biaxial loading conditions. A representative volumetric element (RVE) of myocardium tissue is constructed to parse the contribution of the tissue vasculature to observed volume change under confined compression loading. Simulations of the myocardium microstructure suggest that the vasculature cannot fully account for the experimentally measured volume change. Additionally, the RVE is subjected to six modes of shear loading to investigate the influence of micro-scale fibre alignment and dispersion on tissue-scale mechanical behaviour.

Hypertrophy of the ventricular myocardium develops following a change in cardiovascular loading conditions. The current understanding is that disease progression may be stress or strain driven, but the multi-scale nature of the cellular remodelling processes have yet to be uncovered. A model of the contractile left ventricle is developed, with active cell tension described by a thermodynamically motivated cross-bridge cycling model. Simulation of the transient recruitment of myosin results in correct patterns of ventricular pressure predicted over a cardiac cycle. A myofibril remodelling framework is coupled with the cross-bridge cycling model to investigate how deviations in the transient force generation drive restructuring of cellular myofibrils in the heart wall. Analyses reveal that pathological loading conditions can significantly alter actin-myosin cross-bridge cycling over the course of the cardiac cycle. The resultant alteration in sarcomere stress pushes an imbalance between the internal free energy of the myofibril and that of unbound contractile proteins, which onsets remodelling. Myofibril remodelling associated with concentric and eccentric hypertrophy is predicted to occur following periods of hypertension and volume overload, respectively. The link between cross-bridge thermodynamics and myofibril remodelling proposed may significantly advance current understanding of cardiac disease onset.

ACKNOWLEDGEMENTS

First and foremost, I need to sincerely thank my supervisor, Dr. Patrick McGarry, for his enthusiasm, time, and willingness to let me argue my corner until I figure out why I'm wrong. Pat has impressed on me an immense appreciation for modelling and mechanics, and I can't thank him enough for his support over the past few years.

I would also like to thank Prof. Vikram Deshpande and co. in Cambridge. During my PhD research I've been fortunate to collaborate with Vikram on several projects. A true example of a scholar who believes we should never stop learning.

I owe much to the other members of the McGarry research group at NUI Galway. Dave and Noel, I'm so sorry for my endless questions and bothering during my first year! Thank you both so much for all the help. Thanks to Lizanne, who we can always depend on, you kept me focused on what is most important – banter and stories. Thanks to Breen, who I know I can annoy endlessly, you have been a solid friend since I came to Galway 8 years ago. Also Catherine, Brian, Jamie, Sarah, Enda, Diarmaid, Ryan, and honorary row member Ciara – thank you for the conference craic, vino, poker, and day-to-day support. You've all been fantastic to work alongside.

To all the NUIG postgrads (the numbers have become too high to thank individually!), thanks for all the tea, cake, tag rugby, and nights out. In particular thanks to Ed, Myles, and Niall for the broad and interesting lunchtime chats, and to Eimear for always twisting my arm for a pint.

Thanks to Dave and all technical staff at NUIG, including William who is always reliable for a quiz, cake, or hunting down a Matlab purchase order.

I would like to thank my funding sources, both the Irish Research Council and the Hardiman scholarship at NUI Galway. I would also like to acknowledge the Irish Centre for High-End Computing (ICHEC) for the provision of essential computational facilities and technical support.

To all the housemates and friends from Galway and home (“the bhoys”), thanks for all the music, chats, and chances to get away. I know you'll always keep me good and humble.

I need to thank my family (Sharon, Ron, and Éille) for helping me get to where I am today, and for putting up with my infrequent visits home over the past few years. Finally, thanks to Maud for all the love and support, who's battled through her own PhD alongside me, and our pup Thea, for comfort at times when I was a little bit lost.

PUBLICATIONS, CONFERENCE PROCEEDINGS, AND PRIZES

First-author journal publications

Chapter 2:

McEvoy, E., Deshpande, V.S., McGarry, J.P., (2017). Free energy analysis of cell spreading. *Journal of the Mechanical Behaviour of Biomedical Materials* 74.

Chapter 3:

McEvoy, E., Shishvan, S.S., Deshpande, V.S., McGarry, J.P., (2018). Thermodynamic modelling of the statistics of cell spreading on ligand coated elastic substrates. *Biophysical Journal*

Chapter 4:

McEvoy, E., Deshpande, V.S., McGarry, J.P., (2019). Transient active force generation and stress fibre remodelling in cells under cyclic loading. *Biomechanics and Modelling in Mechanobiology*

Chapter 5:

McEvoy, E., Holzapfel, G.A., McGarry, J.P., (2018). Compressibility and anisotropy of the ventricular myocardium: experimental analysis and microstructural modelling. *Journal of Biomechanical Engineering*.

Chapter 6:

McEvoy, E., Wijns, W., McGarry, J.P. (TBD). Contractility and remodelling of the left ventricular myocardium. In preparation for submission to the *Journal of the Royal Society Interface*

Other journal contributions

Reynolds, N.H., McEvoy, E., McGarry, J.P., (2019). Investigation of cell behaviour in biaxially and uniaxially constrained tissues subjected to cyclic deformation. *Biomaterials* (in review)

International conference proceedings

McEvoy, E., Shishvan, S.S., Deshpande, V.S., McGarry, J.P. (2018). A thermodynamic framework for cell spreading and dynamic contractility. *8th World Congress of Biomechanics (WCB) 2018, Dublin, Ireland*

McEvoy, E., Holzapfel, G.A., McGarry, J.P. (2018). A micro-structural model of the ventricular myocardium. *10th European Solid Mechanics Conference (ESMC) 2018, Bologna, Italy*

McEvoy, E., Shishvan, S.S., McGarry, J.P., Deshpande, V.S. (2017). Modelling cell-substrate interaction to investigate the influence of collagen density and stiffness on cell spreading. *International Conference of Biomedical Technology (ECCOMAS) 2017, Hannover, Germany*

McEvoy, E., Shishvan, S.S., Deshpande, V.S., McGarry, J.P. (2017). A thermodynamic statistical mechanics model to investigate the influence of ligand density and substrate stiffness on cell spreading. *Summer Biomechanics, Bioengineering, and Biotransport Conference 2017, Tucson, USA*

McEvoy, E., Ristori, T., Loerakker, S., Deshpande, V.S., McGarry, J.P. (2016). Analysis of cell spreading on micropatterned substrates using a thermodynamically consistent non-local active model. *Summer Biomechanics, Bioengineering, and Biotransport Conference 2016, Washington DC, USA*

Research has also been disseminated at the following national conferences and meetings:

- *Bioengineering in Ireland (2015, 2016, 2017, 2018)*
- *Sir Bernard Crossland Symposium (2016)*
- *Matrix Biology Ireland (2017)*
- *Joint Meeting for the Irish Mechanics Society (IMS) and the Irish Society for Scientific Engineering & Computation (ISSEC) (2015)*

International prizes

3rd Prize in the *Cardiovascular Mechanics and Cell Biomechanics* PhD paper competition at the *World Congress of Biomechanics (WCB) 2018, Dublin, Ireland*, for paper entitled “*A thermodynamic framework for cell spreading and dynamic contractility*”.

3rd Prize in the *Biomaterials and Material-Cellular Interaction* PhD paper competition at the *Summer Biomechanics, Bioengineering, and Biotransport Conference 2017, Tucson, USA*, for paper entitled “*A thermodynamic statistical mechanics model to investigate the influence of ligand density and substrate stiffness on cell spreading*”.

National prizes

3rd Prize in PhD Paper Competition at the *19th Annual Sir Bernard Crossland Symposium, QUB, NI, 2016*, for paper entitled “*A multi-scale framework for the remodelling of cardiac cells and tissue*”.

1st Prize for Best Overall Paper in *Biomechanics* at the *22nd Annual Conference of the Royal Academy of Medicine in Ireland (BINI22) in Galway, Ireland*, for paper entitled “*Modelling of the ventricular myocardium: anisotropy, compressibility, and contractility*”

CONTENTS

Abstract	iii
Acknowledgements	v
List of publications, conference proceedings, and prizes	vi
1. Introduction and background	1
1.1. Introduction to thesis and structure	1
1.1.1. Objectives	2
1.1.2. Thesis structure	3
1.2. Established theory	6
1.2.1. Continuum mechanics	6
1.2.2. Finite element method	14
1.3. Background and literature	20
1.3.1. Cell structure and forces	20
1.3.2. Computational cell modelling	25
1.3.3. Cardiac myocardium	32
Bibliography	40
2. Free energy analysis of cell spreading	49
2.1. Introduction	49
2.2. Modelling framework	52
2.2.1. Framework for stress fibre remodelling and contractility	52
2.2.2. Framework for focal adhesion development	61
2.2.3. Material parameters	65
2.3. 2D analysis of cell spreading on infinite flat substrates	67
2.4. 2D analysis of circular spreading on micro-patterned substrates	72
2.5. Discussion	78
2.6. Concluding remarks	82
Appendix 2.A: Comparison with previous models	83
Bibliography	84

3. Thermodynamic modelling of the statistics of cell spreading on ligand coated elastic substrates	86
3.1. Introduction.....	86
3.2. Methodology.....	88
3.2.1. Overview of the homeostatic mechanics framework	88
3.2.2. Gibbs free-energy of a morphological state	89
3.2.3. Adhesion complexes between the cell and the extracellular collagen ..	91
3.3. Results and discussion	96
3.3.1. Spread dependence of cells on surface collagen density.....	96
3.3.2. Influence of substrate stiffness on cell spreading.....	98
3.3.3. Coupled dependence of collagen density and substrate stiffness.....	99
3.3.4. Experimental support for predicted cell behaviour	101
3.3.5. Thermodynamically motivated insights for predicted cell behaviour.	103
3.4. Concluding remarks.....	108
Extended data	111
Appendix 3.A: Supplementary information	115
3.A.1. The homeostatic mechanics framework.....	115
3.A.2. The equilibrium Gibbs free-energy of a morphological microstate...	119
Bibliography.....	129
4. Transient active force generation and stress fibre remodelling in cells under cyclic loading	132
4.1. Introduction.....	132
4.2. Model development	135
4.2.1. Cross-bridge modelling	135
4.2.2. Remodelling of stress fibres	140
4.2.3. Non-linear viscoelastic component	143
4.2.4. Modelling parameters.....	144
4.3. Summary of Wille <i>et al.</i> dynamic cell deformation experiments.....	146
4.4. Computational methods	148
4.5. Results and discussion	150
4.5.1. Key trends predicted by model.....	150
4.5.2. Mechanisms underlying observed trends in cell force generation	151
4.5.3. Passive non-linear viscoelastic force contribution	154

4.5.4. Investigation of stretch activated cell signalling	155
4.5.5. Steady state simulations	157
4.6. Concluding remarks.....	159
Appendix 4.A: Non-linear viscoelastic model	162
Appendix 4.B: Phenomenological modelling of transient contractility	165
Bibliography.....	168
5. Compressibility and anisotropy of the ventricular myocardium:	
experimental analysis and microstructural modelling.....	171
5.1. Introduction.....	171
5.2. Compressibility and continuum modelling of myocardium	173
5.2.1. Experimental methods.....	173
5.2.2. Compressible constitutive law for the myocardium.....	176
5.2.3. Experimental results and simulations.....	178
5.2.4. Modelling the behaviour of human tissue	181
5.3. Microstructural modelling	183
5.3.1. RVE constituent materials.....	184
5.3.2. RVE results and discussion	189
5.4. Concluding remarks.....	193
Appendix 5.A: Evidence of weak anisotropy in compression	195
Bibliography.....	197
6. Contractility and remodelling of the left ventricular myocardium	200
6.1. Introduction.....	200
6.2. Computational methodology	202
6.2.1. Passive mechanics	202
6.2.2. Cross-bridge modelling	203
6.2.3. Myofibril remodelling	206
6.2.4. Finite element modelling.....	209
6.2.5. Modelling parameters.....	213
6.3. Results	214
6.4. Concluding remarks.....	220
Bibliography.....	223

7. Concluding remarks	226
7.1. Summary of key contributions.....	226
7.2. Future perspectives	227
Bibliography.....	235

CHAPTER 1

INTRODUCTION AND BACKGROUND



1.1. Introduction to thesis and structure

Cells do not make decisions in a classical conscious sense (Perkins and Swain 2009; Balázsi *et al.* 2011). It is known that they respond to mechanical and biochemical cues from their surrounding environment, such as an substrate ligand density (Gaudet *et al.* 2003) or a glucose source (Adler *et al.* 1973). However, the underlying mechanisms by which cells respond to mechanical cues are not well understood. A cell will typically spread to a higher area on a stiff substrate than on a soft one (Engler *et al.* 2003). Furthermore, differentiation may be controlled by constraining the cells to patches of different shapes (Kilian *et al.* 2010), and cells can even correctly traverse complex mazes in response to applied chemical gradients (Skoge *et al.* 2016).

At a tissue level, pathological remodelling is a leading cause of death and debilitation. In the heart wall, for example, cells grow and synthesize thicker tissue following extended periods of high blood pressure (Rossi 1998). While clinically it is established that such hypertrophy is a comorbidity of hypertension, the mechanisms relating the cellular response to the environmental alteration are not known. There have been many recent

frameworks for phenomenological tissue level remodelling (Rodriguez *et al.* 1994; Humphrey and Rajagopal 2002; Rausch *et al.* 2011), but none explicitly represent such phenomena as cell driven processes. Such models will remain limited in their predictive power and insight until the mechanisms underlying cell remodelling are better understood. In order to develop next generation computational models to guide clinical strategies to counter pathological remodelling, an understanding of what fundamentally drives such cell behaviour must first be established.

1.1.1. Objectives

The overall objective of this thesis is to provide a new understanding of the mechanisms that drive cell spreading and remodelling, and to extend this understanding to remodelling at a tissue and organ level. Novel complex computational methodologies are developed, including a thermodynamic description of stress fibre formation, dynamic contractility, focal adhesion development, and passive tissue mechanics. The specific aims of the current research are given as follows:

1. To provide a fundamental analysis of the system free energy in the spreading of single cells;
2. To investigate the constraint of homeostasis on the spreading behaviour of a cell population;
3. To uncover the link between cross-bridge dynamics and stress fibre remodelling in cells under long term loading;
4. To determine the compressibility and anisotropy of the passive myocardial tissue at a continuum level and the micro-scale;
5. To develop a model of the contractile left ventricle, and investigate the interaction between pathological loading and cellular remodelling in the heart wall.

1.1.2. Thesis structure

This manuscript is presented under the category of an “Article-Based” thesis. Five journal papers (four published, one in preparation) form the backbone of the thesis (Chapters 2-6). A brief outline of each chapter is given as follows:

Chapter 1: The remaining sections of the current chapter present an overview of established theory and relevant literature. In Section 1.2 an overview of relevant theory of continuum mechanics and finite element analysis is provided. The theoretical concepts introduced here are used in the development and implementation of the numerical formulations in the subsequent technical chapters. Section 1.3 provides a general literature review on cell and tissue mechanics. In particular, the structure of the cell and cytoskeleton, and current approaches to computational modelling of cells and tissue are discussed. In addition to the general and broad review of the literature provided in the current chapter, a focused analysis of relevant literature is also provided within each technical chapter (Chapters 2-6).

Chapter 2: I examine the hypothesis that free energy minimization drives the process of cell spreading. Simulations suggest that spreading can be viewed as a competition between (i) decreasing cytoskeletal free energy due to strain induced assembly of cytoskeletal proteins into contractile fibres, and (ii) increasing elastic free energy due to stretching of the mechanically passive components of the cell. Predicted stress fibre (SF) and focal adhesion distributions are shown to correspond closely with experimental observations of cell spreading on ligand patterned substrates Théry *et al.* (2006).

Chapter 3: The *homeostatic ensemble for cells* (as proposed by Shishvan *et al.* (2018)) is expanded to include the free energy associated with formation of adhesion complexes between the cell and substrate. At a low surface collagen density there is a high probability cells will assume rounded morphologies with low spread areas. As the collagen density increases, the probability of cells becoming highly spread with more irregular morphologies increases. This statistical mechanics framework provides new insight into observed cell behaviour on deformable collagen coated substrates (as reported experimentally by Engler *et al.* (2003)).

Chapter 4: A novel cross-bridge cycling model is developed, and coupled with the Vigliotti *et al.* (2015) framework for SF remodelling to describe the dynamic behaviour of the active cytoskeleton. The combined framework provides insight to the mechanisms underlying transient cell force generation during cyclic loading (in relation to the experiments of Wille *et al.* (2006)). A direct link is established between (i) the influence of loading on nanoscale cross-bridge interactions, (ii) the consequential chemical potential imbalance between the attached and detached myosin heads, (iii) the sarcomere stress associated with the number of cycling myosin heads, and (iv) the SF concentration in the cell.

Chapter 5: Experimental evidence that passive excised porcine myocardium exhibits volume change is presented. To simulate the multi-axial passive behaviour of the myocardium a nonlinear volumetric hyperelastic component is combined with the well-established Holzapfel and Ogden (2009) anisotropic model for myocardium. This framework is also shown to describe the experimentally observed behaviour of porcine and human tissue under shear and biaxial loading conditions. A representative volumetric

element (RVE) of myocardium tissue is constructed to parse the contribution of the tissue vasculature to observed volume change under confined compression loading. The RVE is additionally subjected to six modes of shear loading to investigate the influence of micro-scale fibre alignment and dispersion on tissue-scale mechanical behaviour.

Chapter 6: The cross-bridge framework developed in Chapter 4 is incorporated into a contractile model of the left ventricle to examine tissue remodelling associated with cardiac hypertrophy. Physiological levels of ventricular pressure are simulated for healthy conditions, and steady state values of the myofibril concentration and number of in-series sarcomeres (within cells) are determined. Simulation of pathological conditions uncovers a mechanism by which changes to the mechanical environment result in altered actin-myosin cross-bridge cycling, in turn driving remodelling of myofibrils in the heart wall.

Chapter 7: A discussion of key thesis contributions and future perspectives is provided.

1.2. Established theory

1.2.1. Contiuum mechanics

Contiuum mechanics deals with the analysis of kinematics and the mechanical behaviour of materials on a macroscale. In this section the essential elements required for interpretation of the subsequent chapters are outlined. For a more in-depth description the reader is referred to Atkin and Fox (2005) and Holzapfel (2000). Note that vectors, matrices, and tensors are denoted by **bold** typeface. Index notation is often employed to simplify the representation of vector equations. For example, the dot product of two 3D vectors (\mathbf{u}, \mathbf{v}) may be written using summation convention as

$$\mathbf{u} \cdot \mathbf{v} = u_1 v_1 + u_2 v_2 + u_3 v_3 = \sum_{i=1}^3 u_i v_i = u_i v_i, \quad (1.1)$$

where $i = 1, 2, 3$. In the case of a 3x3 tensor, the location of each component may be defined by subscripts $i, j = 1, 2, 3$. As an example, component B_{ij} is the value in the i^{th} row and j^{th} column of tensor \mathbf{B} .

1.2.1.1. Deformation and motion

A classical schematic of a body undergoing motion and deformation is shown in Figure 1.1. A body, encompassing the region Ω_0 in the reference configuration, undergoes a motion χ , such that it subsequently encompasses the region Ω in the current configuration. The position of a material point P in the reference configuration, with respect to the origin O , is denoted by the vector \mathbf{X} . A vector such as \mathbf{X} can be described for all points within the region Ω_0 , known as the material (Lagrangian) coordinates. In the current configuration, the position of P may be defined by

$$\mathbf{x} = \chi(\mathbf{X}, t). \quad (1.2)$$

The coordinates of \mathbf{x} are referred to as the spatial (Eulerian) coordinates. The displacement \mathbf{u} of material point P between the reference and current configuration is therefore $\mathbf{u} = \mathbf{x} - \mathbf{X}$. This may be arranged in terms of \mathbf{X} and t as

$$\mathbf{u} = \chi(\mathbf{X}, t) - \mathbf{X}. \quad (1.3)$$

Consider there exists a second material point Q on the body in the region Ω_0 , and an infinitesimal line element $d\mathbf{X}$ is bound by points P and Q . This is transformed to $d\mathbf{x}$ in the current configuration through the deformation gradient \mathbf{F} , such that:

$$\mathbf{F} = \frac{\partial \chi}{\partial \mathbf{X}} \equiv \frac{\partial \mathbf{x}}{\partial \mathbf{X}}. \quad (1.4)$$

The determinant of \mathbf{F} is known as the Jacobian of the deformation gradient. It denotes the ratio of the volume change from the reference and current configurations at material point P , with

$$J \equiv \det(\mathbf{F}). \quad (1.5)$$

The velocity of material point P is given as

$$\mathbf{v} = \frac{\partial \mathbf{x}}{\partial t}, \quad (1.6)$$

where the partial derivative with respect to time is equivalent to the rate of change of \mathbf{x} for a fixed \mathbf{X} . The spatial velocity gradient \mathbf{L} follows as:

$$\mathbf{L} = \frac{\partial \mathbf{v}}{\partial \mathbf{x}}. \quad (1.7)$$

This may also be calculated as $\mathbf{L} = \dot{\mathbf{F}}\mathbf{F}^{-1}$, where $\dot{\mathbf{F}}$ is the time derivative of the deformation gradient. The spatial velocity gradient is commonly additively decomposed into the symmetric rate of deformation tensor \mathbf{D} and the antisymmetric spin tensor \mathbf{W} , with

$$\mathbf{D} = \frac{1}{2}(\mathbf{L} + \mathbf{L}^T), \text{ and} \quad (1.8)$$

$$\mathbf{W} = \frac{1}{2}(\mathbf{L} - \mathbf{L}^T). \quad (1.9)$$

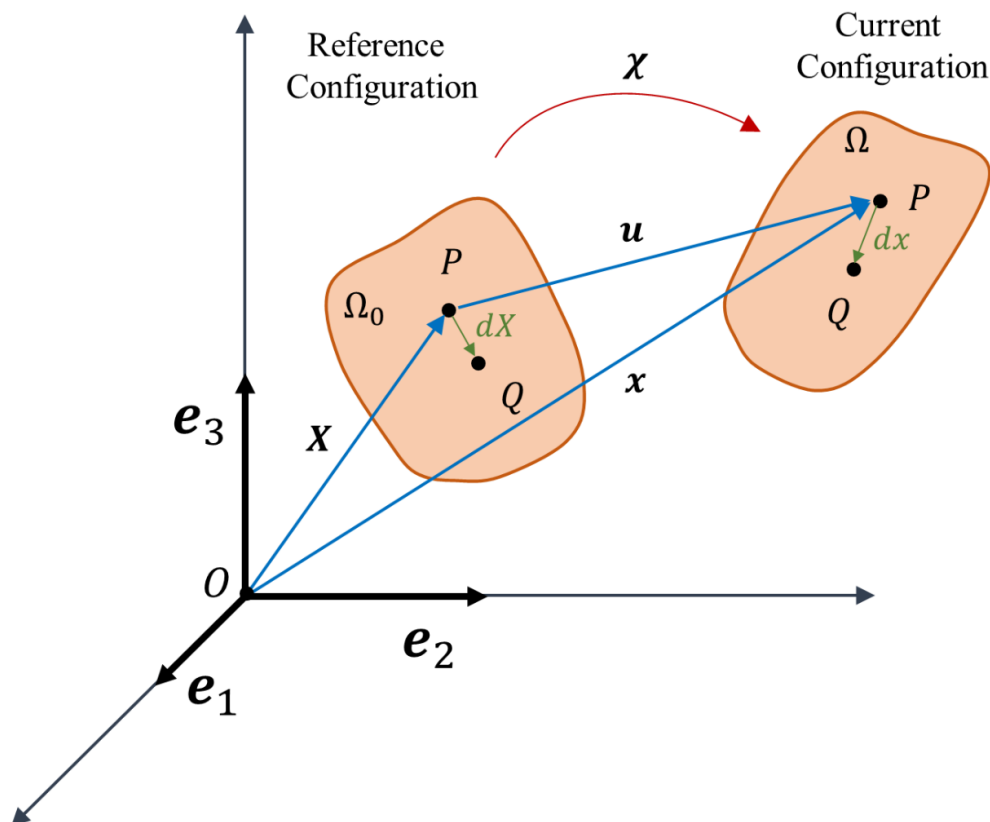


Figure 1.1: Reference (initial/undeformed) and current (deformed) configurations of a body and associated vectors

1.2.1.2. Strain and strain rate measures

There are a variety of different strain measures that may be constructed from the deformation gradient \mathbf{F} . A commonly used strain measure is the Green-Lagrange strain \mathbf{E} , defined as:

$$\mathbf{E} = \frac{1}{2}(\mathbf{F}^T \mathbf{F} - \mathbf{I}), \quad (1.10)$$

where \mathbf{F}^T is the transpose of \mathbf{F} and \mathbf{I} is the identity tensor. The Green-Lagrange strain may also be stated in index notation, with $E_{ij} = \frac{1}{2} \left(\frac{\partial u_i}{\partial X_j} + \frac{\partial u_j}{\partial X_i} + \frac{\partial u_k}{\partial X_i} \frac{\partial u_k}{\partial X_j} \right)$, such that the

infinitesimal strain is found by assuming that the product of the infinitesimals is zero, giving:

$$\epsilon_{ij} = \frac{1}{2} \left(\frac{\partial u_i}{\partial X_j} + \frac{\partial u_j}{\partial X_i} \right). \quad (1.11)$$

The right Cauchy-Green tensor \mathbf{C} , defined in material (Lagrangian) coordinates, is often used as a fundamental measure of deformation in hyperelastic constitutive laws. It is given by:

$$\mathbf{C} = \mathbf{F}^T \mathbf{F}. \quad (1.12)$$

The spatial (Eulerian) counterpart is known as the left Cauchy-Green deformation tensor, and follows as:

$$\mathbf{B} = \mathbf{F} \mathbf{F}^T. \quad (1.13)$$

As the deformation gradient \mathbf{F} is a well-defined second-order tensor, it may be decomposed into an orthogonal rotation tensor \mathbf{R} , and symmetric left (spatial) and right (material) stretch tensors, \mathbf{V} and \mathbf{U} , with

$$\mathbf{F} = \mathbf{R} \mathbf{U} = \mathbf{V} \mathbf{R}. \quad (1.14)$$

Deformation may therefore be considered as a stretch followed by a rotation ($\mathbf{F} = \mathbf{V} \mathbf{R}$) or vice-versa ($\mathbf{F} = \mathbf{R} \mathbf{U}$). These stretch tensors may also be related to the left and right Cauchy-Green tensors:

$$\mathbf{V}^2 = \mathbf{B}; \quad \mathbf{U}^2 = \mathbf{C}. \quad (1.15)$$

The eigenvalues of \mathbf{U} are known as the principal stretches λ_i , and the logarithmic strain tensor may be determined from \mathbf{V} :

$$\boldsymbol{\epsilon}_{\log} = \ln(\mathbf{V}). \quad (1.16)$$

Recall that \mathbf{D} is the symmetric rate of deformation tensor. The logarithmic strain rate is given as:

$$\dot{\boldsymbol{\epsilon}}_{\log} = \mathbf{D}. \quad (1.17)$$

Strain invariants are often useful in defining strain-energy density functions. Three principal invariants may be derived from the Cauchy-Green deformation tensors as follows:

$$I_1 = \text{tr}(\mathbf{C}) = \lambda_1^2 + \lambda_2^2 + \lambda_3^2, \quad (1.18)$$

$$I_2 = \frac{1}{2} [\text{tr}(\mathbf{C})^2 - \text{tr}(\mathbf{C}^2)] = \lambda_1^2 \lambda_2^2 + \lambda_1^2 \lambda_3^2 + \lambda_2^2 \lambda_3^2, \quad \text{and} \quad (1.19)$$

$$I_3 = \det(\mathbf{C}) = J^2 = \lambda_1^2 \lambda_2^2 \lambda_3^2. \quad (1.20)$$

1.2.1.3. Stress measures

If a section is taken through a body in the current configuration (Figure 1.2), the body has a traction tensor \mathbf{t} derived from surface forces, and a vector \mathbf{n} normal to the surface of this section. At a material point P , the Cauchy stress $\boldsymbol{\sigma}$ is a second order symmetric tensor of the force per unit (deformed) surface area ds , given by:

$$\mathbf{t} = \boldsymbol{\sigma} \mathbf{n}. \quad (1.21)$$

The Kirchhoff stress $\boldsymbol{\tau}$ is defined as:

$$\boldsymbol{\tau} = J \boldsymbol{\sigma}, \quad (1.22)$$

where J is the determinant of the deformation gradient \mathbf{F} , a measure of the volume change ratio (between current and reference configuration). The First Piola-Kirchhoff (PK1) stress \mathbf{P} is defined as the force per unit (undeformed) surface area, and is often used for experimental convenience. The nominal stress \mathbf{N} is the transpose of the PK1, such that

$\mathbf{N} = \mathbf{P}^T$. Nanson's formula may be used to map the PK1 stress in the reference configuration to the Cauchy stress in the current configuration:

$$\mathbf{P} = J\boldsymbol{\sigma}\mathbf{F}^{-T}. \quad (1.23)$$

However, the PK1 stress tensor is not necessarily symmetric. The second Piola-Kirchhoff (PK2) stress \mathbf{S} is closely related to the PK1 stress, but is symmetric. It is more often used in the composition of constitutive models, and may be expressed in terms of the Cauchy or PK1 stress as:

$$\mathbf{S} = J\mathbf{F}^{-1}\boldsymbol{\sigma}\mathbf{F}^{-T}; \quad \mathbf{S} = \mathbf{P}\mathbf{F}^T. \quad (1.24)$$

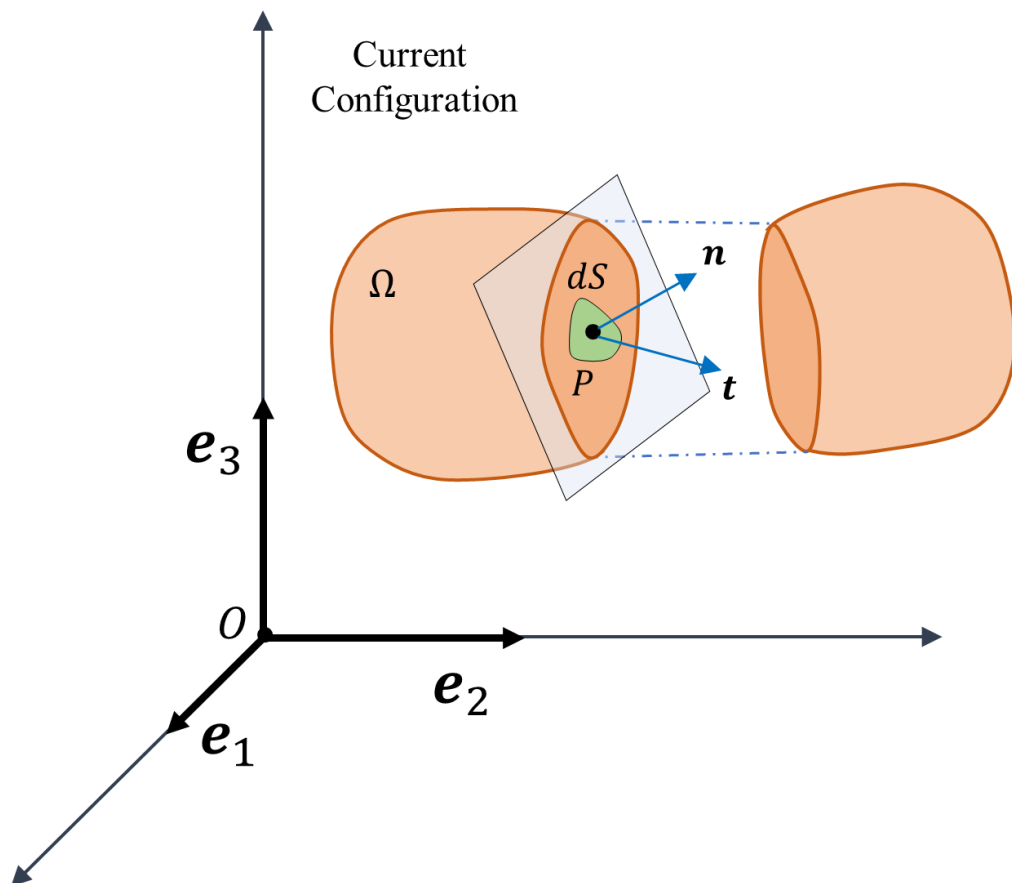


Figure 1.2: Traction \mathbf{t} acting on an infinitesimal surface dS with surface normal \mathbf{n}

1.2.1.4. Hyperelasticity

Hyperelasticity refers to a constitutive material response that is derivable from an elastic free energy potential Ψ . It is particularly useful for materials that experience large deformation, and is widely used in the description of soft tissue mechanical behaviour. The second Piola-Kirchhoff stress may be defined by the derivative of Ψ with respect to the right Cauchy-Green tensor, such that

$$\mathbf{S} = 2 \frac{\partial \Psi(\mathbf{C})}{\partial \mathbf{C}}. \quad (1.25)$$

Through the operation described in equation 1.24, this may be transformed from the reference configuration to the current configuration to yield the Cauchy stress. The strain energy potential may also be phrased in terms of the left Cauchy-Green tensor:

$$\boldsymbol{\sigma} = 2J^{-1} \mathbf{F} \frac{\partial \Psi(\mathbf{C})}{\partial \mathbf{C}} \mathbf{F}^T = 2J^{-1} \mathbf{B} \frac{\partial \Psi(\mathbf{B})}{\partial \mathbf{B}}. \quad (1.26)$$

Strain energy potentials are often stated as functions of strain invariants (as defined in Section 1.2.1.2), with $\Psi(\mathbf{B}) = \Psi(I_1, I_2, I_3)$. For an isotropic strain energy potential, the derivative of Ψ with respect to \mathbf{B} may be determined via the chain rule, such that:

$$\frac{\partial \Psi(\mathbf{B})}{\partial \mathbf{B}} = \frac{\partial \Psi}{\partial I_1} \frac{\partial I_1}{\partial \mathbf{B}} + \frac{\partial \Psi}{\partial I_2} \frac{\partial I_2}{\partial \mathbf{B}} + \frac{\partial \Psi}{\partial I_3} \frac{\partial I_3}{\partial \mathbf{B}}. \quad (1.27)$$

The derivatives of the invariants with respect to the left Cauchy-Green tensor may be determined, giving:

$$\frac{\partial I_1}{\partial \mathbf{B}} = \mathbf{I}, \quad \frac{\partial I_2}{\partial \mathbf{B}} = I_1 \mathbf{I} - \mathbf{B}, \quad \frac{\partial I_3}{\partial \mathbf{B}} = I_3 \mathbf{B}^{-1}. \quad (1.28)$$

Inserting these identities back into equation 1.26, the Cauchy stress may then be expressed as a function of \mathbf{B} , with

$$\boldsymbol{\sigma} = 2J^{-1} \left[I_3 \frac{\partial \Psi}{\partial I_3} \mathbf{I} + \left(\frac{\partial \Psi}{\partial I_1} + I_1 \frac{\partial \Psi}{\partial I_2} \right) \mathbf{B} - \frac{\partial \Psi}{\partial I_2} \mathbf{B}^2 \right]. \quad (1.29)$$

For problems involving compressibility, it is often convenient to additively decompose the isochoric and volumetric response of the free energy potential:

$$\Psi(\mathbf{B}) = \Psi_{vol}(J) + \Psi_{iso}(\bar{\mathbf{B}}). \quad (1.30)$$

Here, $\Psi_{vol}(J)$ is the volumetric response which depends only on the volume ratio J , and $\Psi_{iso}(\bar{\mathbf{B}})$ is the isochoric response, which is a function of the isochoric form of the left Cauchy-Green tensor, given by $\bar{\mathbf{B}} = J^{-2/3}\mathbf{B}$. This operation removes all volumetric contributions. Similarly, the Cauchy stress may be decoupled as follows:

$$\boldsymbol{\sigma} = \boldsymbol{\sigma}_{vol} + \boldsymbol{\sigma}_{iso}. \quad (1.31)$$

These stress contributions are then defined by:

$$\boldsymbol{\sigma}_{vol} = 2J^{-1}\mathbf{B} \frac{\partial \Psi_{vol}(J)}{\partial \mathbf{B}} = \frac{\partial \Psi_{vol}(J)}{\partial J} \mathbf{I}, \quad (1.32)$$

$$\boldsymbol{\sigma}_{iso} = 2J^{-1}\mathbf{B} \frac{\partial \Psi_{iso}(\bar{\mathbf{B}})}{\partial \mathbf{B}} = \bar{\boldsymbol{\sigma}} - \frac{tr(\bar{\boldsymbol{\sigma}})}{3} \mathbf{I}, \quad (1.33)$$

where the stress term $\bar{\boldsymbol{\sigma}}$ is given by the expression

$$\bar{\boldsymbol{\sigma}} = 2J^{-1}\bar{\mathbf{B}} \frac{\partial \Psi_{iso}(\bar{\mathbf{B}})}{\partial \bar{\mathbf{B}}}. \quad (1.34)$$

1.2.2. Finite element method

The numerical solutions of continuum mechanics problems presented in this thesis are solved using the finite element (FE) method. The commercially available software Abaqus (Dassault Systemes, RI, USA) is frequently used in the analyses within subsequent chapters, predominantly due to its customisability via user subroutines (for development of novel material laws, novel surface interaction laws, and bespoke non-local solution schemes) and robust meshing techniques. Here, a brief background on the implicit FE solution scheme and user-defined material subroutines is presented. To facilitate this discussion, Voigt notation is employed in this section.

1.2.2.1. Implicit solutions

The stress state in a body is incrementally updated in the implicit FE method. Following an applied deformation, the stress state at time $t + \Delta t$ is solved iteratively via convergence of a residual force vector to zero. The Abaqus/Standard implicit solver implements a form of the Newton-Raphson method, as described in this section. The principle of virtual work (PVW) provides the fundamental equation of the finite element method:

$$\int_{\Omega} \delta \boldsymbol{\varepsilon}^T \boldsymbol{\sigma} d\Omega = \int_S \delta \mathbf{u}^T \mathbf{t} dS, \quad (1.35)$$

where Ω is a reference volume on which equilibrium is enforced, bounded by a surface S . $\boldsymbol{\sigma}$ and \mathbf{t} are the stress and surface tension, respectively, while $\delta \boldsymbol{\varepsilon}$ and $\delta \mathbf{u}$ are the virtual strain and virtual displacement vectors. The FE approximation can then be introduced over every element e of volume Ω and surface area S_e , allowing the displacements and strain to be rewritten as:

$$\delta \mathbf{u} = \hat{\mathbf{N}}_e \delta \mathbf{u}_e, \quad (1.36)$$

$$\delta \boldsymbol{\varepsilon} = \hat{\mathbf{B}}_e \delta \mathbf{u}_e, \quad (1.37)$$

where $\widehat{\mathbf{N}}_e$ is the global shape function matrix, $\widehat{\mathbf{B}}_e$ is a matrix of spatial gradients of the shape functions, and $\delta \mathbf{u}_e$ is a vector of nodal virtual displacements. The PVW then becomes:

$$\sum_e \int_{\Omega_e} \delta \mathbf{u}_e^T \widehat{\mathbf{B}}_e^T \boldsymbol{\sigma}(\mathbf{u}_e) d\Omega = \sum_e \int_{S_e} \delta \mathbf{u}_e^T \widehat{\mathbf{N}}_e^T \mathbf{t} dS, \quad (1.38)$$

$$\delta \mathbf{u}^T \int_{\Omega} \widehat{\mathbf{B}}^T \boldsymbol{\sigma}(\mathbf{u}) d\Omega - \delta \mathbf{u}^T \int_S \widehat{\mathbf{N}}^T \mathbf{t} dS = 0, \quad (1.39)$$

$$\delta \mathbf{u}^T \left(\int_{\Omega} \widehat{\mathbf{B}}^T \boldsymbol{\sigma}(\mathbf{u}) d\Omega - \int_S \widehat{\mathbf{N}}^T \mathbf{t} dS \right) = 0. \quad (1.40)$$

As the virtual displacement $\delta \mathbf{u}^T$ is arbitrary, it may be stated as:

$$\int_{\Omega} \widehat{\mathbf{B}}^T \boldsymbol{\sigma}(\mathbf{u}) d\Omega - \int_S \widehat{\mathbf{N}}^T \mathbf{t} dS = 0. \quad (1.41)$$

The second term is the external force vector, and may be phrased as follows:

$$\int_S \widehat{\mathbf{N}}^T \mathbf{t} dS = \mathbf{F}_{ext}. \quad (1.42)$$

Introducing linear elasticity:

$$\boldsymbol{\sigma} = \mathbf{D}\boldsymbol{\varepsilon} = \mathbf{D}\widehat{\mathbf{B}}\mathbf{u}_e, \quad (1.43)$$

where \mathbf{D} is a fourth order elasticity tensor. The PVW may again be rewritten with consideration of linear elasticity, such that:

$$\int_{\Omega} \widehat{\mathbf{B}}^T \mathbf{D} \widehat{\mathbf{B}} \mathbf{u}_e d\Omega - \mathbf{F}_{ext} = 0, \quad (1.44)$$

$$\left(\int_{\Omega} \widehat{\mathbf{B}}^T \mathbf{D} \widehat{\mathbf{B}} d\Omega \right) \mathbf{u}_e - \mathbf{F}_{ext} = 0, \quad (1.45)$$

$$\mathbf{K} \mathbf{u}_e - \mathbf{F}_{ext} = 0, \quad (1.46)$$

where \mathbf{K} is the familiar form of the global FE characteristic/ stiffness matrix. Returning to the PVW as shown in equation 1.41, a set of global equations for the out of balance residual force \mathbf{G} (dependent on \mathbf{u}) may be developed:

$$\mathbf{G}(\mathbf{u}) = \int_{\Omega} \hat{\mathbf{B}}^T \boldsymbol{\sigma}(\mathbf{u}) d\Omega - \int_S \hat{\mathbf{N}}^T \mathbf{t} dS. \quad (1.47)$$

This non-linear set of equations must be solved for convergence to attain an equilibrium stress state in the body, with

$$\mathbf{G}(\mathbf{u}) = 0. \quad (1.48)$$

For boundary value problems requiring a non-linear analysis and complex geometries, such a minimisation for convergence must be solved iteratively. As mentioned previously, the Abaqus/Standard implicit solver uses a Newton-Raphson methodology to step from time t to time $t + \Delta t$ by taking an initial guess and iterating until the solution converges. In the Newton-Raphson scheme, a tangent to the function $f(x)$ is used to approximate to a more accurate solution:

$$x_{n+1} = x_n - \frac{f(x_n)}{f'(x_n)}. \quad (1.49)$$

An accurate approximation is deemed to be obtained when a tolerance is achieved, i.e.

$$|x_{i+1} - x_i| < tol. \quad (1.50)$$

Following an initial guess for all nodal displacements $\mathbf{u}_i^{t+\Delta t}$ within an increment of an implicit analysis, the numerical scheme iterates until the internal forces and externally applied loads/boundary conditions achieve a stable equilibrium. As such, the Newton-Raphson minimisation process is applied to the residual force vector:

$$\mathbf{G}(\mathbf{u}^{t+\Delta t}) = 0. \quad (1.51)$$

For the i^{th} iteration:

$$\mathbf{u}_{i+1}^{t+\Delta t} = \mathbf{u}_i^{t+\Delta t} - \left[\frac{\partial \mathbf{G}(\mathbf{u}_i^{t+\Delta t})}{\partial \mathbf{u}} \right]^{-1} \mathbf{G}(\mathbf{u}_i^{t+\Delta t}). \quad (1.52)$$

Considering the change in nodal displacements $\partial \mathbf{u}_{i+1}$ gives:

$$\partial \mathbf{u}_{i+1} = \mathbf{u}_{i+1}^{t+\Delta t} - \mathbf{u}_i^{t+\Delta t} = - \left[\frac{\partial \mathbf{G}(\mathbf{u}_i^{t+\Delta t})}{\partial \mathbf{u}} \right]^{-1} \mathbf{G}(\mathbf{u}_i^{t+\Delta t}). \quad (1.53)$$

This may be expressed in terms of the tangent stiffness matrix \mathbf{K} :

$$\mathbf{K}(\mathbf{u}_{i+1}^{t+\Delta t}) = \frac{\partial \mathbf{G}(\mathbf{u}_i^{t+\Delta t})}{\partial \mathbf{u}}, \quad (1.54)$$

$$\mathbf{K}(\mathbf{u}_{i+1}^{t+\Delta t}) \partial \mathbf{u}_{i+1} = \mathbf{G}(\mathbf{u}_i^{t+\Delta t}). \quad (1.55)$$

These are the finite element equations that must be solved during each iteration of the implicit method. In contrast to the linear elastic form of the FE equations given in equation 1.46, the solution variable in a non-linear implicit scheme is the incremental displacement. Finally, the tangent stiffness matrix may be expressed as:

$$\begin{aligned} \mathbf{K}(\mathbf{u}) &= \frac{\partial \mathbf{G}(\mathbf{u})}{\partial \mathbf{u}} = \frac{\partial}{\partial \mathbf{u}} \left(\int_{\Omega} \widehat{\mathbf{B}}^T \boldsymbol{\sigma}(\mathbf{u}) d\Omega - \mathbf{F}_{ext} \right) \\ &= \frac{\partial}{\partial \mathbf{u}} \left(\int_{\Omega} \widehat{\mathbf{B}}^T \boldsymbol{\sigma}(\mathbf{u}) d\Omega \right) \\ &= \int_{\Omega} \widehat{\mathbf{B}}^T \frac{\partial \boldsymbol{\sigma}(\mathbf{u})}{\partial \mathbf{u}} d\Omega = \int_{\Omega} \widehat{\mathbf{B}}^T \frac{\partial \boldsymbol{\sigma}(\mathbf{u})}{\partial \boldsymbol{\varepsilon}} \frac{\partial \boldsymbol{\varepsilon}}{\partial \mathbf{u}} d\Omega \\ &= \int_{\Omega} \widehat{\mathbf{B}}^T \frac{\partial \boldsymbol{\sigma}(\mathbf{u})}{\partial \boldsymbol{\varepsilon}} \widehat{\mathbf{B}} d\Omega. \\ \text{i.e. } \mathbf{K}(\mathbf{u}) &= \int_{\Omega} \widehat{\mathbf{B}}^T \mathbf{D}^{\text{tan}} \widehat{\mathbf{B}} d\Omega, \end{aligned} \quad (1.56)$$

where \mathbf{D}^{tan} is the consistent tangent matrix, equal to the Jacobian of the constitutive law $\partial \boldsymbol{\sigma} / \partial \boldsymbol{\varepsilon}$. For each iteration of the Newton-Raphson method, it is necessary to calculate and

invert \mathbf{K} . Although this is computationally expensive, it ensures an accurate solution is achieved. Additionally, it permits use of relatively large time steps when compared to alternative approaches such as the explicit method. For more details on the finite element method, the reader is referred to Bathe (2006) and Fagan (1992).

1.2.2.2. Implementation of user defined material subroutines

Abaqus, in addition to providing a wide library of built-in material constitutive laws, allows the user to define new constitutive formulations via a user defined material subroutine (UMAT). At each iteration within each time increment the UMAT is called by the main program at each integration point associated with the novel material law. The material deformation is passed into the subroutine at the beginning of the increment, and the stress state must be calculated and passed out. Additionally, the material Jacobian (consistent tangent matrix) $\partial\Delta\boldsymbol{\sigma}/\partial\Delta\boldsymbol{\varepsilon}$ must be computed. This defines the change in stress at the end of the time increment caused by an infinitesimal perturbation of the strain. A numerical approximation of the material Jacobian may be attained through a perturbation method as previously described by Miehe (1996). Such an approach has been used in non-linear hyperelastic implementations (Sun *et al.* 2008; Nolan *et al.* 2014), and is employed in subsequent chapters of this thesis. The approximation uses a linearised incremental form of the Jaumann rate of the Kirchhoff stress:

$$\Delta\boldsymbol{\tau} - \Delta\mathbf{W}\boldsymbol{\tau} - \boldsymbol{\tau}\Delta\mathbf{W}^T = \mathbb{C}^{\tau J}:\Delta\mathbf{D}, \quad (1.57)$$

where $\boldsymbol{\tau}$ is the Kirchhoff stress, \mathbf{W} and \mathbf{D} are the spin and rate-of deformation tensors (as defined in Section 1.2.1.1), and $\mathbb{C}^{\tau J}$ is the tangent modulus tensor for the Jaumann rate of the Kirchhoff stress. $\Delta\mathbf{W}$ and $\Delta\mathbf{D}$ may be stated in terms of the deformation gradient \mathbf{F} , such that

$$\Delta\mathbf{W} = \frac{1}{2}(\Delta\mathbf{F}\mathbf{F}^{-1} - (\Delta\mathbf{F}\mathbf{F}^{-1})^T), \quad \text{and} \quad (1.58)$$

$$\Delta \mathbf{D} = \frac{1}{2} (\Delta \mathbf{F} \mathbf{F}^{-1} + (\Delta \mathbf{F} \mathbf{F}^{-1})^T). \quad (1.59)$$

Through a perturbation of the deformation gradient the tangent moduli may be approximated by a forward difference scheme. The perturbation is performed on every degree of freedom in an analysis. In a 3D analysis this requires a perturbation of \mathbf{F} six times (once for each independent component of $\Delta \mathbf{D}$):

$$\Delta \mathbf{F}^{(ij)} = \frac{\epsilon}{2} (e_i \otimes e_j \mathbf{F} + e_j \otimes e_i \mathbf{F}), \quad (1.60)$$

where ϵ is a small perturbation parameter, and e_i is the basis vector in the spatial description. The ‘total’ perturbed deformation gradient is given by $\hat{\mathbf{F}}^{(ij)} = \Delta \mathbf{F}^{(ij)} + \mathbf{F}$. The Kirchhoff stress (in Voigt notation) is then calculated from this perturbed deformation gradient, i.e. $\boldsymbol{\tau}(\hat{\mathbf{F}}^{(ij)})$. Finally, the material Jacobian \mathbb{C} is approximated with:

$$\mathbb{C}^{(ij)} = \frac{1}{J} \mathbb{C}^{\tau J (ij)} = \frac{1}{J \epsilon} [\boldsymbol{\tau}(\hat{\mathbf{F}}^{(ij)}) - \boldsymbol{\tau}(\mathbf{F})], \quad (1.61)$$

where J is the determinant of the deformation gradient. For each perturbation of equation 1.61, six independent components of \mathbb{C} will be attained in a 3D simulation, with six perturbations required to construct the 6x6 tangent matrix.

In Abaqus, the user may also define contact or interaction behaviour between two surfaces, by means of a user defined interface subroutine (UINTER). Here the routine is called for every node on a slave surface, again for every iteration. The interface stresses (or tractions) are calculated as functions of the relative displacement between the two surfaces. An interface stiffness matrix $\partial \mathbf{T} / \partial \mathbf{u}$, akin to the UMAT consistent tangent matrix, must also be updated.

1.3. Background and literature

1.3.1. Cell structure and forces

The cell is comprised of a considerable number of molecules and structures that respond to mechanical and chemical stimuli (Alberts 1994), including the nucleus, cytoskeleton, and cytoplasm. The cytoskeleton plays a dominant role in defining the mechanical behaviour of the cell, such as resistance to deformation (Weafer *et al.* 2015; Ronan *et al.* 2012), generating forces that enable the cell to move and change shape (Pollard and Borisy 2003), and connecting physically and biochemically to the microenvironment (Cheng *et al.* 2017). Cells may interact with the surrounding extra-cellular matrix (ECM) or substrate via formation of focal adhesions, which transmit mechanical cues to the cytoskeleton (Pathak *et al.* 2011). The nucleus and cytoplasm also contribute a passive mechanical response to cell deformation (Caille *et al.* 2002). A brief description of the cellular cytoskeleton, active force generation, and adhesion development is provided in the following sections.

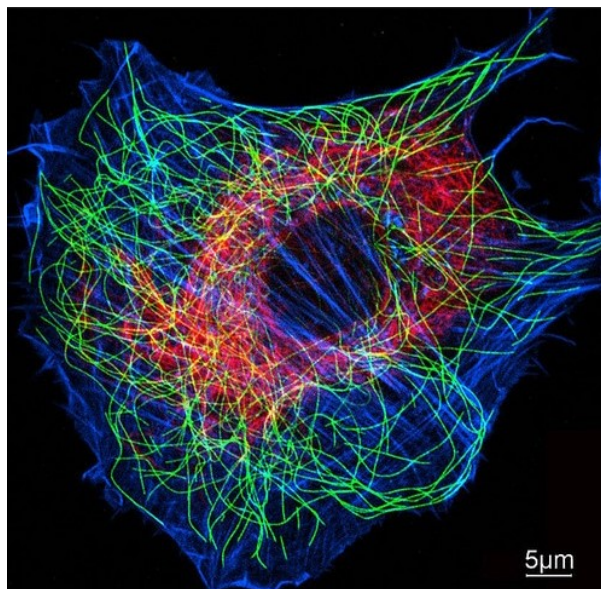


Figure 1.3: Fluorescent image of the actin cytoskeleton in a single cell in 2D culture. Intermediate filaments are shown in red, microtubules are shown in green, and actin filaments are shown in blue. Image courtesy of C-A. Schoenenberger, R. Suetterlin (University of Basel, Switzerland).

1.3.1.1. Microtubules and intermediate filaments

The cytoskeleton can be divided into three main classes of protein groups: microtubules, intermediate filaments, and actin filaments. These elements are highlighted in the cell shown in Figure 1.3. Microtubules (Figure 1.4a) are composed of helically wound α - and β - tubulin proteins (Martini *et al.* 2012), and are the largest cytoskeletal component with a diameter of ~25 nm (Lodish 2000). They are involved in important cell processes such as organelle transport and cell division (Blain 2009; Alberts 1994). In terms of a mechanical contribution, *in-vitro* studies have shown microtubules may play a role in the shear and compression resistance of cells (Dowling *et al.* 2012; Brangwynne *et al.* 2006). Intermediate filaments (Figure 1.4c) are comprised of tetrameric proteins, which assemble into a super-coiled sheet with a rope-like appearance (Fuchs and Weber 1994). They range in diameter from 8-10 nm, and are thought to anchor the nucleus within the cell (Dupin *et al.* 2011). They have been shown to play a role in resisting mechanical deformation (Ofek *et al.* 2009), though their precise function is not fully understood (Eriksson *et al.* 2009).

1.3.1.2. Actin filaments and stress fibres

Actin filaments (Figure 1.4b) are the primary functional cytoskeletal component in regulating cell mechanical behaviour (Trickey, Vail, and Guilak 2004; Yeung *et al.* 2005). G-actin (globular actin) polymerises and coils into a double-helix to create F-actin (filamentous actin), which often anchors to focal adhesions (Cramer *et al.* 1997). Actin filaments continually undergo polymerisation and depolymerisation, due to association and dissociation of G-actin at either end. Phosphorylated myosin spontaneously self-assembles in bi-polar filaments (Alberts 1994). The actin filament interacts with myosin to form tightly woven bundles of “stress fibres”. Cross-bridge cycling of myosin II generates contractile forces required for cell motility, morphology, and adhesion (Sato *et al.* 2006; Blain 2009; Fletcher and Mullins 2010).

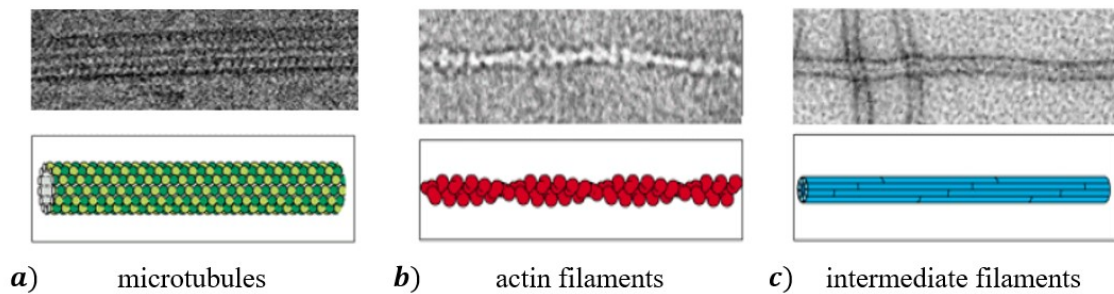


Figure 1.4: The cell cytoskeleton is composed of three filamentous groups: a) microtubules, b) actin filaments, and c) intermediate filaments. Adapted image from Alberts (1994).

1.3.1.3. Force generation via cross-bridge cycling

A standard cross-bridge cycle operates as follows (Lymn and Taylor 1971): Following binding of ATP to myosin, hydrolysis into ADP and P_i (inorganic phosphate) causes a change in configuration/pivot of the myosin head. The myosin head attaches to the actin filament (Figure 1.5a) and, depending on the boundary conditions, a tension generating stroke may occur. The stroke consists of the myosin head returning to an uncocked configuration following release of ADP and P_i (Figure 1.5b). This induces a stretch in the myosin tail thereby exerting traction on the actin filament. The bond between the myosin head and actin dissociates, the head detaches, and the cycle repeats. The tension within a sarcomere depends on the number of actively cycling myosin heads (Huxley 1957).

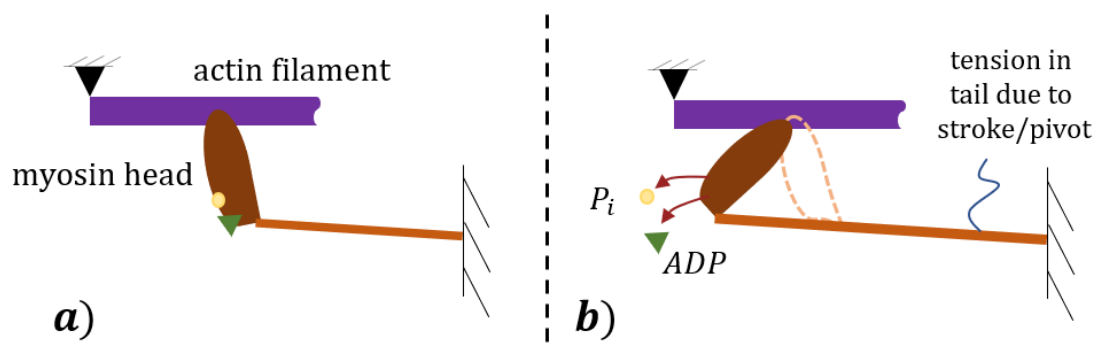


Figure 1.5: Schematic of cross-bridge tension generation: a) myosin head binds to actin filament; b) stroke/pivot of myosin head induces tension in the myosin tail.

1.3.1.4. Focal adhesions

Focal adhesions (FAs) are multi-protein complexes that mediate cell anchorage to the extra-cellular environment (Figure 1.6), also providing a mechanical link to the contractile actin cytoskeleton (Wang *et al.* 1993). While the exact pathways of FA formation are not fully understood, a large body of evidence suggests that it is mechanically controlled. High tractions at contact sites increase the rate of FA assembly (Tan *et al.* 2003; Balaban *et al.* 2001), and FA formation is disrupted by inhibition of SF formation and contractility (Pasapera *et al.* 2010; Burridge and Guilluy 2016). When cells are constrained to patterned ligand geometries, FAs tend to cluster around the patch periphery (Théry *et al.* 2006), with adhesion clustering increased at higher cell spread areas (Chen *et al.* 2003).

Assembly and disassembly of FAs involves the coordinated regulation of the GTP-binding protein RhoA (Ridley and Hall 1992), through cross-talk between integrins and several adhesion receptors (e.g. cadherins). Attachment of the cell to the ECM is mediated by the integrin family of transmembrane proteins. All integrins contain an α and β subunit, and bind to ligands on a substrate surface (in further support of traction mediated FA assembly, these integrins do not bind to ECM ligands in suspension (Gilmore and Burridge 1996)). Integrins cluster at the adhesion site, and form complex structures with cytoskeletal connector proteins such as α -actinin, vinculin, and talin (Wehrle-Haller and Imhof 2002). This allows transmission of mechanical activity from the ECM through to the cytoskeleton. Focal adhesions also orient various signalling proteins (such as paxillin and FAK) at sites of integrin binding and clustering (Sastrý and Burridge 2000), from which numerous intracellular pathways emanate to regulate cell survival, growth, and gene expression (Schwartz *et al.* 1995).

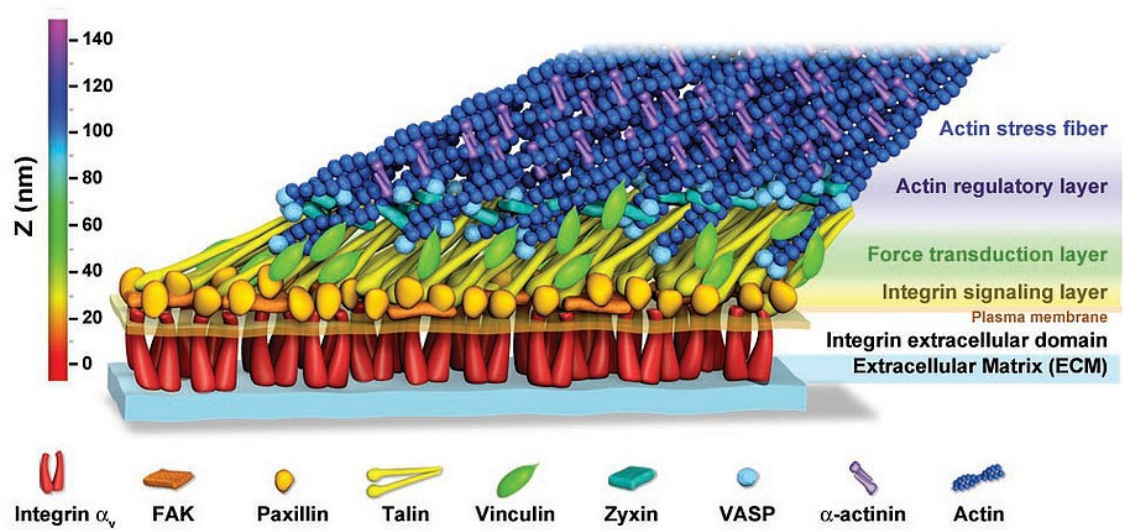


Figure 1.6: Schematic of focal adhesion molecular architecture, depicting interaction between ECM, integrins, and stress fibres (Kanchanawong *et al.* 2010).

1.3.2. Computational cell modelling

Computational models are widely used in engineering and biology to generate new insights, deepen understanding, and to interpret and guide experimental investigation. In this section an overview of cell mechanics modelling is provided, starting with a discussion of the widespread simplified approach of treating the cell as a passive material, followed by an overview of recent models that incorporate active biomechanical processes.

1.3.2.1. Passive cell models

In understanding the mechanical behaviour of cells, simple material laws such as linear elasticity are often used by experimentalists to determine an effective stiffness (Young's modulus) for the cytoplasm or nucleus (Jones *et al.* 1999; Solon *et al.* 2007). Linear elastic material laws have been used to simulate cell compression experiments (Ofek, Natoli, and Athanasiou 2009), and cell deformation due to fluid flow (Zhao, Vaughan, and Mcnamara 2015; McCoy, Jungreuthmayer, and O'Brien 2012; Jungreuthmayer *et al.* 2009). When cells undergo large deformation, hyperelastic models are commonly used to represent experimentally observed non-linear mechanical behaviour (Lim *et al.* 2004; Zhao, Vaughan, and Mcnamara 2015; Caille *et al.* 2002). However, these models do not account for the time dependency in the cell's response. To explain such behaviour, viscoelastic models have been implemented to study cells subjected to micropipette aspiration (Sato *et al.* 1996; Jafari Bidhendi and Korhonen 2012; Trickey *et al.* 2006), unconfined compression (Leipzig and Athanasiou 2005), and cantilever indentation (Koay *et al.* 2003).

While these approaches have had some success in highlighting general trends, they treat the cell as a passive homogeneous continuum. They do not account for the tension generated via stress fibre (SF) contractility or the active remodelling of the cytoskeleton. As a result, they cannot be used to correctly interpret the biomechanisms underlying the

mechanical response of cells to loading. In particular passive models do not describe the changes in cell stiffness that result from spreading, as has been highlighted in several early studies that demonstrate that a unique set of passive parameters cannot be used to describe the mechanical response of a cell at different levels of spreading (McGarry and McHugh 2008; Thoumine *et al.* 1999). Hyperelastic and viscoelastic constitutive laws are not without merit however. The computational-experimental studies of Dowling *et al.* (2012) and Reynolds and McGarry (2015) demonstrate that when the actin cytoskeleton is disrupted using the chemical agent cytochalasin D, the remaining cell components can be accurately described using passive hyper-viscoelastic material laws.

1.3.2.2. Active models

Several models have been developed to explain the cytoskeletal structure and contribution to the cellular stress state. Tensegrity is an early example of such a model, adapted from the architectural system known as tensional integrity (Ingber 1993). It incorporates a series of load bearing rigid struts and tension bearing elastic threads (representing microtubules and actin SFs, respectively). The model therefore allows for a cell to be pre-stressed prior to the application of load. In practice, the framework requires a manual description of strut positioning, and in a finite element simulation a new fibre network must be generated for every cell geometry and spread state considered (McGarry and Prendergast 2004). While the tensegrity model provided the groundwork for modelling tension generating fibres within the cell, it does not allow for an actively remodelling cytoskeleton. Additionally, the model assumes that SFs are supported exclusively by load bearing microtubules. However, experimental evidence has shown disruption of microtubules leads to an increase in the cellular traction force (Kolodney and Elson 1995). Motivated by experimentally observed SF remodelling, Deshpande *et al.* (2007) proposed a bio-chemo-mechanical model that considers (i) SF formation due to activation of proteins and signalling molecules, (ii) tension dependent SF dissociation, and (iii) strain

rate dependent SF tension. A first order kinetic equation is used to describe the formation and dissociation of SFs:

$$\frac{d\eta}{dt} = (1 - \eta) \frac{C k_f}{\theta} - \left(1 - \frac{\sigma}{\sigma_0} \eta \frac{k_b}{\theta}\right), \quad (1.62)$$

where η is a non-dimensional activation level of a SF ($0 \leq \eta \leq 1$). k_f and k_b are forward and backward reaction rate constants, respectively, and C is an activation signal for SF formation that decays over time ($C = \exp(-t/\theta)$). The contractile behaviour of the SF, σ/σ_0 , is described by a Hill-type force/strain-rate dependence. The Deshpande model has been implemented in finite element analysis to explore several key aspects of cell behaviour (Figure 1.7), including the contractile response of cells spread on micro-posts (McGarry *et al.* 2009; Ronan *et al.* 2014), compression resistance of cells (McGarry 2009; Weafer *et al.* 2013), shear resistance of cells (Ofek *et al.* 2010; Dowling *et al.* 2012), cell-cell junctions (Ronan *et al.* 2015), and the active response to micropipette aspiration (Reynolds *et al.* 2014). The framework was extended to describe the transient response of cells to cyclic loading through inclusion of a fading-memory-type model (Reynolds and McGarry 2015), where it was shown the active contractile forces dominate the cellular mechanical response.

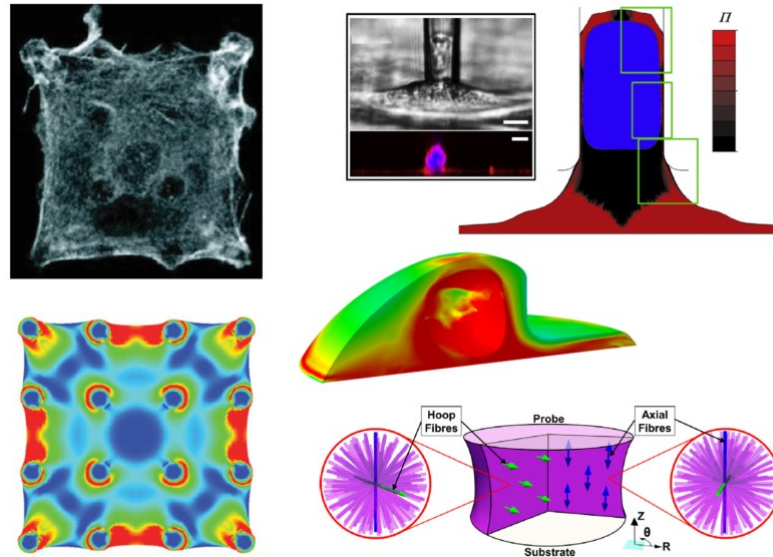


Figure 1.7: Finite element studies based on implementation of Deshpande cytoskeletal model. Images adapted from McGarry *et al.* 2009; Reynolds *et al.* 2014; Reynolds and McGarry 2015; Dowling and McGarry 2014.

Since the development of the bio-chemo-mechanical model Deshpande *et al.* (2007), several other cytoskeletal frameworks have been proposed. Kaunas and Hsu (2009) presented a kinematic model based on mixture theory to describe stress fibre orientation. A total mass fraction of SFs is maintained, and the rate of SF dissociation is governed by excessive fibre stretching or shortening:

$$\frac{d\Phi^i}{dt} = -k^i\Phi^i; \quad k^i = k_0[1 + k_1\Delta\alpha^i], \quad (1.63)$$

where Φ^i is the mass fraction of fibre family i , and $\Delta\alpha^i$ is the (normalized) deviation from a homeostatic level of stretch. It is assumed that SFs assemble as quickly as they disassemble. The model successfully describes the reorientation of SFs subjected to high frequency 2D dynamic stretching (Figure 1.8a). Vernerey and Farsad (2011) proposed a multiphasic formulation motivated by key cellular behaviour: mass exchange of cytoskeletal components, cytosol fluid pressure, actin monomer transport, and SF contractility. Fibre formation arises from mass exchange with dispersed actin monomers, and depends on SF tension. The tension that develops within a SF is both strain and strain

rate dependent. The contractile behaviour of cells on micro-pillars is shown to be predicted by this framework (Figure 1.8b).

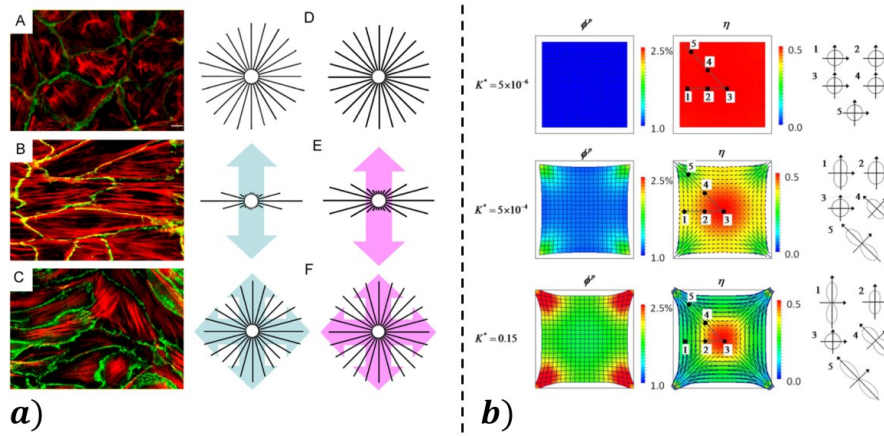


Figure 1.8: a) Experimental and predicted SF alignment under high frequency cyclic loading (Kaunas and Hsu 2009); b) Simulated contractile behaviour of cells on micro-pillars with contours showing SF volume fraction ϕ^p and degree of SF anisotropy η (Vernerey and Farsad 2011).

The model of Obbink-Huizer *et al.* (2014) combines features from Deshpande (2007) with Vernerey and Farad (2011). It also imposes the constraint of constant polymerized plus depolymerized actin quantities, and accounts for strain dependence in the SF kinetics. The rate of change in SF volume fraction (in direction θ) is given by

$$\frac{d\Phi_{\theta}^p}{dt} = (k_0^f + k_1^f \sigma_{max} f_{\varepsilon, \alpha} f_{\dot{\varepsilon}}) \Phi^m - k_d \Phi_{\theta}^p, \quad (1.64)$$

where constants k_0^f , k_1^f , and k_d describe the basal SF formation, stress dependent SF formation, and SF dissociation, respectively. $f_{\varepsilon, \alpha}$ and $f_{\dot{\varepsilon}}$ are functions that govern the dependence of the contractile force on the strain and strain-rate, and Φ^m is the volume fraction of monomers available for SF formation. Fibre formation increases with increasing active stress, and reduces with increasing shortening velocity. The framework accurately predicts the cyclic response of cells in both a 2D and 3D setting (Figure 1.9a), and has subsequently been used to investigate the role of SF contractility in the development of tissue engineered heart valves (Loerakker *et al.* 2016) (Figure 1.9b).

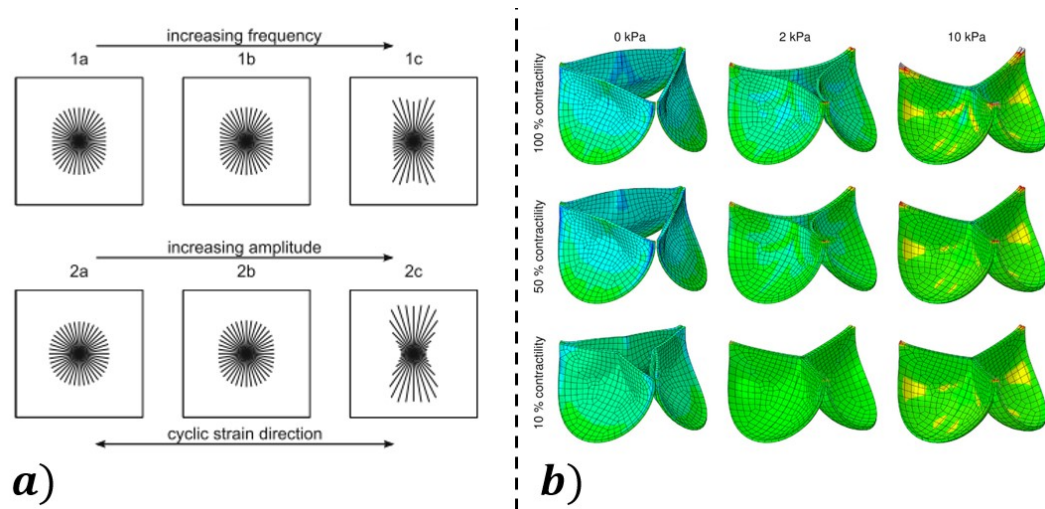


Figure 1.9: a) Predicted equilibrium SF distributions for different strain frequencies (top row) and strain amplitudes (bottom row) from Obbink-Huizer *et al.* (2014); b) Circumferential strain distributions in heart valves following remodelling due to pressure and cell contraction (Loerakker *et al.* 2016).

The role of the active cytoskeleton in trans-endothelial cell migration was recently investigated by Cao *et al.* (2016). A chemo-mechanical description of the SF network is provided, with the contractility ρ given as

$$\rho = \frac{\beta\rho_0}{\beta - \alpha} + \frac{\alpha K - 1}{\beta - \alpha} \varepsilon, \quad (1.65)$$

where ρ_0 is the contractility on the absence of adhesions, K is the effective passive stiffness of the actin filaments, and ε is the filament strain. α and β relate to the molecular mechanisms regulating the stress-dependent signalling pathways and engagement of motors, respectively. This model was also included within a chemo-mechanical description of the cell-matrix system free energy (Shenoy *et al.* 2016), where it is demonstrated that the free energy is lower for cells on stiff substrates (relative to soft substrates), providing a thermodynamic motivation for durotaxis (Figure 1.10a). Recently, Gong *et al.* (2018) demonstrated the important influence of substrate viscoelastic behaviour in the spreading of cells. Cell migration and durotaxis have also

been investigated in the active modelling approaches of González-Valverde and García-Aznar (2018) (Figure 1.10b) and Escribano *et al.* (2018).

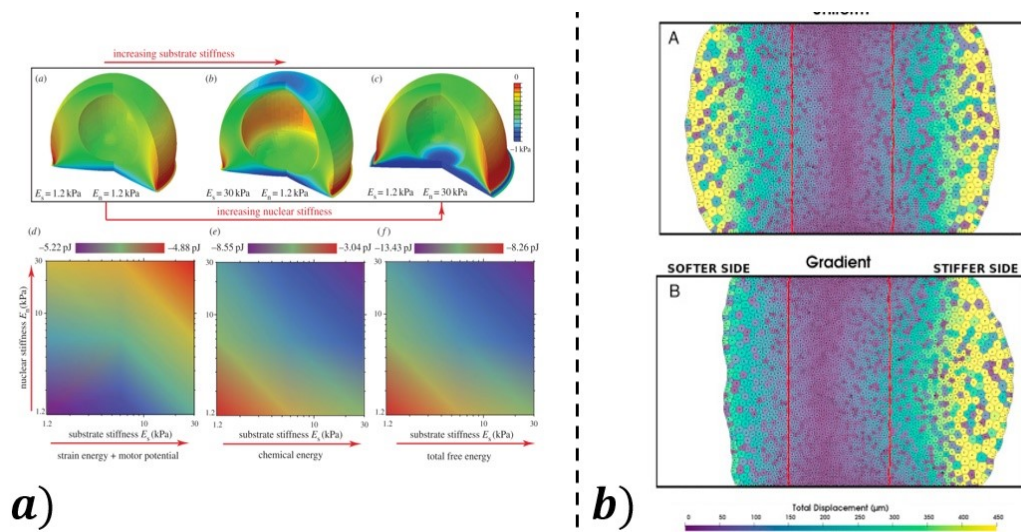


Figure 1.10: a) The cellular free energy decreases with increasing substrate and nucleus stiffness (Shenoy *et al.* 2016); b) Prediction of preferential cell spread towards stiffer substrates (González-Valverde and García-Aznar 2018).

Vigliotti *et al.* (2015) developed a thermodynamically consistent framework to describe the stress, strain, and strain-rate dependence of SF formation and remodelling, while also accounting for global conservation of cytoskeletal proteins. The kinetics of SF remodelling are motivated by considering the enthalpies of the actin/myosin sarcomeres that constitute individual fibres. This model provides the basis for the cytoskeletal framework implemented throughout this thesis and is described in detail in Chapters 2-4.

1.3.3. Cardiac myocardium

1.3.3.1. Structure and mechanics

Cardiac myocardium is a complex composite material, that has been structurally characterized in numerous histological studies (Legrice *et al.* 1997; LeGrice *et al.* 1995; Pope *et al.* 2008; Stoker *et al.* 1982; Legrice *et al.* 2001). The tissue is comprised primarily of cardiomyocytes, in addition to other cell phenotypes (e.g. fibroblasts) and structural components (collagen, elastin). The cardiomyocytes bind end-to-end, forming long myofibrillar arrangements. Endomysial collagen constrains the cells laterally to form sheets (myolaminae), in which perimysial collagen runs parallel to the cells to provide additional passive mechanical support (Pope *et al.* 2008). These sheets form the laminar architecture of the myocardium, and have a spatially variable orientation (Figure 1.11). The composition of the sheets allows the formation of a local right-hand orthogonal set of axes, denoting the myofibre (f) direction, the cross-fibre/sheet direction (s), and the direction normal to the sheet surface (n).

The anisotropic non-linear mechanical behaviour of the tissue has been investigated through biaxial (Demer and Yin 1983; Humphrey and Yin 1988) and shear (Dokos *et al.* 2002) loading. While these studies examined canine or porcine specimens, more recent investigations have focused on human tissue (Sommer *et al.* 2015). The myocardium is shown to exhibit the highest stiffness in the myofibre direction, with the lowest stress observed in the normal direction. All loading modes result in a highly non-linear stress-strain relationship. This behaviour is well characterized by the Holzapfel and Ogden (2009) model:

$$\begin{aligned} \boldsymbol{\sigma}_{aniso} = & \sum_{m=f,s} 2a_m(I_{4m}-1) \exp[b_m(I_{4m}-1)^2] \mathbf{a}_m \otimes \mathbf{a}_m \\ & + a_{fs} I_{8fs} \exp(b_{fs} I_{8fs}^2) (\mathbf{a}_f \otimes \mathbf{a}_s + \mathbf{a}_s \otimes \mathbf{a}_f), \end{aligned} \quad (1.66)$$

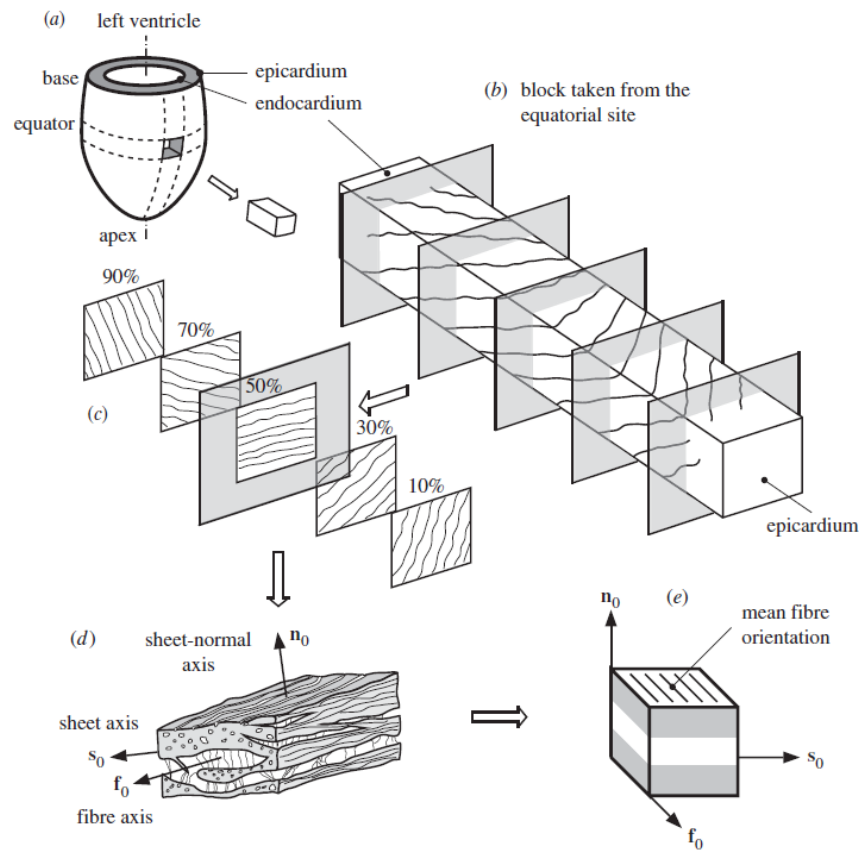


Figure 1.11: Schematic diagram of: (a) the left ventricle with a cut-out from the equator; (b) the structure through the thickness from the epicardium to the endocardium; (c) five longitudinal–circumferential sections showing the transverse variation of layer orientation; (d) the layered organization of myocytes and the collagen fibres between the sheets referred to a right-handed orthonormal coordinate system (fibre axis f_0 , sheet axis s_0 , sheet-normal axis n_0); and (e) a cube of layered tissue with local material coordinates (X_1, X_2, X_3) serving as the basis for the geometrical and constitutive model (Holzapfel and Ogden 2009).

where the first term on the right-hand side represents the mechanical contribution in the myofibre (f) and sheet (s) directions, and the second is an orthotropic term accounting for the shear contribution in the f - s plane. I_{4f} , I_{4s} , and I_{8fs} are anisotropic invariants defined as $I_{4f} = \mathbf{a}_{0f} \cdot (\mathbf{C} \mathbf{a}_{0f})$, $I_{4s} = \mathbf{a}_{0s} \cdot (\mathbf{C} \mathbf{a}_{0s})$, and $I_{8fs} = \mathbf{a}_{0f} \cdot (\mathbf{C} \mathbf{a}_{0s})$. \mathbf{a}_{0m} ($m = f, s$) is a unit vector indicating the myofibre or sheet orientations, and \mathbf{a}_m is the same vector in the deformed configuration given by $\mathbf{a}_m = \mathbf{F} \mathbf{a}_{0m}$. The operator \otimes is the dyadic product of vectors resulting in a second-order structure tensor, and \mathbf{a}_m , \mathbf{b}_m ($m = f, s, fs$) are anisotropic material parameters for each contribution.

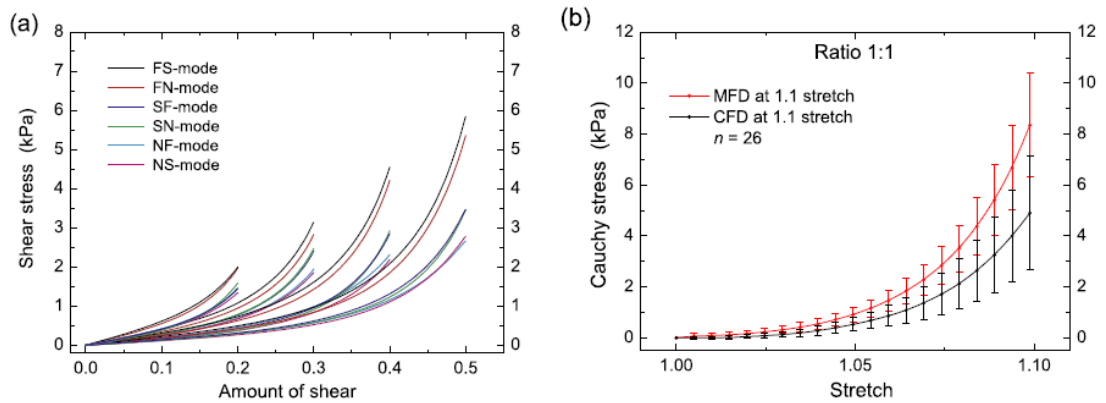


Figure 1.12: Mechanical response of human myocardial tissue to (a) shear and (b) biaxial loading conditions. Figures adapted from (Sommer *et al.* 2015).

The tissue is typically assumed to be incompressible, primarily due to the large content of fluid in the cells and between interstitial components. This assumption is supported by analysis from Vossoughi and Patel (1980). However, recent investigations have revealed there are regional changes in the myocardial volume during the cardiac cycle of up to 10% that cannot be fully accounted for by blood movement through the vasculature (Ashikaga *et al.* 2008), and other studies have highlighted the need for further evidence (Göktepe *et al.* 2011; Soares *et al.* 2017). The compressibility and anisotropy of the myocardium is investigated in Chapter 5.

1.3.3.2. Remodelling and failure

Heart failure (the inability of the heart to pump enough blood to the body) is a global pandemic affecting an estimated 26 million people worldwide. It is the most common cause of hospitalization among individuals above 65 years of age (Ambrosy *et al.* 2014).

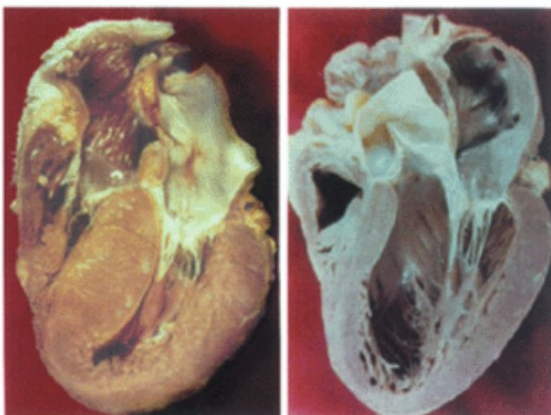


Figure 1.13: Diseased heart following concentric hypertrophy (left) compared to normal human heart (right) (Chung *et al.* 2003).

Heart failure can result from a number of pathologies including hypertension, post-infarct tissue thinning and fibrosis, and

volume overload. In all cases disease can be viewed as a remodelling of the tissue in response to mechanical stimuli. Cardiac hypertrophy is a medical condition whereby the cardiomyocytes (cardiac muscle cells) remodel following a deviation from homeostatic conditions (Chung *et al.* 2003). Cardiac hypertrophy is generally categorised as either concentric or eccentric. Concentric hypertrophy is a condition whereby the ventricle wall becomes thicker as a result of hypertension (Figure 1.13). Consequently, the ventricle volume is reduced, and an insufficient volume of blood is available for pumping during systole. This pathology may lead to *diastolic heart failure*. Eccentric hypertrophy is where the ventricle elongates and becomes thinner as a result of volume overload during diastole. The pumping ability (contractility) of this thin fibrotic ventricle wall is dramatically reduced so very little blood is ejected during systole, despite the fact that the enlarged ventricle can store an increased volume of blood. This pathology may lead to *systolic heart failure*.

At a cellular level concentric hypertrophy is characterized by an increase in cardiomyocyte cell size (Figure 1.14), enhanced protein synthesis, and parallel addition of sarcomeres (Izumo and Nadal-Ginard 1988; Chien *et al.* 1993; Sawada and Kawamura 1991). Elevated pressure also results in increased collagen deposition (fibrosis) from cardiac fibroblasts (Carver *et al.* 1991). In early stages this viewed as an adaptive response to reduce the wall stress, but it can progress to cause diastolic heart failure (Hunter and Chien 1999). In the case of eccentric hypertrophy cardiomyocytes will undergo longitudinal cell growth and addition of sarcomeres in-series (Dorn *et al.* 2003). Non-pathological cardiac remodelling is commonly reported in athletes: endurance-training athletes display ventricular dilatation (physiological eccentric hypertrophy) while strength-training athletes display myocardial thickening (physiological concentric hypertrophy) (Ellison *et al.* 2011; Kemi *et al.* 2002). Although the pathways underlying pathological and physiological hypertrophy differ, the resultant remodelling at a cellular

level is comparable. Eccentric hypertrophy also commonly results from myocardial infarction, which leads to localised cardiomyocyte death and localised loss of contractility (Palojoki *et al.* 2001). In such regions the tissue behaviour is dominated by the passive mechanical response (Holmes *et al.* 2005). Post-infarct, the local collagen structure will rearrange significantly (Fomovsky *et al.* 2012), highlighting an important role of fibroblasts in cardiac remodelling.

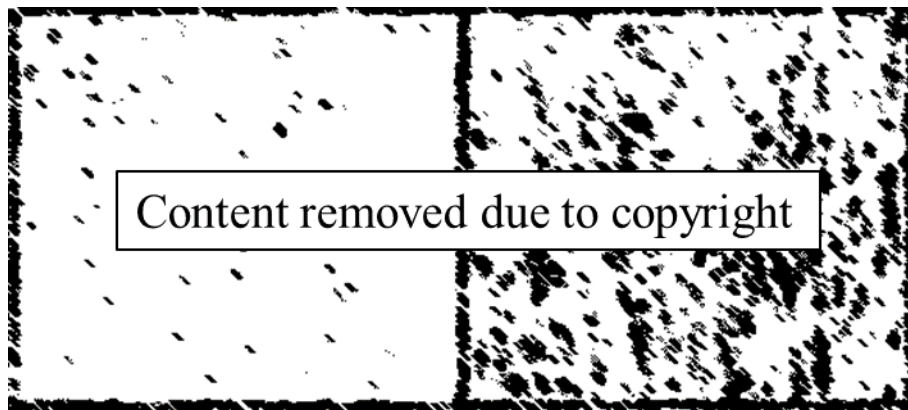


Figure 1.14: Microscopic left ventricle sections of healthy (left) and enlarged hypertrophic (right) cardiomyocytes (Luckey, 2007).

1.3.3.3. Computational modelling

Significant advances have been made in the field of cardiac modelling over the past 20 years. A description of the myofibre structure was provided by LeGrice *et al.* (1995), with more detail uncovered in the years following (LeGrice *et al.* 2001; Pope *et al.* 2008). A number of frameworks for cardiac muscle contractility have been proposed, such as the fading memory model (Hunter *et al.* 1998):

$$\sigma = \frac{\sigma_0(1 + aQ)}{1 - Q}, \quad \text{where } Q = \sum_{i=1} A_i \int_{-\infty}^t e^{-\alpha_i(t-\tau)} \dot{\lambda}(\tau) d\tau. \quad (1.67)$$

In this model the current tension is influenced by the stretch λ history (and more dependent on recent length changes than earlier length changes). α_i and A_i are rate coefficients and weighting coefficients, respectively, and $\dot{\lambda} = d\lambda/dt$. Other models

propose simulating contractility with a phenomenological pre-strain or pre-stress (Pezzuto *et al.* 2014).

The *Living Heart Project* (LHP) is a global research initiative bringing together over 20 Universities and 32 industry partners to develop and validate patient-specific heart models. Recent model constructions contain detailed anatomic geometry of 4 heart chambers and major blood vessels (Figure 1.15), and also includes framework for the passive tissue mechanics, blood flow dynamics, electrical conductance, and active tissue contraction (Baillargeon *et al.* 2014). The contractility is phenomenologically applied in pre-defined fibre directions as motivated by electrical activation and material strain, such that:

$$\sigma^{act} = (\sigma_k^{act} + \varepsilon k_T (\phi - \phi_r) \Delta t) / (1 + \varepsilon \Delta t), \quad (1.68)$$

where ϕ is an electrical potential, and k_T controls the magnitude of σ^{act} for a given potential. The LHP model has also been used in the analysis of coronary stent deployment (Saraswat *et al.* 2016).

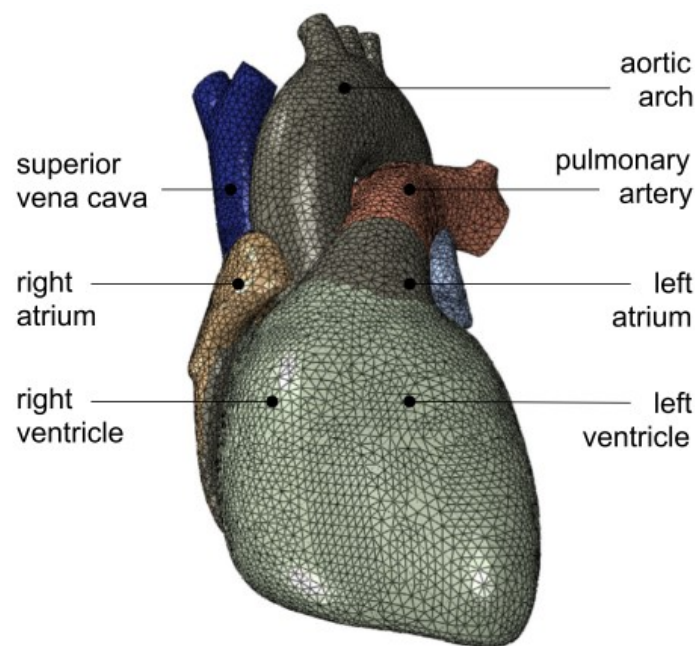


Figure 1.15: Finite element model of the human heart, as developed by the “Living Heart Project” (Baillargeon *et al.* 2014).

In 1994 Rodriguez *et al.* (1994) introduced a framework for volumetric growth in a continuum mechanics setting. Through decomposition of the deformation gradient \mathbf{F} into an elastic and growth component (\mathbf{F}_e and \mathbf{F}_g), the material volume can be altered by a deviation from homeostatic conditions ($\mathbf{F}_g = \theta \mathbf{I}$), where θ may be governed by an input of interest (e.g. strain). Humphrey and Rajagopal (2002) proposed a constrained mixture model for growth and remodelling, accounting for the production and degradation of tissue components. In recent years with the advent of powerful computational modelling tools and facilities, such growth models have been integrated into full 3D models of the heart. The Rodriguez model has been used to simulate cardiac hypertrophy (Rausch *et al.* 2011), as shown in Figure 1.16. Growth is motivated as an adaptive response to an alteration in the system stress, with

$$\dot{\theta} = \frac{1}{t_\theta} \left[\frac{\theta^{max} - \theta}{\theta^{max} - 1} \right]^\gamma (tr(\boldsymbol{\tau}) - p^{crit}). \quad (1.69)$$

The difference between the trace of the Kirchhoff stress $\boldsymbol{\tau}$ and a baseline pressure level p^{crit} is the driving force for growth. The parameters t_θ , θ^{max} , and γ control the rate, magnitude, and non-linearity of the growth, respectively. The framework has also been used to predict remodelling due to myocardial infarction (Sáez and Kuhl 2015), and most recently used alongside the underlying LHP model to simulate the pathologies of diastolic and systolic heart failure (Genet *et al.* 2016). However, this phenomenological approach to describing the growth stimulus provides limited insight, as the key biophysical processes underlying cardiac remodelling have not been considered.

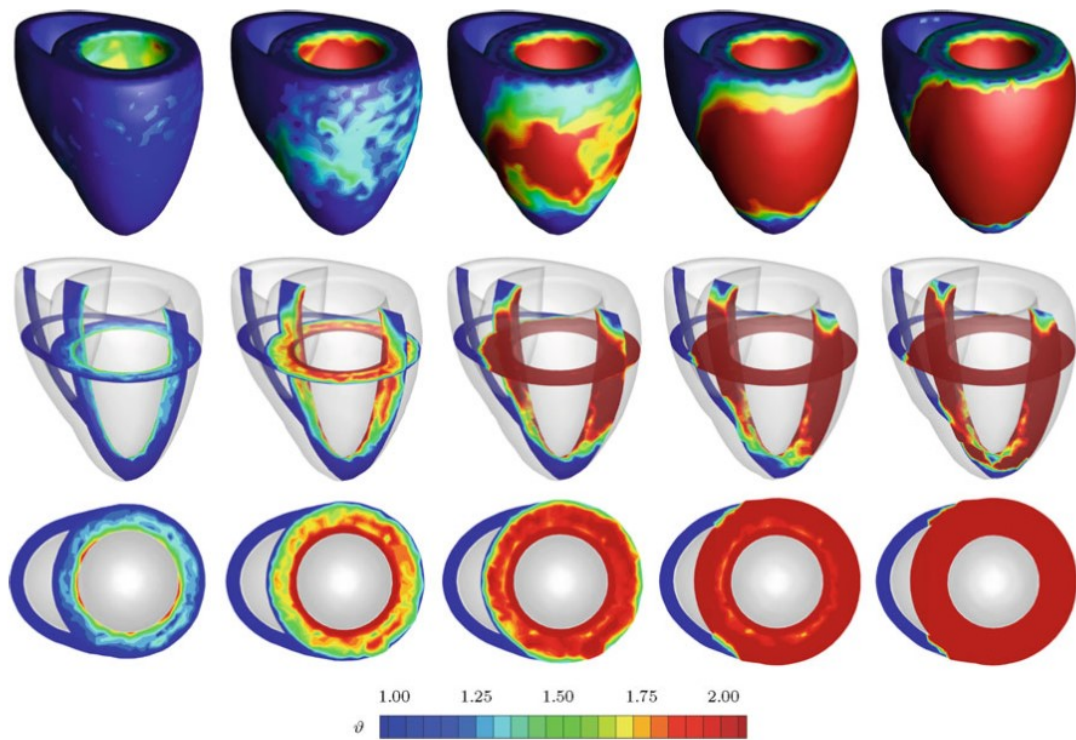


Figure 1.16: Finite element model of volumetric growth in the left ventricle onset by increased ventricular pressure (Rausch *et al.* 2011).

Bibliography

- Adler, J, G L Hazelbauer, and M M Dahl. 1973. "Chemotaxis toward Sugars in Escherichia Coli." *Journal of Bacteriology* 115 (3). American Society for Microbiology: 824–47. <http://www.ncbi.nlm.nih.gov/pubmed/4580570>.
- Alberts, Bruce. 1994. *Molecular Biology of the Cell*. Garland Pub. <https://www.ncbi.nlm.nih.gov/books/NBK20684/>.
- Ambrosy, Andrew P., Gregg C. Fonarow, Javed Butler, Ovidiu Chioncel, Stephen J. Greene, Muthiah Vaduganathan, Savina Nodari, *et al.* 2014. "The Global Health and Economic Burden of Hospitalizations for Heart Failure: Lessons Learned From Hospitalized Heart Failure Registries." *Journal of the American College of Cardiology* 63 (12): 1123–33. doi:10.1016/j.jacc.2013.11.053.
- Ashikaga, Hiroshi, Benjamin a Coppola, Katrina G Yamazaki, Francisco J Villarreal, Jeffrey H Omens, and James W Covell. 2008. "Changes in Regional Myocardial Volume during the Cardiac Cycle: Implications for Transmural Blood Flow and Cardiac Structure." *American Journal of Physiology. Heart and Circulatory Physiology* 295: H610–18. doi:10.1152/ajpheart.00107.2008.
- Atkin, R. J. (Raymond John), and N. (Norman) Fox. 2005. *An Introduction to the Theory of Elasticity*. Dover Publications.
- Baillargeon, Brian, Nuno Rebelo, David D. Fox, and Robert L. Taylor. 2014. "The Living Heart Project: A Robust and Integrative Simulator for Human Heart Function." *European Journal of Mechanics - A/Solids* 48: 38–47. doi:10.1016/j.euromechsol.2014.04.001.
- Balaban, Nathalie Q., Ulrich S. Schwarz, Daniel Riveline, Polina Goichberg, Gila Tzur, Ilana Sabanay, Diana Mahalu, *et al.* 2001. "Force and Focal Adhesion Assembly: A Close Relationship Studied Using Elastic Micropatterned Substrates." *Nature Cell Biology* 3 (5). Nature Publishing Group: 466–72. doi:10.1038/35074532.
- Balázsi, Gábor, Alexander van Oudenaarden, and James J. Collins. 2011. "Cellular Decision Making and Biological Noise: From Microbes to Mammals." *Cell* 144 (6). Cell Press: 910–25. doi:10.1016/J.CELL.2011.01.030.
- Bathe, Klaus-Jürgen. 2006. *Finite Element Procedures*.
- Blain, Emma J. 2009. "Involvement of the Cytoskeletal Elements in Articular Cartilage Homeostasis and Pathology." *International Journal of Experimental Pathology* 90 (1). Wiley-Blackwell: 1–15. doi:10.1111/j.1365-2613.2008.00625.x.
- Brangwynne, Clifford P., Frederick C. MacKintosh, Sanjay Kumar, Nicholas A. Geisse, Jennifer Talbot, L. Mahadevan, Kevin K. Parker, Donald E. Ingber, and David A. Weitz. 2006. "Microtubules Can Bear Enhanced Compressive Loads in Living Cells Because of Lateral Reinforcement." *The Journal of Cell Biology* 173 (5): 733–41. doi:10.1083/jcb.200601060.
- Burrige, Keith, and Christophe Guilly. 2016. "Focal Adhesions, Stress Fibers and Mechanical Tension." *Experimental Cell Research* 343 (1): 14–20. doi:10.1016/j.yexcr.2015.10.029.
- Caille, Nathalie, Olivier Thoumine, Yanik Tardy, and Jean-Jacques Meister. 2002. "Contribution of the Nucleus to the Mechanical Properties of Endothelial Cells." *Journal of Biomechanics* 35 (2). Elsevier: 177–87. doi:10.1016/S0021-9290(01)00201-9.
- Cao, Xuan, Emad Moeendarbary, Philipp Isermann, Patricia M. Davidson, Xiao Wang, Michelle B. Chen, Anya K. Burkart, Jan Lammerding, Roger D. Kamm, and Vivek B. Shenoy. 2016. "A Chemomechanical Model for Nuclear Morphology and Stresses during Cell Transendothelial Migration." *Biophysical Journal* 111 (7): 1541–52. doi:10.1016/j.bpj.2016.08.011.
- Carver, W, ML Nagpal, M Nachtigal, and TK Borg. 1991. "Collagen Expression in Mechanically Stimulated Cardiac Fibroblasts." *Circulation*. <http://circres.ahajournals.org/content/69/1/116.short>.

- Chen, Christopher S., Jose L. Alonso, Emanuele Ostuni, George M. Whitesides, and Donald E. Ingber. 2003. "Cell Shape Provides Global Control of Focal Adhesion Assembly." *Biochemical and Biophysical Research Communications* 307 (2). Academic Press: 355–61. doi:10.1016/S0006-291X(03)01165-3.
- Cheng, Bo, Min Lin, Guoyou Huang, Yuhui Li, Baohua Ji, Guy M. Genin, Vikram S. Deshpande, Tian Jian Lu, and Feng Xu. 2017. "Cellular Mechanosensing of the Biophysical Microenvironment: A Review of Mathematical Models of Biophysical Regulation of Cell Responses." *Physics of Life Reviews* 22–23 (December). Elsevier: 88–119. doi:10.1016/J.PLREV.2017.06.016.
- Chien, KR, H Zhu, and KU Knowlton. 1993. "Transcriptional Regulation during Cardiac Growth and Development." *Annual Review Of*. <http://www.annualreviews.org/doi/pdf/10.1146/annurev.ph.55.030193.000453>.
- Chung, Man-Wei, Tatiana Tsoutsman, and Christopher Semsarian. 2003. "Hypertrophic Cardiomyopathy: From Gene Defect to Clinical Disease." *Cell Research* 13 (1). Nature Publishing Group: 9–20. doi:10.1038/sj.cr.7290146.
- Cramer, L P, M Siebert, and T J Mitchison. 1997. "Identification of Novel Graded Polarity Actin Filament Bundles in Locomoting Heart Fibroblasts: Implications for the Generation of Motile Force." *The Journal of Cell Biology* 136 (6): 1287–1305. <http://www.ncbi.nlm.nih.gov/pubmed/9087444>.
- Demer, L L, and F C Yin. 1983. "Passive Biaxial Mechanical Properties of Isolated Canine Myocardium." *The Journal of Physiology* 339 (1). Wiley/Blackwell (10.1111): 615–30. doi:10.1113/jphysiol.1983.sp014738.
- Deshpande, Vikram S., Robert M. McMeeking, and Anthony G. Evans. 2007. "A Model for the Contractility of the Cytoskeleton Including the Effects of Stress-Fibre Formation and Dissociation." *Proceedings of the Royal Society A: Mathematical, Physical and Engineering Sciences* 463 (2079): 787–815. doi:10.1098/rspa.2006.1793.
- Dokos, Socrates, Bruce H Smaill, Alistair a Young, and Ian J LeGrice. 2002. "Shear Properties of Passive Ventricular Myocardium." *American Journal of Physiology. Heart and Circulatory Physiology* 283 (6): H2650–59. doi:10.1152/ajpheart.00111.2002.
- Dorn, Gerald W., Jeffrey Robbins, and Peter H. Sugden. 2003. "Phenotyping Hypertrophy." *Circulation Research* 92 (11).
- Dowling, Enda P., and J. Patrick McGarry. 2014. "Influence of Spreading and Contractility on Cell Detachment." *Annals of Biomedical Engineering* 42 (5): 1037–48. doi:10.1007/s10439-013-0965-5.
- Dowling, Enda P, William Ronan, Gidon Ofek, Vikram S Deshpande, Robert M McMeeking, Kyriacos a Athanasiou, and J Patrick McGarry. 2012. "The Effect of Remodelling and Contractility of the Actin Cytoskeleton on the Shear Resistance of Single Cells: A Computational and Experimental Investigation." *Journal of the Royal Society, Interface / the Royal Society* 9 (77): 3469–79. doi:10.1098/rsif.2012.0428.
- Dupin, Isabelle, Yasuhisa Sakamoto, Sandrine Etienne-Manneville, W. F. Liu, and C. S. Chen. 2011. "Cytoplasmic Intermediate Filaments Mediate Actin-Driven Positioning of the Nucleus." *Journal of Cell Science* 124 (Pt 6). The Company of Biologists Ltd: 865–72. doi:10.1242/jcs.076356.
- Ellison, GM, CD Waring, C Vicinanza, and D Torella. 2011. "Physiological Cardiac Remodelling in Response to Endurance Exercise Training: Cellular and Molecular Mechanisms." *Heart*. <http://heart.bmj.com/content/early/2011/08/30/heartjnl-2011-300639.short>.
- Engler, A., M. Sheehan, H. L. Sweeney, and D. E. Discher. 2003. "Substrate Compliance vs Ligand Density in Cell on Gel Responses." *European Cells and Materials* 6 (SUPPL. 1). Elsevier: 7–8. doi:10.1016/S0006-3495(04)74140-5.
- Eriksson, John E., Thomas Dechat, Boris Grin, Brian Helfand, Melissa Mendez, Hanna-Mari

- Pallari, and Robert D. Goldman. 2009. “Introducing Intermediate Filaments: From Discovery to Disease.” *Journal of Clinical Investigation* 119 (7): 1763–71. doi:10.1172/JCI38339.
- Escribano, Jorge, Raimon Sunyer, María Teresa Sánchez, Xavier Trepap, Pere Roca-Cusachs, and José Manuel García-Aznar. 2018. “A Hybrid Computational Model for Collective Cell Durotaxis.” *Biomechanics and Modeling in Mechanobiology* 17 (4). Springer Berlin Heidelberg: 1037–52. doi:10.1007/s10237-018-1010-2.
- Fagan, M. J. 1992. *Finite Element Analysis: Theory and Practice*. Longman Scientific & Technical. https://books.google.ie/books/about/Finite_Element_Analysis.html?id=-xJtQgAACAAJ&redir_esc=y.
- Fletcher, Daniel A, and R Dyche Mullins. 2010. “Cell Mechanics and the Cytoskeleton.” *Nature* 463 (7280). NIH Public Access: 485–92. doi:10.1038/nature08908.
- Fomovsky, Gregory M., Andrew D. Rouillard, and Jeffrey W. Holmes. 2012. “Regional Mechanics Determine Collagen Fiber Structure in Healing Myocardial Infarcts.” *Journal of Molecular and Cellular Cardiology* 52 (5): 1083–90. doi:10.1016/j.yjmcc.2012.02.012.
- Fuchs, E, and K Weber. 1994. “Intermediate Filaments: Structure, Dynamics, Function and Disease.” *Annual Review of Biochemistry* 63 (1): 345–82. doi:10.1146/annurev.bi.63.070194.002021.
- Gaudet, Christianne, William a Marganski, Sooyoung Kim, Christopher T Brown, Vaibhavi Gunderia, Micah Dembo, and Joyce Y Wong. 2003. “Influence of Type I Collagen Surface Density on Fibroblast Spreading, Motility, and Contractility.” *Biophysical Journal* 85 (5). Elsevier: 3329–35. doi:10.1016/S0006-3495(03)74752-3.
- Genet, M., L. C. Lee, B. Baillargeon, J. M. Guccione, and E. Kuhl. 2016. “Modeling Pathologies of Diastolic and Systolic Heart Failure.” *Annals of Biomedical Engineering* 44 (1). Springer US: 112–27. doi:10.1007/s10439-015-1351-2.
- Gilmore, Andrew P, and Keith Burrige. 1996. “Molecular Mechanisms for Focal Adhesion Assembly through Regulation of Protein–protein Interactions.” *Structure* 4 (6). Cell Press: 647–51. doi:10.1016/S0969-2126(96)00069-X.
- Göktepe, S., S. N. S. Acharya, J. Wong, and E. Kuhl. 2011. “Computational Modeling of Passive Myocardium.” *International Journal for Numerical Methods in Biomedical Engineering* 27 (1). John Wiley & Sons, Ltd.: 1–12. doi:10.1002/cnm.1402.
- Gong, Ze, Spencer E Szczesny, Steven R Caliari, Elisabeth E Charrier, Ovijit Chaudhuri, Xuan Cao, Yuan Lin, *et al.* 2018. “Matching Material and Cellular Timescales Maximizes Cell Spreading on Viscoelastic Substrates.” *Proceedings of the National Academy of Sciences of the United States of America* 115 (12). National Academy of Sciences: E2686–95. doi:10.1073/pnas.1716620115.
- González-Valverde, Ismael, and José Manuel García-Aznar. 2018. “Mechanical Modeling of Collective Cell Migration: An Agent-Based and Continuum Material Approach.” *Computer Methods in Applied Mechanics and Engineering* 337 (August). North-Holland: 246–62. doi:10.1016/J.CMA.2018.03.036.
- Holmes, Jeffrey W., Thomas K. Borg, and James W. Covell. 2005. “Structure and Mechanics of Healing Myocardial Infarcts.” *Annual Review of Biomedical Engineering* 7 (1). Annual Reviews: 223–53. doi:10.1146/annurev.bioeng.7.060804.100453.
- Holzapfel, Gerhard A. 2000. *Nonlinear Solid Mechanics: A Continuum Approach for Engineering*. Wiley. <https://www.wiley.com/en-us/Nonlinear+Solid+Mechanics%3A+A+Continuum+Approach+for+Engineering-p-9780471823193>.
- Holzapfel, Gerhard A, and Ray W Ogden. 2009. “Constitutive Modelling of Passive Myocardium: A Structurally Based Framework for Material Characterization.” *Philosophical Transactions. Series A, Mathematical, Physical, and Engineering Sciences* 367 (1902):

3445–75. doi:10.1098/rsta.2009.0091.

- Humphrey, J. D., and K. R. Rajagopal. 2002. “A CONSTRAINED MIXTURE MODEL FOR GROWTH AND REMODELING OF SOFT TISSUES.” *Mathematical Models and Methods in Applied Sciences* 12 (03). World Scientific Publishing Company : 407–30. doi:10.1142/S0218202502001714.
- Humphrey, J D, and F C Yin. 1988. “Biaxial Mechanical Behavior of Excised Epicardium.” *Journal of Biomechanical Engineering* 110 (4): 349–51. doi:10.1115/1.3108452.
- Hunter, JJ, and KR Chien. 1999. “Signaling Pathways for Cardiac Hypertrophy and Failure.” *New England Journal of Medicine*. <http://www.nejm.org/doi/full/10.1056/nejm199910213411706>.
- Hunter, P.J., A.D. McCulloch, and H.E.D.J. ter Keurs. 1998. “Modelling the Mechanical Properties of Cardiac Muscle.” *Progress in Biophysics and Molecular Biology* 69 (March): 289–331. doi:10.1016/S0079-6107(98)00013-3.
- Huxley, A F. 1957. “Muscle Structure and Theories of Contraction.” *Progress in Biophysics and Biophysical Chemistry* 7: 255–318. <http://www.ncbi.nlm.nih.gov/pubmed/13485191>.
- Ingber, D E. 1993. “Cellular Tensegrity: Defining New Rules of Biological Design That Govern the Cytoskeleton.” *Journal of Cell Science* 104 (Pt 3) (March): 613–27. <http://www.ncbi.nlm.nih.gov/pubmed/8314865>.
- Izumo, S, and B Nadal-Ginard. 1988. “Protooncogene Induction and Reprogramming of Cardiac Gene Expression Produced by Pressure Overload.” *Proceedings of The*. <http://www.pnas.org/content/85/2/339.short>.
- Jafari Bidhendi, Amirhossein, and Rami K. Korhonen. 2012. “A Finite Element Study of Micropipette Aspiration of Single Cells: Effect of Compressibility.” *Computational and Mathematical Methods in Medicine* 2012 (February). Hindawi: 1–9. doi:10.1155/2012/192618.
- Jones, W R, H P Ting-Beall, G M Lee, S S Kelley, R M Hochmuth, and F Guilak. 1999. “Alterations in the Young’s Modulus and Volumetric Properties of Chondrocytes Isolated from Normal and Osteoarthritic Human Cartilage.” *Journal of Biomechanics* 32 (2). Elsevier: 119–27. doi:10.1016/S0021-9290(98)00166-3.
- Jungreuthmayer, C., M.J. Jaasma, A.A. Al-Munajjed, J. Zanghellini, D.J. Kelly, and F.J. O’Brien. 2009. “Deformation Simulation of Cells Seeded on a Collagen-GAG Scaffold in a Flow Perfusion Bioreactor Using a Sequential 3D CFD-Elastostatics Model.” *Medical Engineering & Physics* 31 (4). Elsevier: 420–27. doi:10.1016/J.MEDENGGPHY.2008.11.003.
- Kanchanawong, Pakorn, Gleb Shtengel, Ana M. Pasapera, Ericka B. Ramko, Michael W. Davidson, Harald F. Hess, and Clare M. Waterman. 2010. “Nanoscale Architecture of Integrin-Based Cell Adhesions.” *Nature* 468 (7323): 580–84. doi:10.1038/nature09621.
- Kaunas, Roland, and Hui-Ju Hsu. 2009. “A Kinematic Model of Stretch-Induced Stress Fiber Turnover and Reorientation.” *Journal of Theoretical Biology* 257 (2). Academic Press: 320–30. doi:10.1016/J.JTBI.2008.11.024.
- Kemi, OJ, JP Loennechen, and U Wisløff. 2002. “Intensity-Controlled Treadmill Running in Mice: Cardiac and Skeletal Muscle Hypertrophy.” *Journal of Applied*. <http://jap.physiology.org/content/93/4/1301.short>.
- Kilian, Kristopher A, Branimir Bugarija, Bruce T Lahn, and Milan Mrksich. 2010. “Geometric Cues for Directing the Differentiation of Mesenchymal Stem Cells.” *Proceedings of the National Academy of Sciences of the United States of America* 107 (11). National Academy of Sciences: 4872–77. doi:10.1073/pnas.0903269107.
- Koay, Eugene J., Adrian C. Shieh, and Kyriacos A. Athanasiou. 2003. “Creep Indentation of Single Cells.” *Journal of Biomechanical Engineering* 125 (3). American Society of

Mechanical Engineers: 334. doi:10.1115/1.1572517.

- Kolodney, M S, and E L Elson. 1995. "Contraction Due to Microtubule Disruption Is Associated with Increased Phosphorylation of Myosin Regulatory Light Chain." *Proceedings of the National Academy of Sciences of the United States of America* 92 (22): 10252–56. <http://www.ncbi.nlm.nih.gov/pubmed/7479762>.
- Legrice, I., P. Hunter, A. Young, and B. Smaill. 2001. "The Architecture of the Heart: A Data-Based Model." *Philosophical Transactions of the Royal Society A: Mathematical, Physical and Engineering Sciences* 359 (1783): 1217–32. doi:10.1098/rsta.2001.0827.
- Legrice, I J, P J Hunter, and B H Smaill. 1997. "Laminar Structure of the Heart: A Mathematical Model." *The American Journal of Physiology* 272: H2466–76.
- LeGrice, I J, B H Smaill, L Z Chai, S G Edgar, J B Gavin, and P J Hunter. 1995. "Laminar Structure of the Heart: Ventricular Myocyte Arrangement and Connective Tissue Architecture in the Dog." *Am J Physiol* 269 (2 Pt 2): H571-82. <http://www.ncbi.nlm.nih.gov/pubmed/7653621>.
- Leipzig, Nic D, and K A Kyriacos A Athanasiou. 2005. "Unconfined Creep Compression of Chondrocytes." *Journal of Biomechanics* 38 (1). Elsevier: 77–85. doi:10.1016/j.jbiomech.2004.03.013.
- Lim, C.T., M. Dao, S. Suresh, C.H. Sow, and K.T. Chew. 2004. "Large Deformation of Living Cells Using Laser Traps." *Acta Materialia* 52 (7). Pergamon: 1837–45. doi:10.1016/J.ACTAMAT.2003.12.028.
- Lodish, Harvey F. 2000. *Molecular Cell Biology*. W.H. Freeman. <https://www.ncbi.nlm.nih.gov/books/NBK21475/>.
- Loerakker, Sandra, Tommaso Ristori, and Frank P T Baaijens. 2016. "A Computational Analysis of Cell-Mediated Compaction and Collagen Remodeling in Tissue-Engineered Heart Valves." *Journal of the Mechanical Behavior of Biomedical Materials* 58. Elsevier: 173–87. doi:10.1016/j.jmbbm.2015.10.001.
- Luckey, Stephen W., Jason Mansoori, Kelly Fair, Christopher L. Antos, Eric N. Olson, and Leslie A. Leinwand. 2007. "Blocking Cardiac Growth in Hypertrophic Cardiomyopathy Induces Cardiac Dysfunction and Decreased Survival Only in Males." *American Journal of Physiology - Heart and Circulatory Physiology* 292 (2).
- Lymn, R W, and E W Taylor. 1971. "Mechanism of Adenosine Triphosphate Hydrolysis by Actomyosin." *Biochemistry* 10 (25): 4617–24. <http://www.ncbi.nlm.nih.gov/pubmed/4258719>.
- Martini, Frederic., Judi Lindsley. Nath, and Edwin F. Bartholomew. 2012. *Fundamentals of Anatomy & Physiology*. Benjamin Cummings.
- McCoy, R.J., C. Jungreuthmayer, and F.J. O'Brien. 2012. "Influence of Flow Rate and Scaffold Pore Size on Cell Behavior during Mechanical Stimulation in a Flow Perfusion Bioreactor." *Biotechnology and Bioengineering* 109 (6). Wiley-Blackwell: 1583–94. doi:10.1002/bit.24424.
- McGarry, J. P. 2009. "Characterization of Cell Mechanical Properties by Computational Modeling of Parallel Plate Compression." *Annals of Biomedical Engineering* 37 (11): 2317–25. doi:10.1007/s10439-009-9772-4.
- McGarry, J. P., J. Fu, M. T. Yang, C. S. Chen, R. M. McMeeking, A. G. Evans, and V. S. Deshpande. 2009. "Simulation of the Contractile Response of Cells on an Array of Micro-Posts." *Philosophical Transactions. Series A, Mathematical, Physical, and Engineering Sciences* 367 (1902): 3477–97. doi:10.1098/rsta.2009.0097.
- McGarry, J. P., and P. E. McHugh. 2008. "Modelling of in Vitro Chondrocyte Detachment." *Journal of the Mechanics and Physics of Solids* 56 (4): 1554–65. doi:10.1016/j.jmps.2007.08.001.

- McGarry, J G, and P J Prendergast. 2004. "A Three-Dimensional Finite Element Model of an Adherent Eukaryotic Cell." *European Cells & Materials* 7 (April): 27-33; discussion 33-4. <http://www.ncbi.nlm.nih.gov/pubmed/15095253>.
- Miehe, Christian. 1996. "Numerical Computation of Algorithmic (Consistent) Tangent Moduli in Large-Strain Computational Inelasticity." *Computer Methods in Applied Mechanics and Engineering* 134 (3-4). North-Holland: 223-40. doi:10.1016/0045-7825(96)01019-5.
- Nolan, D.R., A.L. Gower, M. Destrade, R.W. Ogden, and J.P. McGarry. 2014. "A Robust Anisotropic Hyperelastic Formulation for the Modelling of Soft Tissue." *Journal of the Mechanical Behavior of Biomedical Materials* 39. Elsevier: 48-60. doi:10.1016/j.jmbbm.2014.06.016.
- Obbink-Huizer, Christine, Cees W. J. Oomens, Sandra Loerakker, Jasper Foolen, Carlijn V. C. Bouten, and Frank P. T. Baaijens. 2014. "Computational Model Predicts Cell Orientation in Response to a Range of Mechanical Stimuli." *Biomechanics and Modeling in Mechanobiology* 13 (1). Springer Berlin Heidelberg: 227-36. doi:10.1007/s10237-013-0501-4.
- Ofek, Gidon, Enda P. Dowling, Robert M. Raphael, J. Patrick McGarry, and Kyriacos A. Athanasiou. 2010. "Biomechanics of Single Chondrocytes under Direct Shear." *Biomechanics and Modeling in Mechanobiology* 9 (2): 153-62. doi:10.1007/s10237-009-0166-1.
- Ofek, Gidon, Roman M Natoli, and Kyriacos A Athanasiou. 2009. "In Situ Mechanical Properties of the Chondrocyte Cytoplasm and Nucleus." *Journal of Biomechanics* 42 (7). Elsevier: 873-77. doi:10.1016/j.jbiomech.2009.01.024.
- Ofek, Gidon, Dena C. Wiltz, and Kyriacos A. Athanasiou. 2009. "Contribution of the Cytoskeleton to the Compressive Properties and Recovery Behavior of Single Cells." *Biophysical Journal* 97 (7): 1873-82. doi:10.1016/j.bpj.2009.07.050.
- Palojoki, E, A Saraste, A Eriksson, K Pulkki, M Kallajoki, L M Voipio-Pulkki, and I Tikkanen. 2001. "Cardiomyocyte Apoptosis and Ventricular Remodeling after Myocardial Infarction in Rats." *American Journal of Physiology. Heart and Circulatory Physiology* 280 (6): H2726-31. <http://www.ncbi.nlm.nih.gov/pubmed/11356629>.
- Pasapera, Ana M, Ian C Schneider, Erin Rericha, David D Schlaepfer, and Clare M Waterman. 2010. "Myosin II Activity Regulates Vinculin Recruitment to Focal Adhesions through FAK-Mediated Paxillin Phosphorylation." *The Journal of Cell Biology* 188 (6). Rockefeller University Press: 877-90. doi:10.1083/jcb.200906012.
- Pathak, Amit, Robert M. McMeeking, Anthony G. Evans, and Vikram S. Deshpande. 2011. "An Analysis of the Cooperative Mechano-Sensitive Feedback Between Intracellular Signaling, Focal Adhesion Development, and Stress Fiber Contractility." *Journal of Applied Mechanics* 78 (4). American Society of Mechanical Engineers: 041001. doi:10.1115/1.4003705.
- Perkins, Theodore J, and Peter S Swain. 2009. "Strategies for Cellular Decision-Making." *Molecular Systems Biology* 5 (1). EMBO Press: 326. doi:10.1038/msb.2009.83.
- Pezzuto, S., D. Ambrosi, and A. Quarteroni. 2014. "An Orthotropic Active-Strain Model for the Myocardium Mechanics and Its Numerical Approximation." *European Journal of Mechanics, A/Solids* 48 (1). Elsevier Masson SAS: 83-96. doi:10.1016/j.euromechsol.2014.03.006.
- Pollard, Thomas D., and Robert D. Goldman, eds. 2017. *The Cytoskeleton*. Cold Spring Harbor Laboratory Press.
- Pollard, Thomas D, and Gary G Borisy. 2003. "Cellular Motility Driven by Assembly and Disassembly of Actin Filaments." *Cell* 112 (4): 453-65. <http://www.ncbi.nlm.nih.gov/pubmed/12600310>.
- Pope, Adèle J., Gregory B. Sands, Bruce H. Smaill, and Ian J. LeGrice. 2008. "Three-Dimensional

- Transmural Organization of Perimysial Collagen in the Heart.” *American Journal of Physiology - Heart and Circulatory Physiology* 295 (3). <http://ajpheart.physiology.org/content/295/3/H1243>.
- Rausch, M. K., A. Dam, S. Göktepe, O. J. Abilez, and E. Kuhl. 2011. “Computational Modeling of Growth: Systemic and Pulmonary Hypertension in the Heart.” *Biomechanics and Modeling in Mechanobiology* 10 (6): 799–811. doi:10.1007/s10237-010-0275-x.
- Reynolds, N. H., and J. P. McGarry. 2015. “Single Cell Active Force Generation under Dynamic Loading - Part II: Active Modelling Insights.” *Acta Biomaterialia* 27. Acta Materialia Inc.: 251–63. doi:10.1016/j.actbio.2015.09.004.
- Reynolds, Noel H., W. Ronan, Enda P. Dowling, P. Owens, Robert M. McMeeking, and J. Patrick McGarry. 2014. “On the Role of the Actin Cytoskeleton and Nucleus in the Biomechanical Response of Spread Cells.” *Biomaterials* 35 (13). Elsevier Ltd: 4015–25. doi:10.1016/j.biomaterials.2014.01.056.
- Ridley, Anne J., and Alan Hall. 1992. “The Small GTP-Binding Protein Rho Regulates the Assembly of Focal Adhesions and Actin Stress Fibers in Response to Growth Factors.” *Cell* 70 (3). Cell Press: 389–99. doi:10.1016/0092-8674(92)90163-7.
- Rodriguez, Edward K., Anne Hoger, and Andrew D. McCulloch. 1994. “Stress-Dependent Finite Growth in Soft Elastic Tissues.” *Journal of Biomechanics* 27 (4): 455–67. doi:10.1016/0021-9290(94)90021-3.
- Ronan, William, Vikram S. Deshpande, Robert M. McMeeking, and J. Patrick McGarry. 2012. “Numerical Investigation of the Active Role of the Actin Cytoskeleton in the Compression Resistance of Cells.” *Journal of the Mechanical Behavior of Biomedical Materials* 14. Elsevier: 143–57. doi:10.1016/j.jmbbm.2012.05.016.
- . 2014. “Cellular Contractility and Substrate Elasticity: A Numerical Investigation of the Actin Cytoskeleton and Cell Adhesion.” *Biomechanics and Modeling in Mechanobiology* 13 (2): 417–35. doi:10.1007/s10237-013-0506-z.
- Ronan, William, Robert M. McMeeking, Christopher S. Chen, J. Patrick McGarry, and Vikram S. Deshpande. 2015. “Cooperative Contractility: The Role of Stress Fibres in the Regulation of Cell-Cell Junctions.” *Journal of Biomechanics* 48 (3): 520–28. doi:10.1016/j.jbiomech.2014.11.025.
- Ronan, William, Amit Pathak, Vikram S. Deshpande, Robert M. McMeeking, and J. Patrick McGarry. 2013. “Simulation of the Mechanical Response of Cells on Micropost Substrates.” *Journal of Biomechanical Engineering* 135 (10): 1–10. doi:10.1115/1.4025114.
- Rossi, M. A. 1998. “Pathologic Fibrosis and Connective Tissue Matrix in Left Ventricular Hypertrophy Due to Chronic Arterial Hypertension in Humans.” *Journal of Hypertension* 16 (7): 1031–41. <http://www.ncbi.nlm.nih.gov/pubmed/9794745>.
- Sáez, P., and E. Kuhl. 2015. “Computational Modeling of Acute Myocardial Infarction.” *Computer Methods in Biomechanics and Biomedical Engineering* 5842 (November): 1–9. doi:10.1080/10255842.2015.1105965.
- Saraswat, Prabhav, Manoj Chinnakonda, and Brian Baillargeon. 2016. “Living Heart Human Model: Cardiovascular Stent Deployment and Cardiac Cycle Simulation ¹.” *Journal of Medical Devices* 10 (3). American Society of Mechanical Engineers: 030945. doi:10.1115/1.4033869.
- Sastry, Sarita K., and Keith Burridge. 2000. “Focal Adhesions: A Nexus for Intracellular Signaling and Cytoskeletal Dynamics.” *Experimental Cell Research* 261 (1). Academic Press: 25–36. doi:10.1006/EXCR.2000.5043.
- Sato, Katsuya, Taiji Adachi, Yasuhito Shirai, Naoaki Saito, and Yoshihiro Tomita. 2006. “Local Disassembly of Actin Stress Fibers Induced by Selected Release of Intracellular Tension in Osteoblastic Cell.” *Journal of Biomechanical Science and Engineering* 1 (1). The Japan Society of Mechanical Engineers: 204–14. doi:10.1299/jbse.1.204.

- Sato, M, N Ohshima, and R M Nerem. 1996. “Viscoelastic Properties of Cultured Porcine Aortic Endothelial Cells Exposed to Shear Stress.” *Journal of Biomechanics* 29 (4): 461–67. <http://www.ncbi.nlm.nih.gov/pubmed/8964775>.
- Sawada, K, and K Kawamura. 1991. “Architecture of Myocardial Cells in Human Cardiac Ventricles with Concentric and Eccentric Hypertrophy as Demonstrated by Quantitative Scanning Electron Microscopy.” *Heart and Vessels*. <http://link.springer.com/article/10.1007/BF02058278>.
- Schwartz, Martin A., Michael D. Schaller, and Mark H. Ginsberg. 1995. “Integrins: Emerging Paradigms of Signal Transduction.” *Annual Review of Cell and Developmental Biology* 11 (1): 549–99. doi:10.1146/annurev.cb.11.110195.003001.
- Shenoy, Vivek B, Hailong Wang, and Xiao Wang. 2016. “A Chemo-Mechanical Free-Energy-Based Approach to Model Durotaxis and Extracellular Stiffness-Dependent Contraction and Polarization of Cells.” *Interface Focus* 6 (1): 20150067. doi:10.1098/rsfs.2015.0067.
- Shishvan, S. S., A. Vigliotti, and V. S. Deshpande. 2018. “The Homeostatic Ensemble for Cells.” *Biomechanics and Modeling in Mechanobiology*, July. Springer Berlin Heidelberg, 1–32. doi:10.1007/s10237-018-1048-1.
- Skoge, Monica, Elisabeth Wong, Bashar Hamza, Albert Bae, Joseph Martel, Rama Kataria, Ineke Keizer-Gunnink, *et al.* 2016. “A Worldwide Competition to Compare the Speed and Chemotactic Accuracy of Neutrophil-Like Cells.” Edited by Ger van Zandbergen. *PLOS ONE* 11 (6). Public Library of Science: e0154491. doi:10.1371/journal.pone.0154491.
- Soares, Joao S., David S. Li, Eric Lai, Joseph H. Gorman III, Robert C. Gorman, and Michael S. Sacks. 2017. “Modeling of Myocardium Compressibility and Its Impact in Computational Simulations of the Healthy and Infarcted Heart.” In , 493–501. Springer, Cham. doi:10.1007/978-3-319-59448-4_47.
- Solon, Jérôme, Ilya Levental, Kheya Sengupta, Penelope C. Georges, and Paul A. Janmey. 2007. “Fibroblast Adaptation and Stiffness Matching to Soft Elastic Substrates.” *Biophysical Journal* 93 (12). Cell Press: 4453–61. doi:10.1529/BIOPHYSJ.106.101386.
- Sommer, Gerhard, Andreas J. Schriebl, Michaela Andrä, Michael Sacherer, Christian Viertler, Heimo Wolinski, and Gerhard A. Holzapfel. 2015. “Biomechanical Properties and Microstructure of Human Ventricular Myocardium.” *Acta Biomaterialia* 24 (September): 172–92. doi:10.1016/j.actbio.2015.06.031.
- Stoker, M E, a M Gerdes, and J F May. 1982. “Regional Differences in Capillary Density and Myocyte Size in the Normal Human Heart.” *The Anatomical Record* 202 (2): 187–91. doi:10.1002/ar.1092020203.
- Sun, Wei, Elliot L Chaikof, and Marc E Levenston. 2008. “Numerical Approximation of Tangent Moduli for Finite Element Implementations of Nonlinear Hyperelastic Material Models.” *Journal of Biomechanical Engineering* 130 (6): 061003. doi:10.1115/1.2979872.
- Tan, J. L., J. Tien, D. M. Pirone, D. S. Gray, K. Bhadriraju, and C. S. Chen. 2003. “Cells Lying on a Bed of Microneedles: An Approach to Isolate Mechanical Force.” *Proceedings of the National Academy of Sciences* 100 (4): 1484–89. doi:10.1073/pnas.0235407100.
- Théry, Manuel, Anne Pépin, Emilie Dressaire, Yong Chen, and Michel Bornens. 2006. “Cell Distribution of Stress Fibres in Response to the Geometry of the Adhesive Environment.” *Cell Motility and the Cytoskeleton* 63 (6): 341–55. doi:10.1002/cm.20126.
- Thoumine, O., Olivier Cardoso, and Jean-Jacques Meister. 1999. “Changes in the Mechanical Properties of Fibroblasts during Spreading: A Micromanipulation Study.” *European Biophysics Journal* 28 (3). Springer-Verlag: 222–34. doi:10.1007/s002490050203.
- Trickey, W, T Vail, and F Guilak. 2004. “The Role of the Cytoskeleton in the Viscoelastic Properties of Human Articular Chondrocytes.” *Journal of Orthopaedic Research* 22 (1): 131–39. doi:10.1016/S0736-0266(03)00150-5.

- Trickey, Wendy R, Frank P T Baaijens, Tod A Laursen, Leonidas G Alexopoulos, and Farshid Guilak. 2006. "Determination of the Poisson's Ratio of the Cell: Recovery Properties of Chondrocytes after Release from Complete Micropipette Aspiration." *Journal of Biomechanics* 39 (1). Elsevier: 78–87. doi:10.1016/j.jbiomech.2004.11.006.
- Vernerey, Franck J., and Mehdi Farsad. 2011. "A Constrained Mixture Approach to Mechano-Sensing and Force Generation in Contractile Cells." *Journal of the Mechanical Behavior of Biomedical Materials* 4 (8): 1683–99. doi:10.1016/j.jmbbm.2011.05.022.
- Vigliotti, A., W. Ronan, F. P T Baaijens, and V. S. Deshpande. 2015. "A Thermodynamically Motivated Model for Stress-Fiber Reorganization." *Biomechanics and Modeling in Mechanobiology*. Springer Berlin Heidelberg. doi:10.1007/s10237-015-0722-9.
- Vossoughi, Jafar, and Dali J Patel. 1980. "Compressibility of the Myocardial Tissue." *Adv Bioeng*, 45–48.
- Wang, N, J. Butler, and D. Ingber. 1993. "Mechanotransduction across the Cell Surface and through the Cytoskeleton." *Science* 260 (5111): 1124–27. doi:10.1126/science.7684161.
- Weafer, P. P., N. H. Reynolds, S. P. Jarvis, and J. P. McGarry. 2015. "Single Cell Active Force Generation under Dynamic Loading - Part I: AFM Experiments." *Acta Biomaterialia* 27. Acta Materialia Inc.: 236–50. doi:10.1016/j.actbio.2015.09.006.
- Weafer, P. P., W. Ronan, S. P. Jarvis, and J. P. McGarry. 2013. "Experimental and Computational Investigation of the Role of Stress Fiber Contractility in the Resistance of Osteoblasts to Compression." *Bulletin of Mathematical Biology* 75 (8): 1284–1303. doi:10.1007/s11538-013-9812-y.
- Wehrle-Haller, Bernhard, and Beat Imhof. 2002. "The Inner Lives of Focal Adhesions." *Trends in Cell Biology* 12 (8): 382–89. <http://www.ncbi.nlm.nih.gov/pubmed/12191915>.
- Wille, Jeremiah J., Elliot L. Elson, and Ruth J. Okamoto. 2006. "Cellular and Matrix Mechanics of Bioartificial Tissues During Continuous Cyclic Stretch." *Annals of Biomedical Engineering* 34 (11). Kluwer Academic Publishers-Plenum Publishers: 1678–90. doi:10.1007/s10439-006-9153-1.
- Yeung, Tony, Penelope C. Georges, Lisa A. Flanagan, Beatrice Marg, Miguelina Ortiz, Makoto Funaki, Nastaran Zahir, Wenyu Ming, Valerie Weaver, and Paul A. Janmey. 2005. "Effects of Substrate Stiffness on Cell Morphology, Cytoskeletal Structure, and Adhesion." *Cell Motility and the Cytoskeleton* 60 (1): 24–34. doi:10.1002/cm.20041.
- Zhao, Feihu, Ted J. Vaughan, and Laoise M. Mcnamara. 2015. "Multiscale Fluid–structure Interaction Modelling to Determine the Mechanical Stimulation of Bone Cells in a Tissue Engineered Scaffold." *Biomechanics and Modeling in Mechanobiology* 14 (2). Springer Berlin Heidelberg: 231–43. doi:10.1007/s10237-014-0599-z.

CHAPTER 2

FREE ENERGY ANALYSIS OF CELL SPREADING



2.1. Introduction

Several experimental studies demonstrate that control of cell spreading using substrate micro-patterning has a significant impact on cell behavior. A study by McBeath *et al.* (2004) reveals that stem cell differentiation can be controlled by limiting cell spread area. It has also been shown that the contractility of smooth muscle cells increases with increasing cell area (Tan *et al.* (2003)). Lamers *et al.* (2010) show the spread geometry and stress fibre (SF) distribution of osteoblasts on grooved surfaces is highly dependent on groove spacing. Wide grooves result in polarized cells with SFs aligned along the grooves. Narrow groove spacing leads to randomly oriented cells and SFs. Finally, a study by Théry *et al.* (2006) has shown that when a cells spread on a “V-shaped” or “Y-shaped” ligand patch SFs align predominantly along the free edge of the cell and focal adhesions assemble along the perimeter of the ligand patch.

The bio-chemo-mechanical model proposed by Deshpande, *et al.* (2006) was used by McGarry *et al.* (2009) to analyze the aforementioned micro-post experiments of Tan *et*

al. Simulations reveal that as cells spread the increasing number of adhered posts provide increasing support for SF tension and therefore reduce SF dissociation. Simulations also correctly predict that SFs are highly aligned along the free edges of the cell where the stress state is uniaxial. Using the same framework Pathak *et al.* (2008) analyzed the experiments of Théry *et al.* and, similar to McGarry *et al.*, highly aligned stress fibres are predicted along the free edge of the cell. While these studies demonstrate the importance of tension support for stress fibre formation, they reveal a number of shortcomings of the phenomenological framework of Deshpande *et al.* (2006). Firstly, a high level of isotropic SF formation is incorrectly predicted to occur in regions of biaxial stress in the center of the cell. Experiments reveal that limited SF formation occurs in such regions. Secondly, the spread-state of the cell is assumed as the undeformed reference configuration. Clearly the cell deforms significantly from its spherical suspended state to reach the final spread-state.

In the current study we attempt to address these shortcomings by developing a steady-state finite element implementation of the recent thermodynamically motivated stress fibre model of Vigliotti *et al.* (2015). Our simulations of cells on micro-patterned substrates incorporate the following significant improvements on previous approaches: (i) The spread-state of the cell is not assumed as the strain free reference configuration. Rather, the cell deforms from a suspended geometry to reach its final spread configuration. The strain state of the deformed configuration is a key determinant of SF distribution in the cell. (ii) The number of cytoskeletal proteins in the cell is a finite and conserved quantity, requiring the development of a non-local numerical implementation. In contrast, McGarry *et al.* and Pathak *et al.* do not impose a global limit on SF formation. (iii) In addition to the advances presented in terms of our SF finite element model, we also propose a further development of the thermodynamically motivated focal

adhesion assembly model of Deshpande *et al.* (2008) so that focal adhesion formation may be limited by a prescribed ligand density on the substrate to which a cell adheres.

An important consequence of the modelling approach is that there is not a unique final spread-state for the cell. Even in experiments such as those of Théry *et al.* and Tan *et al.* where the outline of the final spread shape is prescribed by micro-patterning ligand patches on the substrate, there is still an infinite number of ways in which the cell can spread across the patch geometry. Each final spread-state would have a different strain distribution and resultant SF distribution. Despite the infinite ways in which a cell can spread, the experimental heat maps of SF distribution in the study of Théry *et al.* reveal a strong trend of SF formation along free edges for a large number of cells. This suggests that the final spread state of a cell is not randomly generated. In this study we use our modelling framework to determine the free energy of the cell for a number of spread states and we hypothesize that cell spreading is driven by free energy minimization. Furthermore we ask if predicted SF and focal adhesion distributions for minimum free energy spread states are in agreement with experimentally observed distributions.

This chapter is structured as follows: In Section 2.2 we present our steady-state non-local stress fibre formation and cell spreading framework, followed by our model for ligand dependent focal adhesion assembly. We also introduce the factors contributing to the cell free energy. In Section 2.3 we consider a simplified example of axisymmetric spreading of a round cell on a flat substrate in order to demonstrate the key features of the computational framework and predict experimental trends observed by Engler *et al.* (2003). Finally, in Section 2.4 we simulate the experiments of Théry *et al.* by analyzing a number of spread-states for cells adhered to “V-shaped” and “Y-shaped” ligand patches.

2.2. Modelling framework

2.2.1. Framework for stress fibre remodelling and contractility

The cytoskeleton is composed of actin-myosin SFs, which actively generate tension through cross-bridge cycling between the actin and myosin filaments. The thermodynamically consistent model from Vigliotti *et al.* (2015) captures key features of SF dynamics, including (i) The kinetics of stress fibre formation and dissociation as motivated by thermodynamic considerations, (ii) the stress, strain, and strain-rate dependence of SF remodelling, and (iii) global conservation of the cytoskeletal proteins. Here we implement a steady-state form of this continuum model in a two-dimensional finite element setting.

We envisage a two-dimensional (2D) cell of thickness b lying in the $x_1 - x_2$ plane (Figure 2.1a). A representative volume element (RVE) in the undeformed state is defined as a disk of radius $n^R l_0/2$. Stress fibres emanate from the center of this disk, each comprised of n^R functional units (of length l_0) in their initial ground state. In 2D plane stress SFs can form in a large number of directions, with each direction defined by an angle ϕ with respect to the x_1 -axis. At steady state, we consider that the (normalized) number of actin-myosin contractile units within a SF in direction ϕ in the RVE is given by:

$$\hat{n}(\phi) = \frac{n(\phi)}{n^R} = (1 + \varepsilon_n(\phi))/(1 + \tilde{\varepsilon}_{ss}) \quad (2.1)$$

where $\varepsilon_n(\phi)$ is the nominal strain in the direction ϕ . When a SF is extended, contractile units are added, with the effect that the internal strain in the SF is reduced until a steady state value $\tilde{\varepsilon}_{ss}$ is achieved (Figure 2.1b). $\tilde{\varepsilon}_{ss}$ is given by the positive root of the relation:

$$(p - 1)\tilde{\varepsilon}_{ss}^p + p\tilde{\varepsilon}_{ss}^{p-1} - \frac{1}{\beta} = 0 \quad (2.2)$$

where β and p are non-dimensional constants that govern the internal energy ψ of n^R functional units within a SF. Conversely, when a SF shortens, functional units are removed. In both cases, the internal fibre steady state strain $\tilde{\epsilon}_{ss}$ is fixed and in general different from the axial material strain in the direction of the fibre, $\epsilon_n(\phi)$.

2.2.1.1. Mass conservation of cytoskeletal proteins

We assume spreading takes place during the interphase period of the cell cycle when the cell is in a homeostatic state (i.e. the concentration of all proteins within the cell is constant) (Weiss 1996). Therefore, in the finite element framework developed in this study a global conservation of the total number of SF proteins N_0 within the entire cell is enforced. Cytoskeletal proteins are considered to exist in two states: a bound state and an unbound state. The bound proteins make up the functional units of the stress fibres within the RVE and thus are not mobile. The unbound proteins are mobile and can diffuse throughout the cell cytoplasm. The global conservation of cytoskeletal proteins may be expressed as

$$N_0 = N_u^{tot} + N_b^{tot} \quad (2.3)$$

where N_u^{tot} and N_b^{tot} are the total numbers of unbound and bound cytoskeletal proteins in the entire cell. We next introduce the local normalized quantities: $\hat{N}_u = N_u/N_0$, $\hat{N}_b = N_b/N_0$, and $\hat{N}_t = N_t/N_0$, where N_u and N_b are the local number of unbound and bound proteins within a given RVE, and the total number of proteins N_t locally in the RVE is obtained from

$$\hat{N}_t = \hat{N}_u + \hat{N}_b \quad (2.4)$$

Recall that the unbound proteins are mobile. Cytoskeletal proteins can diffuse through the cytoplasm at a rate of $1.5 \mu\text{m/s}$ (McGrath *et al.* 1998) which is considered fast relative to the timescales of SF remodelling (several studies report remodelling takes place over the course of hours (Wang *et al.* 2001; Kaunas *et al.* 2005)). Therefore it is

reasonable to assume that for time-scales over which SFs remodel the total number of unbound proteins in the entire cell, N_u^{tot} , is uniformly distributed across all RVEs, i.e. \hat{N}_u is the same in all RVEs. Bound proteins, on the other hand, are not uniformly distributed throughout the cell, and \hat{N}_b in a given RVE must be computed from:

$$\hat{N}_b = \int_{-\pi/2}^{+\pi/2} \hat{\eta}(\phi) \hat{n}(\phi) d\phi \quad (2.5)$$

where $\eta(\phi)$ is the angular SF concentration per unit surface area of the RVE, with $\hat{\eta}(\phi) = \eta(\phi)n^R/N_0$. The global conservation condition (equation 2.3) can therefore be expressed as:

$$\hat{N}_u = 1 - \frac{1}{V_c} \int_{V_c} \hat{N}_b dV \quad (2.6)$$

where V_c is the total cell volume. In a numerical implementation, the global integral across the cell volume V_c in equation 2.6 requires a non-local summation of \hat{N}_b across all integration points in the cell, as described in Section 2.2.1.5.

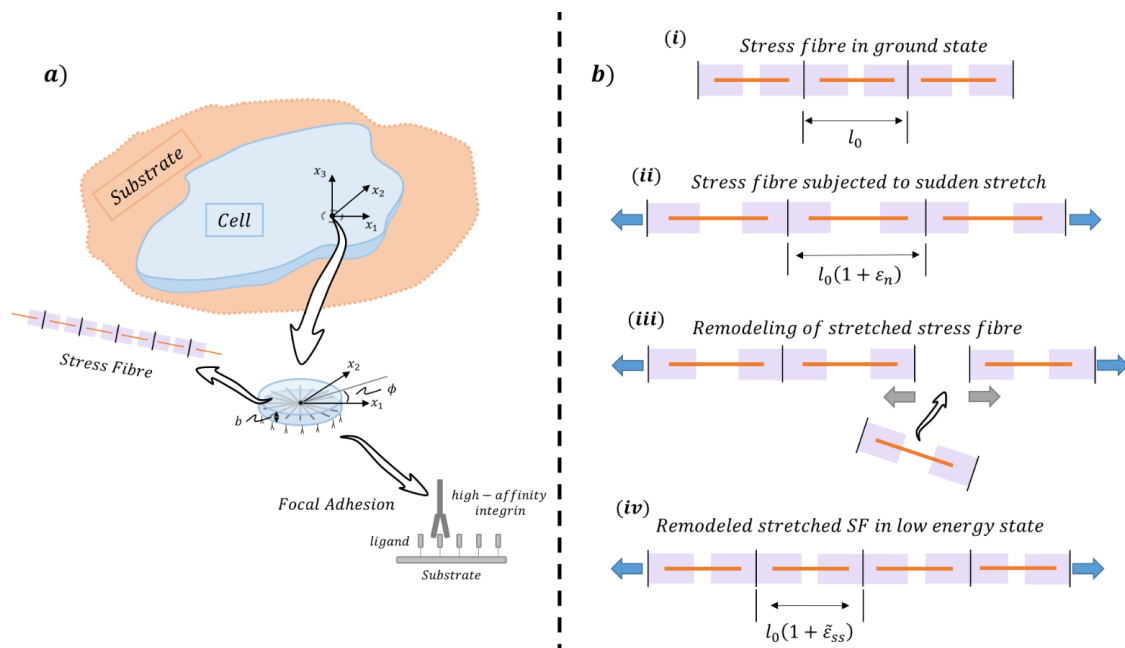


Figure 2.1: a) Schematic of a 2D cell on a ligand-coated substrate with the coordinate system marked. The networks of stress fibres and focal adhesions within the 2D RVE are shown in the inset; b) Remodelling of a SF subjected to a nominal tensile strain ϵ_n : (i) SF in ground state, with functional unit strain $\tilde{\epsilon}_n = 0$; (ii) SF subjected to tensile strain ϵ_n which reduces the actin-myosin overlap; (iii) Remodelling of SF by addition of functional unit; (iv) Remodeled SF now in low energy state, with functional unit strain $\tilde{\epsilon}_n = \tilde{\epsilon}_{ss}$. (Vigliotti *et al.*, 2015)

2.2.1.2. SF angular concentration and active stress tensor

We next consider the kinetic equation for SF formation and dissociation proposed by

Vigliotti *et al.*:

$$\dot{\hat{\eta}}(\phi) = \frac{\hat{N}_u}{\pi \hat{n}(\phi)} \omega_n \exp \left[-\hat{n}(\phi) \frac{\mu_a - \mu_u}{kT} \right] - \hat{\eta}(\phi) \omega_n \exp \left[-\hat{n}(\phi) \frac{\mu_a - \mu_b(\phi)}{kT} \right] \quad (2.7)$$

The first term on the right is the forward reaction rate for the formation of SFs, where ω_n is the molecular collision frequency of the SF proteins, k is the Boltzmann constant, T the absolute temperature, and μ_a is the activation enthalpy that must be surpassed for n^R proteins to form a SF. Here μ_u is the standard enthalpy of n^R unbound SF proteins, with $\mu_u = \mu_{u0} + \Delta\mu_{u0}C$. The unbound proteins are affected by an activation signal C and form more readily into their bound states as the signal (e.g. concentration of unfolded ROCK) increases, with μ_{u0} is the standard enthalpy of the unbound SF proteins in the absence of a signal ($C = 0$) and $\Delta\mu_{u0}$ the increase in the enthalpy of the unbound molecules at full

signal activation ($C = 1$). At steady state we assume a continuous fully activated signal, i.e. $C = 1$. The second term on the right is the backward reaction rate for SF dissociation, with μ_b the standard enthalpy of n^R bound SF proteins, given as:

$$\mu_b \equiv \psi - \sigma_f(\phi)[1 + \varepsilon_n(\phi)]\Omega \quad (2.8)$$

where Ω is the volume of n^R functional units in a SF in an undeformed RVE, and ψ is the internal energy of n^R functional units within a SF, given by:

$$\psi \equiv \mu_{b0} + \beta\mu_{b0}|\tilde{\varepsilon}_{ss}|^p \quad (2.9)$$

where μ_{b0} is the internal energy of n^R functional units within a SF in their ground state, and $\sigma_f(\phi)$ is the tensile stress actively generated by a SF. In this paper we develop a steady state solution, hence Hill tension-velocity relationship does not need to be considered as $\sigma_f(\phi)$ is necessarily equal to the maximum isometric tension σ_{max} . Here we consider steady state conditions so that $\dot{\eta}(\phi) = 0$, therefore equation 2.7 reduces to:

$$\hat{\eta}(\phi) = \frac{\hat{N}_u}{\pi\hat{n}(\phi)} \frac{\exp\left[-\hat{n}(\phi)\frac{\mu_a - \mu_u}{kT}\right]}{\exp\left[-\hat{n}(\phi)\frac{\mu_a - \mu_b(\phi)}{kT}\right]} \quad (2.10)$$

and the normalized SF concentration in direction ϕ is given as:

$$\hat{\eta}(\phi) = \frac{\hat{N}_u}{\pi\hat{n}(\phi)} \exp\left[-\hat{n}(\phi)\frac{\mu_b(\phi) - \mu_u}{kT}\right] \quad (2.11)$$

or from equation 2.5:

$$\hat{\eta}(\phi) = \frac{\hat{N}_t - \int_{-\pi/2}^{+\pi/2} \hat{\eta}(\phi)\hat{n}(\phi) d\phi}{\pi\hat{n}(\phi)} B(\phi) \quad (2.12)$$

where $B(\phi) = \exp[-\hat{n}(\phi)(\mu_b(\phi) - \mu_u)/kT]$, \hat{N}_t is the total number of cytoskeletal proteins locally in an RVE, and the integral provides the total number of bound proteins in the RVE. Finally the 2D active stress tensor follows as:

$$\sigma_{act} = \frac{\sigma_{max} f_0}{J} \int_{-\frac{\pi}{2}}^{\frac{\pi}{2}} \left(\hat{\eta}(\phi) [1 + \varepsilon_n(\phi)] \begin{bmatrix} \cos^2 \phi & \frac{\sin 2\phi}{2} \\ \frac{\sin 2\phi}{2} & \sin^2 \phi \end{bmatrix} \right) d\phi \quad (2.13)$$

where f_0 is the volume fraction of cytoskeletal proteins in the cell, and J is the determinant of the deformation gradient \mathbf{F} .

2.2.1.3. Cytoskeletal free energy

The cytoskeletal free energy (g_{cyto}) is given as follows:

$$g_{cyto} = N_u^{tot} \chi_u + \int_{V_c} N_b \chi_b dV \quad (2.14)$$

where χ_u is the chemical potential of the unbound proteins that form a single SF functional unit, and χ_b is the chemical potential of a functional unit within a SF. From equation 2.5:

$$g_{cyto} = N_u^{tot} \chi_u + \int_{V_c} \left(\int_{-\frac{\pi}{2}}^{\frac{\pi}{2}} \eta(\phi) n(\phi) d\phi \right) \chi_b dV \quad (2.15)$$

As previously mentioned we assume infinitely fast diffusion of SF proteins and therefore a homogeneous distribution throughout the cell. Also equation 2.10 implies thermodynamic equilibrium with $\chi_u = \chi_b$ which then simplifies equation 2.15 to:

$$g_{cyto} = N_u^{tot} \chi_u + \chi_u \int_{V_c} \left(\int_{-\frac{\pi}{2}}^{\frac{\pi}{2}} \eta(\phi) n(\phi) d\phi \right) dV \quad (2.16)$$

Here the double integral represents the total number of bound proteins in all RVEs in the cell. Therefore:

$$g_{cyto} = N_u^{tot} \chi_u + (N_0 - N_u^{tot}) \chi_u = N_0 \chi_u \quad (2.17)$$

The chemical potential of the unbound proteins is $\chi_u = \mu_u + kT \ln(\hat{N}_u)$ and thus:

$$g_{cyto} = N_0 (\mu_u + kT \ln(\hat{N}_u)) \quad (2.18)$$

with the cytoskeletal energy per unit volume of the cell then given as

$$\bar{G}_{cyto} = \rho (\mu_u + kT \ln(\hat{N}_u)) \quad (2.19)$$

where $\rho \equiv N_0/V_c$ is the concentration of cytoskeletal proteins.

2.2.1.4. Passive elasticity

The formulation is completed by the addition of a non-linear hyperelastic Ogden model (Ogden 1972) in parallel with the SF model in order to represent the strain stiffening of the mechanically passive cell components. As we consider the cell volume to remain constant during the analysis, the incompressible formulation is implemented:

$$\boldsymbol{\sigma}_{pas} = \sum_{i=1,2} \frac{2\mu}{\alpha} (\lambda_i^\alpha - (\lambda_1\lambda_2)^{-\alpha}) (\mathbf{m}_i \otimes \mathbf{m}_i) \quad (2.20)$$

where μ is the material shear modulus, $\lambda_{1,2}$ are the principal stretches, $\mathbf{m}_{1,2}$ are the principal stretch directions, and α is a material constant. Here the passive elastic free energy per unit volume (\bar{G}_{elas}) is given by the Ogden strain energy density function:

$$\bar{G}_{elas} = \frac{2\mu}{\alpha^2} (\lambda_1^\alpha + \lambda_2^\alpha - (\lambda_1\lambda_2)^{-\alpha} - 3) \quad (2.21)$$

The total Cauchy stress tensor at an integration point is obtained by summation of the passive and active contributions:

$$\boldsymbol{\sigma}_{cauchy} = \boldsymbol{\sigma}_{pas} + \boldsymbol{\sigma}_{act} \quad (2.22)$$

2.2.1.5. Numerical implementation

In our numerical implementation we consider SF formation in a large number of discrete directions M ($M=36$ is found to provide a converged solution) in the 2D plane of each RVE in the cell. equation 2.5 is approximated as

$$\hat{N}_b = \frac{\pi}{M} \sum_{i=1}^M \hat{\eta}_i \hat{n}_i \quad (2.23)$$

where $\hat{\eta}(\phi_i)\hat{n}(\phi_i)$ is written in shorthand as $\hat{\eta}_i\hat{n}_i$. Equation 2.12 is therefore approximated as

$$\hat{\eta}_j\hat{n}_j\pi = B_j\hat{N}_t - B_j\left(\frac{\pi}{M}\sum_{i=1}^M\hat{\eta}_i\hat{n}_i\right), \quad j = 1, M \quad (2.24)$$

Rearranging, we obtain

$$\hat{\eta}_j\hat{n}_j\left(\frac{1}{B_j}\right) - \left(\frac{1}{M}\sum_{i=1}^M\hat{\eta}_i\hat{n}_i\right) = \frac{\hat{N}_t}{\pi}, \quad j = 1, M \quad (2.25)$$

or, in matrix form:

$$\begin{bmatrix} \left(\frac{1}{B_1} + \frac{1}{M}\right)\hat{n}_1 & \frac{1}{M}\hat{n}_2 & \dots & \frac{1}{M}\hat{n}_M \\ \frac{1}{M}\hat{n}_2 & \left(\frac{1}{B_2} + \frac{1}{M}\right)\hat{n}_2 & \dots & \frac{1}{M}\hat{n}_M \\ \dots & \dots & \dots & \dots \\ \frac{1}{M}\hat{n}_M & \frac{1}{M}\hat{n}_M & \dots & \left(\frac{1}{B_M} + \frac{1}{M}\right)\hat{n}_M \end{bmatrix} \begin{Bmatrix} \hat{\eta}_1 \\ \hat{\eta}_2 \\ \dots \\ \hat{\eta}_M \end{Bmatrix} = \frac{\hat{N}_t}{\pi} \begin{Bmatrix} 1 \\ 1 \\ \dots \\ 1 \end{Bmatrix} \quad (2.26)$$

A solution for $\hat{\eta}_j$ ($j=1, M$) is obtained by matrix inversion. This steady-state model for SF formation and contractility is implemented via a *user-defined material* (UMAT) subroutine in the commercial finite element (FE) software package Abaqus. Prescribed boundary conditions are applied to the cell at the start of an analysis step, and contact conditions (see Section 2.2.2) with a substrate are enforced at cell nodes where appropriate. The solution is progressed through the analysis step, with each increment representing an iteration towards the final steady state solution. At each integration point the axial material nominal strains $\varepsilon_n(\phi)$ in each of the M stress fibre directions are determined from the material log strain tensor (STRAN), and number of functional units $\hat{n}(\phi)$ in each of the M directions is obtained from equation 2.1. In the first increment of the analysis step it is assumed that all cytoskeletal proteins are unbound and uniformly distributed across all integration points in the cell mesh so that $\hat{N}_t = \hat{N}_u$. The solution for

$\hat{\eta}(\phi)$ in M directions is obtained by inversion of the matrix on the left of equation 2.26. The local Cauchy stress tensor σ is computed from equations 2.13, 2.20, 2.22 and the consistent tangent matrix $\partial\Delta\sigma/\partial\Delta\epsilon$ is approximated numerically based on a forward difference perturbation of the deformation gradient matrix (Sun *et al.* 2008; Nolan *et al.* 2014; Reynolds and McGarry 2015). At each integration point the local number of bound proteins \hat{N}_b is calculated at the end of the increment, as per equation 2.23. At the end of an increment i , the total number of bound cytoskeletal proteins throughout the entire cell is computed through volume averaged summation of $\hat{N}_b|{}^i$ across every integration point in the mesh in a *user-defined external database* (UEXTERNALDB) file, as outlined in Figure 2.2. In the subsequent increment the remaining available unbound proteins are redistributed so that a homogeneous distribution of $\hat{N}_u|{}^{i+1}$ unbound proteins is obtained in every RVE. The total number of proteins in the RVE is updated so that $\hat{N}_t|{}^{i+1} = \hat{N}_u|{}^{i+1} + \hat{N}_b|{}^i$. Equation 2.26 is then solved and new values for $\hat{\eta}(\phi)|{}^{i+1}$, and thus $\sigma|{}^{i+1}$ and $\hat{N}_b|{}^{i+1}$ are obtained. Following the final increment of the analysis step the steady-state solution is achieved, and the cytoskeletal free energy \bar{G}_{cyto} and elastic free energy \bar{G}_{elas} are computed (equations 2.19, 2.21).

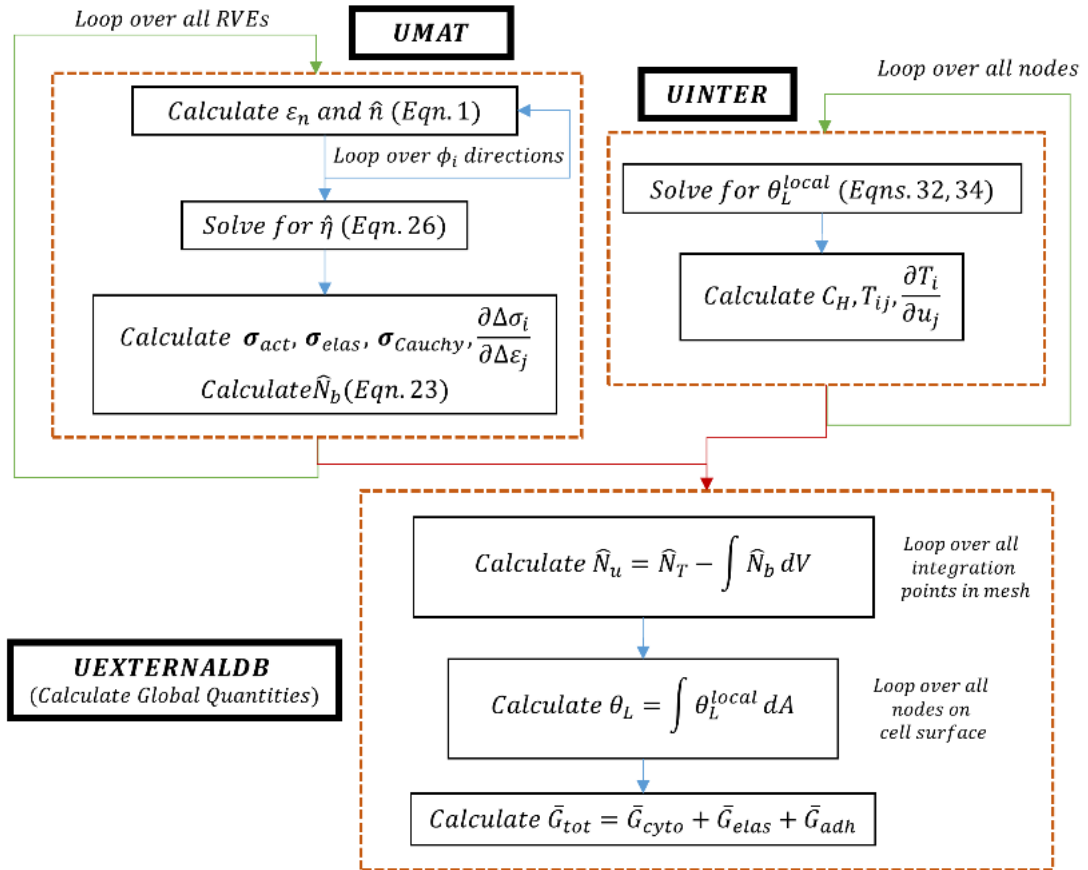


Figure 2.2: Outline of solution scheme. Total steady state energy density \bar{G}_{tot} is calculated at the end of the analysis through the use of a **UEXTERNALDB** subroutine.

2.2.2. Framework for focal adhesion development

Binding integrins on the cell surface exist in two conformational states: a low affinity (bent) state or an active (straight) state with a high affinity to the appropriate ligand. Only high affinity integrins will bind to the substrate. Here we introduce an extension of the thermodynamic focal adhesion (FA) model from Deshpande *et al.* (2008), whereby we include a dependence of bond formation on ligand availability.

2.2.2.1. Focal adhesion model

We first define $\theta_L = C_L/N_L$ and $\theta_H = C_H/N_H$, with $\theta_L, \theta_H \leq 1$. Here C_L and C_H are the area densities of the unbound low affinity integrins and bound high affinity integrins, respectively, N_L is the area density of the unbound low affinity sites on the cell surface, and N_H is the area density of ligands on the substrate surface. The chemical potential of

low affinity integrins at a density C_L is dependent on their internal energy and configurational entropy given by:

$$\chi_L = \mu_L + kT \ln \left(\frac{\theta_L}{1 - \theta_L} \right) \quad (2.27)$$

where μ_L is the enthalpy of the low affinity integrins, while k and T are the Boltzmann constant and absolute temperature. As only high affinity (or straight) integrins interact with substrate ligands, the high affinity chemical potential (at a density C_H) includes additional contributions due to the stretching of the bonds:

$$\chi_H = \mu_H + kT \ln \left(\frac{\theta_H}{1 - \theta_H} \right) + \Phi(\Delta_i) - F_i \Delta_i \quad (2.28)$$

where μ_H is the enthalpy of the high affinity integrins, $\Phi(\Delta_i)$ is the strain energy of the integrin-ligand complex, and the $-F_i \Delta_i$ term is the mechanical work that represents the loss in free energy due to the stretch Δ_i of the integrin-ligand (analogous to the pressure-volume term in the thermodynamics of gases), with:

$$F_i = \frac{\partial \Phi}{\partial \Delta_i} \quad (2.29)$$

The stretch energy Φ is expressed as a piecewise quadratic potential:

$$\Phi = \begin{cases} \kappa_s \Delta_e^2 & \Delta_e \leq \Delta_n \\ -\kappa_s \Delta_n^2 + 2\kappa_s \Delta_n \Delta_e - \kappa_s \Delta_e^2 & \Delta_n < \Delta_e \leq 2\Delta_n \\ \kappa_s \Delta_n^2 & \Delta_e > 2\Delta_n \end{cases} \quad (2.30)$$

where κ_s is the stiffness of the integrin-ligand bond, $\Delta_e = \sqrt{\Delta_1 + \Delta_2}$ is the stretch magnitude, and Δ_n is the peak bond length. The bond stretch Δ_i is related to the displacement u_i of the cell membrane relative to the substrate as:

$$\Delta_i = \begin{cases} u_i & \Delta_e \leq \Delta_n \text{ or } \left[\frac{\partial \Phi}{\partial \Delta_e} \Delta_e < 0 \right] \\ 0 & \text{otherwise} \end{cases} \quad (2.31)$$

At thermodynamic equilibrium $\chi_H = \chi_L$, so equations 2.27, 2.28 lead to:

$$\left(\frac{1-\theta_L}{\theta_L}\right)\left(\frac{\theta_H}{1-\theta_H}\right) = Z^* \quad (2.32)$$

$$\text{with } Z^* = \exp\left(\frac{\mu_L - \mu_H - \Phi(\Delta_i) + F_i \Delta_i}{kT}\right) \quad (2.33)$$

which gives the local area densities of low and high affinity integrins. Similar to the SF model, we implement global conservation of integrins on the cell surface:

$$S_0 C_0 = S_0(1-\delta)N_L^0 \theta_L + \int_{S_a} \left[N_L \theta_L + \frac{N_H Z^* \theta_L}{(1-\theta_L) + Z^* \theta_L} \right] dS \quad (2.34)$$

where S_0 is the undeformed reference surface area of the cell, and C_0 is the initial density of integrins on the cell surface. The term on the left $S_0 C_0$ is a conserved value, giving the total number of integrins on the cell surface. S_a is the surface area in contact with the substrate, δ is the fraction of the cell adhered to the substrate, and N_L^0 is the initial undeformed area density of low affinity binding sites on the cell surface. The first term on the right gives the total number of low affinity integrins on the unadhered cell surface, while the second term gives the total number of integrins (high and low affinity) on the adhered cell surface. The local tractions on the cell surface are depend on the concentration of bound high affinity integrins and the force on each ligand-integrin complex, and are balanced by the stresses in the cell:

$$T_i = \sigma_{ij} n_{ij} = -C_H F_i \quad (2.35)$$

where σ_{ij} is the Cauchy stress in the cell, and n_{ij} is the surface normal.

2.2.2.2. Focal adhesion free energy

The adhesion free energy is given by:

$$g_{adh} = \int_{S_a} (C_L \chi_L + C_H \chi_H) dS \quad (2.36)$$

However at thermodynamic equilibrium $\chi_H = \chi_L$, so:

$$g_{adh} = \chi_L S_0 C_0 \quad (2.37)$$

with the adhesion energy per unit cell volume given as

$$\bar{G}_{adh} = \frac{\chi_L S_0 C_0}{b S_0} \quad (2.38)$$

where b is the cell thickness in its undeformed configuration. Then, \bar{G}_{adh} follows as:

$$\bar{G}_{adh} = \frac{C_0}{b} \left(\mu_L + kT \ln \left(\frac{\theta_L}{1 - \theta_L} \right) \right) \quad (2.39)$$

2.2.2.3. Numerical implementation

The focal adhesions between the cell and the micro-patterned substrates are included in the analysis through a *user-defined interface* (UINTER) subroutine in Abaqus. Adhesions can develop at any node on the cell surface that comes in contact with the substrate, dependent on the local tractions and availability of integrins. At each node θ_L is recorded at the end of the increment, as per equation 2.32. Recall that the area density of low affinity integrins $C_L = \theta_L N_L$. At the end of an increment i , the global area density of low affinity integrins on the cell surface is computed through area averaged summation of $\theta_L|^i$ across every node on the surface in a *user-defined external database* (UEXTERNALDB) file (Figure 2.2). Mass conservation of integrins is enforced by equation 2.34. In the subsequent increment the remaining available unbound low affinity integrins are redistributed so that a homogeneous distribution of $\theta_L|^{i+1}$ is obtained across the surface. We assume the time-scales associated with integrin diffusion are fast relative to the time-scales of focal adhesion assembly. Efficient achievement of a converged solution the UINTER requires the specification of an accurate stiffness matrix. An exact analytical solution is obtained from:

$$\frac{\partial T_i^A}{\partial u_j} = - \left[C_H \frac{\partial F_i}{\partial u_j} + F_i \frac{\partial C_H}{\partial u_j} \right] \quad (2.40)$$

Rigid glass substrates are assumed to be infinitely stiff relative to the cell, and therefore have a negligible free energy.

2.2.3. Material parameters

All simulations are reported for cells at a temperature $T = 310K$. The parameters for the SF framework are fixed at those used in Vigliotti *et al.* (2015) with the volume fraction $f_0 = 0.032$, $\Omega = 10^{-7.1} \mu m^3$, $\beta = 1.2$, $p = 2$, $\tilde{\epsilon}_{ss} = 0.35$, and the maximum isometric tension $\sigma_{max} = 240 kPa$ (Lucas *et al.* 1987). In keeping with the parameter studies of Vigliotti *et al.* $(\mu_{u0} + \Delta\mu_{u0}) = 8 kT$, $\mu_{b0} = 9 kT$. The density of cytoskeletal proteins in the cell ρ is $2 \times 10^6 \mu m^{-3}$, calibrated such that the cytoskeletal free energy is competitive with the passive free energy. The passive elastic parameters are $\mu = 1.66 kPa$ and $\alpha = 8$, determined through simulation of the Engler *et al.* (2003) experiments for cells spreading on substrates of increasing stiffness. For the FA model, parameters were constrained to lie within commonly accepted ranges as per Deshpande *et al.* (2008). The total area density of integrins C_0 is $5000 \mu m^{-2}$ (Lauffenburger and Linderman 1993), the bond stiffness $\kappa_s = 0.15 nN \mu m^{-1}$, and the maximum allowable stretch in the bond $\Delta_n = 50 nm$, such that the surface energy $\bar{\gamma} = \kappa_s \Delta_n^2 / kT$ is in the upper end of the range reported by Leckband and Israelachvili (2001). The difference in the reference chemical potentials for the low and high affinity integrins is taken as $\mu_H - \mu_L = 5kT$ (McCleverty and Liddington 2003). The model was extended to allow for dependence on the number of available ligands and non-local conservation of integrins. A parametric study was performed to determine an appropriate ligand density to ensure sufficient adhesions could form, taken to be $N_H = 25 \times 10^3 \mu m^{-2}$. The availability of binding sites is assumed to be greater than the maximum number of bound high affinity integrins, [continued page 67]

Parameter symbol	Brief description
$n; n^R$	Number of functional units in a stress fibre; reference number of functional units within stress fibre in an undeformed RVE
η	Angular concentration of stress fibres at orientation (ϕ)
Ω	Volume of n^R functional units of the stress fibre
l_0	Undeformed length of a functional unit
$\varepsilon_n; \tilde{\varepsilon}_{ss}$	Nominal strain of a stress fibre; functional unit strain at steady state
$N_b; N_u$	Number of cytoskeletal proteins bound in functional units; number of unbound cytoskeletal proteins
$\mu_a; \mu_u; \mu_b$	Activation enthalpy for n^R cytoskeletal proteins; enthalpy of n^R cytoskeletal proteins in the unbound state; enthalpy of n^R cytoskeletal proteins in bound state
$\mu_{u0}; \mu_{b0}$	Standard enthalpy of n^R functional units in the unbound and bound states
ψ	Internal energy of n^R functional units within a stress fibre
$\sigma_f; \sigma_{max}$	Stress fibre stress; maximum tensile stress of a stress fibre
$f_0; \rho$	Volume fraction of cytoskeletal proteins in the cell; concentration of cytoskeletal proteins
$\chi_u; \chi_b$	Chemical potential of the unbound cytoskeletal proteins that form a single functional unit; chemical potential of a functional unit within a stress fibre
$C_0; C_L; C_H$	Initial area density of integrins on the cell surface; area densities of the unbound low affinity integrins and bound high affinity integrins
$S_0; S_a$	Undeformed reference surface area of the cell; surface area in contact with substrate
$N_L; N_H$	Area density of the unbound low affinity sites on the cell surface; Area density of ligands on the substrate surface
$\theta_L; \theta_H$	$C_L / N_L; C_H / N_H$
$\mu_L; \mu_H$	Enthalpy of the low affinity integrins; enthalpy of the high affinity integrins
Φ	Strain energy of the integrin-ligand complex
$\Delta_i; \Delta_n$	Stretch of the integrin-ligand complex; peak bond length
κ_s	Stiffness of the integrin-ligand complex
$\chi_L; \chi_H$	Chemical potential of low affinity integrins; chemical potential of high affinity integrins
$\bar{G}_{tot}; \bar{G}_{cyto}; \bar{G}_{elas}; \bar{G}_{adh}; \bar{G}_{sub}$	Total, cytoskeletal, elastic, adhesion, and substrate free energy densities

Table 2.1: A summary of key parameters of the model

taken here as $N_L = 50 \times 10^3 \mu m^{-2}$. A summary of key parameters is provided in Table 2.1.

2.3. 2D analysis of cell spreading on infinite flat substrates

We illustrate the features of the modelling framework by considering the axisymmetric spreading of a round cell on flat substrates under plane stress conditions, as shown in Figure 2.3. A mesh sensitivity study showed that a converged solution is obtained with 185 membrane elements. Material incompressibility is assumed. Solutions are presented for both a rigid and a compliant substrate. Additionally the solutions are presented for both a high and low substrate ligand density. In the undeformed configuration the cell has a radius r and thickness b . Cell spreading is simulated in two analysis steps: (i) Displacement (“pre-stretch”) boundary conditions are applied to the cell so that its radius is increased to λr with a uniform strain state throughout; (ii) Contact is implemented between the deformed cell and the substrate and the displacement boundary condition is removed. Surface and integrin-ligand attachments are formed in accordance with equations 2.27-2.35. The active cell stress tensor is computed from equation 2.13 and is added to the passive stress tensor (equation 2.22). In addition to deformation of the cell and integrin-ligand attachments, the substrate will also deform due to the passive and active cell stress (except in cases where the substrates can be considered to be infinitely stiff compared to the cell). This finite element scheme determines the steady state configuration of the cell, adhesions, and substrate. For a given steady state configuration the total free energy density of the system is computed from

$$\bar{G}_{tot} = \bar{G}_{cyto} + \bar{G}_{elas} + \bar{G}_{adh} + \bar{G}_{sub} \quad (2.41)$$

Analyses are performed for a range of “pre-stretch” (λ) values and the free energy density of the system is plotted as a function of the steady-state spread area of the cell. As stated

in Section 2.1, we hypothesize that a cell tends towards a spread-state that reduces the free energy of the system.

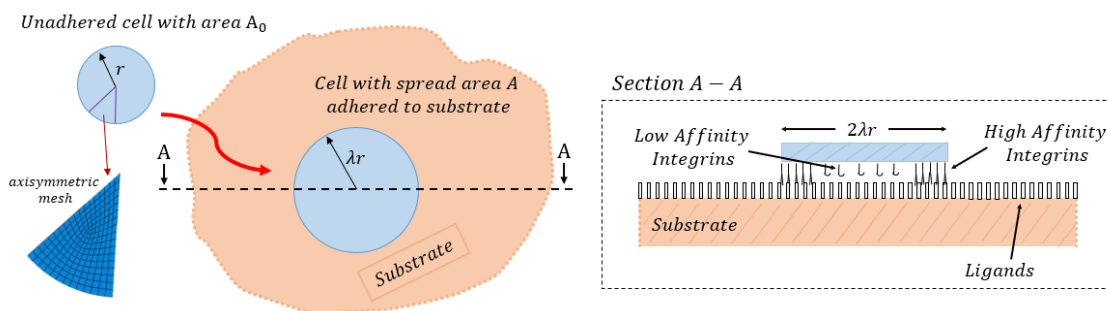


Figure 2.3: Axisymmetric cell spread schematic. A cell of radius r stretches over an infinite ligand patterned substrate.

2.3.1. Results

We first consider the case of cell spreading on a rigid substrate. The force generation by the actin-myosin machinery lowers the chemical potential of the stress fibre proteins in the bound state and thereby favors the formation of stress fibres. As the cell stretches to its spread configuration, functional units are added to the stress fibre chain in order to reduce the internal SF strain ($\tilde{\epsilon}_n$) to the ground state (dictated by $\tilde{\epsilon}_{SS}$). Thereby an increase in cell spreading results in a decrease in \hat{N}_u (Figure 2.4a), and consequently the free energy of the cytoskeletal proteins (\bar{G}_{cyto}) is lowered (Figure 2.4b). However as shown in Figure 2.4c, an increase in spreading also results in an increase in the elastic free energy of the cell due to straining of the passive (hyperelastic) non-contractile components of the cell. This framework therefore presents cell spreading as a competition between a decrease in cytoskeletal free energy due to strain induced stress fibre formation and an increase in elastic free energy due to straining of the passive cell components. As illustrated in Figure 2.4e, for the limited number of spread states considered here, a low free energy configuration is computed at an area of $A/A_0 \approx 2.75$. Any further spreading beyond this point will incur a significant elastic penalty due to the strain stiffening hyperelastic passive component of the model. Our computed low free energy spread area

corresponds closely to the experimental observations of Engler *et al.* (2003), where cell spread areas on rigid substrates are approximately three times higher than unspread cell areas.

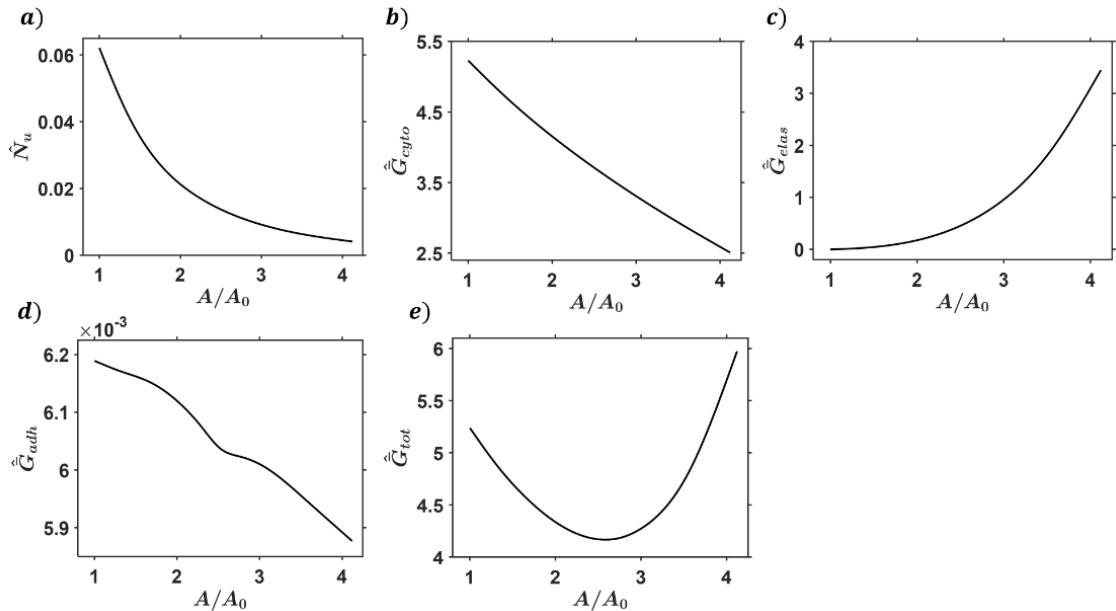


Figure 2.4: For a rigid substrate, the relationship between cellular spread area and (a) the number of available unbound cytoskeletal proteins (\hat{N}_u), (b) the cytoskeletal free energy (\hat{G}_{cyto}), (c) the elastic free energy (\hat{G}_{elas}), (d) the adhesion free energy (\hat{G}_{adh}), and (e) the combined total free energy density (\hat{G}_{tot}). Free energy densities characterized by normalized quantity $\hat{G} = \bar{G}/\rho kT$.

In the case of cell spreading on a compliant substrate, an increase in cell spread area incurs an elastic penalty (increasing free energy) from both the passive elastic components of the cell and the elastically deformed substrate. These elastic penalties are plotted in Figures 2.5c and 2.5e for cell spreading on a compliant neo-Hookean substrate ($\mu = 8\text{kPa}$), and once again are in direct competition with the reducing cytoskeletal free energy (Figure 2.5b) as the cell spreads. When $A/A_0 < 1$ the cell has contracted below the reference area due to substrate deformation. In such cases \bar{G}_{elas} increases due to compression of the passive cell components. The lowest free energy configuration on this compliant substrate is computed at a spread area of $A/A_0 \approx 1.8$ (Figure 2.5f). This spread area is 30% lower than the low energy spread area on a rigid substrate (Figure

2.4e). Once again, this result corresponds closely to the experimental study of Engler *et al.* (2003) where the cell spread areas of on 8kPa substrates are observed to be $\sim 25\%$ lower than on rigid substrates. This further supports our hypothesis that the cell will tend towards a spread state that reduces its free energy.

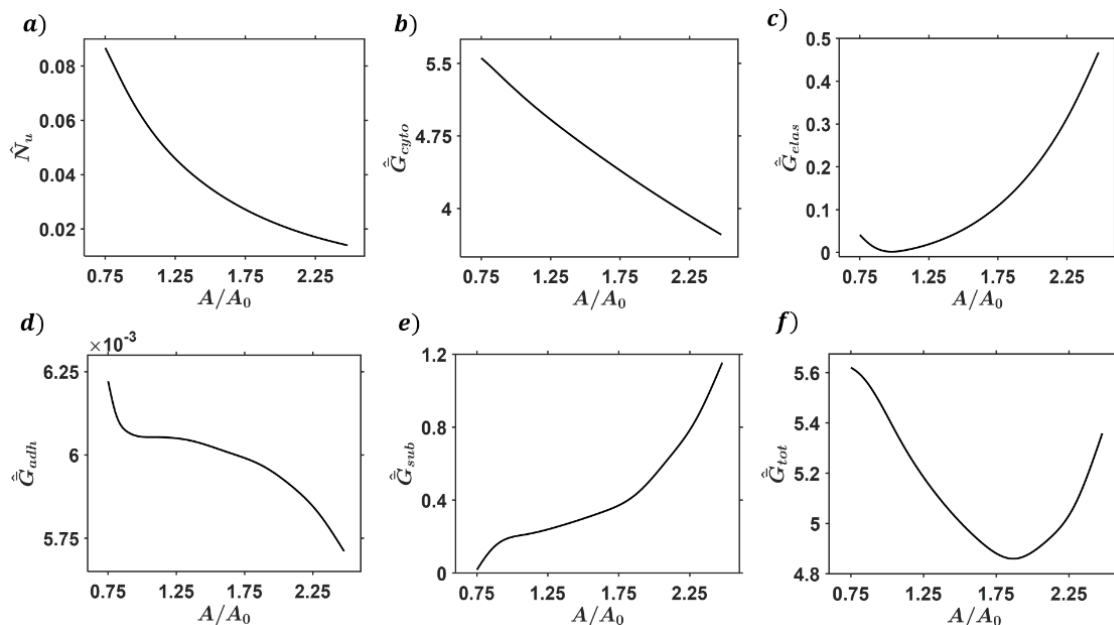


Figure 2.5: For a compliant neo-Hookean substrate ($\mu = 8\text{kPa}$), the relationship between cellular spread area and (a) the number of available unbound cytoskeletal proteins (\hat{N}_u), (b) the cytoskeletal free energy (\bar{G}_{cyto}), (c) the elastic free energy (\bar{G}_{elas}), (d) the adhesion free energy (\bar{G}_{adh}), (e) the substrate free energy (\bar{G}_{sub}), and (f) the combined total free energy density (\bar{G}_{tot}). Free energy densities characterized by normalized quantity $\hat{G} = \bar{G}/\rho kT$.

Figure 2.4d and 2.5d demonstrate that cell spreading also results in increased focal adhesion formation, with a consequent reduction in the adhesion free energy. The change in adhesion free energy over the range of spread configurations is ~ 3 orders of magnitude lower than the cell cytoskeletal and elastic free energies. Therefore focal adhesion formation does not significantly contribute to the energetic competition that governs cell spreading in Figures 2.4 and 2.5. However, cell spreading is not possible without a sufficient degree of traction mediated focal adhesion assembly, as mechanical equilibrium of the spread cell is only achieved by traction interaction with the substrate. An increase in traction results in an increase in the density of high affinity integrins (C_H).

As the cell spreads, the tractions between the cell and substrate increase (due to both elastic stretching of passive components and higher contractility due to increased strain induced SF formation), and consequently C_H increases. The entropy of integrins on the cell surface increases as more integrins are in a bound state (in accordance with equation 2.39). Therefore, an increase in C_H during spreading results in a decrease in \bar{G}_{adh} , as shown in Figure 2.4d. A higher ligand density will inherently allow the cell to spread further as higher cellular tractions can be supported by the focal adhesions. In contrast, Figure 2.6 considers the case of a rigid substrate with a low ligand density ($N_H = 2500 \mu m^{-2}$), which limits the cell spreading. The final spread area increases with the initially applied cell pre-stretch up to a value of $\lambda \approx 1.5$. If the cell is initially stretched beyond this point, a sufficient number of integrin-ligand bonds cannot be formed to support the resultant tractions, and the cell shrinks to a steady-state area of $A/A_0 \approx 1.85$. This is the maximum spread area that the cell can reach for this low ligand density. Note that if the cell cannot adhere to the substrate (e.g. ligand density of zero), an unadhered cell is predicted to shrink to an area of $A/A_0=0.735$ and a total free energy density of $\hat{G}_{tot} = 5.65$ is observed. As shown in Figure 2.6b, the total free energy reduces with increasing spread area, but spread states with $A/A_0 \geq 1.85$ cannot occur due to the low ligand density. Recall from Figure 2.4e that a high ligand density $N_H = 25000 \mu m^{-2}$ results in a low free energy spread area of $A/A_0 = 2.75$ (also shown in Figure 2.6a for comparison). Our predicted ~33% reduction in cell spread area for a 10-fold decrease in ligand density is again supported by the experimental results of Engler *et al.* (2003).

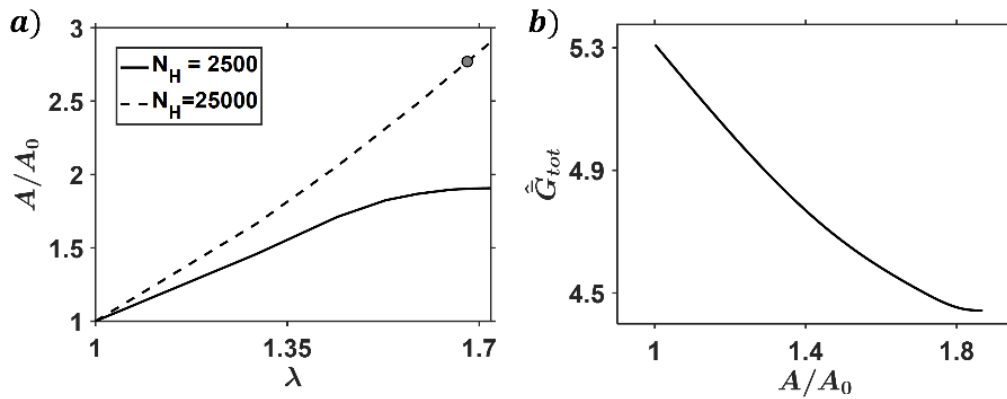


Figure 2.6: (a) Steady state cell spread area as a function of applied cell “pre-stretch” λ for a low and high ligand density N_H (μm^{-2}) on a rigid substrate. The spread area with the lowest free energy (from Figure 2.4e) is marked by the grey circle. (b) The relationship between cell spread area and the total free energy (\hat{G}_{tot}) for a low ligand density ($N_H = 2500 \mu\text{m}^{-2}$). Free energy densities characterized by normalized quantity $\hat{G} = \bar{G}/\rho kT$.

2.4. 2D analysis of circular spreading on micro-patterned substrates

We next attempt to simulate the experiments of Théry *et al.* (2006) whereby cells are spread on micro-patterned ligand patches under plane stress conditions. Two patch geometries are considered: “V-shaped” patches, and “Y-shaped” patches, as shown in Figure 2.7. For simplicity we assume that the cell is initially circular with radius r_c when in suspension. A mesh sensitivity study showed that a converged solution is obtained with 1079 membrane elements. It is important to note that there is an infinite number of spread states (strain distributions) that can be assumed by the cell in order to spread on the ligand patch. Here we attempt to parameterize the spreading process by considering a subset of possible spread states. In the case of the “V-shaped” patch the cell is stretched so that proportion of the cell perimeter ωr_c can adhere to the outer edge of the “V”. The stretch is assumed to be uniform along the patch and is given as $\lambda_c = L_s/\omega r_c$, where L_s is the fixed patch length. Therefore, by considering a range of values of λ_c (or ω) we can simulate a number of spread states and determine which of these states produces the lowest total free energy. The cell radius in the initial configuration is $r_c = 17 \mu\text{m}$ and the

thickness $b = 1 \mu\text{m}$. The substrate dimensions are based on the experiments of Théry *et al.* (2006), i.e. $L_s = 46 \mu\text{m}$ and the substrate letter width was determined to be $7 \mu\text{m}$. Once again the total steady state free energy density is computed from equation 2.41.

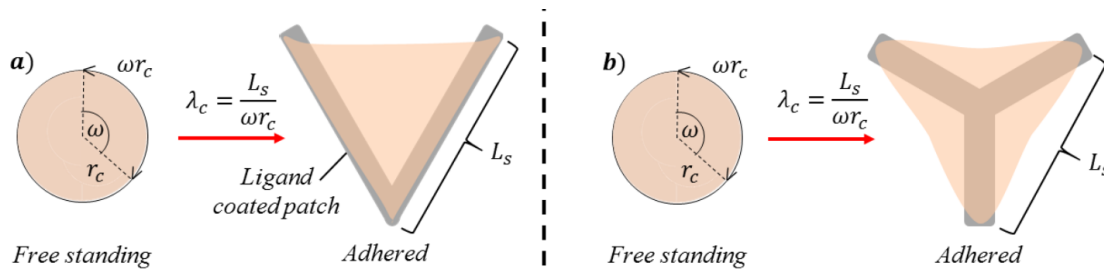


Figure 2.7: Parametric study schematic of cell spreading on a) V- and b) Y- shaped substrates. For a cell of radius r_c , the spreading process is parameterized in terms of the proportion of the cell perimeter ωr_c that stretches along the ligand coated patch ($\lambda_c = L_s / \omega r_c$). The shaded patch represents locations focal adhesions may form with the cell surface.

2.4.1. Results

Similar to the simplified axisymmetric example presented in Section 2.4, the cell free energy during spreading can be interpreted as a competition between the increasing elastic free energy (\bar{G}_{elas}) and the decreasing cytoskeletal free energy (\bar{G}_{cyto}). Simulations of cell spread on a V-shaped substrate reveal that \bar{G}_{tot} is minimized at a cell perimeter stretch of $\lambda_c = 1.3$ (Figure 2.8a). Examination of the strain distribution in this lowest free energy (LFE) configuration (Figure 2.8b) reveals that the maximum tensile strain occurs close to the free unadhered edge of the spread cell. A spread state characterized by a lower stretch ($\lambda_c = 1.1$) results in an elevated total free energy \bar{G}_{tot} , despite a high concentration of straight SFs directly along the free edge. Such a configuration results in extremely high strains along the free unadhered edge, causing a very high elastic free energy penalty. A spread state characterized by a higher stretch ($\lambda_c = 1.6$) results in a high strain in the region of the adhered edges. Although this allows more a similar level of SF formation on all three edges of the spread cell (Figure 2.8c), the high elastic penalty due to stretching along the adhered edges is too large to be compensated for by the

reduction in \bar{G}_{cyto} due to SF formation along all three edges. The density of bound SF proteins is characterized by $\zeta^{SF}(\phi) = \hat{n}(\phi) * \hat{\eta}(\phi)$, with Figure 2.8c showing the dominant SF orientation at each material point. The focal adhesion distribution in these highlighted configurations (Figure 2.8c) show evident clustering in the direction of traction, denoted by $\hat{C}_H = C_H/N_H$. However, the variance in \bar{G}_{adh} between these configurations was negligible.

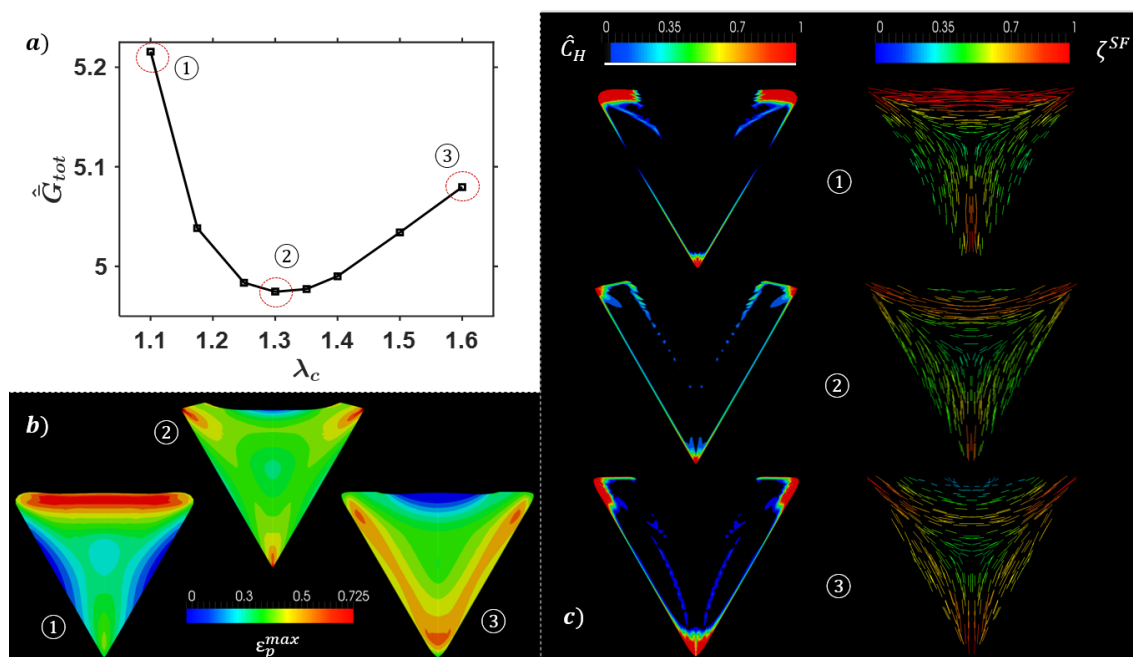


Figure 2.8: Predicted steady-state cell spread on V-shaped ligand pattern in a series of configurations: a) Free energy of the system ($\hat{G}_{tot} = \bar{G}_{tot}/\rho kT$) for a range of spread states characterized by the stretch of the cell on the fixed edge (λ_c). Three states are highlighted: 1. A large stretch on the unadhered edge ($\lambda_c = 1.1$); 2. The lowest free energy configuration ($\lambda_c = 1.3$); 3. A large stretch on the adhered edge ($\lambda_c = 1.6$); b) Maximum principal strain (ε_p^{max}) distribution in the spread cell in the highlighted states; c) Distribution of vinculin or focal adhesions characterized by normalized quantity $\hat{C}_H = C_H/N_H$, and the dominant SF alignment in the highlighted configurations with $\zeta^{SF}(\phi) = \hat{n}(\phi) * \hat{\eta}(\phi)$.

Figure 2.9 shows the dominant SF alignment (d) and FA distribution (c) in the LFE configuration for cells spread on the V-shaped substrate. We see that the highest SF concentration and actin density (ζ^{SF}) is in the region of the free edge where an arc of SFs curve towards the center of the cell. A similar distribution is reported in the experimentally determined heat maps of SF distribution reported by Théry *et al.* (Figure

2.9b). At the center of the cell, where the strain is lowest in both cases, equation 2.12 dictates that the SF concentration in any direction will be lower than that along the free edge. Focal adhesions (\hat{C}_H) are predicted to form along the perimeter of the ligand patch due to a shear-lag type distribution of traction between the cell and the patch. Such a FA distribution is also reported in the experimental study of Théry *et al.* (2006) (Figure 2.9a).

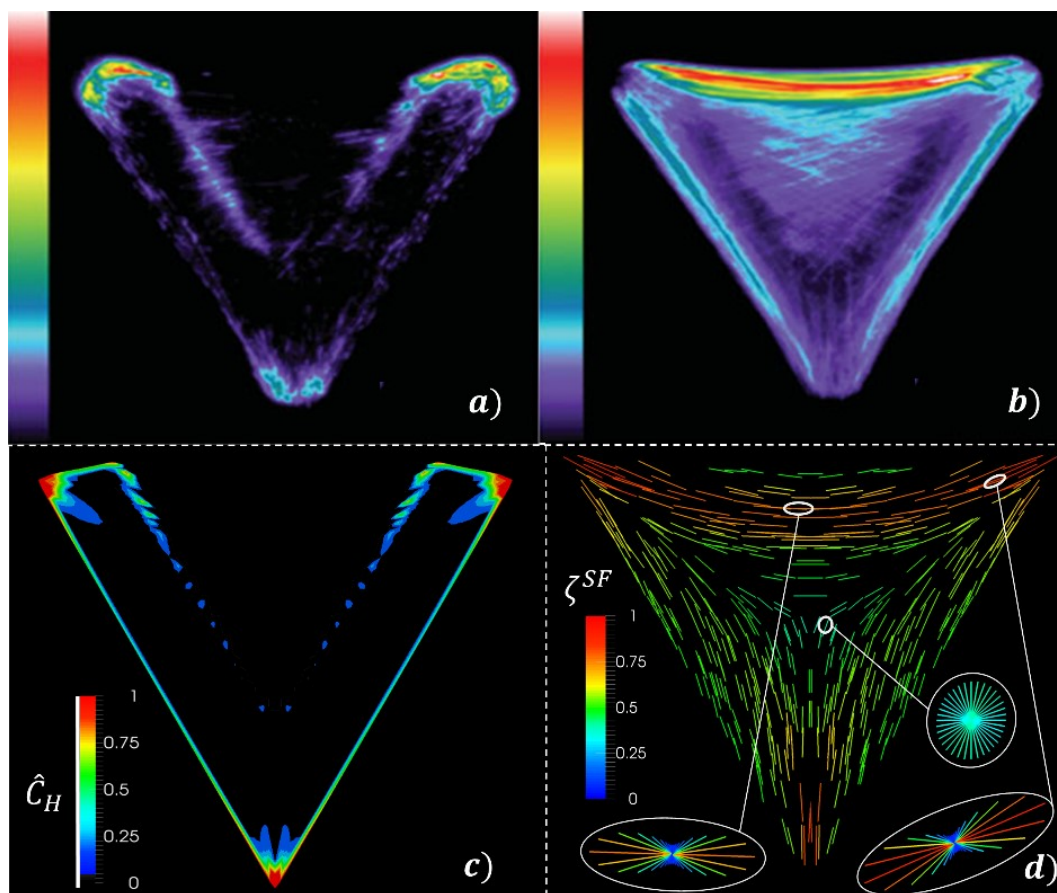


Figure 2.9: Cell spread on V-shaped micro-patterned substrates: Experimental images of average (a) vinculin and (b) actin distributions (Reproduced with some modifications from Théry *et al.* (2006). Copyright © John Wiley & Sons, Ltd.); (c) Distribution of vinculin or focal adhesions in the LFE configuration, characterized by normalized quantity $\hat{C}_H = C_H/N_H$; (d) Dominant SF alignment in the LFE configuration, with $\zeta^{SF}(\phi) = \hat{n}(\phi) * \hat{\eta}(\phi)$. The insets show full SF distribution for all M discrete directions.

Simulations of cell spread on a Y-shaped substrate reveal that \bar{G}_{tot} is minimized at a perimeter stretch of $\lambda_c = 1.34$ (Figure 2.10a) on two of the free edges, with a slightly higher strain and SF concentration on the third (top) edge. Once again a spread state

characterized by a higher or lower value of λ_c results in an elevated \bar{G}_{tot} due to an extremely high elastic free energy.

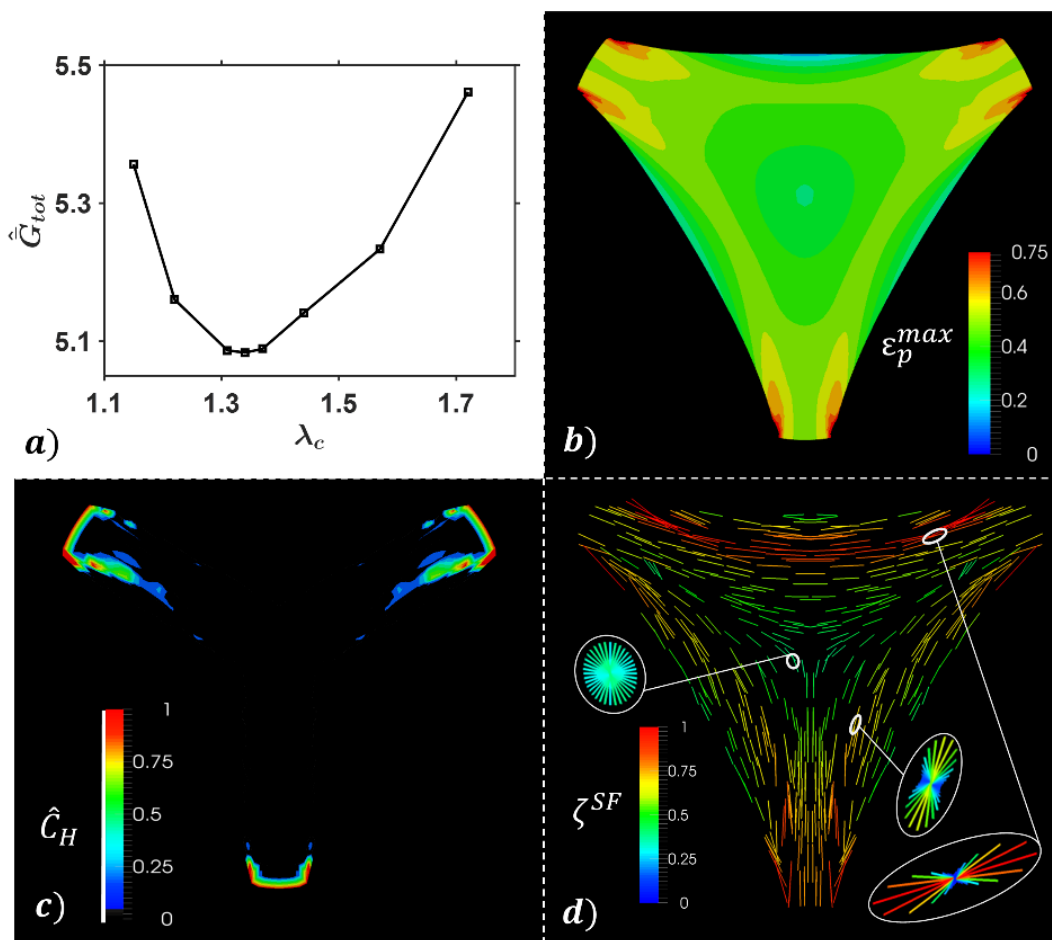


Figure 2.10: Predicted steady-state cell spread on Y-shaped ligand pattern in a low free energy configuration: a) Free energy of the system ($\hat{G}_{tot} = \bar{G}_{tot}/\rho kT$) for a range of spread states characterized by the stretch of the cell on the fixed edge (λ_c). A lowest free energy (LFE) configuration is observed at $\lambda_c = 1.34$; b) Maximum principal strain distribution in the spread cell; c) Distribution of vinculin or focal adhesions in the LFE configuration, characterized by normalized quantity $\hat{C}_H = C_H/N_H$ d) Dominant SF alignment in the LFE configuration, with $\zeta^{SF}(\phi) = \hat{n}(\phi)\hat{\eta}(\phi)$. The insets show full SF distribution for all M discrete directions.

The experimental SF heat maps for the Y-patterned substrate from Théry *et al.* (2006) exhibit an expected symmetry, with similar SF patterns on all three free edges. However, in the computed LFE configuration (Figure 2.10) one edge has a higher strain and SF concentration. In order to compare our computational results to an experimental heat map (constructed using data from several observations) we should acknowledge that there are three LFE configurations due to symmetry of the Y-shape. Therefore we rotate the

distributions shown in Figure 2.10c-d through 120° and 240° we then construct a “computational heat map” by taking the average of these three LFE distributions. The “computational heat map” is shown in Figure 2.11c-d and exhibits an identical SF distribution on all three free edges and can be directly compared to the experimental heat maps. Notably the “computational heat map” free edge SF concentration is lower than that along the free edge of the V-shape (Figure 2.9d) (“heat map averaging” is not necessary for the V-shape as it has only one free edge). This prediction is supported by experimental results (Figures 2.9b and 2.11b).

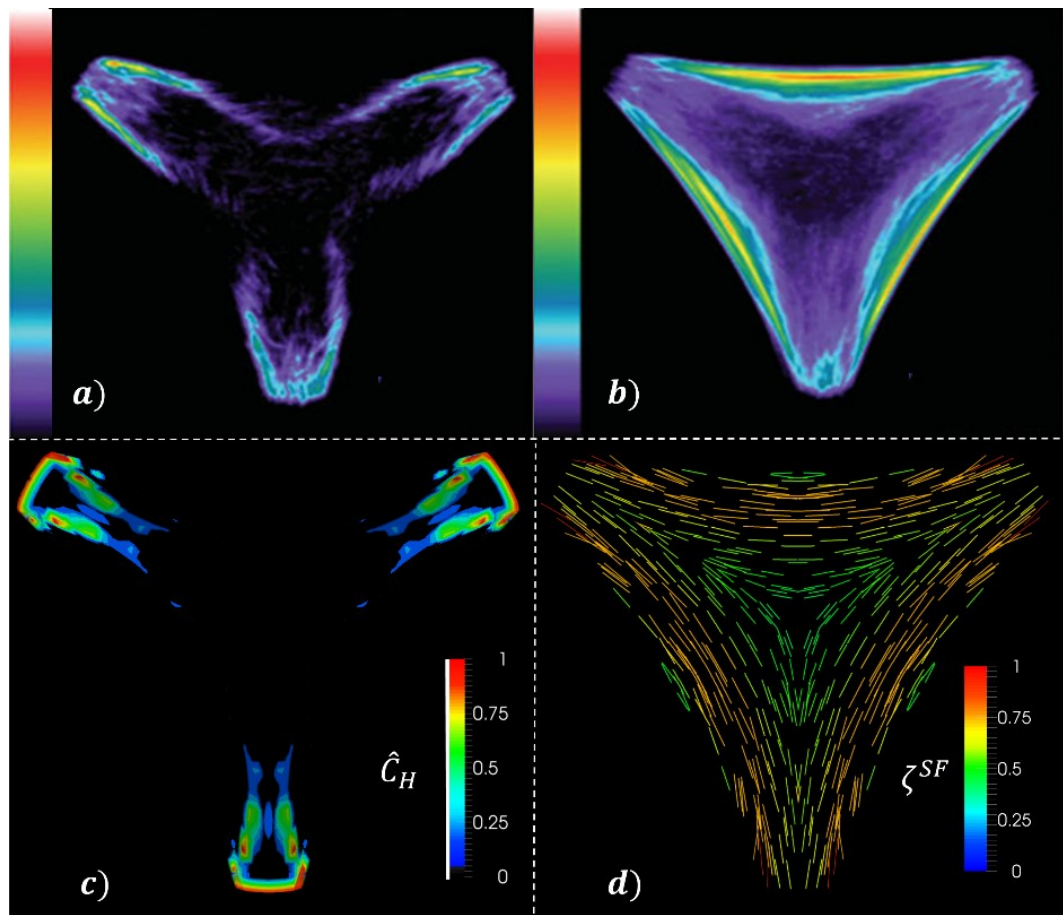


Figure 2.11: Cell spread on Y-shaped micro-patterned substrates: Experimental images of average vinculin (a) and actin (b) distributions (Reproduced with some modifications from Théry *et al.* (2006). Copyright © John Wiley & Sons, Ltd.); (c) Predicted average distribution of vinculin or focal adhesions, characterized by normalized quantity $\hat{C}_H = C_H/N_H$; (d) Predicted average actin distribution, with $\zeta^{SF}(\phi) = \hat{n}(\phi) * \hat{\eta}(\phi)$.

2.5. Discussion

In this paper we present a steady-state adaptation of the thermodynamically motivated continuum SF model of Vigliotti *et al.* (2015). We implement this formulation in a non-local finite element setting where we consider global conservation of the total number of cytoskeletal proteins within the cell, global conservation of the number of binding integrins on the cell membrane, and a finite ligand density on the substrate surface.

When a number of cytoskeletal proteins assemble to form contractile SFs, the free energy of the proteins bound within the SF is lower than the total free energy of the same proteins when they are unbound (not assembled in a SF). During spreading the strain in a cell increases. This results in assembly of cytoskeletal proteins into contractile SFs, and a consequent lowering of the total cytoskeletal free energy in the cell. Of course an increase in cell strain during spreading also results in an increase in the elastic free energy of the mechanically passive components of the cell (e.g. the membrane, intermediate filaments etc.). Therefore cell spreading can be viewed as a competition between the reducing cytoskeletal free energy and the increasing elastic free energy. Our analyses suggest that the driver of cell spreading is a lowering (or perhaps a minimization) of the total free energy of the system.

To simulate cell-substrate contact we present an extension of the Deshpande *et al.* (2008) model for FA kinematics, whereby we account for a dependence on the substrate ligand density. Variance of the substrate ligand density has significant impact on cell behaviour. Combined with the mass conservation of integrins, this affects the maximum cellular tractions the FAs can withstand, and therefore the spread shape and area.

In Section 2.3 the key features of the model are examined through a series of simplified simulations of axisymmetric cell spreading. By considering a number of parameterized cell spread states on a rigid substrate our analyses suggest that the lowest free energy

spread-state has an area that is 2.75 times higher than an unspread cell area. This prediction is in agreement with the experimental measurements of Engler *et al.* (2003). Furthermore, when cells spread on compliant substrates ($\mu = 8\text{kPa}$) we predict that the lowest free energy spread area is $\sim 30\%$ lower than the corresponding area on a rigid substrate. Once again this finding is supported by the experimental trends reported in Engler *et al.* (2003). Finally, we predict that a low substrate ligand density will limit the spread area of a cell, with a 10-fold decrease in ligand density on a rigid substrate resulting in a $\sim 33\%$ reduction in spread area on a rigid substrate. Again, this prediction is in broad agreement with the experimental measurements of Engler *et al.* (2003) and Gaudet *et al.* (2003). Our hypothesis that cell spreading is driven by a lowering of free energy appears to provide an explanation for the broad trends observed by Engler *et al.* (2003).

A recent study by Shenoy *et al.* (2016) suggests that the cellular free energy decreases with increasing substrate stiffness, which provides an energetic basis for durotaxis. The results from Section 2.3 of the current study also provides insight to this phenomenon. In the lowest energy spread configuration on a compliant substrate, the cell has a predicted free energy of $\widehat{G}_{\text{tot}} = 4.85$. However, on a rigid substrate the lowest free energy configuration is observed at $\widehat{G}_{\text{tot}} = 4.2$. Therefore, we suggest that durotaxis is the result of a cell attempting to lower its free energy by migrating towards a stiffer substrate. Similarly, chemotaxis may be explained by the inability of a cell to attain a minimum free energy configuration if the concentration of ligands is very low, thus inducing the cell to migrate to a region of higher ligand density in order to reduce the free energy.

In Section 2.4 a number of parameterized spread-states are simulated, whereby a circular cell adheres to “V-shaped” and “Y-shaped” ligand patches based on the experiments of Théry *et al.* (2006). The free energy associated with each spread state is computed, and we demonstrate that the spread-state with the lower free energy exhibits a SF distribution

that corresponds to experimental observations, i.e. a high concentration of highly aligned SFs occurs along free edges, with lower SF concentrations at the interior of the cell. The simulation of the complex SF and FA distributions observed experimentally in cells spread on the V- and Y- shaped ligand patterns demonstrates the predictive power of the model. Future implementations will also consider cell spreading on grooves (Lamers *et al.* 2010) and micro-posts (McGarry *et al.* 2009; Ronan *et al.* 2013). The current analysis presents a movement away from traditional deterministic approaches to computational cell biomechanics in which the experimentally observed spread state is incorrectly assumed to be the reference undeformed state. Such approaches neglect cell strain as a driver of SF assembly. Also, global conservation of a finite number of cytoskeletal proteins within the cell has been neglected. The model of Pathak *et al.* (2008) simulates the experiments of Théry *et al.* (2006) using such assumptions. The degree of SF alignment (characterized by a variance parameter) is correctly predicted, with uniaxial SFs being predicted in a region of uniaxial stress along the cell free edge (in accordance with the model of Deshpande *et al.* (2006) SFs orthogonal to the free edge dissociate due to the stress-free condition). However, the framework incorrectly predicts full SF formation in all directions (isotropic distribution) in areas of biaxial stress and in regions where the cell is bonded to the ligand patch. The current study corrects such shortcomings by considering strain associated with cell spreading, in addition to implementing a global conservation of cytoskeletal proteins.

In this study we consider a very small subset* of the possible spread-states of a cell on a micro-patterned substrate, in order to examine the dependence of the SF distribution on the manner in which a cell spreads (*our subset is primarily chosen based on ease of parameterization, as illustrated in Figure 2.7, rather than on any consideration of the actual cell spreading process). Our analysis of a number of spread states allows us to examine the hypothesis that the final spread state is driven by minimization of the free

energy of the system. In reality however, there are an infinite number of spread configurations that the cell can assume. A rigorous treatment of the stochastic problem of cell spreading requires the development of a statistical mechanics framework that allows for the analysis of an extremely large number of spread states. The finite element framework developed here is prohibitively computationally expensive for such an approach.

The underlying premise in this work is that minimum/low free-energy configurations are the most likely states to be observed. In statistical thermodynamics a closed system in a constant temperature and pressure environment attains equilibrium at minimum Gibbs free-energy. However, a cell is not a closed system and in fact never attains an equilibrium state in this sense while alive. The approach taken here of searching for low free-energy states rests on the “homeostatic ensemble” developed by Shishvan *et al.* (2018) who show that in their homeostatic state cells attain a fluctuating equilibrium where low free-energy states are more probable. The results presented here should be viewed in this light, in the sense that the minimum free-energy configurations predicted in our analyses have the highest probability of being observed in experiments.

2.6. Concluding remarks

We combine the thermodynamically consistent model for the stress fibre cytoskeleton developed by Vigliotti *et al.* (2015) with a focal adhesion model (again motivated by thermodynamic considerations) to analyze two problems: (i) spreading of cells on elastic substrates and (ii) spreading of cells on substrates with specific geometrical ligand patterns.

Spreading of cells is shown to be a competition mainly between the elastic energy and cytoskeletal energy of the cell, as well as the elastic energy of the substrate. With increasing cell spreading the elastic energy of the cell and substrate typically increases, but the cytoskeletal energy decreases as a larger fraction of the cytoskeletal proteins form stress fibres. The equilibrium configuration is assumed to be that corresponding to the lowest free energy. In agreement with the experiments of Engler *et al.* (2003) we show that the spread area of the cell increases with increasing substrate stiffness. When the spreading of cells is constrained by specific geometric patterns of ligands, we show that, in the lowest free-energy configuration, stress fibres preferentially form along the unadhered edges of the cell, in line with the observations of Théry *et al.* (2006). This framework presents a potential computational tool to design substrates and scaffolds that will yield a desired cell spread state.

The simulations presented here suggest that computed low (or minimum) free-energy spread cell configurations are broadly consistent with experimentally observed spread cell configurations. However, it is worth emphasizing that cells do not attain an equilibrium minimum free-energy configuration in the traditional sense, as observations clearly show that spread cells are in a perpetually fluctuating state. Thus, the minimum free-energy configuration is best viewed as the most probable state to be observed, rather than a unique equilibrium state.

Appendix 2.A: Comparison with previous models

The influence of an applied steady-state nominal strain ε_n on the steady-state active and passive Cauchy stress is illustrated in Figure 2.A1(a) (material parameters as per Section 2.2.3) for a cell subjected to series of uniaxial stretches. The dependence of stress fibre formation (equation 2.12) on steady-state strain (Figure 2.A1(b)) is reflected in the strain dependence of the active stress (through equation 2.13). It must be noted that the active stress curve in Figure 2.A1(a) is not representative of a stress-strain constitutive law. Rather, it is a plot of the steady-state active stress computed for an applied steady-state strain. In contrast, previous modelling approaches (e.g. Deshpande *et al* 2006) do not include a dependence of stress fibre formation on applied strain, so that the computed stress fibre activation-level (SFA) and, consequently, the active stress are independent of the applied steady state strain in Figure 2.A1.

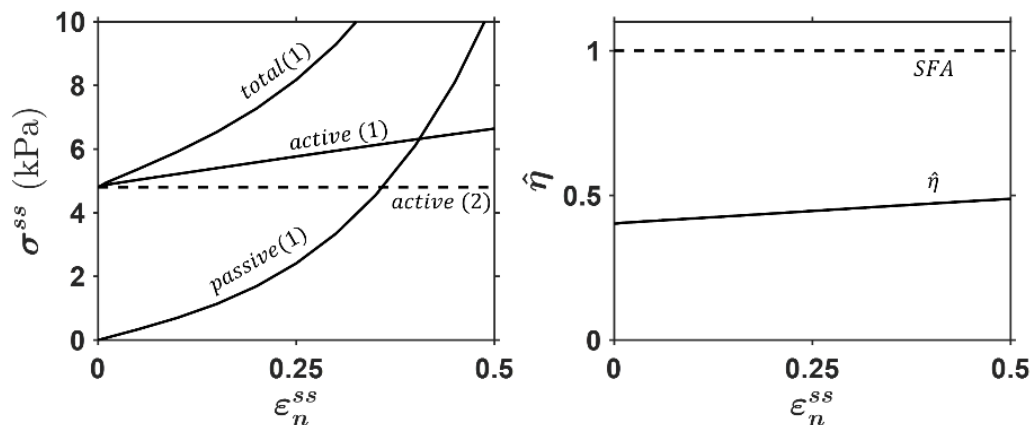


Figure 2.A1. (a) Computed active steady state stress as a function of applied steady state nominal strain ε_n for the current model (active(1)). The passive and total stresses are also shown. For comparison the active stress computed by the Deshpande *et al.* (2006) model (active(2)) is shown. (b) Computed values of $\hat{\eta}$ as a function of applied steady state nominal strain ε_n for the current model. For comparison the stress fibre activation (SFA) level computed by the Deshpande *et al.* (2006) model is plotted to highlight the absence of strain dependence on SF remodelling in this previous model.

Bibliography

- Deshpande, Vikram S., Milan Mrksich, Robert M. McMeeking, and Anthony G. Evans. 2008. "A Bio-Mechanical Model for Coupling Cell Contractility with Focal Adhesion Formation." *Journal of the Mechanics and Physics of Solids* 56 (4): 1484–1510. doi:10.1016/j.jmps.2007.08.006.
- Deshpande, Vikram S, Robert M McMeeking, and Anthony G Evans. 2006. "A Bio-Chemo-Mechanical Model for Cell Contractility." *Proceedings of the National Academy of Sciences of the United States of America* 103 (38): 14015–20. doi:10.1073/pnas.0605837103.
- Engler, A., M. Sheehan, H. L. Sweeney, and D. E. Discher. 2003. "Substrate Compliance vs Ligand Density in Cell on Gel Responses." *European Cells and Materials* 6 (SUPPL. 1). Elsevier: 7–8. doi:10.1016/S0006-3495(04)74140-5.
- Gaudet, Christianne, William a Marganski, Sooyoung Kim, Christopher T Brown, Vaibhavi Gunderia, Micah Dembo, and Joyce Y Wong. 2003. "Influence of Type I Collagen Surface Density on Fibroblast Spreading, Motility, and Contractility." *Biophysical Journal* 85 (5). Elsevier: 3329–35. doi:10.1016/S0006-3495(03)74752-3.
- Kaunas, R., P. Nguyen, S. Usami, and S. Chien. 2005. "From The Cover: Cooperative Effects of Rho and Mechanical Stretch on Stress Fiber Organization." *Proceedings of the National Academy of Sciences* 102 (44): 15895–900. doi:10.1073/pnas.0506041102.
- Lamers, Edwin, X. Frank Walboomers, Maciej Domanski, Joost te Riet, Falco C M J M van Delft, Regina Lutge, Louis A J A Winnubst, Han J G E Gardeniers, and John A. Jansen. 2010. "The Influence of Nanoscale Grooved Substrates on Osteoblast Behavior and Extracellular Matrix Deposition." *Biomaterials* 31 (12). Elsevier Ltd: 3307–16. doi:10.1016/j.biomaterials.2010.01.034.
- Lauffenburger, Douglas A., and Jennifer J. Linderman. 1993. *Receptors : Models for Binding, Trafficking, and Signaling*. Oxford University Press.
- Leckband, D, and J Israelachvili. 2001. "Intermolecular Forces in Biology." *Quarterly Reviews of Biophysics* 34 (2): 105–267. <http://www.ncbi.nlm.nih.gov/pubmed/11771120>.
- Lucas, S M, R L Ruff, and M D Binder. 1987. "Specific Tension Measurements in Single Soleus and Medial Gastrocnemius Muscle Fibers of the Cat." *Experimental Neurology* 95 (1): 142–54. <http://www.ncbi.nlm.nih.gov/pubmed/2947808>.
- McBeath, Rowena, Dana M Pirone, Celeste M Nelson, Kiran Bhadriraju, and Christopher S Chen. 2004. "Cell Shape, Cytoskeletal Tension, and RhoA Regulate Stem Cell Lineage Commitment." *Developmental Cell* 6 (4): 483–95. doi:10.1016/S1534-5807(04)00075-9.
- McCLEVERTY, Clare J., and Robert C. LIDDINGTON. 2003. "Engineered Allosteric Mutants of the Integrin AlphaMbeta2 I Domain: Structural and Functional Studies." *Biochemical Journal* 372 (1).
- McGarry, J. P., J. Fu, M. T. Yang, C. S. Chen, R. M. McMeeking, A. G. Evans, and V. S. Deshpande. 2009. "Simulation of the Contractile Response of Cells on an Array of Micro-Posts." *Philosophical Transactions. Series A, Mathematical, Physical, and Engineering Sciences* 367 (1902): 3477–97. doi:10.1098/rsta.2009.0097.
- McGrath, J.L., Y. Tardy, C.F. Dewey, J.J. Meister, and J.H. Hartwig. 1998. "Simultaneous Measurements of Actin Filament Turnover, Filament Fraction, and Monomer Diffusion in Endothelial Cells." *Biophysical Journal* 75 (4): 2070–78. doi:10.1016/S0006-3495(98)77649-0.
- Nolan, D.R., A.L. Gower, M. Destrade, R.W. Ogden, and J.P. McGarry. 2014. "A Robust Anisotropic Hyperelastic Formulation for the Modelling of Soft Tissue." *Journal of the Mechanical Behavior of Biomedical Materials* 39. Elsevier: 48–60. doi:10.1016/j.jmbbm.2014.06.016.
- Ogden, R. W. 1972. "Large Deformation Isotropic Elasticity - On the Correlation of Theory and

- Experiment for Incompressible Rubberlike Solids.” *Proceedings of the Royal Society of London A: Mathematical, Physical and Engineering Sciences* 326 (1567).
- Pathak, Amit, Vikram S Deshpande, Robert M McMeeking, and Anthony G Evans. 2008. “The Simulation of Stress Fibre and Focal Adhesion Development in Cells on Patterned Substrates.” *Journal of the Royal Society, Interface / the Royal Society* 5 (22): 507–24. doi:10.1098/rsif.2007.1182.
- Reynolds, N. H., and J. P. McGarry. 2015. “Single Cell Active Force Generation under Dynamic Loading - Part II: Active Modelling Insights.” *Acta Biomaterialia* 27. Acta Materialia Inc.: 251–63. doi:10.1016/j.actbio.2015.09.004.
- Ronan, William, Amit Pathak, Vikram S Deshpande, Robert M McMeeking, and J Patrick McGarry. 2013. “Simulation of the Mechanical Response of Cells on Micropost Substrates.” *Journal of Biomechanical Engineering* 135 (10): 1–10. doi:10.1115/1.4025114.
- Shenoy, Vivek B, Hailong Wang, and Xiao Wang. 2016. “A Chemo-Mechanical Free-Energy-Based Approach to Model Durotaxis and Extracellular Stiffness-Dependent Contraction and Polarization of Cells.” *Interface Focus* 6 (1): 20150067. doi:10.1098/rsfs.2015.0067.
- Shishvan, S. S., A. Vigliotti, and V. S. Deshpande. 2018. “The Homeostatic Ensemble for Cells.” *Biomechanics and Modeling in Mechanobiology*, July. Springer Berlin Heidelberg, 1–32. doi:10.1007/s10237-018-1048-1.
- Sun, Wei, Elliot L Chaikof, and Marc E Levenston. 2008. “Numerical Approximation of Tangent Moduli for Finite Element Implementations of Nonlinear Hyperelastic Material Models.” *Journal of Biomechanical Engineering* 130 (6): 061003. doi:10.1115/1.2979872.
- Tan, J. L., J. Tien, D. M. Pirone, D. S. Gray, K. Bhadriraju, and C. S. Chen. 2003. “Cells Lying on a Bed of Microneedles: An Approach to Isolate Mechanical Force.” *Proceedings of the National Academy of Sciences* 100 (4): 1484–89. doi:10.1073/pnas.0235407100.
- Théry, Manuel, Anne Pépin, Emilie Dressaire, Yong Chen, and Michel Bornens. 2006. “Cell Distribution of Stress Fibres in Response to the Geometry of the Adhesive Environment.” *Cell Motility and the Cytoskeleton* 63 (6): 341–55. doi:10.1002/cm.20126.
- Vigliotti, A., W. Ronan, F. P T Baaijens, and V. S. Deshpande. 2015. “A Thermodynamically Motivated Model for Stress-Fiber Reorganization.” *Biomechanics and Modeling in Mechanobiology*. Springer Berlin Heidelberg. doi:10.1007/s10237-015-0722-9.
- Wang, J H, P Goldschmidt-Clermont, J Wille, and F C Yin. 2001. “Specificity of Endothelial Cell Reorientation in Response to Cyclic Mechanical Stretching.” *Journal of Biomechanics* 34 (12): 1563–72. <http://www.ncbi.nlm.nih.gov/pubmed/11716858>.
- Weiss, T.F. 1996. *Cellular Biophysics (Vol. 1)*. MIT Press.

CHAPTER 3

THERMODYNAMIC MODELLING OF THE STATISTICS OF CELL SPREADING ON LIGAND COATED ELASTIC SUBSTRATES



3.1. Introduction

There is no unique outcome for tissue development in nature. For example, examination of arterial tissue across several samples reveals non-homogenous structures with non-uniform collagen fibre alignment, tissue thickness, and smooth muscle cell (SMC) morphology (Lange *et al.* 2002; Chow *et al.* 2014; Engler *et al.* 2003). The same is true *in-vitro*, where cells of the same phenotype exhibit a diverse range of spread shapes, area, stress fibre alignments, and focal adhesion distributions. However, over large populations the statistics of observables is highly reproducible. Several experimental studies have demonstrated that the microenvironment has a significant impact on cell behavior. Jacot *et al.* (2008) show that sarcomere development and alignment in cardiomyocytes is dependent on substrate stiffness. A study by Arnold *et al.* (2004) reveals that focal adhesion (FA) and stress fibre (SF) formation is limited by ligand spacing on the substrate. Engler *et al.* (2003) show that both the mean and standard error of SMC spread

area depends on substrate rigidity and ligand density. With decreasing surface collagen density and decreasing substrate stiffness, the standard error reported for the experiment reduces.

It is therefore evident that in order to uncover the biomechanisms underlying such observations, a stochastic approach to cell modelling is required. McEvoy *et al.* (2017) recently implemented a framework whereby an initially unadhered cell deforms to a range of possible spread states, and the system free energy is computed for each configuration. It is demonstrated that cell spreading entails a competition between the increasing elastic free energy due to stretching of passive cell components, and the decreasing cytoskeletal free energy as contractile proteins assemble to form SFs. Such a competition allows for the identification of a low free energy state, and it is shown that the predicted cell areas and SF alignments in these configurations are similar to reported experimental measurements (Théry *et al.* 2006). However, in the study of McEvoy *et al.* a single low energy spread state is identified. This deterministic approach neglects the fact that cells display a fluctuating response to their microenvironment in terms of observables such as SF alignment and spread area.

In this study, we implement a statistical mechanics framework for the *homeostatic ensemble of spread cells*, following the approach of Shishvan *et al.* (2018). This methodology allows for the simulation of a large collection of spread microstates the cell-substrate system assumes while maintaining its homeostatic state. The framework incorporates mathematical models to describe SF formation and cell-substrate deformation. In this study, we expand the statistical mechanics framework to include a model for traction dependent focal adhesion assembly. Simulations accurately predict the dependence of cell area and shape on surface collagen density and substrate stiffness, as reported in the experimental study of Engler *et al.*

3.2. Methodology

We aim to analyze the response of cells adhered to elastic substrates. This experimental system is responding to both mechanical and chemical cues from its environment, viz. the stiffness of the substrate and the extra-cellular proteins (collagen) through which the cells adhere to the substrates. The response of this complex system is recorded through a range of observables, all of which exhibit large variations but with trends clearly emerging when the statistics of these observables are analysed. This motivates our choice of a modelling framework, called homeostatic mechanics (Shishvan *et al.* (2018)), in which, just as in the experimental system, observables fluctuate while trends (and understanding) emerge once these observables are viewed statistically. This framework has previously been shown to successfully capture a range of observations for smooth muscle cells (SMCs) seeded on elastic substrates, in which perfect adhesion was assumed and the role of the extra-cellular matrix neglected. Here we extend the framework to include an adhesion model and thus will first give a brief overview of the modelling framework (details in Appendix Section 3.A.1) and then focus on the adhesion model.

3.2.1. Overview of the homeostatic mechanics framework

The homeostatic mechanics framework recognises that the cell is an open system which exchanges nutrients with the surrounding nutrient bath. These high-energy nutrient exchanges fuel large fluctuations (much larger than thermal fluctuations) in cell responses associated with various intracellular biochemical processes. However, these biochemical processes attempt to maintain the cell in a homeostatic state, i.e. the cell actively maintains its various molecular species at a specific average number over these fluctuations that is independent of the environment. This translates to the constraint on the average Gibbs free-energy (Jaynes 1957) of the cell. Employing the *ansatz* that biochemical processes such as actin polymerisation and treadmilling provide the mechanisms to maximise the morphological entropy of the cell subject to the constraint

that the cell maintains a homeostatic state, Shishvan *et al.* (2018) obtained the distribution of states the cell assumes in terms of the Gibbs free-energy $G^{(j)}$ of morphological state (j) of the system as

$$P_{\text{eq}}^{(j)} = \frac{1}{Z} \exp(-\zeta G^{(j)}). \quad (3.1)$$

$Z \equiv \sum_j \exp(-\zeta G^{(j)})$ is the partition function of the morphological microstates, and the distribution parameter ζ follows from the homeostatic constraint

$$\frac{1}{Z} \sum_j G^{(j)} \exp(-\zeta G^{(j)}) = G_S, \quad (3.2)$$

where G_S is the homeostatic free energy, equal to the equilibrium Gibbs free-energy of an isolated cell in suspension (free-standing cell), i.e. the homeostatic processes maintain the average biochemical state of the system equal to that of a cell in suspension. Thus, the distribution (equation 3.1) is characterised by a homeostatic temperature $1/\zeta$ that is conjugated to the morphological entropy of the cell.

3.2.2. Gibbs free-energy of a morphological state

Much like conventional statistical mechanics frameworks that require a model for the energy of molecular systems, the homeostatic statistical mechanics framework requires a model for the Gibbs free-energy $G^{(j)}$ of a morphological state (j) of the system. Here, we employ a relatively simple model for the Gibbs free-energy wherein the cell consists of a passive elastic nucleus within a cytoplasm that is modelled as comprising an active stress fibre cytoskeleton and elements such as the cell membrane, intermediate filaments and microtubules that are all lumped into a single passive elastic contribution.

Details of the model including the parameters used to characterise the SMCs are given in Appendix Section 3.A.2. Here we briefly describe the salient features of the model for SMCs on elastic substrates. The SMCs are modelled as two-dimensional (2D) bodies in

the $x_1 - x_2$ plane lying on the surface of an elastic substrate such that the out-of-plane Cauchy stress $\Sigma_{33} = 0$. The substrates are modelled as linear elastic half-spaces while the cells are modelled using the approach of Vigliotti *et al.* (2015) as modified by Shishvan *et al.* The Vigliotti *et al.* model assumes only two elements within the cell: (i) a passive elastic contribution from elements such as the cell membrane, intermediate filaments and microtubules and (ii) contractile acto-myosin stress fibres that are modelled explicitly. The cell in its undeformed state is a circle of radius R_0 and for a given morphological microstate (j), the strain distribution within the cell is specified. This directly gives the elastic strain energy of the cell \hat{F}_{passive} via a 2D Ogden-type hyperelastic model for both the nucleus and cytoplasm. The passive hyperelastic behaviour of the cytoplasm and nucleus has been characterised for several cell types using experimental techniques in which stress fibres are disrupted using cyto-D (Weafer *et al.* 2013; Reynolds *et al.* 2014; Dowling *et al.* 2012). The stress fibre cytoskeleton within the cytoplasm is modelled as a distribution of stress fibres such that at each location x_i within the cell $\hat{\eta}(\varphi)$ parameterises the angular concentration of stress fibres over all angles φ , while $\hat{n}^{ss}(\varphi)$ denotes the number of functional units within each stress fibre. Thus, at any x_i there is a total concentration \hat{N}_b of bound stress fibre proteins obtained by integrating $\hat{\eta}\hat{n}^{ss}$ over all orientations φ and these bound proteins are in chemical equilibrium with the unbound stress fibre proteins. The unbound proteins are free to diffuse within the cell and thus at equilibrium of a morphological microstate the concentration \hat{N}_u of these unbound stress fibre proteins is spatially uniform. This chemical equilibrium condition along with the conservation of stress fibre proteins within the cell provides the spatial and angular distributions of stress fibres from which the free-energy of the cytoskeleton \hat{F}_{cyto} is evaluated. The total normalised free-energy of the cell morphological microstate (j) then follows as $\hat{G}^{(j)} \equiv \hat{F}_{\text{passive}}^{(j)} + \hat{F}_{\text{cyto}}^{(j)} + \hat{F}_{\text{sub}}^{(j)}$, where $\hat{F}_{\text{sub}}^{(j)}$ is the elastic energy of the substrate

($\hat{G}^{(j)}$ is the normalized value of $G^{(j)}$; see Appendix Section 3.A.2.4 for details of the normalizations).

In addition to the contributions to $\hat{G}^{(j)}$ from the passive elasticity and cytoskeleton of the cell, here we also include the contribution from the focal adhesions between the cell and the collagen extra cellular matrix (ECM) laid on the elastic substrates on which the SMCs are seeded. Shishvan *et al.* implicitly assumed an unlimited supply of adhesion proteins as well as extra-cellular proteins to form adhesion complexes and thereby neglected the contribution of adhesion to $\hat{G}^{(j)}$. Here we extend the approach of Shishvan *et al.* for the case of a finite quantity of both focal adhesion proteins and extra-cellular collagen and thus explicitly include an adhesion contribution to $\hat{G}^{(j)}$, i.e. we write $\hat{G}^{(j)}$ as

$$\hat{G}^{(j)} \equiv \hat{F}_{\text{passive}}^{(j)} + \hat{F}_{\text{cyto}}^{(j)} + \hat{F}_{\text{sub}}^{(j)} + \hat{F}_{\text{adh}}^{(j)}. \quad (3.3)$$

We now proceed to make explicit this adhesion model.

3.2.3. Adhesion complexes between the cell and the extra-cellular collagen

The focal adhesion model proposed here is a modification to the model of McEvoy *et al.* (2017) where adhesion is assumed to be via integrins that exist in a single state. These integrins form complexes by binding to ligands that have a density N_H per unit area on the surface of the elastic substrate. For a given morphological microstate (j), the strain state of the cell is specified and this implies that the tractions $T_i(x_i)$ the cells exert on the substrate are also fixed from the cell model; see Appendix Section 3.A.2.1 (for the sake of brevity here we have dropped the superscript (j) to indicate that these are tractions for a given morphological microstate (j). These tractions are transmitted to the substrate through the focal adhesion complexes and here we specify the adhesion model with the tractions $T_i(x_i)$ specified.

When in local equilibrium at a location x_i on the surface of the cell, the integrins with a local concentration $C_I(x_i)$ have a chemical potential at temperature T in terms of the Boltzmann constant k_B

$$\chi_I(x_i) = \mu_I(x_i) + k_B T \ln \left(\frac{\bar{C}(x_i)}{1 - \bar{C}(x_i)} \right), \quad (3.4)$$

where μ_I is their enthalpy while $\bar{C}(x_i) \equiv C_I(x_i)/C_r$, in terms of the number of integrin sites per unit area C_r on the cell membrane. The enthalpy of the integrins follows from recalling that each integrin molecule transmits a force $F(x_i)$ related to the traction $T(x_i) \equiv \sqrt{T_1(x_i)^2 + T_2(x_i)^2}$ on the cell surface via $T(x_i) = F(x_i)N_H$. Then,

$$\mu_I(x_i) = \Phi(\Delta(x_i)) - F(x_i)\Delta(x_i), \quad (3.5)$$

where Δ is the stretch of the focal adhesion complex and Φ the internal energy of the complex subjected to a stretch Δ . Now assuming linear behaviour of the complex with a stiffness κ_s , such that $F(x_i) \equiv \kappa_s \Delta(x_i)$, equation 3.5 reduces to $\mu_I(x_i) = -F(x_i)^2 / 2\kappa_s$ and the chemical potential follows as

$$\chi_I(x_i) = k_B T \ln \left(\frac{\bar{C}(x_i)}{1 - \bar{C}(x_i)} \right) - \frac{F(x_i)^2}{2\kappa_s}. \quad (3.6)$$

The integrins are mobile over the surface membrane and at equilibrium, their chemical potentials are spatially uniform such that $\chi_I(x_i) = \chi_C$. The equilibrium concentrations $\bar{C}_{eq}(x_i)$ then follow in terms of χ_C as

$$\left(\frac{\bar{C}_{eq}(x_i)}{1 - \bar{C}_{eq}(x_i)} \right) = \exp \left(\frac{\chi_C + \frac{F(x_i)^2}{2\kappa_s}}{k_B T} \right). \quad (3.7)$$

However, χ_C is as yet unknown and the conservation of integrins provides the additional constraint to determine χ_C , viz. given a spatially uniform surface density C_0 of integrins for a cell in suspension, the conservation statement reads

$$A_0 C_0 = C_r \int_A \bar{C}_{eq}(x_i) dA, \quad (3.8)$$

where A_0 is the surface area of the cell in suspension and A its area in the current configuration. The simultaneous solution of equation 3.7 and equation 3.8 gives χ_C and the adhesion free-energy of the cell is then given as $F_{adh} = A_0 C_0 \chi_C$.

The above analysis assumes the adhesion complexes can sustain any required force $F(x_i)$ via the assumed linearity of the complex response. However, it has been demonstrated that complexes cannot support a force greater than a critical value F_{max} (Dowling and McGarry 2014; McGarry and McHugh 2008; Selhuber-Unkel *et al.* 2010). Direct enforcement of the condition that no complex force exceeds F_{max} at the cell-substrate interface would require an iterative adjustment of spread state (as implemented for simplified microstates by McEvoy *et al.* (2017)), and is therefore excessively computationally expensive in the context of the Monte Carlo simulations required for sampling the homeostatic ensemble. Here we use the alternative approach of a penalty scheme to ensure that a very small number of spread states contain complexes with forces $F > F_{max}$. In summary, we define a penalty force

$$F^p = \int_A \Delta F^p(x_i) dA, \quad (3.9)$$

where

$$\Delta F^p(x_i) = \begin{cases} F(x_i) - F_{max} & F(x_i) > F_{max} \\ 0 & \text{otherwise} \end{cases}. \quad (3.10)$$

A penalty energy is then defined as $\chi_p = (F^p)^2 / (2\kappa_p)$, where the parameter κ_p has the units of stiffness and sets the magnitude of the penalty. The total focal adhesion free-energy including the penalty contribution is then defined as

$$F_{adh} = A_0 C_0 (\chi_C + \chi_p), \quad (3.11)$$

with the normalised energy \hat{F}_{adh} following from the definitions detailed in Appendix Section 3.A.2.4 along with the model parameters. In order to compare model predictions with the experimental results of Engler *et al*, the number of ligands per unit area, N_H , can be expressed as surface collagen density ρ_{col} through the following expression:

$$\rho_{\text{col}} = \frac{N_H M_{\text{col}}}{L}, \quad (3.12)$$

where M_{col} is the molar mass of collagen and L is Avogadro's constant.

3.2.4. Numerical methods

We employ Markov Chain Monte Carlo (MCMC) to construct a Markov chain that is representative of the homeostatic ensemble. This involves three steps: (i) a discretization scheme to represent morphological microstate (j), (ii) calculation of $G^{(j)}$ for a given morphological microstate (j), and (iii) construction of a Markov chain comprising these morphological microstates. Here, we briefly describe the procedure which was implemented in MATLAB with readers referred to Shishvan *et al*. for further details. Typical Markov chains comprised in excess of 2.5 million samples.

In the general setting of a three-dimensional (3D) cell, a morphological microstate is defined by the connection of material points on the cell membrane to the surface of the collagen coated substrate. In the 2D context of cells on collagen coated substrates, this reduces to specifying the connection of all material points of the cell to locations within the collagen coated substrate, i.e. a displacement field $u_i^{(j)}(X_i)$ is imposed on the cell with X_i denoting the location of material points on the cell in the undeformed configuration, and these are then displaced to $x_i^{(j)} = X_i + u_i^{(j)}$ in morphological microstate (j). These material points located at $x_i^{(j)}$ are then connected to material points on the collagen coated substrate at the same location $x_i^{(j)}$, completing the definition of the morphological microstate in the 2D setting.

The cell is modelled as a continuum and thus $u_i^{(j)}$ is a continuous field. To calculate the density of the morphological microstates, we define $u_i^{(j)}$ via Non-Uniform Rational B-splines (NURBS) such that the morphological microstate is now defined by M pairs of weights $[U_L^{(j)}, V_L^{(j)}]$ ($L = 1, \dots, M$). In all the numerical results presented here, we employ

$M = 16$ with 4×4 weights $U_L^{(j)}$ and $V_L^{(j)}$ governing the displacements in the x_1 and x_2 directions, respectively. The NURBS employ fourth order base functions for both the x_1 and x_2 directions, and the knots vector included two nodes each with multiplicity four, located at the extrema of the interval. We emphasise here that this choice of representing the morphological microstates imposes restrictions on the morphological microstates that will be considered. Therefore, the choice of the discretisation used to represent $u_i^{(j)}$ needs to be chosen so as to be able to represent the microstates we wish to sample, e.g. the choice can be based on the minimum width of a filopodium one expects for the given cell type. Given $u_i^{(j)}$, we can calculate $G^{(j)}$ using the model described in Section 2.1 with the cell discretised using constant strain triangles of size $e \approx R_0/10$, where R_0 is the radius of the cell in its undeformed configuration (see Extended Data Figure 3.5).

We construct the Markov chain using the Metropolis algorithm that gives a sequence of random samples from the exponential equilibrium distribution. We employ the Metropolis algorithm in an iterative manner so as to enforce the homeostatic constraint. The scheme is summarised as follows:

- (i) Assume a value of ζ and use the undeformed cell configuration as the starting configuration and label it as morphological microstate $j = 0$ with equilibrium free-energy $G^{(0)}$ calculated as described in equation 3.3.
- (ii) Randomly pick one pair of the M weights $U_L^{(j)}, V_L^{(j)}$ and perturb them by two independent random numbers picked from a uniform distribution over the interval $[-\Delta, \Delta]$.
- (iii) Compute the new free-energy of this perturbed state and thereby the change in free-energy $\Delta G = G^{(j)} - G^{(j-1)}$.
- (iv) Use the Metropolis criterion to accept this perturbed state or not, i.e.
 - a. if $\Delta G \leq 0$, accept the perturbed state;
 - b. if $\Delta G > 0$, compute $P^{acc} = \exp(-\zeta \Delta G)$ and accept the perturbed state if $P^{acc} > \mathcal{R}$, where \mathcal{R} is a random number drawn from a uniform distribution over $[0, 1]$.
- (v) If the perturbed state is accepted, add it to the list of samples as a new morphological microstate, else repeat the configuration prior to step (ii) in the sample list and return to step (ii).

- (vi) Keep repeating this procedure until a converged distribution is obtained. Here, we typically use the criterion that the average of $G^{(j)}$ within the generated sample list (labelled $\langle G^{(j)} \rangle$) changes by less than 1% over 100,000 steps of the Markov chain.
- (vii) If $\langle G^{(j)} \rangle$ is within $\pm 2\%$ of the homeostatic value of G_s , we accept this distribution, else we modify ζ and repeat from step (i).

3.3. Results and discussion

3.3.1. Spread dependence of cells on surface collagen density

The influence of surface collagen density ρ_{col} on cell spreading is shown in Figure 3.1. Cells are spread on rigid substrates coated with three different values of ρ_{col} (6, 33, and 250 ng cm^{-2}). A sample of predicted cell spread states are shown in Figure 3.1a, including stress fibre distributions (green), focal adhesion distributions (red), and nuclei (blue). In the case of a low ρ_{col} (6 ng cm^{-2}) cells are not highly spread and they maintain regular rounded morphologies. A low concentration smeared actin cytoskeleton is observed throughout the cell, with no regions of highly aligned stress fibres. For a higher ρ_{col} of 33 ng cm^{-2} , cells become more highly spread. Additionally, the spread shapes become quite irregular, in contrast to the rounded shapes observed on a lower ρ_{col} . Regions of aligned stress fibres are observed and focal adhesions cluster towards the cell periphery. In the case of the highest ρ_{col} of 250 ng cm^{-2} , a further increase in spread area is observed and the spread shape becomes highly irregular, with cells exhibiting elongated protrusions. High concentrations of aligned stress fibres are observed, and focal adhesions are highly localised at the cell periphery and cell nucleus.

Probability density functions (pdfs) for cell spread area (Figure 3.1b) and for aspect ratio (AR) of a best fit ellipse (Figure 3.1c) are constructed from the full population of spread states for each surface collagen density. With increasing ρ_{col} , the mean cell spread area increases and the variance in spread area increases (i.e. in Figure 3.1b, as ρ_{col} increases

the pdf moves to the right and becomes less peaked). A similar trend is observed for cell aspect ratio (Figure 3.1c), where the mean is closer to 1 and the variance is very low (the pdf is more peaked) for the lowest ρ_{col} .

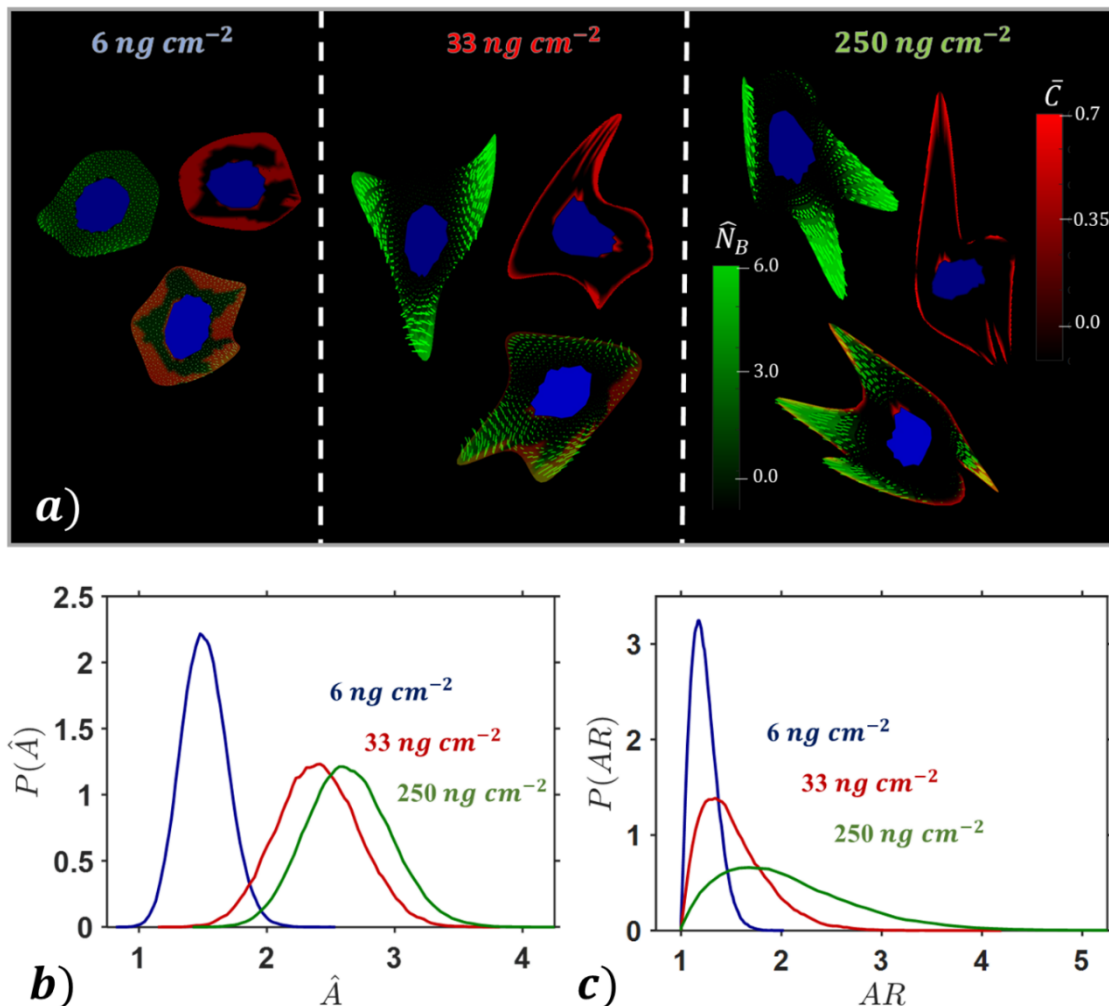


Figure 3.1: (a) Contours of bound stress fibre protein concentrations \hat{N}_B (green) with dominant alignment, focal adhesion distributions \hat{C} (red), and overlays in commonly observed cell shapes at a given surface collagen density ρ_{col} . Nucleus highlighted in blue; Probability density functions for cells spread on a rigid substrate for 3 collagen densities, of (b) cell spread area ($\hat{A} = A/A_0$), and (c) cell aspect ratio.

In summary, the pdfs presented in Figures 3.1b and 3.1c show that a population of cells on a lower ρ_{col} will have a lower mean spread area and a lower variance of spread area, in addition to being rounded (AR close to 1) with a low variance of spread shape. As ρ_{col} is increased, a higher mean spread area is obtained for a population of cells, with a higher

variance of spread area and spread shape. Additional spread shapes are presented in Extended Data Figures 3.1 and 3.2.

3.3.2. Influence of substrate stiffness on cell spreading

The influence of substrate stiffness E_{sub} on cell spreading is shown in Figure 3.2. Cells are spread on substrates of stiffness 8 kPa and 32 kPa, in addition to a rigid substrate. All substrates have a ρ_{col} of 33 ng cm^{-2} . A sample of cell spread states shown in Figure 3.2a suggests that cell spread area increases with E_{sub} . Cells on the compliant (8kPa) substrate exhibit a low concentration smeared actin cytoskeleton, compared to the highly aligned stress fibres on the stiff and rigid substrate. The irregularity of the spread shape increases with E_{sub} , with longest protrusions occurring on the rigid substrate.

Pdfs for cell spread area (Figure 3.2b) and aspect ratio (Figure 3.2c) are constructed from the full population of spread states for each value of E_{sub} . Clearly both the mean spread area and the variance in spread area increase with E_{sub} (i.e. in Figure 3.2b the pdf moves to the right and becomes less peaked as E_{sub} is increased). The effect of E_{sub} on cell shape is less pronounced, with only a minor increase in the mean and variance of cell aspect ratio with increasing stiffness (Figure 3.2c).

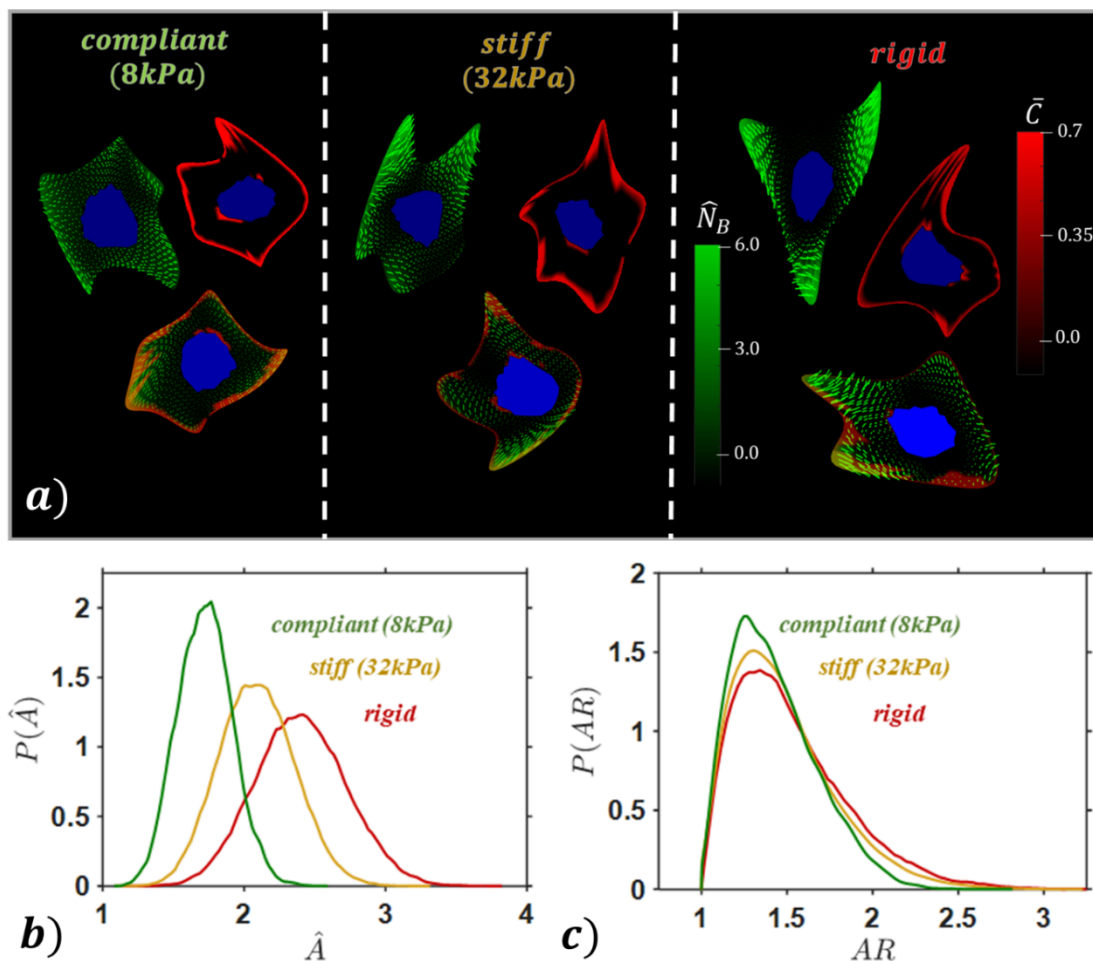


Figure 3.2: (a) Contours of bound stress fibre protein concentrations \hat{N}_B (green) with dominant alignment, focal adhesion distributions \hat{C} (red), and overlays in commonly observed cell shapes at a given substrate stiffness E_{sub} . Nucleus highlighted in blue; Probability density functions for cells spread on substrates of different stiffness at a surface collagen density ρ_{col} of 33 ng cm^{-2} , of (b) cell spread area ($\hat{A} = A/A_0$), and (c) cell aspect ratio.

3.3.3. Coupled dependence of collagen density and substrate stiffness

The coupled interplay between the influence of ρ_{col} and E_{sub} on cell spreading is next considered. Heat maps are constructed from mean spread areas (Figure 3.3a) and mean aspect ratios (Figure 3.3b). Representative spread states are superimposed for illustrative purposes. As shown in Figure 3.3a, a very low ρ_{col} results in a very weak dependence of mean spread area on E_{sub} . However, for moderate and high ρ_{col} the mean spread area is highly dependent on E_{sub} . As shown in Figure 3.3b, the cell aspect ratio exhibits a very

weak dependence on E_{sub} (the contours in 3.4b are almost vertical), while exhibiting a very strong dependence on ρ_{col} .

Both the mean and standard deviation of cell spread area is shown in Figure 3.3c. A number of features should be noted: (i) as ρ_{col} is increased, both the mean and standard deviation increase up to a peak value. This trend is observed for all values of E_{sub} ; (ii) if ρ_{col} is increased beyond the peak value, a slight reduction in mean spread area (and its standard deviation) is observed. Again, this trend is observed for all values of E_{sub} ; (iii) the ρ_{col} at which the mean spread area reaches a peak value increases with increasing E_{sub} ; (iv) for a given ρ_{col} , both the mean and standard deviation increase with increasing E_{sub} . Figure 3.3d shows that cell aspect ratio is highly dependent on ρ_{col} , with both the mean and standard deviation increasing with increasing ρ_{col} . It is interesting to note that even though the cell mean spread area decreases when the ρ_{col} is increased beyond the critical value, the mean aspect ratio continues to increase. However, mean aspect ratio and its standard deviation exhibits a weak dependence on E_{sub} .

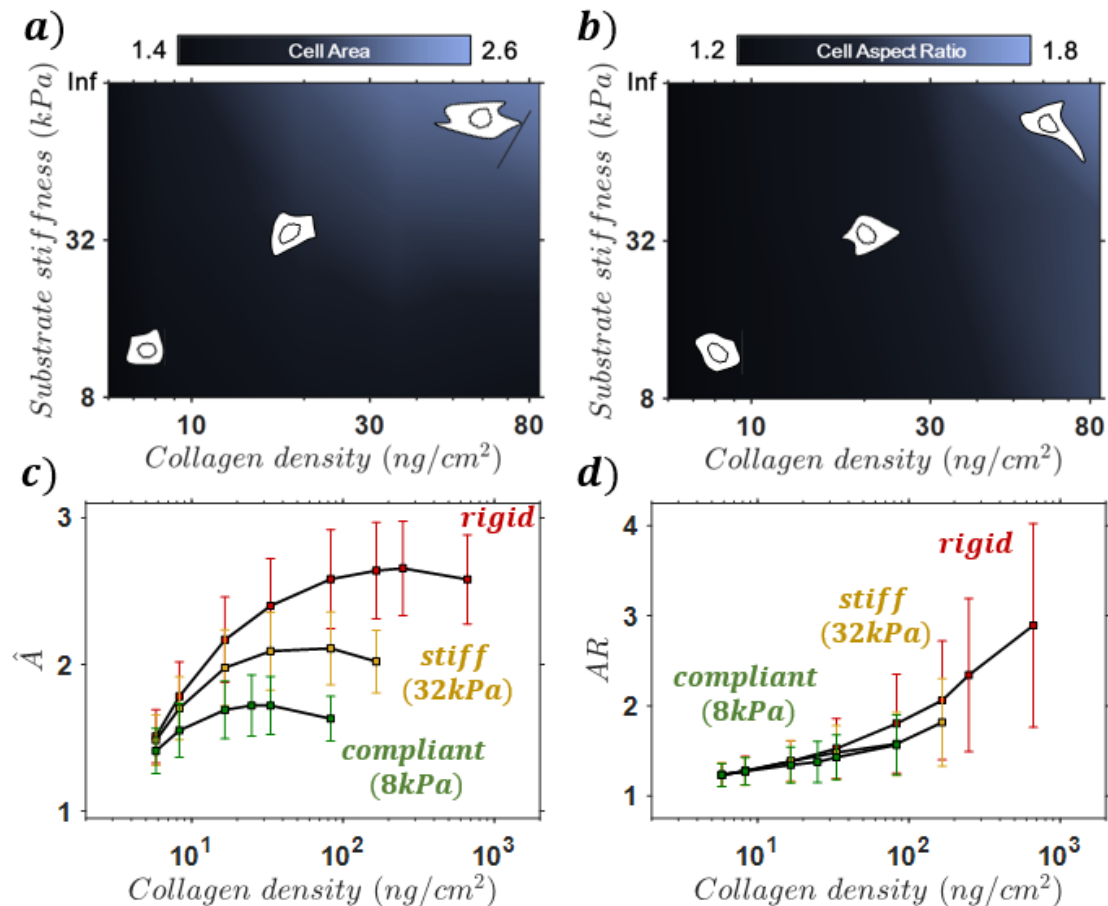


Figure 3.3: (a,c) Predicted cell area (mean \pm SD) at a given surface collagen density ρ_{col} for cells spread on substrates of different stiffness (red-rigid, yellow-32kPa, green-8kPa). Cell area is normalized such that $\hat{A} = A/A_0$; (b,d) Predicted cell aspect ratio (mean \pm SD). Sample cell spread shapes shown for a given substrate.

3.3.4. Experimental support for predicted cell behaviour

Remarkably, all the features described by Figure 3.3 are directly supported by the experimental study of Engler *et al.* (2003), where the response of smooth muscle cells (SMCs) to E_{sub} and ρ_{col} was investigated. At a low ρ_{col} on all substrates, SMCs that were detectably spread were found to be rounded with a low spread area. As the ρ_{col} was increased, the spread area (mean and standard deviation) was observed to increase up to a peak value. Following this peak, any increase to the density of ρ_{col} resulted in a reduction of mean spread area. This behaviour is further supported by the experimental study of Gaudet *et al.* (2003). Engler *et al.* noted that the ρ_{col} at which the peak mean spread area occurs is dependent on E_{sub} (i.e. it increases with increasing E_{sub} , as

predicted by our models). Engler *et al.* also reported that an increase in E_{sub} resulted in a higher mean cell spread area for a fixed ρ_{col} .

Although the aspect ratio is not directly measured in the experimental work of Engler *et al.*, with an increase in cell area (due to E_{sub} or ρ_{col}) it was reported that cell shapes became less rounded and more irregular when cell spread area increases as a result of increased E_{sub} and/or ρ_{col} . Such a reduction in cell roundness with increasing E_{sub} has also been observed in the experimental study of Ren *et al.* (2010) for skeletal muscle cells. Additionally, Prager-Khoutorsky *et al.* (2011) reported that cells readily elongate (i.e. high aspect ratio) when plated on rigid substrates, with the behaviour significantly less pronounced with decreasing E_{sub} . Similar to our predictions for stress fibre distributions, Engler *et al.* report that highly spread cells display a well-ordered stress fibre network. Such ordered fibres were far less probable on rounded cells on low ρ_{col} and on softer substrates. Similar observations are also reported in the experimental study by Deroanne *et al.* (2001) in which a significant reduction in stress fibre and focal adhesions formation was observed in endothelial cells on soft gels compared to stiff substrates. Pelham and Wang (2018) also show such dependence of adhesion formation on substrate stiffness. The predicted trends of SF and FA organisation in Figures 3.1 and 3.2 of the current study are strongly supported by the aforementioned experimental studies. Additional samples of computed cell spread states are shown in Extended Data Figures 3.1 and 3.2.

3.3.5. Thermodynamically motivated insights for predicted cell behaviour

We next provide a thermodynamically motivated explanation for the computed results in Figures 3.1-3.3, and, by extension, for the experimental observations of Engler *et al.* In Figure 3.4a we plot the pdf of total free energy for the three values of ρ_{col} on a rigid substrate. Recall that the system is subject to the homeostatic constraint, such that the mean free energy of all states is equal to the cellular homeostatic free energy G_S , which can be identified from the unique state of a free-standing cell. Therefore, the mean free energy is similar for all values of ρ_{col} (Figure 3.4a). The adhesion free energy pdf (Figure 3.4b) is highly peaked and negative for a high ρ_{col} of 250 ng cm^{-2} . This indicates a high probability that adhesion complex forces are close to F_{max} so that a low adhesion energy is obtained. On the other hand, there is a low probability that adhesion complex forces exceed F_{max} and incur a (positive) adhesion energy penalty.

In the case of a high ρ_{col} of 250 ng cm^{-2} , the cell-substrate tractions for a wide range of highly spread states can be supported without incurring an adhesion energy penalty (i.e. the adhesion free energy remains low). As a result the entropy of the spread states is very high for high values of ρ_{col} . Correspondingly, a high variance in the (negative) cytoskeletal and (positive) elastic free energies (Figures 3.4c,d) occurs. In effect, cell spreading on a rigid substrate coated with a high ρ_{col} can be viewed as a competition between positive elastic free energy due to stretching of passive cell components and negative free energy due to assembly of contractile stress fibres, with an additional negative free energy contribution from the adhesion complexes.

When ρ_{col} is reduced, higher forces occur in ligand complexes, resulting in a higher probability that F_{max} is exceeded and an adhesion energy penalty is incurred. Therefore, there is a low probability that highly spread states will occur, and the entropy of the spread states decreases. In other words, a highly spread cell on a low ρ_{col} will result in adhesion

complex forces that exceed the maximum value, and the imposition of an energetic penalty results in a low probability that such highly spread states will occur. This explains the high probability of rounded cells with low spread areas on a ρ_{col} of 6 ng cm^{-2} , as reported in Figures 3.1 and 3.3. Correspondingly, as shown in Figures 3.4c and 3.4d, the cytoskeletal and elastic free energy pdfs are highly peaked with mean values close to zero (as expected for the observed low spread areas and low variance in spread shapes (AR)).

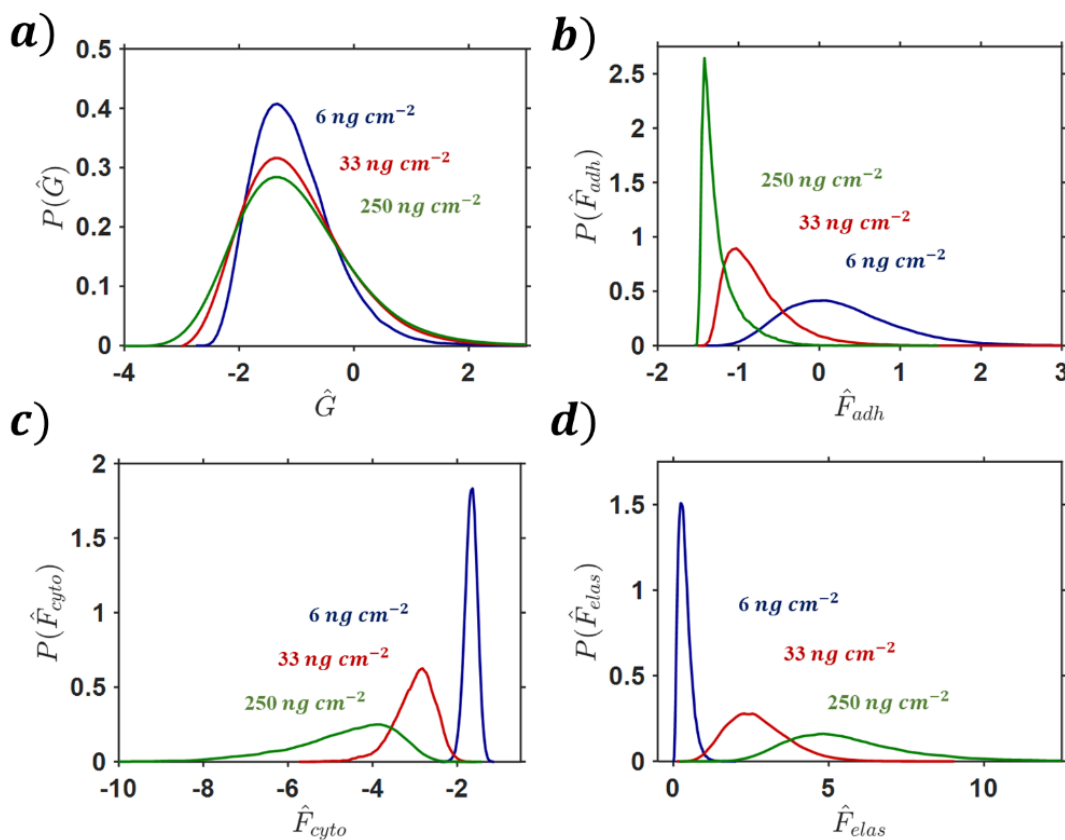


Figure 3.4: Probability density functions for cells spread on a rigid substrate for 3 surface collagen densities ρ_{col} , of (a) total free energy, (b) cytoskeletal free energy, (c) elastic free energy, and (d) adhesion free energy.

Recall from Figure 3.3 that, for all values of E_{sub} , cell spread area increases with increasing ρ_{col} up to a peak value. In Figure 3.5, we report the mean and standard deviation of the free energy densities across all ρ_{col} and E_{sub} (the standard deviation is indicative of the variance observed in the corresponding pdfs). The peak spread areas

shown in Figure 3.3b coincide with the lowest mean adhesion free energy for each substrate (Figures 3.5(a-c)). The ρ_{col} associated with such a peak spread area on each substrate is hereafter referred to as “optimal”. At this optimal ρ_{col} there is a high probability that the forces in adhesion complexes will result in a low adhesion free energy. For sub-optimal ρ_{col} , highly spread states will result in an increased probability of adhesion complex forces higher than F_{max} , resulting in an energetic penalty, as explained in Figure 3.4 above. On the other hand, when the ρ_{col} is increased beyond the “optimal” value, the cell must spread to a higher area in order to generate sufficient tractions to achieve sufficiently high adhesion complex forces (i.e. $F(x_i) \cong F_{max}$) and a low adhesion free energy. However, spreading to such a high area results in an increased elastic strain energy. There is a low probability that the adhesion (Figure 3.5 (a-c)) and cytoskeletal (Figure 3.5 (d-f)) free energy will overcome this “elastic penalty” and achieve the homeostatic state, i.e. \hat{G}_s . Therefore, on “post-optimal” ρ_{col} there is a low probability that the cell area will increase beyond the peak spread area. In fact, a “post-optimal” ρ_{col} leads to a reduction in mean spread area, as shown in Figure 3.3c (this has been also observed experimentally by Engler *et al.* and Gaudet *et al.*, as discussed in Section 3.3.4 above). This occurs because cellular tractions are supported by a higher number of complexes, so that individual bond forces are reduced. Therefore, the cell adhesion free energy moves closer to zero (Figure 3.5(a-c)), providing a weaker competition to the elastic strain energy (Figures 3.5 (g-i)) so that there is a lower probability that the cell will achieve the peak spread area. This behaviour is summarized in Figure 3.6. Although the mean spread area decreases for “post-optimal” ρ_{col} , the mean elastic free energy increases on rigid and stiff substrates (Figure 3.5g-h). This is due to a high variability in spread shape on stiffer substrates with high ρ_{col} (see plots of cell aspect ratio in Figure 3.3d).

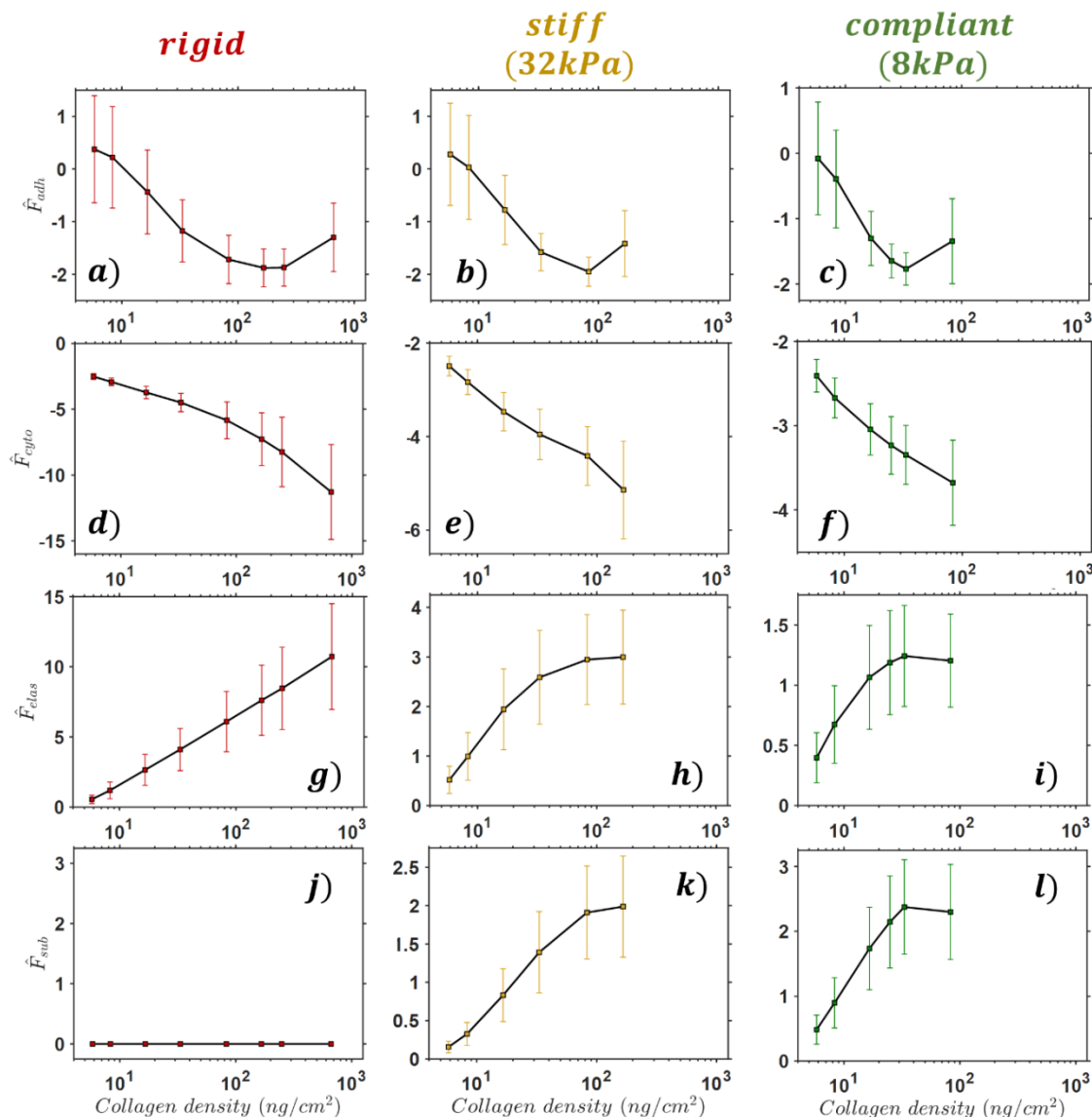


Figure 3.5: Predicted adhesion (a-c), cytoskeletal (d-f), elastic (g-i), and substrate (j-l) free energy (mean \pm SD) at a given surface collagen density ρ_{col} for cells spread on rigid, stiff, and compliant substrates.

A reduction in E_{sub} lowers the probability of the cell achieving a high spread area, with rounded low spread morphologies more frequently observed (Figure 3.3c). On a rigid material, there is no contribution from the elastic strain energy of the substrate (Figure 3.5j) as it is not deformed by the contractile activity of the cell. However, as the E_{sub} is reduced (Figures 3.5 k,l), it will be deformed by the cell. The associated substrate free energy causes the total system free energy to become increasingly positive. Thus, to achieve a homeostatic state, there is a high probability the cell area will be lower on more

compliant substrates. The highly coupled balance between the contributions to the system free energy causes the peak cell area to occur at a lower ρ_{col} for a lower E_{sub} . As mentioned above, a low E_{sub} results in lower spread areas, which leads to lower cell-substrate tractions. Therefore, a lower ρ_{col} is required for an increased probability of optimal forces in adhesion complexes ($F(x_i) \cong F_{max}$) and a correspondingly low adhesion free energy. Peak spreading occurs on lower ρ_{col} for lower E_{sub} , as shown in Figure 3.3c (and as reported in the experimental of Engler *et al.*).

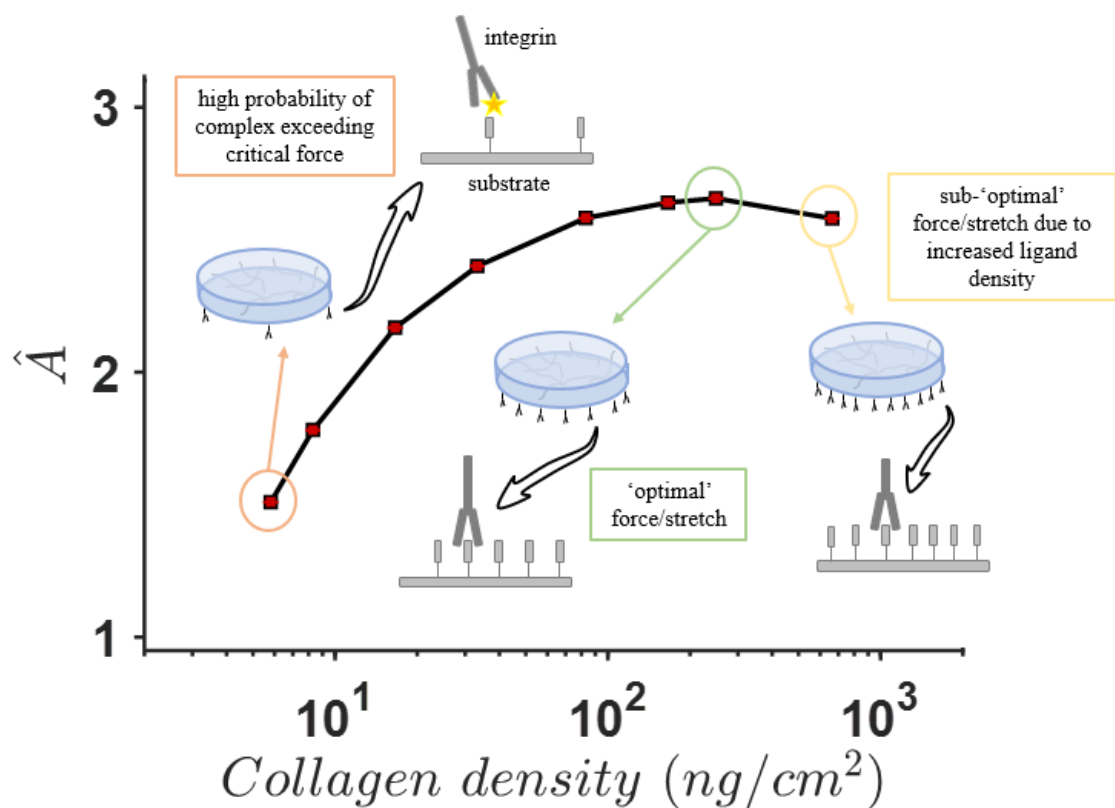


Figure 3.6: Schematic of thermodynamically motivated explanation for the influence of collagen (ligand) density on cell spread area.

3.4. Concluding remarks

The equilibrium statistical mechanics framework developed by Shishvan *et al.* (2018) allows for the simulation of the homeostatic ensemble for cells on an elastic substrate in a nutrient bath. Cells assume a dynamic homeostatic equilibrium by means of a free energy competition between the increasing elastic free energy due to stretching of passive cell components (and substrate deformation), and the decreasing cytoskeletal free energy as contractile proteins assemble to form stress fibres. In the current study, the framework is expanded to include the free energy associated with formation of focal adhesions between the cell and a collagen coated substrate.

The expanded framework allows for the simulation of the coupled influence of surface collagen density ρ_{col} and substrate stiffness E_{sub} on cell spreading, as reported in the experimental study of Engler *et al.* (2003). The key experimental observations predicted by our modelling framework are summarized as follows:

- With increasing substrate ρ_{col} , cell spread area (mean and standard deviation) increases up to a peak value.
- A further increase in ρ_{col} beyond this peak results in a reduction of the cell spread area (mean and standard deviation).
- The ρ_{col} at which the mean cell area reaches a peak decreases with decreasing E_{sub} .
- At a fixed ρ_{col} , the mean and standard deviation of the spread area increase with increasing E_{sub} .

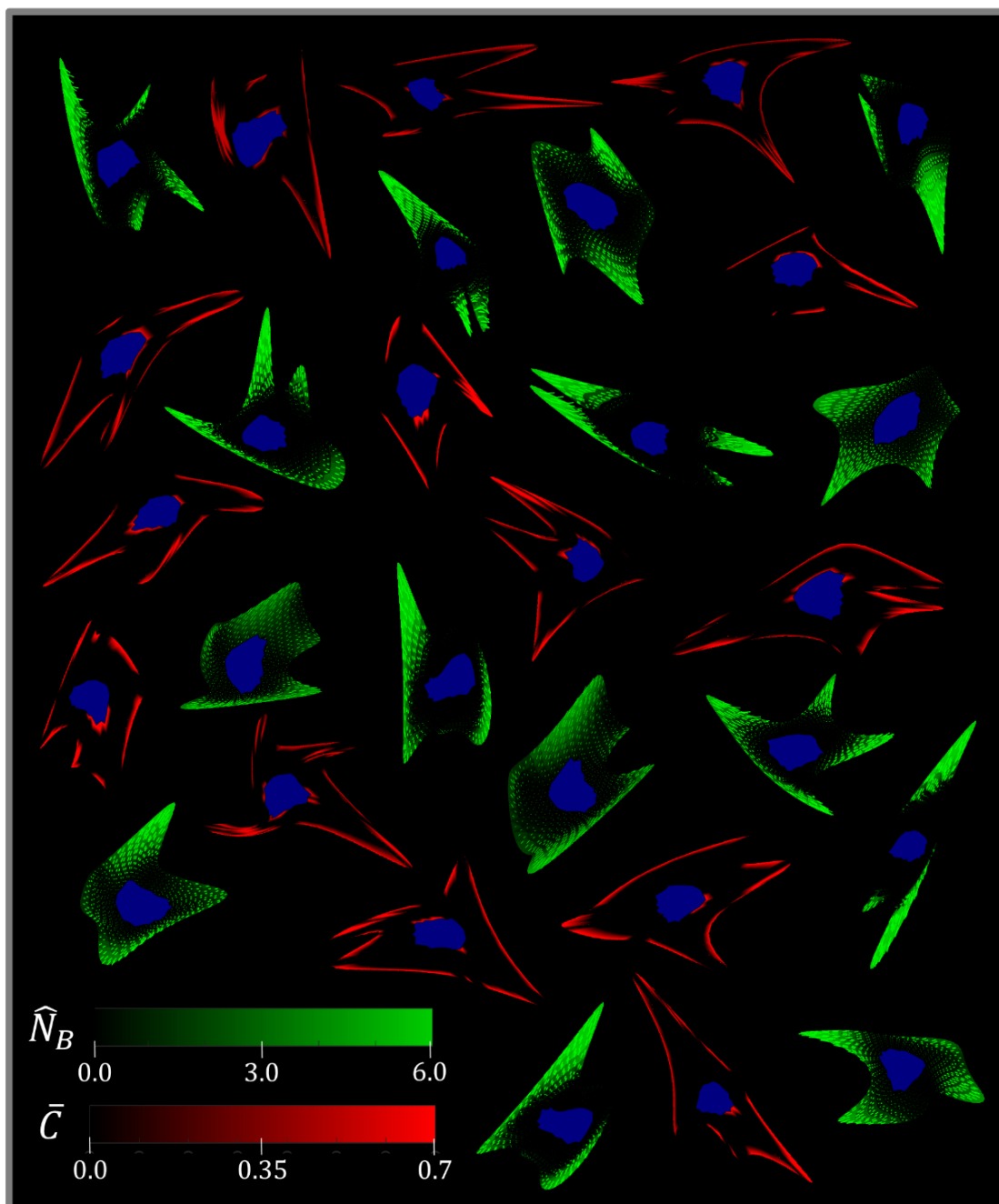
The ρ_{col} directly influences the forces in adhesion complexes and, consequently, the adhesion free energy. This, in turn, influences the spread states that cells assume in achieving homeostasis. A low ρ_{col} lowers the probability of a cell becoming highly spread, as sufficient complexes cannot form to support the tractions imposed by the

substrate. Conversely, at a high ρ_{col} the cell may form more adhesion complexes, lowering the associated free energy. Thus, the probability of cells having a high spread area increases. The influence of E_{sub} and ρ_{col} is highly coupled, as demonstrated in Figure 3.3 and 3.5. A deformable substrate lowers the probability of a cell becoming highly spread, reducing the cell tractions and thereby causing the peak mean spread area to occur at a lower ρ_{col} .

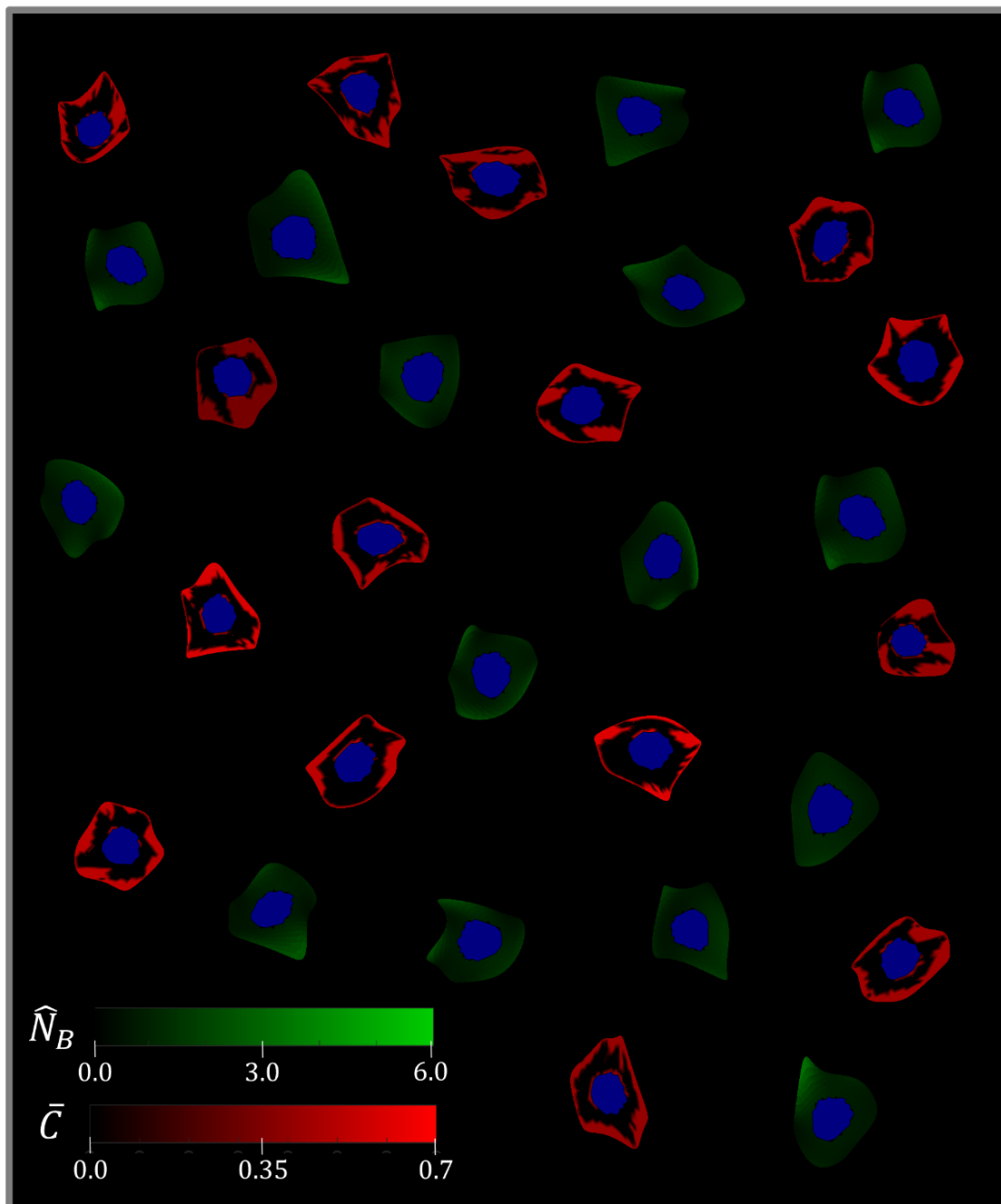
In statistical thermodynamics a closed system in a constant temperature and pressure environment attains equilibrium at minimum Gibbs free-energy. However, metabolic systems such as cells cannot be viewed in this manner; in fact cells never attain an equilibrium minimum free energy state while alive. The approach developed by Shishvan *et al* and extended in the current study to account for free energy associated with focal adhesion formation recognizes this and predicts the statistics of biological observables (e.g. cell area, aspect ratio etc.) under the constraint that the cell maintains a homeostatic state. In a previous study, McEvoy *et al.* (2017) identified low (or minimum) free energy cell spread states within a limited phase space of axisymmetric configurations. This simplified approach provided a reasonable approximation of the detailed trends computed in the current study (and observed experimentally (Engler *et al.*)), which can be explained by the realisation that low free energy states will of course be highly probable within the *homeostatic ensemble*; see equation 3.1. While McEvoy *et al.* correctly demonstrate that cell spreading is governed by a competition between decreasing cytoskeletal and adhesion free energy and increasing elastic energy, the identification of a low or minimum free energy configuration is not physically appropriate for a fluctuating system. Therefore, the emergence of such an energetic competition within the statistical mechanics framework of the homeostatic ensemble provides a significant advance in current understanding of the influence of ligand density and substrate stiffness on cell spreading. Importantly, this framework correctly predicts the trends for observables such the spread area and spread

shape as a function of environmental cues such as stiffness and ligand density, while also quantifying inherent statistical variability in these observations. The *homeostatic ensemble for cells*, expanded to include the focal adhesion formation and an associated adhesion free energy contribution, provides new insight into observed cell behaviour on deformable collagen coated substrate. In future, the kinetic monte carlo method may be employed to simulate the time evolution of the spreading process. In its current form the model may readily be used to simulate more complex extra-cellular environments, including the spreading of cells on ligand patterned ridges and ligand patterned micro-pillars.

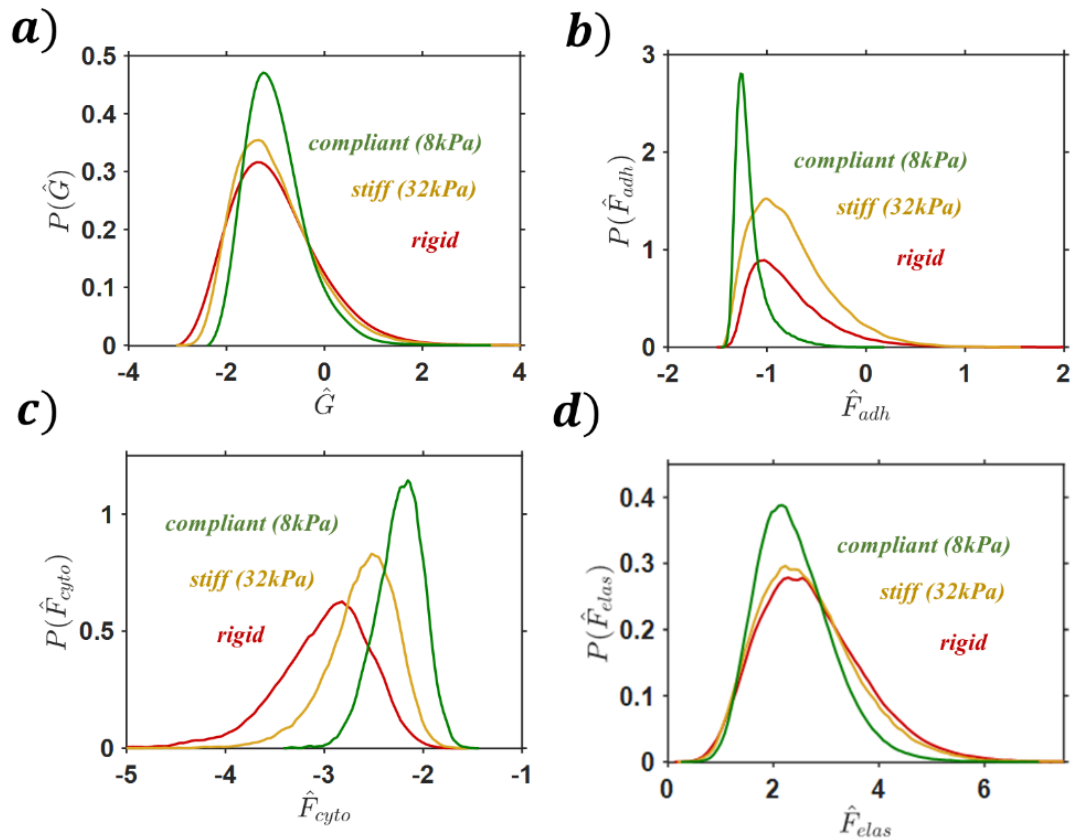
Extended data



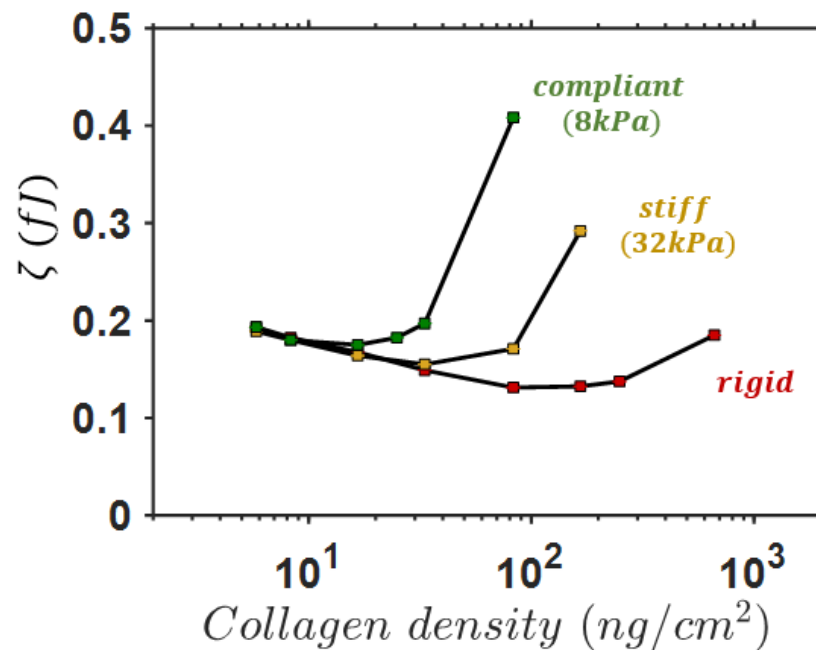
Extended Data Figure 3.1: Additional configurations of bound stress fibre protein concentrations \hat{N}_B (green) with dominant alignment, and focal adhesion distributions \bar{C} (red). Nucleus highlighted in blue. The configurations are all from the median of the free-energy \hat{G} distribution for cells spread on a rigid substrate with a surface collagen density ρ_{col} of 250 ng/cm^2 .



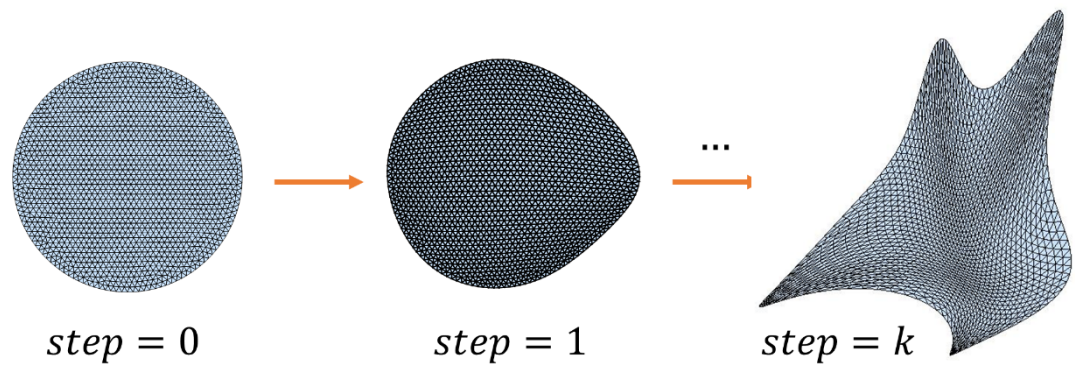
Extended Data Figure 3.2: Additional configurations of bound stress fibre protein concentrations \hat{N}_B (green), and focal adhesion distributions \bar{C} (red). Nucleus highlighted in blue. The configurations are all from the median of the free-energy \hat{G} distribution for cells spread on a rigid substrate with a surface collagen density ρ_{col} of 250 ng/cm^2 .



Extended Data Figure 3.3: Probability density functions for cells spread on substrates of different stiffness at a collagen density of 33 ng cm^{-2} , of (a) total free energy, (b) adhesion free energy, (c) cytoskeletal free energy, and (d) elastic free energy.



Extended Data Figure 3.4: Predictions of ζ , where the homeostatic temperature is given by $1/\zeta$.



Extended Data Figure 3.5: Evolution of cell spread shapes over steps of Markov Chain Monte Carlo simulation.

Appendix 3.A: Supplementary information

3.A.1. The homeostatic mechanics framework

Here, we provide a brief overview of the homeostatic mechanics framework of Shishvan *et al.* (2018) with the aim to provide the reader the key aspects of the framework required for fully appreciating the computational results presented in the main text. Readers are referred to Shishvan *et al.* for a more complete treatment including the derivations of the relevant equations.

Making the ansatz that *living cells are entropic*, Shishvan *et al.* introduced the concept of the *homeostatic ensemble* with cellular homeostasis providing the additional constraints and mechanisms for entropy maximisation. This defined the notion of a (dynamic) *homeostatic equilibrium* state that intervenes to allow living cells to elude thermodynamic equilibrium. They thus developed a statistical mechanics framework for living cells using the notions of statistical inference (Jaynes 1957) applicable over a timescale from a few hours to a few days as long as the cell remains as a single undivided entity (i.e. the interphase period of the cell cycle). The key ideas behind the framework can be summarised as follows. A system comprising the cell and the extracellular matrix (ECM) is an open system with the cell exchanging nutrients with the surrounding bath. These nutrients fuel a large number of coupled biochemical reactions that include actin polymerisation, treadmilling and dendritic nucleation that effect changes to the cell morphology. These biochemical reactions change the morphology of the cell but are not precisely controlled, and this manifests via the observed morphological fluctuations of the cell. Shishvan *et al.* made the *ansatz* that these biochemical reactions provide the mechanisms to maximise the morphological entropy of the cell, but constrained by the fact that the cell maintains a homeostatic state over the interphase period. Cellular homeostasis is the ability of cells to actively regulate their internal state, and maintain the concentration of all internal species* at specific average values over their morphological

fluctuations independent of the environment (*chemical species here are defined in a manner analogous to the Gibbs definition for a grand canonical ensemble, viz. chemical species are an ensemble of chemically identical molecular entities that can explore the same set of molecular energy levels on the timescale of a morphological microstate).

3.A.1.1. Morphological microstates, entropy, fluctuations, and the homeostatic temperature

Controlling only macro variables (i.e. macrostate) such as the temperature, pressure, and nutrient concentrations in the nutrient bath results in inherent uncertainty (referred to here as missing information) in micro variables (i.e. microstates) of the system. This includes a level of unpredictability in homeostatic process variables, such as the spatio-temporal distribution of chemical species, that is linked to Brownian motion and the complex feedback loops in the homeostatic processes. Thus, this system not only includes the usual lack of precise information on the positions and velocities of individual molecules associated with the thermodynamic temperature, but also an uncertainty in cell shape resulting from imprecise regulation of the homeostatic processes. The consequent entropy production forms the basis of this new statistical mechanics framework motivated by the following two levels of microstates:

- (i) *Molecular microstates*. Each molecular microstate has a specific configuration (position and momentum) of all molecules within the system.
- (ii) *Morphological microstates*. Each morphological microstate is specified by the mapping (connection) of material points on the cell membrane to material points on the collagen coated substrate. In broad terms, a morphological microstate specifies the shape and size of the cell.

Shishvan *et al.* identified the (dynamic) homeostatic or equilibrium state of the system by entropy maximisation. Subsequently, we shall simply refer to this state as an equilibrium state to emphasise that it is a stationary macrostate of the system inferred via entropy

maximisation as in conventional equilibrium analysis. The total entropy of the system is written in terms of the conditional probability $P^{(i|j)}$ of the molecular microstate (i) given the morphological microstate (j) and the probability $P^{(j)}$ of morphological microstate (j) as

$$I_T = \sum_j P^{(j)} I_M^{(j)} + I_\Gamma. \quad (3.A1)$$

In equation 3.A1, $I_M^{(j)} \equiv -\sum_{i \in j} P^{(i|j)} \ln P^{(i|j)}$ and $I_\Gamma \equiv -\sum_j P^{(j)} \ln P^{(j)}$ are the entropies of molecular microstates in morphological microstate (j) and the morphological microstates, respectively. Equilibrium then corresponds to molecular and morphological macrostates that maximise I_T subject to appropriate constraints. The molecular macrostate evolves on the order of seconds, limited by processes such as the diffusion of unbound actin. By contrast, transformation of the morphological macrostate involves cell shape changes and therefore, the morphological macrostate evolves on the order of minutes, limited by co-operative cytoskeletal processes within the cell such as meshwork actin polymerisation and dendritic nucleation. The evolutions of the molecular and morphological macrostates are therefore temporally decoupled, and Shishvan *et al.* showed that equation 3.A1 can be maximised by independently maximising $I_M^{(j)}$ at the smaller timescale to determine the equilibrium distribution of molecular microstates for a given morphological microstate, and then maximising I_Γ at the larger timescale to determine the equilibrium distribution of the morphological microstates.

Over the (short) timescale on the order of seconds, the only known constraint on the system is that it is maintained at a constant temperature, pressure and strain distribution.

The equilibrium of a given morphological microstate (j) obtained by maximising $I_M^{(j)}$ (denoted by $S_M^{(j)}$) corresponds to molecular arrangements that minimise the Gibbs free-energy with $G^{(j)}$. Since the connection between the cell and the substrate is fixed for a

given morphological microstate, the determination of $G^{(j)}$ is a standard boundary value problem as described in Section 3.A.2.2. Over the (long) timescale on the order of several minutes to hours, the equilibrium distribution $P_{\text{eq}}^{(j)}$ is determined by maximising I_{Γ} , but now with the additional constraint that the cell is maintained in its homeostatic state. For the case of a cell on an ECM in a constant temperature and pressure nutrient bath, the homeostatic constraint translates to the fact that the average Gibbs free-energy of the system over all the morphological microstates it assumes, is equal to the equilibrium Gibbs free-energy G_{S} of an isolated cell in suspension (free-standing cell), i.e. the homeostatic processes maintain the average biochemical state of the system equal to that of a cell in suspension. In deriving this result, Shishvan *et al.* did not consider every individual homeostatic process, but rather used just the coarse-grained outcome of the homeostatic processes. The application of this coarse-grained constraint is the key element of the *homeostatic mechanics* framework, with the morphological entropy I_{Γ} parameterising the information lost by not modelling all variables associated with the homeostatic processes.

The maximisation of I_{Γ} while enforcing $\sum_j P^{(j)} G^{(j)} = G_{\text{S}}$ gives the *homeostatic equilibrium* state such that

$$P_{\text{eq}}^{(j)} = \frac{1}{Z} \exp(-\zeta G^{(j)}), \quad (3.A2)$$

where $Z \equiv \sum_j \exp(-\zeta G^{(j)})$ is the partition function of the morphological microstates, and the distribution parameter ζ follows from the homeostatic constraint

$$\frac{1}{Z} \sum_j G^{(j)} \exp(-\zeta G^{(j)}) = G_{\text{S}}. \quad (3.A3)$$

The collection of all possible morphological microstates that the system assumes while maintaining its homeostatic equilibrium state is referred to as the *homeostatic ensemble*.

The homeostatic ensemble can therefore be viewed as a large collection of copies of the system, each in one of the equilibrium morphological microstates. The copies (j) are distributed in the ensemble such that the free-energies $G^{(j)}$ follow an exponential distribution $P_{\text{eq}}^{(j)}$ with the distribution parameter ζ .

The equilibrium morphological entropy $S_{\Gamma} = -\sum_j P_{\text{eq}}^{(j)} \ln P_{\text{eq}}^{(j)}$ (i.e. the maximum value of I_{Γ}) follows from (S2) as

$$S_{\Gamma} = \zeta G_S + \ln Z, \quad (3.A4)$$

where $P_{\text{eq}}^{(j)}$ is substituted from equation 3.A2. Thus, S_{Γ} is related to ζ via the conjugate relation $\partial S_{\Gamma} / \partial G_S = \zeta$. Thus, analogous to $1/T$ that quantifies the increase in uncertainty of the molecular microstates (i.e. molecular entropy $S_{\text{M}}^{(j)}$) with average enthalpy, ζ specifies the increase in uncertainty of the morphological microstates (i.e. morphological entropy S_{Γ}) with the average Gibbs free-energy. We therefore refer to $1/\zeta$ as the *homeostatic temperature* with the understanding that it quantifies the fluctuations on a timescale much slower than that characterised by T .

3.A.2. The equilibrium Gibbs free-energy of a morphological microstate

Similar to conventional statistical mechanics calculations that require a model for the energy of the system, the homeostatic statistical mechanics framework requires a model for the Gibbs free-energy $G^{(j)}$ of morphological microstate (j). Here, we calculate $G^{(j)}$ using the free-energy model of Vigliotti *et al.* (2015) (as modified by Shishvan *et al.*) that includes contributions from cell elasticity and the actin/myosin stress fibre cytoskeleton, with the cell modelled as a two-dimensional (2D) body in the $x_1 - x_2$ plane adhered to a deformable collagen coated substrate, such that the out-of-plane Cauchy stress $\Sigma_{33} = 0$. The key differences are that (i) we include a nucleus that was neglected in Shishvan *et al.* (ii) and also add in explicit contribution from the focal adhesions as described in the main

body of the paper. The state of the system changes as the cell moves, spreads, and changes shape on the substrate. Here, we shall give a prescription to calculate the Gibbs free-energy of the system when the cell is in a specific morphological microstate (j), where the connections of material points on the cell membrane to the surface of the substrate are specified.

With the system comprising the cell and the rigid substrate within a constant temperature and pressure nutrient bath, the Gibbs free-energy $\mathcal{G}^{(j)}$ of the system in morphological microstate (j) is given by $\mathcal{G}^{(j)} = \int_{V_{\text{cell}}} f dV + F_{\text{sub}}^{(j)}$, where f is the specific Helmholtz free-energy of the cell. Here, we assume the substrate to be linear elastic so $F_{\text{sub}}^{(j)}$ is calculated directly from knowing the tractions the cells exert on a linear elastic half-space and thus we focus our description for the calculation of f . The equilibrium free-energy $G^{(j)}$ is then the value of $\mathcal{G}^{(j)}$ at $d\mathcal{G}^{(j)} = 0$. In the following, for the sake of notational brevity, we shall drop the superscript (j) that denotes the morphological microstate, as the entire discussion refers to a single morphological microstate.

The Vigliotti *et al.* model assumes only two elements within the cell: (i) a passive elastic contribution from elements such as the cell membrane, intermediate filaments and microtubules, and (ii) an active contribution from contractile acto-myosin stress fibres that are modelled explicitly. This model was modified in Shishvan *et al.* (2018) to incorporate a non-dilute concentration of stress fibres and here we further modify this model by including the nucleus in the analysis as a passive elastic body, in addition to the cytoplasm comprising the two above mentioned components. We shall first describe the modelling of the active acto-myosin stress fibres in the cytoplasm and then discuss the elastic model of both the nucleus and the cytoplasm.

Consider a two-dimensional (2D) cell of thickness b_0 and volume V_0 in its elastic resting state comprising a nucleus of volume V_N and cytoplasm of volume V_C such that $V_0 =$

$V_N + V_C$. The representative volume element (RVE) of the stress fibres within the cytoplasm in this resting configuration is assumed to be a cylinder of volume $V_R = \pi b_0 (n^R \ell_0 / 2)^2$, where ℓ_0 is the length of a stress fibre functional unit in its ground-state, and n^R is the number of these ground-state functional units within this reference RVE. The total number of functional unit packets within the cell is N_0^T , and we introduce $N_0 = N_0^T V_R / V_C$ as the average number of functional unit packets available per RVE; N_0 shall serve as a useful normalisation parameter. The state of stress fibres at location x_i within the cell is described by their angular concentration $\eta(x_i, \varphi)$, and there are $n(x_i, \varphi)$ functional units in series along the length of each stress fibre in the RVE. Here, φ is the angle of the stress fibre bundle in the undeformed configuration with respect to the x_2 – direction. Vigliotti *et al.* (2015) showed that, at steady-state, the number n^{ss} of functional units within the stress fibres is given by

$$\hat{n}^{ss} \equiv \frac{n^{ss}}{n^R} = \frac{[1 + \varepsilon_{\text{nom}}(x_i, \varphi)]}{1 + \tilde{\varepsilon}_{\text{nom}}^{ss}}, \quad (3.A5)$$

where $\tilde{\varepsilon}_{\text{nom}}^{ss}$ is the strain at steady-state within a functional unit of the stress fibres, and $\varepsilon_{\text{nom}}(x_i, \varphi)$ is the nominal strain in direction φ . The chemical potential of the functional units within the stress fibres in terms of the Boltzmann constant k_B is given by

$$\chi_b = \frac{\mu_b}{n^R} + k_B T \ln \left[\left(\frac{\pi \hat{\eta} \hat{n}^{ss}}{\hat{N}_u \left(1 - \frac{\hat{\eta}}{\hat{\eta}_{\text{max}}}\right)} \right)^{\frac{1}{n^{ss}}} \left(\frac{\hat{N}_u}{\pi \hat{N}_L} \right) \right], \quad (3.A6)$$

where the normalized concentration of the unbound stress fibre proteins is $\hat{N}_u \equiv N_u / N_0$ with $\hat{\eta} \equiv \eta n^R / N_0$, while $\hat{\eta}_{\text{max}}$ is the maximum normalised value of $\hat{\eta}$ corresponding to full occupancy of all available sites for stress fibres (in a specific direction). Here, \hat{N}_L is the number of lattice sites available to unbound proteins. The enthalpy μ_b of n^R bound

functional units at steady-state is given in terms of the isometric stress fibre stress σ_{\max} and the internal energy μ_{b0} as

$$\mu_b = \mu_{b0} - \sigma_{\max} \Omega (1 + \tilde{\varepsilon}_{\text{nom}}^{\text{SS}}), \quad (3.A7)$$

where Ω is the volume of n^{R} functional units. By contrast, the chemical potential of the unbound proteins is independent of stress and given in terms of the internal energy μ_u as

$$\chi_u = \frac{\mu_u}{n^{\text{R}}} + k_B T \ln \left(\frac{\hat{N}_u}{\pi \hat{N}_L} \right). \quad (3.A8)$$

For a fixed configuration of the 2D cell (i.e. a fixed strain distribution $\varepsilon_{\text{nom}}(x_i, \varphi)$), the contribution to the specific Helmholtz free-energy of the cell f from the stress fibre cytoskeleton follows as

$$f_{\text{cyto}} = \rho_0 \left(\hat{N}_u \chi_u + \int_{-\frac{\pi}{2}}^{\frac{\pi}{2}} \hat{\eta} \hat{n}^{\text{SS}} \chi_b d\varphi \right), \quad (3.A9)$$

where $\rho_0 \equiv N_0/V_{\text{R}}$ is the number of protein packets per unit reference volume available to form functional units in the cell. However, we cannot yet evaluate f_{cyto} as $\hat{N}_u(x_i)$ and $\hat{\eta}(x_i, \varphi)$ are unknown. These will follow from the chemical equilibrium of the cell as will be discussed in Section 3.A.2.1.

The total stress Σ_{ij} within the cell includes contributions from the passive elasticity provided mainly by the intermediate filaments of the cytoskeleton attached to the nuclear and plasma membranes and the microtubules, as well as the active contractile stresses of the stress fibres. The total Cauchy stress is written in an additive decomposition as

$$\Sigma_{ij} = \sigma_{ij} + \sigma_{ij}^{\text{p}}, \quad (3.A10)$$

where σ_{ij} and σ_{ij}^{p} are the active and passive Cauchy stresses, respectively. In the 2D setting with the cell lying in the $x_1 - x_2$ plane, the active stress is given in terms of the volume fraction v_0 of the stress fibre proteins as

$$\begin{bmatrix} \sigma_{11} & \sigma_{12} \\ \sigma_{12} & \sigma_{22} \end{bmatrix} = \frac{\nu_0 \sigma_{\max}}{2} \int_{-\frac{\pi}{2}}^{\frac{\pi}{2}} \hat{\eta} [1 + \varepsilon_{\text{nom}}(\varphi)] \begin{bmatrix} 2\cos^2 \varphi^* & \cos 2\varphi^* \\ \cos 2\varphi^* & 2\sin^2 \varphi^* \end{bmatrix} d\varphi, \quad (3.A11)$$

where φ^* is the angle of the stress fibre measured with respect to x_2 , and is related to its orientation φ in the undeformed configuration by the rotation with respect to the undeformed configuration. The passive elasticity in the 2D setting is given by a 2D specialization of the Ogden (Ogden 1972) hyperelastic model as derived in (Shishvan, Vigliotti, and Deshpande 2018). The strain energy density function of this 2D Ogden model is

$$\Phi_C \equiv \frac{2\mu_C}{m_C^2} \left[\left(\frac{\lambda_I}{\lambda_{II}} \right)^{\frac{m_C}{2}} + \left(\frac{\lambda_{II}}{\lambda_I} \right)^{\frac{m_C}{2}} - 2 \right] + \frac{\kappa_C}{2} (\lambda_I \lambda_{II} - 1)^2, \quad (3.A12)$$

for the cytoplasm and

$$\Phi_N \equiv \frac{2\mu_N}{m_N^2} \left[\left(\frac{\lambda_I}{\lambda_{II}} \right)^{\frac{m_N}{2}} + \left(\frac{\lambda_{II}}{\lambda_I} \right)^{\frac{m_N}{2}} - 2 \right] + \frac{\kappa_N}{2} (\lambda_I \lambda_{II} - 1)^2, \quad (3.A13)$$

for the nucleus where λ_I and λ_{II} are the principal stretches, μ_C (μ_N) and κ_C (κ_N) the shear modulus and in-plane bulk modulus of cytoplasm (nucleus), respectively, while m_C (m_N) is a material constant governing the non-linearity of the deviatoric elastic response of cytoplasm (nucleus). The cell is assumed to be incompressible, and thus throughout the cell, we set the principal stretch in the x_3 –direction $\lambda_{III} = 1/(\lambda_I \lambda_{II})$. The (passive) Cauchy stress then follows as $\sigma_{ij}^p p_j^{(k)} = \sigma_k^p p_i^{(k)}$ in terms of the principal (passive) Cauchy stresses σ_k^p ($\equiv \lambda_k \partial \Phi_C / \partial \lambda_k$ for the cytoplasm and $\equiv \lambda_k \partial \Phi_N / \partial \lambda_k$ for the nucleus) and the unit vectors $p_j^{(k)}$ ($k = I, II$) denoting the principal directions. The total specific Helmholtz free-energy of the cell is then $f = f_{\text{cyto}} + \Phi_C + \Phi_N$.

3.A.2.1. Equilibrium of the morphological microstate

Shishvan *et al.* have shown that equilibrium of a morphological microstate reduces to two conditions: (i) mechanical equilibrium with $\Sigma_{ij,j} = 0$ throughout the system, and (ii) chemical equilibrium such that $\chi_u(x_i) = \chi_b(x_i, \varphi) = \text{constant}$, i.e. the chemical potentials of bound and unbound stress fibre proteins are equal throughout the cell. The condition $\chi_u = \chi_b$ implies that $\hat{\eta}(x_i, \varphi)$ is given in terms of \hat{N}_u by

$$\hat{\eta}(x_i, \varphi) = \frac{\hat{N}_u \hat{\eta}_{\max} \exp\left[\frac{\hat{\eta}^{ss}(\mu_u - \mu_b)}{k_B T}\right]}{\pi \hat{\eta}^{ss} \hat{\eta}_{\max} + \hat{N}_u \exp\left[\frac{\hat{\eta}^{ss}(\mu_u - \mu_b)}{k_B T}\right]}, \quad (3.A14)$$

and \hat{N}_u follows from the conservation of stress fibre proteins throughout the cytoplasm, viz.

$$\hat{N}_u + \frac{1}{V_C} \int_{V_C} \int_{-\frac{\pi}{2}}^{\frac{\pi}{2}} \hat{\eta} \hat{\eta}^{ss} d\varphi dV = 1. \quad (3.A15)$$

Knowing \hat{N}_u and $\hat{\eta}(x_i, \varphi)$, the stress Σ_{ij} can now be evaluated and these stresses within the system (i.e. cell and substrate) need to satisfy mechanical equilibrium, i.e. $\Sigma_{ij,j} = 0$. In this case, the mechanical equilibrium condition is readily satisfied as the stress field Σ_{ij} within the cell is equilibrated by a traction field T_i exerted by the substrate on the cell such that $b\Sigma_{ij,j} = -T_i$, where $b(x_i)$ is the thickness of the cell in the current configuration. The substrate energy F_{sub} is calculated by applying these tractions to a linear elastic half-space as described in Shishvan *et al.*

The equilibrium value of \mathcal{G} denoted by G is then given as $G = F_{\text{cell}}$ where

$$F_{\text{cell}} \equiv \rho_0 V_C \chi_u + \int_{V_C} \Phi_C dV + \int_{V_N} \Phi_N dV + F_{\text{adh}}. \quad (3.A16)$$

Here, χ_u is given by equation 3.A8 with the equilibrium value of \widehat{N}_u obtained from equation 3.A15. For the purposes of further discussion, we label the equilibrium value $F_{\text{cyto}} \equiv \rho_0 V_C \chi_u$ as the cytoskeletal free-energy of the cell, and $F_{\text{passive}} \equiv \int_{V_C} \Phi_C dV + \int_{V_N} \Phi_N dV$ as the passive elastic energy of the cell.

3.A.2.2. Numerical methods

We employ Markov Chain Monte Carlo (MCMC) to construct a Markov chain that is representative of the homeostatic ensemble. This involves three steps: (i) a discretization scheme to represent morphological microstate (j), (ii) calculation of $G^{(j)}$ for a given morphological microstate (j), and (iii) construction of a Markov chain comprising these morphological microstates. Here, we briefly describe the procedure which was implemented in MATLAB with readers referred to Shishvan *et al.* (2018) for further details.

In the general setting of a three-dimensional (3D) cell, a morphological microstate is defined by the connection of material points on the cell membrane to the surface of the substrate. In the 2D context of cells on micropatterned substrates, this reduces to specifying the connection of all material points of the cell to locations within the collagen coated substrate, i.e. a displacement field $u_i^{(j)}(X_i)$ is imposed on the cell with X_i denoting the location of material points on the cell in the undeformed configuration, and these are then displaced to $x_i^{(j)} = X_i + u_i^{(j)}$ in morphological microstate (j). These material points located at $x_i^{(j)}$ are then connected to material points on the substrate at the same location $x_i^{(j)}$, completing the definition of the morphological microstate in the 2D setting.

The cell is modelled as a continuum and thus $u_i^{(j)}$ is a continuous field. To calculate the density of the morphological microstates, we define $u_i^{(j)}$ via Non-Uniform Rational B-splines (NURBS) such that the morphological microstate is now defined by M pairs of

weights $[U_L^{(j)}, V_L^{(j)}]$ ($L = 1, \dots, M$). In all the numerical results presented here, we employ $M = 16$ with 4×4 weights $U_L^{(j)}$ and $V_L^{(j)}$ governing the displacements in the x_1 and x_2 directions, respectively. The NURBS employ fourth order base functions for both the x_1 and x_2 directions, and the knots vector included two nodes each with multiplicity four, located at the extrema of the interval. We emphasise here that this choice of representing the morphological microstates imposes restrictions on the morphological microstates that will be considered. Therefore, the choice of the discretization used to represent $u_i^{(j)}$ needs to be chosen so as to be able to represent the microstates we wish to sample, e.g. the choice can be based on the minimum width of a filopodium one expects for the given cell type. Given $u_i^{(j)}$, we can calculate $G^{(j)}$ using the model described in Section 3.2.2 with the cell discretised using constant strain triangles of size $e \approx R_0/10$, where R_0 is the radius of the cell in its undeformed configuration.

We construct, via MCMC, a Markov chain that serves as a sample of the homeostatic ensemble for cells on collagen coated substrates. The algorithm follows the approach developed by Shishvan *et al.* (2018) (see *section 4.3* therein), using the Metropolis (Metropolis *et al.* 1953) algorithm in an iterative manner. Typical Markov chains comprised in excess of 2.5 million samples.

3.A.2.3. Material parameters

All simulations are reported at a reference thermodynamic temperature $T = T_0$, where $T_0 = 310$ K. Most of the parameters of the model are related to the properties of the proteins that constitute stress fibres. These parameters are thus expected to be independent of cell type. Notable exceptions to this are: (i) the stress fibre protein volume fraction v_0 ; and (ii) the passive elastic properties. Here, we use parameters calibrated for smooth muscle cells that give good correspondence with the wide range of measurements reported here. The passive elastic parameters of the cytoplasm are taken to be $\mu_C =$

1.67 kPa, $\kappa_C = 35$ kPa and $m_C = 5$, while the corresponding values for the nucleus are $\mu_N = 3.33$ kPa, $\kappa_N = 35$ kPa and $m_N = 20$ (Ronan *et al.* 2012; Dowling *et al.* 2012; Dowling and McGarry 2014). The maximum contractile stress $\sigma_{\max} = 240$ kPa is consistent with a wide range of measurements on muscle fibres (Lucas *et al.* 1987), and the density of stress fibre proteins was taken as $\rho_0 = 3 \times 10^6 \mu\text{m}^{-3}$ with the volume fraction of stress fibre proteins $v_0 = 0.032$. Following Vigliotti *et al.*, we assume that the steady-state functional unit strain $\tilde{\epsilon}_{\text{nom}}^{\text{ss}} = 0.35$ with $\mu_{b_0} - \mu_u = 2.3 kT_0$ and $\Omega = 10^{-7.1} \mu\text{m}^3$. The maximum angular concentration of stress fibre proteins is set to $\hat{\eta}_{\max} = 1$. The cell in its undeformed state is a circle of radius R_0 and thickness $b_0 = 0.05R_0$, with a circular nucleus of radius $R_N = 10b_0$ whose centre coincides with that of the cell. Results are presented in terms of normalised cell area $\hat{A}^{(j)} \equiv A^{(j)}/A_0$, where $A^{(j)}$ is the area of a morphological microstate (j) while $A_0 = \pi R_0^2$ is the area of the undeformed cell. Thus, we do not explicitly need to specify R_0 .

Results are presented for adhesion to incompressible linear elastic substrates with Young's modulus $E_{\text{sub}} = 8$ kPa, 32 kPa and a rigid substrate with $E_{\text{sub}} \rightarrow \infty$ coated with surface densities of collagen ranging between 6 ng cm^{-2} to 665 ng cm^{-2} . Using a molecular weight of collagen, M_{col} , to be 200 kDa (Raj *et al.* 1979) (i.e. 200 kg mol^{-1}) with 1 ligand per molecule, a surface collagen density ρ_{col} of 1 g/cm^2 corresponds to $3.011 \times 10^9 \text{ ligands/cm}^2$. A range of ligand densities from $N_H = 175 \mu\text{m}^{-2}$ to $N_H = 20 \times 10^3 \mu\text{m}^{-2}$ are analysed, corresponding to the range of ρ_{col} investigated in the experiments of Engler *et al.* (2003). The other parameters of the focal adhesion model are based on commonly accepted ranges; see for example Deshpande *et al.* (2008). Specifically, we assumed a uniform surface density of $C_0 = 5 \times 10^3 \mu\text{m}^{-2}$ of integrin molecules with surface density of integrins sites $C_r = 20 \times 10^3 \mu\text{m}^{-2}$. The complex

stiffness $\kappa_S = \kappa_p = 0.3 \text{ nN } \mu\text{m}^{-1}$ while the maximum complex force $F_{max} = 0.01 \text{ nN}$ (Kong *et al.* 2009).

3.A.2.4. Definitions of normalised quantities and observables

Following Shishvan *et al.* (2018), the free-energy $G^{(j)}$ can be decomposed as $G^{(j)} = Y^{(j)} + Y_0$, where $Y_0 = \rho_0 V_0 [\mu_u / n^R - kT \ln(\pi \hat{N}_L)]$ is independent of the morphological microstate. It is thus natural to subtract out Y_0 and define a normalised free-energy as

$$\hat{G}^{(j)} \equiv \frac{Y^{(j)}}{|G_S - Y_0|} = \frac{G^{(j)} - Y_0}{|G_S - Y_0|}, \quad (3.A17)$$

where G_S is the equilibrium free-energy of a free-standing cell (i.e. a cell in suspension with traction-free surfaces). Then, the distribution given by equation 3.A6 can be rewritten as

$$P_{eq}^{(j)} = \frac{1}{\hat{Z}} \exp[-\hat{\zeta} \hat{G}^{(j)}], \quad (3.A18)$$

with $\hat{Z} \equiv \sum_j \exp[-\hat{\zeta} \hat{G}^{(j)}]$ and $\hat{\zeta} \equiv \zeta |G_S - Y_0|$. It then immediately follows that the distributions of states are not influenced by the values of n^R , \hat{N}_L and V_0 and these parameters need not be specified so long as energies are quoted in terms of the normalised energies $\hat{G}^{(j)}$. Analogously, we define the normalised elastic, cytoskeletal, adhesion, and substrate free-energies of the spread microstate (j) as

$$\hat{F}_{passive}^{(j)} \equiv \frac{F_{passive}^{(j)}}{|G_S - Y_0|}, \quad \hat{F}_{cyto}^{(j)} \equiv \frac{F_{cyto}^{(j)} - Y_0}{|G_S - Y_0|} \quad (3.A19)$$

And

$$\hat{F}_{sub}^{(j)} \equiv \frac{F_{sub}^{(j)}}{|G_S|}, \quad \hat{F}_{adh}^{(j)} \equiv \frac{F_{adh}^{(j)}}{|G_S - Y_0|}, \quad (3.A20)$$

respectively.

Bibliography

- Arnold, Marco, Elisabetta Ada Cavalcanti-Adam, Roman Glass, Jacques Blümmel, Wolfgang Eck, Martin Kantlehner, Horst Kessler, and Joachim P. Spatz. 2004. "Activation of Integrin Function by Nanopatterned Adhesive Interfaces." *ChemPhysChem* 5 (3): 383–88. doi:10.1002/cphc.200301014.
- Chow, Ming Jay, Rapha??l Turcotte, Charles P. Lin, and Yanhang Zhang. 2014. "Arterial Extracellular Matrix: A Mechanobiological Study of the Contributions and Interactions of Elastin and Collagen." *Biophysical Journal* 106 (12): 2684–92. doi:10.1016/j.bpj.2014.05.014.
- Deroanne, C, Charles M. Lapiere, and Betty V. Nusgens. 2001. "In Vitro Tubulogenesis of Endothelial Cells by Relaxation of the Coupling Extracellular Matrix-Cytoskeleton." *Cardiovascular Research* 49 (3). Oxford University Press: 647–58. doi:10.1016/S0008-6363(00)00233-9.
- Deshpande, Vikram S., Milan Mrksich, Robert M. McMeeking, and Anthony G. Evans. 2008. "A Bio-Mechanical Model for Coupling Cell Contractility with Focal Adhesion Formation." *Journal of the Mechanics and Physics of Solids* 56 (4): 1484–1510. doi:10.1016/j.jmps.2007.08.006.
- Dowling, Enda P., and J. Patrick McGarry. 2014. "Influence of Spreading and Contractility on Cell Detachment." *Annals of Biomedical Engineering* 42 (5): 1037–48. doi:10.1007/s10439-013-0965-5.
- Dowling, Enda P, William Ronan, Gidon Ofek, Vikram S Deshpande, Robert M McMeeking, Kyriacos a Athanasiou, and J Patrick McGarry. 2012. "The Effect of Remodelling and Contractility of the Actin Cytoskeleton on the Shear Resistance of Single Cells: A Computational and Experimental Investigation." *Journal of the Royal Society, Interface / the Royal Society* 9 (77): 3469–79. doi:10.1098/rsif.2012.0428.
- Engler, A., M. Sheehan, H. L. Sweeney, and D. E. Discher. 2003. "Substrate Compliance vs Ligand Density in Cell on Gel Responses." *European Cells and Materials* 6 (SUPPL. 1). Elsevier: 7–8. doi:10.1016/S0006-3495(04)74140-5.
- Gaudet, Christianne, William a Marganski, Sooyoung Kim, Christopher T Brown, Vaibhavi Gunderia, Micah Dembo, and Joyce Y Wong. 2003. "Influence of Type I Collagen Surface Density on Fibroblast Spreading, Motility, and Contractility." *Biophysical Journal* 85 (5). Elsevier: 3329–35. doi:10.1016/S0006-3495(03)74752-3.
- Jacot, JG, AD McCulloch, and JH Omens. 2008. "Substrate Stiffness Affects the Functional Maturation of Neonatal Rat Ventricular Myocytes." *Biophysical Journal*. <http://www.sciencedirect.com/science/article/pii/S000634950878490X>.
- Jaynes, E. T. 1957. "Information Theory and Statistical Mechanics." *Physical Review* 106 (4). American Physical Society: 620–30. doi:10.1103/PhysRev.106.620.
- Kong, Fang, Andrés J García, A Paul Mould, Martin J Humphries, and Cheng Zhu. 2009. "Demonstration of Catch Bonds between an Integrin and Its Ligand." *The Journal of Cell Biology* 185 (7). Rockefeller University Press: 1275–84. doi:10.1083/jcb.200810002.
- Lange, Leslie A, Donald W Bowden, Carl D Langefeld, Lynne E Wagenknecht, J Jeffrey Carr, Stephen S Rich, Ward A Riley, Barry I Freedman, B.A. Oostra, and C.M. van Duijn. 2002. "Heritability of Carotid Artery Intima-Medial Thickness in Type 2

- Diabetes.” *Stroke* 33 (7). American Heart Association, Inc.: 1876–81. doi:10.1161/01.str.0000019909.71547.aa.
- Lucas, S M, R L Ruff, and M D Binder. 1987. “Specific Tension Measurements in Single Soleus and Medial Gastrocnemius Muscle Fibers of the Cat.” *Experimental Neurology* 95 (1): 142–54. <http://www.ncbi.nlm.nih.gov/pubmed/2947808>.
- McEvoy, E., V.S. Deshpande, and P. McGarry. 2017. “Free Energy Analysis of Cell Spreading.” *Journal of the Mechanical Behavior of Biomedical Materials* 74. doi:10.1016/j.jmbbm.2017.06.006.
- McGarry, J. P., and P. E. McHugh. 2008. “Modelling of in Vitro Chondrocyte Detachment.” *Journal of the Mechanics and Physics of Solids* 56 (4): 1554–65. doi:10.1016/j.jmps.2007.08.001.
- Metropolis, Nicholas, Arianna W. Rosenbluth, Marshall N. Rosenbluth, Augusta H. Teller, and Edward Teller. 1953. “Equation of State Calculations by Fast Computing Machines.” *The Journal of Chemical Physics* 21 (6). American Institute of Physics: 1087–92. doi:10.1063/1.1699114.
- Ogden, R. W. 1972. “Large Deformation Isotropic Elasticity - On the Correlation of Theory and Experiment for Incompressible Rubberlike Solids.” *Proceedings of the Royal Society A: Mathematical, Physical and Engineering Sciences* 326 (1567). The Royal Society: 565–84. doi:10.1098/rspa.1972.0026.
- Pelham, Robert J., and Yu-Li Wang. 2018. “Cell Locomotion and Focal Adhesions Are Regulated by Substrate Flexibility.” *Proceedings of the National Academy of Sciences of the United States of America*. National Academy of Sciences. Accessed January 18. doi:10.2307/43789.
- Prager-Khoutorsky, Masha, Alexandra Lichtenstein, Ramaswamy Krishnan, Kavitha Rajendran, Avi Mayo, Zvi Kam, Benjamin Geiger, and Alexander D. Bershadsky. 2011. “Fibroblast Polarization Is a Matrix-Rigidity-Dependent Process Controlled by Focal Adhesion Mechanosensing.” *Nature Cell Biology* 13 (12). Nature Publishing Group: 1457–65. doi:10.1038/ncb2370.
- Raj, C V, I L Freeman, R L Church, and S I Brown. 1979. “Biochemical Characterization of Procollagen-Collagen Synthesized by Rabbit Corneal Endothelial Cells in Culture.” *Investigative Ophthalmology & Visual Science* 18 (1): 75–84. <http://www.ncbi.nlm.nih.gov/pubmed/759387>.
- Ren, Kefeng, Laure Fourel, Cécile Gauthier Rouvière, Corinne Albiges-Rizo, and Catherine Picart. 2010. “Manipulation of the Adhesive Behaviour of Skeletal Muscle Cells on Soft and Stiff Polyelectrolyte Multilayers.” *Acta Biomaterialia* 6 (11). Elsevier: 4238–48. doi:10.1016/J.ACTBIO.2010.06.014.
- Reynolds, Noel H., W. Ronan, Enda P. Dowling, P. Owens, Robert M. McMeeking, and J. Patrick McGarry. 2014. “On the Role of the Actin Cytoskeleton and Nucleus in the Biomechanical Response of Spread Cells.” *Biomaterials* 35 (13). Elsevier Ltd: 4015–25. doi:10.1016/j.biomaterials.2014.01.056.
- Ronan, William, Vikram S. Deshpande, Robert M. McMeeking, and J. Patrick McGarry. 2012. “Numerical Investigation of the Active Role of the Actin Cytoskeleton in the Compression Resistance of Cells.” *Journal of the Mechanical Behavior of Biomedical Materials* 14. Elsevier: 143–57. doi:10.1016/j.jmbbm.2012.05.016.
- Selhuber-Unkel, C., T. Erdmann, M. López-García, H. Kessler, U.S. Schwarz, and J.P. Spatz. 2010. “Cell Adhesion Strength Is Controlled by Intermolecular Spacing of

-
- Adhesion Receptors.” *Biophysical Journal* 98 (4). Cell Press: 543–51. doi:10.1016/J.BPJ.2009.11.001.
- Shishvan, S. S., A. Vigliotti, and V. S. Deshpande. 2018. “The Homeostatic Ensemble for Cells.” *Biomechanics and Modeling in Mechanobiology*, July. Springer Berlin Heidelberg, 1–32. doi:10.1007/s10237-018-1048-1.
- Théry, Manuel, Anne Pépin, Emilie Dressaire, Yong Chen, and Michel Bornens. 2006. “Cell Distribution of Stress Fibres in Response to the Geometry of the Adhesive Environment.” *Cell Motility and the Cytoskeleton* 63 (6): 341–55. doi:10.1002/cm.20126.
- Vigliotti, A., W. Ronan, F. P. T. Baaijens, and V. S. Deshpande. 2015. “A Thermodynamically Motivated Model for Stress-Fiber Reorganization.” *Biomechanics and Modeling in Mechanobiology*. Springer Berlin Heidelberg. doi:10.1007/s10237-015-0722-9.
- Weafer, P. P., W. Ronan, S. P. Jarvis, and J. P. McGarry. 2013. “Experimental and Computational Investigation of the Role of Stress Fiber Contractility in the Resistance of Osteoblasts to Compression.” *Bulletin of Mathematical Biology* 75 (8): 1284–1303. doi:10.1007/s11538-013-9812-y.

CHAPTER 4

TRANSIENT ACTIVE FORCE GENERATION AND STRESS FIBRE REMODELLING IN CELLS UNDER CYCLIC LOADING



4.1. Introduction

Many non-muscle cells in the body, such as fibroblasts in the heart wall, are subject to continuous dynamic mechanical loading. In the characterization of cell behaviour, several *in-vitro* studies have investigated the response of the cellular cytoskeleton to cyclic deformation. Hara *et al.* (2001) show that dynamic tensile stretching of cells promotes stress fibre (SF) development. A study by Weafer *et al.* (2015) reveals the importance of the actin cytoskeleton in the resistance of osteoblasts to cyclic compression and stretching. More frequently, cells are seeded in 3D gels and subjected to an applied deformation (Foolen *et al.* 2012; Balestrini and Billiar 2009). SFs have been shown to align in the constrained direction, with the alignment maintained during cyclic stretch (Nieponice *et al.* 2007). Wille *et al.* (2006) subjected fibroblast-populated collagen scaffolds to dynamic loading, and revealed a complex dependence of cell force on applied strain rate and magnitude.

Similar to skeletal muscle, active contractility in non-muscle cells is generated via cross-bridge cycling between myosin motor proteins and actin filaments. Active force generation has been extensively studied for muscle. The experimental investigations of A. V. Hill (1938) uncovered the force-velocity relationship for skeletal muscle, whereby an increase in actively generated force results in a decrease in shortening velocity. The sliding filament theory (Huxley 1957) provides key insight into the molecular mechanisms underlying such behaviour through the development of a 2-state model to describe binding of myosin heads to actin filaments. Time-dependent changes in tension in response to small ($\sim 5\text{nm}$) step changes in length were observed in the experiments of (Huxley and Simmons 1971). T. L. Hill (1974) formalised the Huxley sliding filament theory by relating the strain dependence of the equilibrium constants to the difference in standard Gibbs energies of multiple states in a cross-bridge cycle. Smith and Geeves (1995) expanded this framework to include a strain-blocking of ADP release mechanism. The model has subsequently been adapted to investigate the myosin stroking pathways associated with the transient tension response to small length step changes (Offer and Ranatunga 2013). A series of experiments on the response of cardiac muscle provided motivation for the empirically based fading memory contractility model for the transient response of cardiac muscle to a range of applied loading regimes, including step changes in length, isotonic shortening, and sinusoidal perturbations in length (Hunter *et al.* 1998). In contrast to skeletal and cardiac muscle, models for active processes in non-muscle cells have not evolved until recent decades. A number of phenomenological models have been developed to describe formation/dissociation of cytoskeletal SFs (Deshpande *et al.* 2007; Vernerey and Farsad 2011; Obbink-Huizer *et al.* 2014; Kaunas *et al.* 2010). Vigliotti *et al.* (2015) developed a thermodynamically consistent framework to describe the stress, strain, and strain-rate dependence of SF formation and remodelling. A steady state implementation of this thermodynamically motivated framework, coupled with an active

thermodynamically consistent focal adhesion assembly accurately predicts cell cytoskeletal distributions on micro-patterned substrates (McEvoy *et al.* 2017). All of these cell mechanics formulations use a phenomenological Hill type stress-strain rate relationship to represent active contractility of SFs. Such a modelling approach provides very good agreement with experimental data for cells subjected to static or monotonic loading conditions. For example, active and passive cell forces were accurately predicted for shear deformation (Dowling *et al.* 2012; Dowling and McGarry 2014) and compression (Weafer *et al.* 2013). Also, cell force generation when seeded on micro-pillar substrates has been predicted (Vernerey and Farsad 2011; McGarry *et al.* 2009). However, the accurate prediction of transient force generation during dynamic cell deformation is not possible in the aforementioned cell models due to the use of the Hill contractility law, which is based upon experimental observations for monotonically shortening contractile muscle. The experimental study of Weafer *et al.* (2015) demonstrates that a single cell subjected to dynamic loading exhibits a highly transient pattern of force generation within each loading cycle. A computational analysis of such dynamic loading regimes by Reynolds and McGarry (2015) confirms that a Hill-type model does not capture such transient force generation, and a modified fading memory model is shown to predict the transient force-deformation relationship. However, such an empirically motivated fading memory formulation provides limited insight into the biomechanics of actin-myosin interactions that underlie active transient stress generation. In this paper, we propose a new thermodynamically motivated cross-bridge cycling framework that describes actin-myosin interactions in cell SFs under dynamic loading regimes. We incorporate this cross-bridge model into a thermodynamically consistent framework for SF formation/dissociation (Vigliotti *et al.*, 2015). This combined framework is shown to accurately predict complex patterns of active cell force generation under dynamic loading reported in the experimental investigation of Wille *et al.* (2006).

We demonstrate that coupling between transient force generation and SF remodelling plays a critical role in the response of cells to dynamic loading and we provide a thermodynamic explanation for fading memory effects observed in dynamic active cell force generation.

4.2. Model development

4.2.1. Cross-bridge modelling

SFs in a cell are comprised of individual actin-myosin sarcomeric structures, which actively generate tension via cross-bridge cycling. A typical cross-bridge cycle operates as follows (Lymn and Taylor 1971): Following attachment of ATP to the myosin head, and hydrolysis into ADP and inorganic phosphate, the configuration of the myosin head is changed such that the head is cocked (or primed). The myosin head binds to the actin filament and, under isometric conditions, a power stroke will occur (see Figure 4.1 - isometric). The stroke consists of the myosin head returning to an uncocked (unprimed) configuration, which stretches the myosin tail thereby developing tension in the system. The bond between the myosin head and actin filament then dissociates, and the head detaches. Chemical equilibrium favours a high ADP concentration (Alberts *et al.* 2002). However, the cell maintains ATP in excessive abundance (such that it is not a rate limiting factor in the cross-bridge cycle). As concentrations of ATP and ADP are very far from thermodynamic equilibrium, ATP spontaneously binds to myosin (which acts as a catalyst), and forms ADP and inorganic phosphate. Thus it is assumed that unattached myosin predominantly exists in a primed state. It is worth noting a key difference between cytoskeletal SFs and skeletal muscle myofibrils. In muscle cells, myosin attachment in the myofibril is inhibited by a troponin-tropomyosin complex which blocks the actin binding site. An action potential typically triggers release of calcium, which subsequently binds to troponin and unblocks the actin binding site (Greaser and Gergely, 1971). In

contrast, SFs do not contain troponin (Smith and Marston, 1985) and the role of tropomyosin in dynamic SF contractility is not well understood. Therefore, such interactions are not considered in the current framework.

Tension is assumed to develop primarily in the myosin tail, with the strain energy given by

$$\phi_m = \frac{1}{2} \kappa_m \Delta_m^2, \quad (4.1)$$

where κ_m is the tail stiffness (pN/nm), and Δ_m is the myosin tail extension. The progression of a cross-bridge cycle depends on the local loading conditions. Under isometric conditions (when the sarcomere strain rate $\dot{\epsilon}_n = 0$), the cycle will proceed as outlined in the previous paragraph (i.e. Figure 4.1 - isometric), with the strain energy in the myosin tail depending only on the stroke distance l_s (i.e. $\Delta_m = l_s$). Following a stroke, the head will remain attached for a period of time t_s . If a sarcomere shortens ($\dot{\epsilon}_n < 0$), as a result of external loading and/or the contractile effort of cross-bridge cycling, displacement of the actin binding site relative to the myosin filament will reduce the tail extension (Figure 4.1- shortening). With increasing shortening velocity, a greater reduction in the tail extension will occur during a single cross-bridge cycle. The mean extension offset Δ_m^s for a given (negative) sarcomere strain rate $\dot{\epsilon}_n$ follows as

$$\Delta_m^s = L_{sarc} \dot{\epsilon}_n t_s, \quad (4.2)$$

where L_{sarc} is the length of a half sarcomere. In such a case, the tail extension is a function of the stroke distance and the negative offset, with $\Delta_m = l_s + \Delta_m^s$. It has been shown that when the sarcomere is being stretched ($\dot{\epsilon}_n > 0$) ATPase activity is not observed (Curtin and Davies 1975), and tension increases. This indicates that stroking does not occur under such conditions. The head remains in a primed configuration, and the force generated is due to tail extension induced by a passive displacement (Δ_m^l) of the

bound myosin head, whereby $\Delta_m^l = L_{sarc} \tilde{\epsilon}_n$ (Figure 4.1-lengthening). During such a stretch, the energy in the actin-myosin bond may reach critical point (at Δ_m^{l-max}) beyond which it will dissociate. The detached myosin head, which remains in a primed configuration, can reattach to an actin binding site. Over a large population of attaching myosin heads in a stress fibre subjected to lengthening conditions, this process can be viewed as slipping-type behaviour such that if $\Delta_m^l \geq \Delta_m^{l-max}$, $\Delta_m = \Delta_m^{l-max}$.

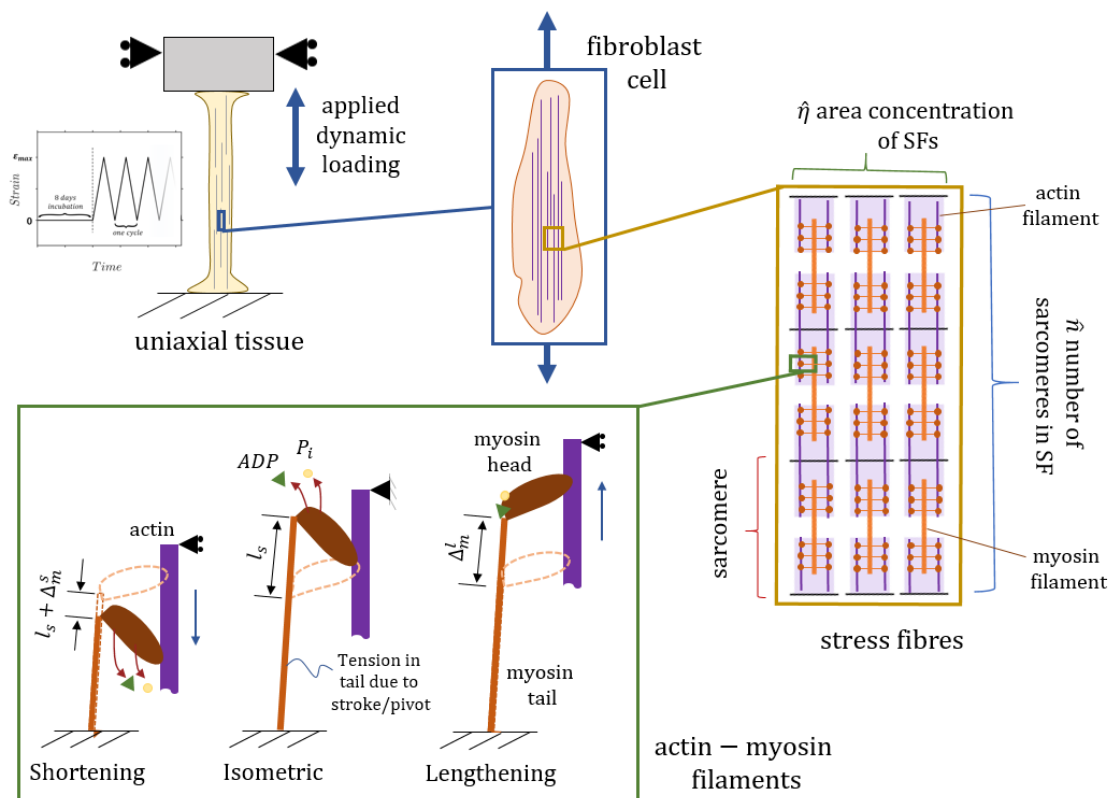


Figure 4.1: Schematic linking the scales: applied tissue loading drives SF and cross-bridge remodelling. At the actin-myosin filament level (green box), the tension that develops in the myosin tail depends on external loading and the contractile effort of cross-bridge cycling.

Of the total number of available myosin heads within a sarcomere, m_{tot} , a certain number of myosin heads are attached and cycling. We consider a 2-state model to account for the number of attached heads, as motivated by Huxley (1957). The rate of myosin binding is given by:

$$\frac{d\hat{m}_a}{dt} = -k_d\hat{m}_a + k_a\hat{m}_d, \quad (4.3)$$

where $\hat{m}_a = m_a/m_{tot}$ is the (normalised) number of attached myosin heads, $\hat{m}_d = \hat{m}_{tot} - \hat{m}_a$ is the (normalised) number of detached heads, and k_d and k_a are rate coefficients. The rate coefficients are derived from steady state equilibrium, i.e. $d\hat{m}_a/dt = 0$, giving

$$\frac{\hat{m}_a}{\hat{m}_d} = \frac{k_a}{k_d}. \quad (4.4)$$

We propose a thermodynamically motivated model to determine the rate coefficient k_a .

The chemical potential of the unattached heads is given as:

$$\chi_d = \mu_d + k_B T \ln(\hat{m}_d), \quad (4.5)$$

where μ_d is the enthalpy of the unattached heads, k_B is the Boltzmann constant, and T is the absolute temperature. The chemical potential of the attached heads is given as:

$$\chi_a = \mu_a + k_B T \ln(\hat{m}_a) + \phi_m - F\Delta_m, \quad (4.6)$$

where μ_a is the enthalpy of the attached heads, ϕ_m is the stored elastic energy (equation 4.1), and $F\Delta_m$ is the mechanical work performed by attached heads (where $F = \delta\phi_m/\delta\Delta_m$). At thermodynamic equilibrium the chemical potential of the attached and unattached heads is equal, i.e. $\chi_d = \chi_a$, giving

$$\ln\left(\frac{\hat{m}_a}{\hat{m}_d}\right) = \frac{\mu_d - \mu_a - \phi_m + F\Delta_m}{k_B T}. \quad (4.7)$$

Substituting equation 4.4, we obtain

$$k_a = k_d \exp\left(\frac{\mu_d - \mu_a - \phi_m + F\Delta_m}{k_B T}\right). \quad (4.8)$$

The influence of the enthalpies (μ_a and μ_d) and k_d on the rate and level of myosin binding under isometric conditions is shown in Figure 4.2. The total number of myosin

heads available for binding m_{tot} depends on the overlap s between the actin and myosin filaments, with the availability being a maximum at the optimum overlap s_0 . Motivated by data for muscle fibres (McMahon 1984), we propose a functional form for the overlap as a Cauchy-type distribution:

$$\hat{s} = \frac{1}{\varepsilon_s \pi \left(1 + \left(\frac{\tilde{\varepsilon}_n - \tilde{\varepsilon}_{ss}}{\varepsilon_s} \right)^2 \right)} s_0, \quad (4.9)$$

where $\tilde{\varepsilon}_n$ is the internal nominal strain of a sarcomere, $\tilde{\varepsilon}_{ss}$ is the sarcomere strain at an optimal overlap, and ε_s is a distribution parameter. The distribution is normalized by $s_0 = 1/(\pi \varepsilon_s)$, which corresponds to an optimal overlap at $\tilde{\varepsilon}_n = \tilde{\varepsilon}_{ss}$ (Figure 4.2c). The number of myosin heads available for binding is then given as

$$m_{tot} = \hat{s} m_0 \quad (4.10)$$

where m_0 is the total number of myosin heads in the sarcomere. The sarcomere tension is calculated as a function of the tension in the myosin tails and the total number of activated myosin heads:

$$T_s = \hat{m}_a \kappa_m \Delta_m. \quad (4.11)$$

During a transition from stretching to shortening, not all cross-bridges will immediately detach and enter a stroking cycle. As the extension of the myosin tail decreases, the probability of the myosin head stroking increases. The transition is governed by equations that account for the fact that not all myosin tails in the sarcomere are at the same extension at the point of a change in the strain rate. Δ_m represents a distribution of the tail extensions. For isometric/shortening to stretching conditions:

$$\Delta_m = \Delta_m^{l-max} \left(1 - \exp \left(-\frac{\Delta_m^l \gamma}{\Delta_m^{l-max}} \right) \right) + l_s \left(\exp \left(-\frac{\Delta_m^l \gamma}{\Delta_m^{l-max}} \right) \right), \quad (4.12)$$

and for stretching to shortening conditions:

$$\Delta_m = \Delta_m^{l-max} \left(\exp \left(- \frac{(\Delta_m^{l-max} - \Delta_m^l) \gamma}{\Delta_m^{l-max}} \right) \right) + (l_s + \Delta_m^s) \left(1 - \exp \left(- \frac{(\Delta_m^{l-max} - \Delta_m^l) \gamma}{\Delta_m^{l-max}} \right) \right). \quad (4.13)$$

During isometric conditions, as $\dot{\tilde{\epsilon}}_n = 0$, $\Delta_m^s = 0$. A change from isometric to shortening conditions requires no transition (and vice-versa).

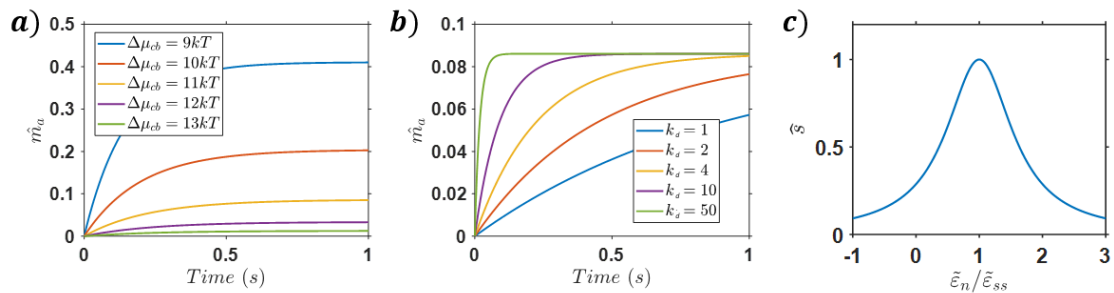


Figure 4.2: (a) Influence of enthalpy difference ($\Delta\mu_{cb} = \mu_a - \mu_d$) on isometric myosin transients; (b) Influence of rate coefficient k_d (s^{-1}) on isometric myosin transients; (c) Effect of sarcomere strain $\tilde{\epsilon}_n$ on actin-myosin overlap \hat{s} .

4.2.2. Remodelling of stress fibres

The cellular cytoskeleton is comprised of SFs, assembled from actin-myosin sarcomeres which actively generate tension through cross-bridge cycling, as described in Section 4.2.1. The thermodynamically consistent model from Vigliotti *et al.* (2015) captures key features of SF dynamics, including: (i) the kinetics of SF formation and dissociation as motivated by thermodynamic considerations; (ii) the stress, strain, and strain-rate dependence of SF remodelling; (iii) conservation of cytoskeletal proteins. Here we summarise key equations.

Consider an existing SF in its ground state with a number of sarcomeres n^R along its length. Should a nominal material strain ϵ_n be applied to the cell (and directly translated to the SFs), it will cause a reduction in the overlap s between the actin and myosin filaments of an individual sarcomere. Such a reduced overlap is expected to initiate a remodelling process (due to the associated increase in the internal energy). The case of

an applied stretch would result in the addition of sarcomeres in-series, with the opposite occurring for a compressive strain. Following remodelling, the internal strain within a sarcomere $\tilde{\varepsilon}_n$ would differ from an applied material strain, such that

$$\tilde{\varepsilon}_n = \frac{1 + \varepsilon_n}{\hat{n}} - 1, \quad (4.14)$$

where $\hat{n} = n/n^R$. The kinetic law for SF remodelling is given by

$$\hat{n} = \begin{cases} -\frac{1}{\hat{n}} \left(\frac{\hat{N}_u}{\hat{\eta}} \right)^2 \left[\psi(\tilde{\varepsilon}_n) - \frac{\delta\psi}{\delta\tilde{\varepsilon}_n} (1 + \tilde{\varepsilon}_n) \right] \frac{\alpha_n}{\mu_{b0}}, & \text{if } \frac{\delta\Psi}{\delta n} \leq 0 \\ -\frac{\hat{n}}{4} \left[\psi(\tilde{\varepsilon}_n) - \frac{\delta\psi}{\delta\tilde{\varepsilon}_n} (1 + \tilde{\varepsilon}_n) \right] \frac{\alpha_n}{\mu_{b0}}, & \text{otherwise,} \end{cases} \quad (4.15)$$

where \hat{N}_u is the (normalized) number of available cytoskeletal proteins, $\hat{\eta}$ is the concentration of SFs (see Figure 4.1), and α_n is a rate constant. The internal energy of n^R sarcomeres ψ increases as the internal strain $\tilde{\varepsilon}_n$ changes, with a functional form given by

$$\psi = \mu_{b0} + \beta\mu_{b0}|\tilde{\varepsilon}_n|^p, \quad (4.16)$$

where μ_{b0} is the internal energy of n^R sarcomeres in their ground state, and β and p are non-dimensional constants that govern the sarcomere strain at an optimal overlap $\tilde{\varepsilon}_{ss}$, such that

$$(p-1)\tilde{\varepsilon}_{ss}^p + p\tilde{\varepsilon}_{ss}^{p-1} - \frac{1}{\beta} = 0. \quad (4.17)$$

The rate of change of the internal energy follows as

$$\frac{\delta\Psi}{\delta n} \dot{n} = \dot{\hat{n}} \left[\psi(\tilde{\varepsilon}_n) - \frac{\delta\psi}{\delta\tilde{\varepsilon}_n} (1 + \tilde{\varepsilon}_n) \right]. \quad (4.18)$$

Formation and dissociation of SFs is governed by thermodynamic equilibrium of proteins available for binding (unbound), and those already bound in SF sarcomeres. The standard enthalpy μ_b of n^R sarcomeres within a SF is written as

$$\mu_b = \psi - \sigma_f [1 + \tilde{\varepsilon}_n] \Omega \quad (4.19)$$

where Ω is the volume of n^R sarcomeres in a SF, and σ_f is the SF stress given by

$$\sigma_f = \frac{T_s}{T_{s0}} \sigma_{iso}, \quad (4.20)$$

where T_s is the sarcomere tension, T_{s0} is the sarcomere tension computed at steady state isometric conditions, and σ_{iso} is the maximum isometric stress. Unbound proteins are affected by an activation signal level, and tend to transform into their bound states more readily when the activation signal is increased. The standard enthalpy μ_u of unbound SF proteins follows as

$$\mu_u = \mu_{u0} + \Delta\mu_{u0}C, \quad (4.21)$$

where μ_{u0} is the standard enthalpy of the unbound proteins in the absence of a signal C and $\Delta\mu_{u0}$ is the increase in the enthalpy of the unbound molecules at full activation ($C = 1$). SF formation is initiated by a biochemical or mechanical perturbation that triggers a signalling cascade within the cell. We model this signal as an externally initiated exponentially decaying pulse with level $0 \leq C \leq 1$ given by

$$C = \exp\left(-\frac{t_I}{\tau}\right), \quad (4.22)$$

where τ is a time constant that controls the decay rate of the signal, and t_I is the time measured from the instant the most recent signal is imposed. For a detailed explanation of the signalling pathways, or more rigorous signal formulations, the reader is referred to Vigliotti *et al.* (2015) and Pathak *et al.* (2011). The rate of SF formation/dissociation follows as

$$\dot{\hat{\eta}} = \frac{\hat{N}_u}{\hat{n}} \omega_n \exp\left[-\hat{n} \frac{\mu_{ab} - \mu_u}{k_B T}\right] - \hat{\eta} \omega_n \exp\left[-\hat{n} \frac{\mu_{ab} - \mu_b}{k_B T}\right] \quad (4.23)$$

where ω_n is the collision frequency of the unbound molecules, and μ_{ab} is an activation barrier. The (normalized) number of unbound cytoskeletal proteins may be calculated as

$$\hat{N}_u = 1 - \hat{\eta}\hat{n}, \quad (4.24)$$

where $\hat{\eta}\hat{n}$ determines the (normalized) number of bound SF proteins. The nominal cell stress due to active SF contractility is given by

$$\sigma_{cell}^{act} = \hat{\eta} \sigma_f f_0, \quad (4.25)$$

where f_0 is the volume fraction of SF proteins in the cell. The dynamic SF and cross-bridge framework is hereafter referred to as the active SF-CB model.

4.2.3. Non-linear viscoelastic component

In addition to the contractile cytoskeleton, the cell contains a number of non-active components. It has been shown that passive behaviour of such components may be described by non-linear viscoelastic material models, that act in parallel with the active cytoskeleton (Weafer *et al.* 2015; Reynolds and McGarry 2015; Reynolds *et al.* 2014).

Here we implement a non-linear three-component visco-elastic model (Figure 4.3).

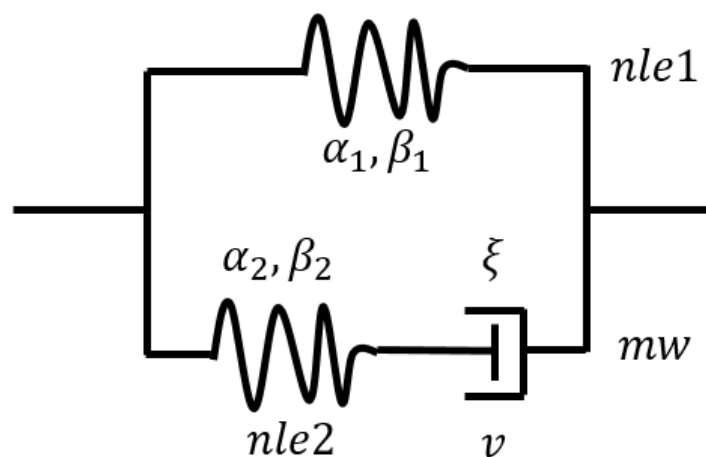


Figure 4.3: Schematic of non-linear viscoelastic model, comprised of a non-linear spring (*nle*) in parallel with a non-linear Maxwell (*mw*) unit (consisting of a non-linear spring in-series with a linear dashpot (*v*)).

In summary, the stress-strain relationship of a non-linear elastic component is given by:

$$\sigma_{nle} = \beta(\exp(\alpha \epsilon_{nle}) - 1), \quad (4.26)$$

where ε_{nle} is the strain in the component, α and β (kPa) are material constants. The stress in the viscous component is given as:

$$\sigma_v = \xi \dot{\varepsilon}_v, \quad (4.27)$$

where ξ is the viscosity ($kPa \cdot s$). The constitutive equation for the complete non-linear viscoelastic model is:

$$\dot{\sigma}_{cell}^{pass} = \alpha_1 \beta_1 \exp(\alpha_1 \varepsilon) \dot{\varepsilon} + \alpha_2 \left\{ \beta_2 + \sigma_{cell}^{pass} - \beta_1 (\exp(\alpha_1 \varepsilon) - 1) \right\} \left(\dot{\varepsilon} - \frac{1}{\xi} \left(\sigma_{cell}^{pass} - \beta_1 (\exp(\alpha_1 \varepsilon) - 1) \right) \right), \quad (4.28)$$

where σ_{cell}^{pass} is the total passive stress contribution in a cell due to the nonlinear viscoelastic component, and ε is the total strain applied to the cell. The full derivation for this model can be found in Appendix 4.A.

4.2.4. Modelling parameters

All simulations are reported for cells at a temperature $T = 310 K$. Cross-bridge parameters were constrained to lie within commonly accepted ranges (Smith and Geeves 1995; Offer and Ranatunga 2013). The stroke distance $l_s = 6.5 nm$, the maximum allowable stretch during lengthening $\Delta_m^{l-max} = 7.25 nm$, and the myosin tail stiffness $\kappa_m = 1.75 pN nm^{-1}$. The length of a half sarcomere is taken from values measured from chicken fibroblasts (Langanger *et al.* 1986), with $L_{sarc} = 200 nm$, and $t_s = .001 s$ is approximated from derived attached cross-bridge duty cycle times (Rastogi *et al.* 2016). The calibrated parameters $k_i = 4 s^{-1}$, $\gamma = 3$, and $\varepsilon_s = 0.225$. As there is no definitive data in the literature on the values for the enthalpies of attached and unattached cross-bridges, or bound and unbound SF proteins, parameter studies were performed to find appropriate values ($\mu_d = 5k_B T$, $\mu_a = 16k_B T$, $\mu_{u0} = \Delta\mu_{u0} = 8k_B T$, $\mu_{b0} = 14k_B T$, and $\mu_{ab} = 20k_B T$). Parametric studies for $\Delta\mu_{cb} = \mu_a - \mu_d$ and k_d are shown in Figure 4.2. The remaining parameters for the SF framework are confined within ranges reported by

Vigliotti *et al.* (2015), with $\Omega = 10^{-71} \mu m^3$, $\beta = 1.2$, $p = 2$, and $f_0 = 0.011$. The remodelling rates $\omega_n = 2 \text{ Hz}$ and $\alpha_n = 0.4 \text{ mHz}$, and the time constant for signal decay is $\tau = 0.05 \text{ s}$. The maximum isometric stress $\sigma_{iso} = 240 \text{ kPa}$ is consistent with a wide range of measurements on muscle fibres (Lucas *et al.* 1987). The material parameters for the non-linear viscoelastic component are taken to be $\alpha_1 = 8$, $\beta_1 = 0.25 \text{ kPa}$, $\alpha_2 = 15$, $\beta_2 = 0.382 \text{ kPa}$, and $\xi = 25 \times 10^3 \text{ kPa s}^{-1}$. A summary of key parameters is provided in Table 4.1.

Parameter symbol	Brief description
$m_{tot}; m_a; m_d$	Total number of myosin heads available for binding; number of attached myosin heads; number of unattached myosin heads
Δ_m	Extension imposed on the myosin tail due to stroke or actin displacement
l_s	Stroke distance of the myosin head
$\mu_a; \mu_d$	Enthalpy of the attached myosin heads; enthalpy of the unattached myosin heads
s	Overlap of the actin and myosin filaments
$n; n^R$	Number of sarcomeres in a stress fibre; reference number of sarcomeres within stress fibre in ground state
η	Concentration of stress fibres
$\tilde{\epsilon}_n; \tilde{\epsilon}_{ss}$	Nominal sarcomere strain; sarcomere strain at optimal actin-myosin overlap
N_u	Number of unbound cytoskeletal proteins
$\mu_{ab}; \mu_u; \mu_b$	Activation barrier for n^R cytoskeletal proteins; enthalpy of n^R cytoskeletal proteins in the unbound state; enthalpy of n^R cytoskeletal proteins in bound state
ψ	Internal energy of n^R sarcomeres within a stress fibre
f_0	Volume fraction of cytoskeletal proteins in the cell;
$\sigma_f; \sigma_{iso}$	Stress fibre stress; maximum isometric tensile stress of a stress fibre

Table 4.1: A summary of key parameters of the model

4.3. Summary of Wille *et al.* dynamic cell deformation experiments

Here we discuss the experiments of Wille *et al.*, focusing on the measured active cell forces shown in Figure 4.4. Cardiac fibroblasts were seeded in a collagen hydrogel, and incubated for 8 days. Following incubation, the scaffolds were dynamically loaded at a frequency of 0.1 *Hz* under uniaxial conditions for 12 hours. Cells and SFs were observed to align in the direction of stretching. To parse the force contribution of the cells from the collagen fibres, the experiment is repeated with the addition of Cytochalasin D, which inhibits actin polymerization and therefore development of SFs. In a series of experiments, maximum nominal strains of 5%, 10%, 20% and 25% were considered, with the boundary conditions summarised in Table 4.2.

	ε_{max}	$f(Hz)$	$\dot{\varepsilon}_{loading} (s^{-1})$	$\dot{\varepsilon}_{unloading} (s^{-1})$
<i>Case 1</i>	0.05	0.1	0.01	-0.01
<i>Case 2</i>	0.1	0.1	0.02	-0.02
<i>Case 3</i>	0.2	0.1	0.04	-0.04
<i>Case 4</i>	0.25	0.1	0.05	-0.05

Table 4.2: Boundary conditions for the fixed frequency experiments of Wille *et al.*

The evolution of the peak force (at mid-point of each cycle) over a 12-hour period is reproduced in Figure 4.4a. Force deformation loops for the first five cycles (Figure 4.4b) and the final five cycles (Figure 4.4c) are also reproduced. A number of key features should be noted:

- Figure 4.4b: during the first five cycles, the highest forces are measured for the highest applied strain (-rates) ($\varepsilon_{max} = 25\%$), with the peak force decreasing with decreasing strain amplitude.
- Figure 4.4a: Force relaxation is observed during the high strain experiments ($\varepsilon_{max} = 25\%$ and 20%). In contrast, the force increases during the low strain (-rate) experiments ($\varepsilon_{max} = 5\%$ and 10%).

- Figure 4.4c: By the final cycle, the highest peak force is measured for the lowest applied strain, with the peak force decreasing with increasing strain amplitude.
- In the final cycle, the minimum force at the end of a cycle is non-zero (~ 1 mN), while for high strain amplitudes the minimum forces are close to zero.

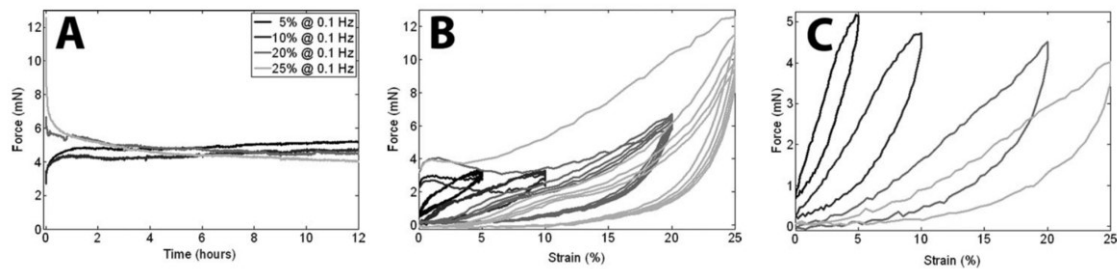


Figure 4.4: Cell force versus strain amplitudes after 8 days of static incubation. (a) Peak cell force over 12 hours of cyclic loading. Peak cell force increased for 5% and 10% strain amplitudes while it decreased for 20% and 25% amplitudes; (b) First 5 loading cycles; (c) Last 5 loading cycles after 12 hours of cyclic loading. The peak cell force and cell stiffness decreased with increased amplitude. Reproduced with permission from Wille *et al* (2006).

An additional series of experiments was also performed by Wille *et al.* in which the peak strain is fixed at strain amplitude of 10%, and the influence of the frequency of the applied cyclic deformation on cell force is investigated. The following interesting features are noted:

- During the first loading cycle, the highest force is measured for the lowest frequency (0.001 Hz), with the peak force decreasing with increasing cycle frequency.
- For all cycle frequencies, the peak force is higher in the final cycle than the first cycle.
- By the final cycle, the highest peak force is measured for the highest applied cycle frequency (0.25 Hz), with the peak force decreasing with decreasing cycle frequency.

4.4. Computational implementation

Cyclic strain boundary conditions are imposed on the cell model (equations 4.1-4.25) based on the experimental test protocols of Wille *et al.* In all computations incubation under static conditions is simulated by imposing a nominal strain of 0% until steady state distributions of \hat{m}_a , $\hat{\eta}$, \hat{n} , and contractile force is obtained. Dynamic loading is then imposed, based on the loading protocols of Wille *et al.*, i.e. a series of simulations are performed where the applied nominal strain cycles between 0% and ϵ_{max} (5%, 10%, 20% and 25%) at a frequency of 0.1 Hz (Table 4.2). The constant loading and unloading strain rate magnitudes are equal, resulting in a saw-tooth wave form (Figure 4.5a). In the experiments of Wille *et al.* all cells are observed to oriented in the stretching direction throughout the experiment. In this study we therefore assume cells and SFs are aligned in the direction of applied loading (the prediction of such cell alignment in the direction of stretching has previously been presented by Vigliotti *et al.* 2015). The full active SF-CB model is implemented, with constitutive equations solved via a 4th order Runge-Kutta iterative method in Matlab.

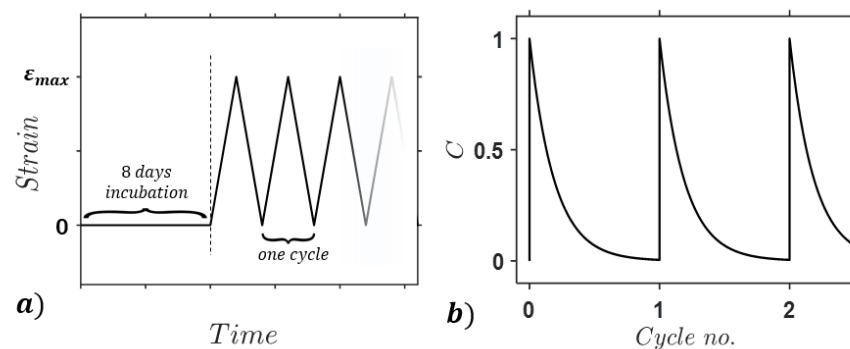


Figure 4.5: (a) Experimental loading conditions from Wille *et al.* Following 8 days of static incubation, a saw-tooth strain waveform is applied. Cycle duration and ϵ_{max} vary as shown in Table 4.2; (b) Signal C is initiated at the onset of every cycle.

Computed force in a single cell must also be scaled to determine the total force in a multi-cell tissue. Wille *et al.* report a cell quantity of ~ 2.4 million in the tissue post-incubation, with a typical cell length of $80 \mu m$. A cardiac fibroblast has an approximate volume of

$2625 \mu\text{m}^3$ (Abercrombie 1978), so the cross-sectional area of a cell in the experiments of Wille *et al.* is approximated as $A_{cs} = 32.81 \mu\text{m}^2$, assuming incompressibility and a cylindrical deformed configuration. The total tissue length (i.e. circumference of tissue ring) is approx. 30.5 mm with a CSA of 0.41 mm^2 . Experimental images suggest that cells are uniformly distributed throughout the tissue, leading to the approximation that a cross-section of the tissue orthogonal to the stretching direction contains $N = 6283$ cells. In the experiment the gel is a ring constrained at two ends, so the typical cross-sectional number of cells is doubled. The total force contribution by all cells in the tissue (referred to as the “cell force” in the study of Wille *et al.*) is given as

$$F_{cell}^{total} = 2N A_{cs} (\sigma_{cell}^{act} + \sigma_{cell}^{pass}) \quad (4.29)$$

where the factor of 2 is due to the experimental set-up, whereby a “tissue ring” is stretched by the loading bars. Similarly, the active force contribution is given as $F_{cell}^{act} = 2N \sigma_{cell}^{act} A_{cs}$, and the passive force contribution is given as $F_{cell}^{pass} = 2N \sigma_{cell}^{pass} A_{cs}$.

Unless otherwise stated, simulations assume a stretch activated exponentially decaying signal. At the onset of each loading cycle the signal increases instantaneously to a maximum value ($C=1$). This signal is assumed to decay exponentially during each loading cycle, until full signal activation ($C=1$) is again initiated at the start of the subsequent cycle. For a detailed explanation of the signalling pathways, or more rigorous signal formulations, the reader is referred to Pathak *et al.* (2011).

4.5. Results and discussion

The tissue loading regimes outlined in Table 4.2 are simulated using the model described in Section 4.2. In Section 4.5.1 we demonstrate the ability of the model to capture the key experimental trends in cell force generation outlined in Section 4.3. In Section 4.5.2 we provide insight into the mechanisms underlying such complex patterns of cell force generation by analysing cross-bridge dynamics and SF remodelling.

4.5.1. Key trends predicted by model

For direct comparison with the experimental results of Wille *et al.* (Figure 4.4) the predicted total force due to all cells in the tissue (F_{cell}^{total}) is shown in Figure 4.6. Figure 4.6a shows the evolution of peak force at the end of each loading half-cycle. During the first two hours of cyclic deformation a significant increase in peak force (from ~ 2 mN during the first cycle up to a steady state value of ~ 5.2 mN) is computed for the lowest applied strain rate ($\varepsilon_{max}=5\%$). A similar, but less pronounced, increase in peak force is also predicted for the case of $\varepsilon_{max}=10\%$. In contrast, a significant reduction in peak force (from ~ 12.5 mN during the first cycle down to a steady state value of ~ 3.3 mN) for $\varepsilon_{max}=25\%$. A similar trend is computed for $\varepsilon_{max}=20\%$. Steady state peak forces are computed to increase with decreasing deformation strain-rate.

Computed force-strain loops are shown for the first two loading cycles in Figure 4.6b. In the cases of $\varepsilon_{max}=5\%$ and 10% , the first loading-half cycle is characterised by an approximately constant force. After the first loading-half-cycle, transient force-strain loops are computed, with a gradual increase in force during loading half-cycles and a gradual decrease in force during unloading half-cycles. A similar initially constant force is also computed for $\varepsilon_{max}=20\%$ and 25% , but when the strain increases beyond 10% a non-linear increase in force is computed. Computed force strain loops are shown for the final two loading cycles (following 12 hours of applied cyclic loading) in Figure 4.6c. A

minimum force of $\sim 1\text{mN}$ is computed for $\varepsilon_{max}=5\%$. The value of the minimum force decreases with increasing strain rate.

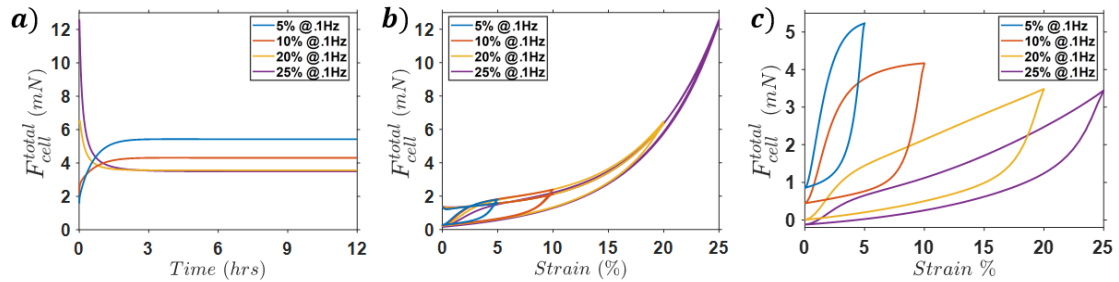


Figure 4.6: Cell force versus strain amplitudes. (a) Peak cell force over 12 hours of cyclic loading; (b) First 2 loading cycles; (c) Final loading cycle following 12 hours of cyclic loading.

4.5.2. Mechanisms underlying observed trends in cell force generation

The active myosin transient behaviour during a single cycle (at steady state) is shown in Figure 4.7a. Myosin binding increases during the loading half cycle in all cases. The myosin tail is predominantly exposed to lengthening conditions, generating a higher strain energy than encountered during shortening in the previous unloading half-cycle. The alteration in strain energy causes a change in the chemical potential (equation 4.6), therefore increasing k_a (equation 4.8), and resulting in the recruitment of a higher number of attached myosin heads \hat{m}_a during the loading half-cycle (via equation 4.3). During the subsequent unloading half-cycle the sarcomeres shorten and the myosin tail strain energy significantly reduces, resulting in a rapid decline in \hat{m}_a . At the lowest strain rate (i.e. $\varepsilon_{max}=5\%$) the stroking of myosin heads with actin filaments that are moving in the direction of the stroke (with a *low* velocity) results in generation of significant tension in the myosin tail, and consequently \hat{m}_a remains high (equations 4.3-4.8). This results in a high non-zero force ($\sim 1\text{ mN}$) at the end of the unloading half-cycle (as shown in Figure 4.6c). For higher strain rate simulations (e.g. $\varepsilon_{max}=25\%$), the stroking of myosin heads with actin filaments that are moving in the stroking direction (with a *high* velocity) results in the generation of a low tension in the myosin tail (via equation 4.2), and consequently

\hat{m}_a significantly reduces. This results in a near-zero value of actively generated force at the end of each loading cycle (as shown in Figure 4.6c).

The total number of myosin heads available for binding, m_{tot} , is a function of the overlap of the actin-myosin filaments, \hat{s} , which is in turn a function of the internal sarcomere nominal strain $\tilde{\epsilon}_n$ (equations 4.9 and 4.10). This interaction results in complex patterns of myosin head binding in cells under cyclic loading. The overlap \hat{s} is shown in Figure 4.7b for a single cycle at steady state. SFs have remodelled such that an optimal \hat{s} is attained close to the peak cycle strain. At low strain amplitudes (e.g. $\epsilon_{max}=5\%$) the overlap is always near-optimal, and thus during the cycle $m_{tot} \cong m_0$. With increasing ϵ_{max} , the overlap is sub-optimal as the internal sarcomere strain $\tilde{\epsilon}_n$ is lowered. Following unloading, $\hat{s} \cong .42$ for the case of $\epsilon_{max}=25\%$ (i.e. the only 42% of all myosin heads are available for binding at the end of each unloading half-cycle). The gradual increase in \hat{s} to a near optimal value also contributes to the transients in myosin binding shown in Figure 4.7a, and to the transient increase in force shown in Figure 4.6c. The computed evolution of SF concentration $\hat{\eta}$ and sarcomere assembly \hat{n} during 12 hours of dynamic loading is shown in Figures 4.7c and 4.7d, respectively. Prior to the onset of cyclic loading (after 8 days of static incubation), SFs attain a steady state concentration $\hat{\eta}$ of ~ 0.25 . Following the onset of cyclic loading, $\hat{\eta}$ rises steadily for the case of $\epsilon_{max}=5\%$, with a 3-fold increase predicted ($\hat{\eta} \cong 0.86$) at steady state ($t > 3$ hours). With the transition from static conditions to a lengthening-shortening cycle, the internal fibre stress σ_f increases (due to increased myosin binding). A higher fibre stress directly promotes an increase in the SF concentration via a reduction in the enthalpy of the bound proteins (equation 4.19). The steady state value of $\hat{\eta}$ is lower at high applied strain amplitudes. This is because the higher magnitudes of shortening strain rates result in lower values of \hat{m}_a . This in turn

causes a reduction in σ_f , and the bound protein enthalpy is increased. As a result, the rate of SF dissociation is increased (via equation 4.23).

SFs remodel the number of sarcomeres in-series via equation 4.15 to achieve an optimum overlap \hat{s} of the actin-myosin filaments (i.e. when $\tilde{\epsilon}_n = \tilde{\epsilon}_{ss}$). Following incubation, SFs are predicted to remodel such that $\hat{n} \cong 0.74$ (Figure 4.7d). With the onset of cyclic loading \hat{n} increases in all cases, ranging from 0.76 to 0.93. Higher steady state values of \hat{n} are predicted for higher strain amplitudes, where more sarcomeres are required to reduce the internal strain $\tilde{\epsilon}_n$ of individual sarcomeres (and achieve an optimal overlap \hat{s}).

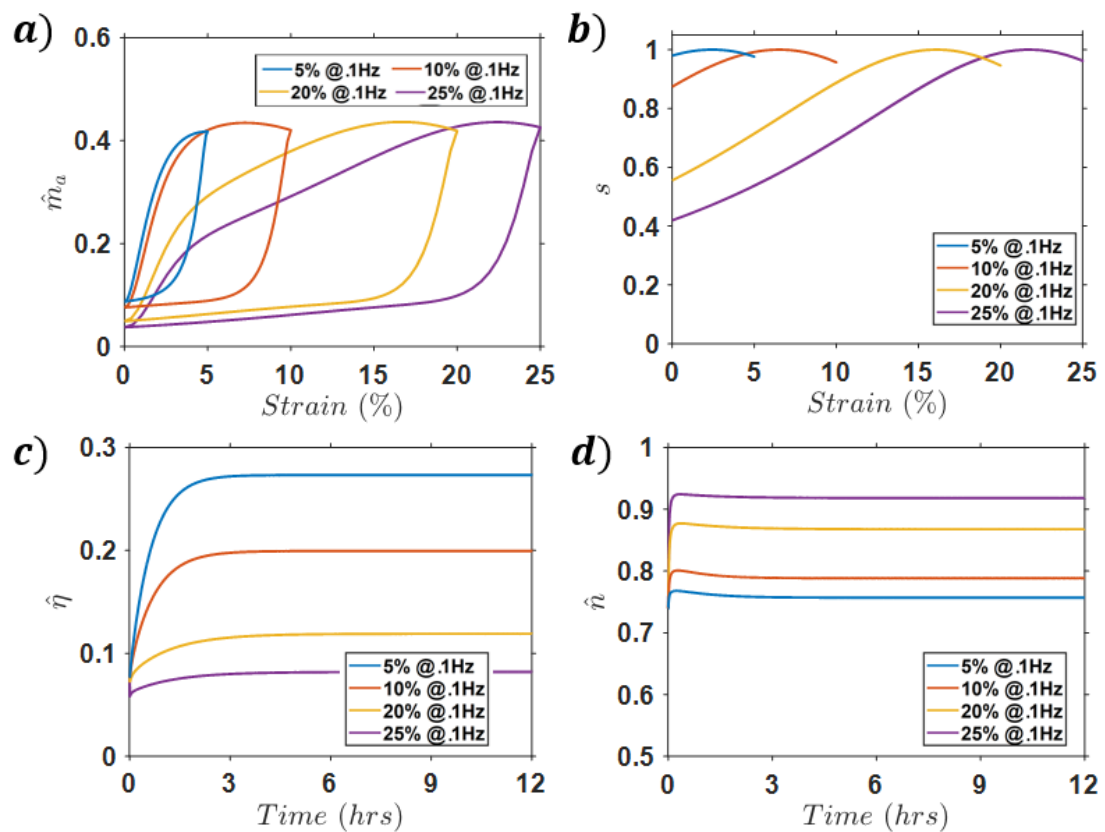


Figure 4.7: (a) Number of attached myosin heads \hat{m}_a during a single loading cycle at steady state; (b) Actin-myosin overlap \hat{s} during a single loading cycle at steady state; (c) SF concentration over 12 hours of cyclic loading; (d) Number of sarcomeres within a SF over 12 hours of cyclic loading.

4.5.3. Passive non-linear viscoelastic force contribution

Despite the increase in SF concentration $\hat{\eta}$ during the first two hours of cyclic loading (Figure 4.7a), the peak force reduces during this period for $\varepsilon_{max}=20\%$ and 25% , while peak force increases (in accordance with increasing $\hat{\eta}$) for $\varepsilon_{max}=5\%$ and 10% . This can be explained by the force contribution of the non-linear viscoelastic passive component of the cells, F_{cell}^{pass} , as described in Section 4.2.3. Figure 4.8 shows the passive forces F_{cell}^{pass} computed for all four loading regimes. As shown in Figure 4.8a, an expected viscoelastic stress relaxation response occurs in all cases. However, passive forces are extremely low for $\varepsilon_{max}=5\%$ and 10% due to the non-linear strain stiffening elastic component of the passive model. This is illustrated in Figure 4.8b, where the computed force strain curve during the first loading cycle is shown. At this early stage the strain in the dashpot is minimal, so the passive force F_{cell}^{pass} (is essentially determined by the non-linear elastic components *nle1* and *nle2* (see Figure 4.3). This results in very low peak forces for $\varepsilon_{max}=5\%$ and 10% , in comparison to the high passive forces for $\varepsilon_{max}=20\%$ and 25% . As cycling progresses, an increasing proportion of the applied strain is taken up by the viscous dashpot component. This leads to a significant decrease in passive force (Figure 4.8a), as the reduced strain in the non-linear elastic component *nle2* leads to an exponential decrease in its force contribution (equation 4.28). As shown in Figure 4.8c, following 12 hours of cyclic loading the peak value of F_{cell}^{pass} is only 0.4mN for $\varepsilon_{max}=5\%$ and 10% , respectively, suggesting that $F_{cell}^{total} \approx F_{cell}^{act}$ for this loading regime. However, for higher values of applied strain ($\varepsilon_{max}=20\%$ and 25%) F_{cell}^{total} is comprised of a significant passive and active force contributions. In general, the non-linear viscoelastic passive component of the model explains why the total force is observed to decrease in the case of $\varepsilon_{max}=20\%$ and 25% during the 12-hour cyclic loading experiments (strong passive contribution), whereas the total force is observed to increase for $\varepsilon_{max}=5\%$ and 10% (weak passive contribution, active behaviour dominates measured force).

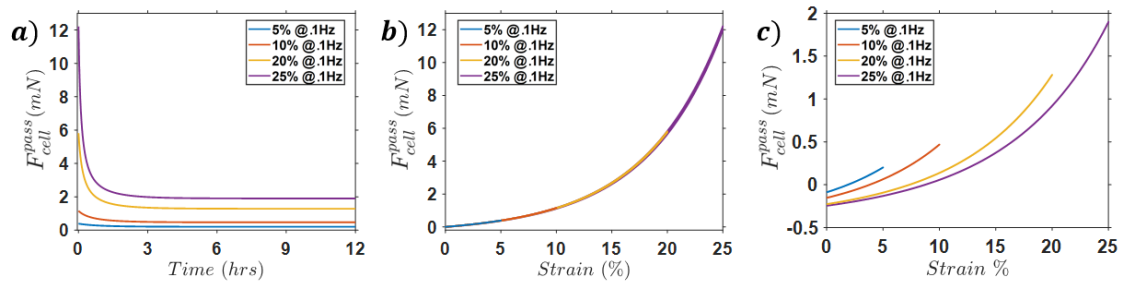


Figure 4.8: Passive cell force versus strain amplitudes. (a) Peak cell force over 12 hours of cyclic loading; (b) First 2 loading cycles; (c) Final loading cycle following 12 hours of cyclic loading.

4.5.4. Investigation of stretch activated cell signalling

As stated in Section 4.4, the results shown in Figure 4.6 and 4.7 are computed assuming that an exponentially decaying signal initiated by the onset of cell stretching at the start of each loading cycle, as shown in Figure 4.5b. However, in the loading regimes considered thus far (Table 4.2 and Figure 4.6) the period of each cycle is constant, so identical signalling is obtained, regardless of the value of ϵ_{max} . Extremely similar results to those shown in Figure 4.6 can be computed by assuming a constant signal throughout each simulation/experiment. In order to examine the assumed signalling regime, we consider loading regimes in which the loading period is changed. Specifically we compute the response of cells to loading frequencies of $f = 0.001$ Hz and $f = 0.25$ Hz, with $\epsilon_{max} = 10\%$ in both cases (again these loading parameters are based on the experiments of Wille *et al.*). Simulations are performed for three different signalling regimes: (i) an exponentially decaying signal initiated by the onset of stretching, (ii) a permanent continuous signal, and (iii) no signal. Computed results are shown in Figure 4.9. For $f = 0.001$ Hz, F_{cell}^{total} is predicted to increase during the first 2 hours of cyclic loading, reaching a steady state value of ~ 4 mN. For $f = 0.25$ Hz, F_{cell}^{total} is predicted to increase more dramatically, reaching a higher steady state value of ~ 6 mN. The increase in F_{cell}^{total} in both simulations is due to the dominant active force contribution. This is expected for $\epsilon_{max} = 10\%$, for which the passive stress relaxation contribution is very small (see

Figure 4.8). A higher steady state force is computed for $f = 0.25$ Hz because the high frequency of signalling results in a higher rate of SF formation (via equation 4.21) over the course of the simulation. This directly results in a higher steady state SF concentration $\hat{\eta}$, resulting in a higher steady state force (equations 4.20 and 4.25). The predicted trends are similar to the experimental results of Wille *et al.* (Figure 4.9c): (i) an increase in force during the first two hours of cyclic loading is observed for both $f = 0.25$ Hz and $f = 0.001$ Hz, indicating that active behaviour is dominant (passive stress relaxation is not observed); (ii) Following 12 hours of loading, a force of ~ 6.5 mN is observed for $f = 0.25$ Hz, compared to ~ 4 mN for $f = 0.001$ Hz.

As shown in Figure 4.9a, a continuous signal (dotted line) does not accurately predict the experimentally observed behaviour. Steady state forces are incorrectly predicted to be very similar for both $f = 0.25$ Hz and $f = 0.001$ Hz, with excessively high values of ~ 7.6 mN and ~ 7.3 mN, respectively. This results from the nearly identical and excessively high SF concentrations predicted for both frequencies. For the case of zero signalling for $f = 0.001$ Hz, computed results are almost identical to the case of the exponentially decaying signal. However, for the case of $f = 0.25$ Hz, the absence of signalling results in an excessively low steady state force of ~ 4.2 mN. These results suggest that stretch activated signalling at the low frequency of $f = 0.001$ Hz does not have any significant influence on SF formation (i.e. the frequency of signalling is so low it approximates to the zero signal case). However, for the higher loading frequency of $f = 0.25$ Hz, stretch activated signalling results in a significant increase in SF formation.

Finally, it should be noted from Figure 4.9b that for case of $f = 0.001$ Hz, the loading and unloading cycles are so slow (period = 16.6 minutes) that significant SF remodelling occurs within a single cycle, with $\hat{\eta}$ at steady state ranging from 0.44 to 0.5 for an exponentially decaying signal. This is due to the influence of the active SF force (via

equation 4.20) during lengthening and shortening. Identical changes in $\hat{\eta}$ are computed for the zero signalling case, again confirming that remodelling is not driven by signalling in the case of $f = 0.001$ Hz. In contrast, in the high frequency case the exponentially decaying signal is initiated every 4 seconds, and is responsible for a significantly higher $\hat{\eta}$ (0.82) when compared to no signal (0.54). In this case, the period of each loading cycle is far too low to allow significant remodelling of $\hat{\eta}$ within a single cycle, resulting in the computation of a smooth evolution of $\hat{\eta}$.

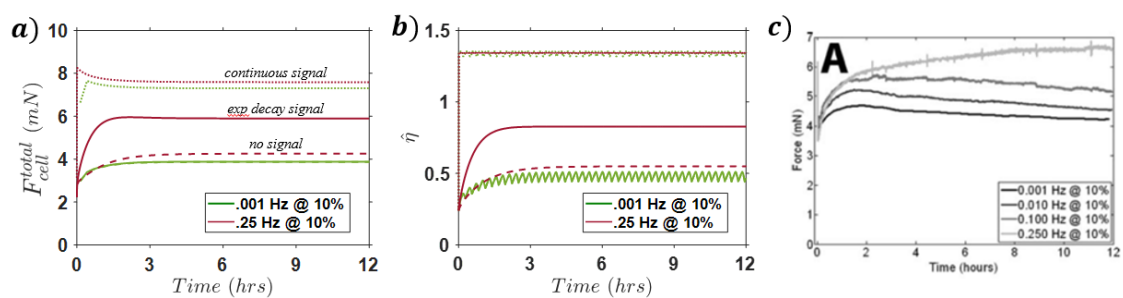


Figure 4.9: Cell force versus loading frequencies with different signal types: exponentially decaying (continuous line), constant signal (dotted line), no signal (broken line). (a) Peak cell force over 12 hours of cyclic loading; (b) SF concentration over 12 hours of cyclic loading; (c) Experimental peak cell force over 12 h of cyclic stretch. Reproduced with permission from Wille *et al* (2006).

4.5.5. Steady state simulations

In a final series of simulations, we demonstrate that our modelling framework predicts a classical Hill-type force-velocity relationship under non-dynamic boundary conditions. The short-term response of a cell to a range of applied shortening velocities is computed. Simulations predict a Hill-type relationship in which F_{cell}^{total} is predicted to decrease with increasing shortening velocity. These predictions are closely aligned with the single cell AFM measurements of Mitrossilis *et al.* (2009). A high shortening velocity is associated with a low contractile force (Figure 4.10a). Actin displacement reduces the strain energy in the myosin tail via equation 4.2 (as shown in Figure 4.1 – shortening). The alteration in strain energy causes a change in the chemical potential (equation 4.6), therefore reducing k_a (equation 4.8), and resulting in the recruitment of a lower number of attached

myosin heads \hat{m}_a (via equation 4.3). As the shortening velocity decreases, actin displacement in the stroke direction decreases. A higher tension is generated by a stroke of the myosin head, consequently resulting in a higher \hat{m}_a and active cell force. Under isometric conditions, the position of the actin is fixed, and the power stroke results in the development of a high tension (corresponding to isometric tension) in the myosin tail. Accurate prediction of the force-velocity relationship trivially leads to the accurate prediction of the power-velocity relationship for a single cells, also shown in Figure 4.10a.

In an additional series of experiments, Mitrossilis *et al.* measured the actively generated cell force following addition of blebbistatin to the cell media. Force measurements were performed for a range of blebbistatin concentrations. Blebbistatin is a compound used to inhibit cross-bridge activity. It binds to a primed myosin head and prevents attachment to the actin filament (Kovács *et al.* 2004). To simulate this experiment we assume a linear relationship between blebbistatin concentration and the number of blocked myosin heads. Figure 4.10b shows the predicted reduction in F_{cell}^{total} as a function of blebbistatin concentration (under steady state isometric conditions). Computed forces are shown for two modelling assumptions: (i) Addition of blebbistatin affects only the cross-bridge cycling dynamics, but does not result in alterations of SF structures (i.e. $\hat{\eta}$ and \hat{n} remain unchanged); (ii) Addition of blebbistatin affects the cross-bridge cycling dynamics, and the consequent reduction in active stress leads to remodelling of SF structures (i.e. $\hat{\eta}$ and \hat{n} remodel due to blebbistatin addition).

When the SF concentration $\hat{\eta}$ is fixed, the force decreases linearly as a function of blebbistatin concentration (i.e. as a function of the number of blocked myosin heads). The effect is similar to the influence of a reduced overlap of the actin-myosin filaments (equation 4.10). This prediction is not supported by experimental evidence (Mitrossilis *et*

al. 2009). However, when SF remodelling is allowed, the resulting non-linear relationship between force and blebbistatin concentration is extremely similar to the experimental measurement of Mitrossilis *et al.* SF remodelling is highly sensitive to the internal SF stress (generated by cross-bridge cycling) via equation 4.20. As previously described a lower fibre stress σ_f increases the enthalpy of the bound proteins (equation 4.19), increasing the dissociation rate of SFs (equation 4.23). Therefore, in addition to disrupting tension generation via blocking of the myosin head, blebbistatin also has the knock-on effect of promoting SF dissociation.

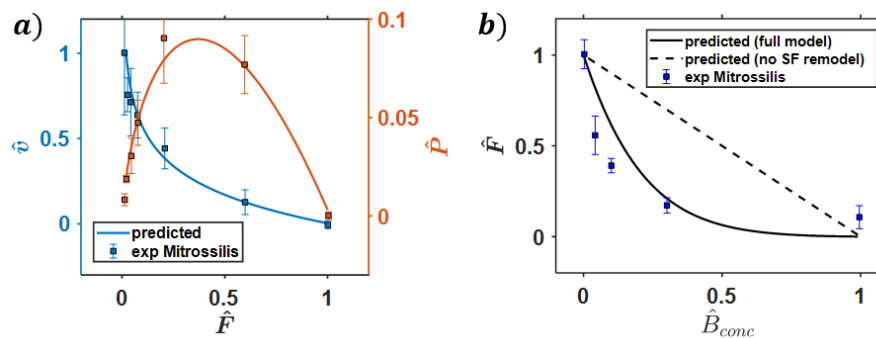


Figure 4.10: (a) Normalized predicted and experimental shortening velocity $\hat{v} = v/v_{max}$ (blue) and mechanical power $\hat{P} = P/(F_{max}v_{max})$ (orange) as functions of generated force $\hat{F} = F/F_{max}$; (b) Predicted and experimental (Mitrossilis *et al.* 2009) contractile activity of cells in response to an applied concentration of myosin inhibitor blebbistatin (\hat{B}_{conc}). Force normalized by maximal force without blebbistatin.

4.6. Concluding remarks

In this study a novel dynamic cell contractility model is developed, including a 2-state cross-bridge cycling model with rate coefficients governed by thermodynamic equilibrium. This model is coupled with the Vigliotti framework for SF remodelling to describe the dynamic behaviour of the active cytoskeleton. The model uncovers the mechanisms underlying transient cell force generation during cyclic loading, as observed by Wille *et al.* Generation of tension in the myosin tail (either through a myosin head power stroke, or by an external load, will result in an imbalance between the chemical potentials of attached and unattached myosin heads. This results in a transient change in

the number of attached heads \hat{m}_a , and consequently a transient change in the actively generated sarcomere stress. In turn, the concentration of SFs in the cell is highly dependent on the sarcomere stress. Previous work by McEvoy *et al.* (2017) and Shishvan *et al.* (2018) has demonstrated that the cellular SF concentration and associated cytoskeletal free energy has a significant effect on cellular spreading and remodelling. The current study highlights the influence of transient nano-scale actin-myosin interactions have on stress fibre remodelling under dynamic loading conditions.

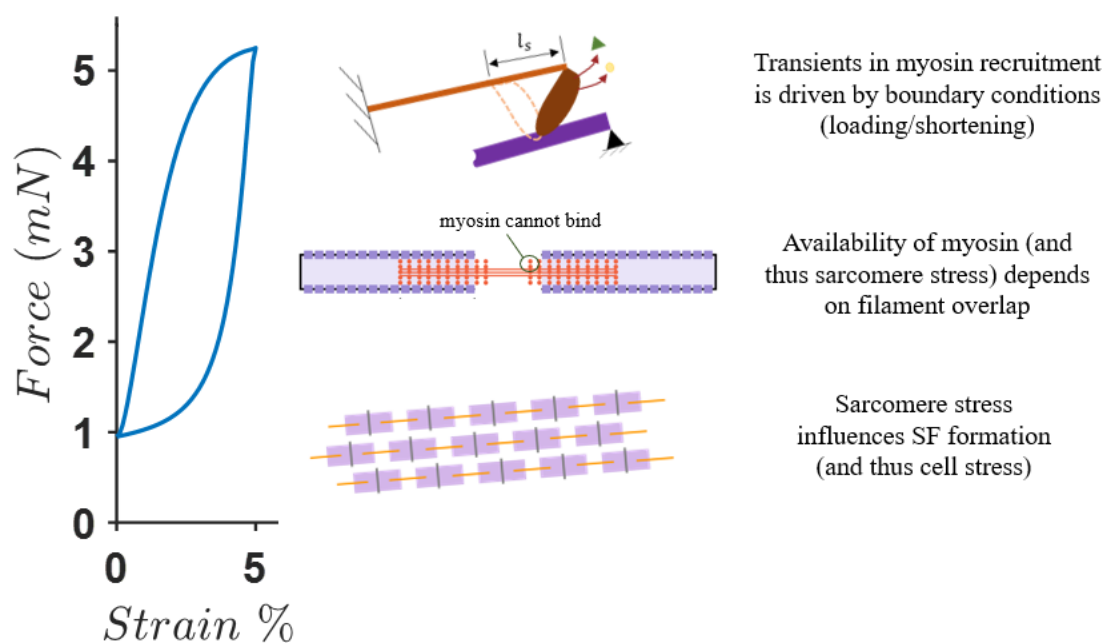


Figure 4.11: Schematic of mechanisms contributing to transient behaviour

The predictions of transient active cell force provide a mechanistic explanation for phenomenological fading-memory type models (e.g. Hunter *et al.*, 1998), as outlined in Appendix 4.B. The current study reveals that the effective “catching up” of the strain rate in such fading-memory formulations is a phenomenological representation of (i) the alteration in the number of attached myosin heads during a loading cycle, and (ii) the transition of a population of myosin heads from stretching to shortening conditions (or vice-versa). The fading memory framework has previously been coupled with models for SF remodelling to describe the transient behaviour of single cells under dynamic loading

(Reynolds and McGarry, 2015) based on the experiments of Weafer *et al.* (2015) in which isolated osteoblasts were subjected to cyclic loading using a modified AFM. The mechanistically based cross-bridge model developed in the current study will be used to simulate the single cell experiments of Weafer *et al.* (2015) in follow-on study. The modelling framework may also be further developed to investigate the link between cell contractility and tissue level remodelling, including the analysis of cardiac hypertrophy (Chung *et al.* 2003), or the effect of dynamic loading on cartilage (Dowling *et al.* 2013) and tendon remodelling.

Appendix 4.A: Non-linear viscoelastic model

Here we provide a more detailed derivation for the non-linear model summarised in Section 4.2.3. We consider a non-linear Maxwell unit (non-linear spring in series with a linear dashpot) in parallel with a second non-linear spring. The following assumptions may be made regarding the system shown in Figure 4.3:

(i) The total stress $\sigma_{cell}^{pass} = \sigma_{nle1} + \sigma_{mw}$ (A1),

(ii) The total strain $\varepsilon = \varepsilon_{mw} = \varepsilon_{nle1}$ (A2),

(iii) $\sigma_{mw} = \sigma_{nle2} = \sigma_v$ (A3),

(iv) and $\varepsilon_{mw} = \varepsilon_{nle2} + \varepsilon_v$ (A4).

Initially, let us describe the spring stress-strain relations as

$$\sigma_i = f(\varepsilon_i) = f_i, \quad i = nle1, nle2 \quad (A5)$$

Differentiating a non-linear elastic spring with respect to time gives

$$\dot{\sigma}_{nle} = \frac{d}{dt}(\sigma_{nle}) = \frac{df_{nle}}{d\varepsilon_{nle}} \frac{d\varepsilon_{nle}}{dt} = \frac{df_{nle}}{d\varepsilon_{nle}} \dot{\varepsilon}_{nle}, \quad (A6)$$

Combining with the strain (rate) constraint, we find:

$$\dot{\varepsilon}_{mw} = \dot{\varepsilon}_{nle2} + \dot{\varepsilon}_v = \frac{\dot{\sigma}_{nle2}}{\frac{df_{nle2}}{d\varepsilon_{nle2}}} + \dot{\varepsilon}_v, \quad (A7)$$

so that

$$\frac{df_{nle2}}{d\varepsilon_{nle2}} \dot{\varepsilon} = \dot{\sigma} + \frac{df_{nle2}}{d\varepsilon_{nle2}} \dot{\varepsilon}_v. \quad (A8)$$

Also, considering the stress rate:

$$\dot{\sigma}_{cell}^{pass} = \dot{\sigma}_{nle2} + \dot{\sigma}_{nle1}, \quad (A9)$$

so that

$$\dot{\sigma}_{cell}^{pass} = \frac{df_{nle2}}{d\varepsilon_{nle2}} \dot{\varepsilon} + \frac{df_{nle1}}{d\varepsilon_{nle1}} \dot{\varepsilon} - \frac{df_{nle1}}{d\varepsilon_{nle1}} \dot{\varepsilon}_v \quad (A10.1)$$

$$= \left(\frac{df_{nle1}}{d\varepsilon_{nle1}} + \frac{df_{nle2}}{d\varepsilon_{nle2}} \right) \dot{\varepsilon} - \frac{df_{nle2}}{d\varepsilon_{nle2}} \dot{\varepsilon}_v \quad (A10.2)$$

$$= \frac{df_{nle2}}{d\varepsilon_{nle2}} (\dot{\varepsilon} - \dot{\varepsilon}_v) + \frac{df_{nle1}}{d\varepsilon_{nle1}} \dot{\varepsilon}. \quad (A10.3)$$

The specific form for the non-linear spring function is given by:

$$\sigma_{nle} = \beta(\exp(\alpha \varepsilon_{nle}) - 1) = f_{nle}, \quad (A11)$$

where ε_{nle} is the strain in the spring, and α_{nle} and β_{nle} (kPa) are material constants. The derivative with respect to strain is then:

$$\frac{df_{nle}}{d\varepsilon_{nle}} = \alpha\beta \exp(\alpha \varepsilon_{nle}). \quad (A12)$$

The dashpot stress is:

$$\sigma_v = \xi \dot{\varepsilon}_v, \quad (A13)$$

where ξ is the viscosity of the dashpot ($kPa \cdot s$). Rearranging:

$$\dot{\varepsilon}_v = \frac{\sigma_v}{\xi} = \frac{1}{\xi} (\sigma_{vis} - \sigma_{nle1}) \quad (A14.1)$$

$$= \frac{1}{\xi} (\sigma_{vis} - \beta_1(\exp(\alpha_1 \varepsilon) - 1)). \quad (A14.2)$$

$df_{nle2}/d\varepsilon_{nle2}$ may be arranged as:

$$\frac{df_{nle2}}{d\varepsilon_{nle2}} = \alpha_2 \beta_2 \exp(\alpha_2 \varepsilon_{nle2}) \quad (A15.1)$$

$$= \alpha_2 (\beta_2 + \beta_2(\exp(\alpha_2 \varepsilon_{nle2}) - 1)) \quad (A15.2)$$

$$= \alpha_2 (\beta_2 + \sigma_{nle2}) = \alpha_2 (\beta_2 + \sigma_{vis} - \sigma_{nle1}) \quad (A15.3)$$

$$= \alpha_2 (\beta_2 + \sigma_{vis} - \beta_1(\exp(\alpha_1 \varepsilon) - 1)). \quad (A15.4)$$

From equation 4.A10 the constitutive equation for the complete viscoelastic model follows as:

$$\dot{\sigma}_{cell}^{pass} = \alpha_1 \beta_1 \exp(\alpha_1 \varepsilon) \dot{\varepsilon} + \alpha_2 \left\{ \beta_2 + \sigma_{cell}^{pass} - \beta_1 (\exp(\alpha_1 \varepsilon) - 1) \right\} \left(\dot{\varepsilon} - \frac{1}{\xi} \left(\sigma_{cell}^{pass} - \beta_1 (\exp(\alpha_1 \varepsilon) - 1) \right) \right). \quad (A16)$$

Appendix 4.B: Phenomenological modelling of transient cytoskeletal contractility

Active force generation by cells under dynamic loading conditions has previously been investigated using phenomenological models for cross-bridge cycling and SF remodelling (McGarry *et al.* 2009; Reynolds and McGarry 2015). In summary, the cross-bridge tension-strain rate relationship is described by the phenomenological Hill-type relationship:

$$\frac{T}{T_0} = \begin{cases} \frac{1 - k_v \dot{\epsilon}/\eta_{al}}{1 + k_k \dot{\epsilon}/\eta_{al}}, & h < 0 \\ 1.8 - 0.8 \left(\frac{1 - k_v \dot{\epsilon}/\eta_{al}}{1 + k_k \dot{\epsilon}/\eta_{al}} \right), & h \geq 0 \end{cases} \quad (B1)$$

where $\dot{\epsilon}$ is the effective SF strain rate and k_v and k_k are model parameters. T and T_0 are the SF tension and isometric tension, respectively. η_{al} is a non-dimensional SF activation level, and its tension dependent evolution is given as

$$\frac{d\eta_{al}}{dt} = [1 - \eta_{al}]Ck_f - \left[1 - \frac{T}{T_0}\right]\eta_{al}k_b \quad (B2)$$

where C is again a non-dimensional signal and k_f and k_b are formation and dissociation rate constants (Deshpande, McMeeking, and Evans 2006). We now consider three forms of $\dot{\epsilon}$:

(i) A Hill-type model where $\dot{\epsilon}$ is taken to be the instantaneous SF strain, $\dot{\epsilon}_{sf}$, i.e. $\dot{\epsilon} = \dot{\epsilon}_{sf}$.

Results are shown in Figure 4.B1a.

(ii) A fading memory type model based on the formulation of Hunter *et al.* (1998) where $\dot{\epsilon}$ is determined from the SF strain rate history, such that

$$\dot{\epsilon} = \alpha \int_{-\infty}^t e^{-\alpha(t-\tau)} \dot{\epsilon}_{sf} d\tau. \quad (B3)$$

For a constant loading and unloading strain rate magnitude, $|\dot{\epsilon}_{sf}|$, $\dot{\epsilon}$ is given as

$$\dot{\epsilon} = |\dot{\epsilon}_{sf}| \left\{ -e^{-\alpha t} + 2e^{-\alpha(t-P/2)} - 2e^{-\alpha(t-P)} + 2e^{-\alpha(t-3P/2)} - 2e^{-\alpha(t-2P)} + 1 \right\}, \quad (B4)$$

with results shown in Figure 4.B1b.

(iii) A modified fading memory type model where only shortening (negative) strain rates contribute to $\dot{\epsilon}$, such that

$$\dot{\epsilon} = \alpha \int_{-\infty}^t e^{-\alpha(t-\tau)} \dot{\epsilon}_m d\tau, \quad (B5)$$

$$\dot{\epsilon}_m = \begin{cases} \dot{\epsilon}_{sf} & \dot{\epsilon}_{sf} \leq 0 \\ 0 & \dot{\epsilon}_{sf} > 0 \end{cases}. \quad (B6)$$

For a constant loading and unloading strain rate magnitude, $|\dot{\epsilon}_{sf}|$, $\dot{\epsilon}$ is given as

$$\dot{\epsilon} = |\dot{\epsilon}_{sf}| \left\{ e^{-\alpha(t-P/2)} - e^{-\alpha(t-P)} + e^{-\alpha(t-3P/2)} - e^{-\alpha(t-2P)} \right\}, \quad (B7)$$

With results shown in Figure 4.B1c.

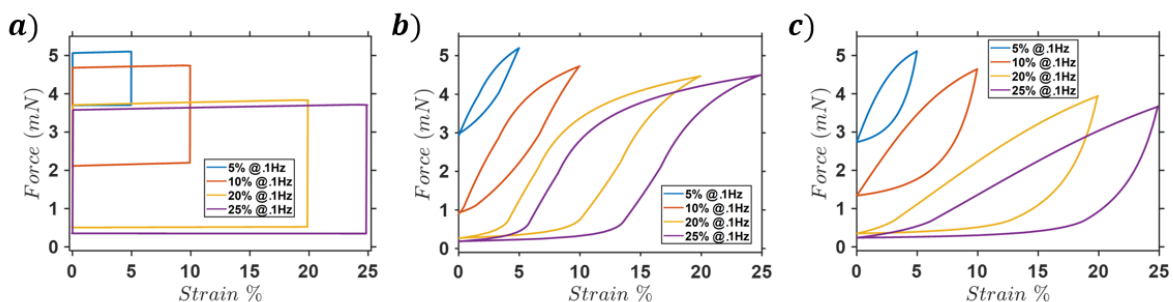


Figure 4.B1: Steady state force-strain loops for (a) Hill-type model; (b) Fading memory model; (c) Modified fading memory model.

Predicted results are shown in Figure 4.B1a. All models approximate the following features of the experimental measurements of Wille *et al.*: (i) a reduction of peak tension with increasing ϵ_{max} , and (ii) a non-zero tension at the end of each cycle for $\epsilon_{max}=5\%$ and 10% . However, the Hill-type model incorrectly predicts a nearly constant cell force during loading and unloading. The fading memory model predicts a transient change in

force during each loading cycle, but the concave-convex curve shapes do not resemble experimental curves. The modified fading memory predicts near linear behaviour during loading and a convex unloading curve. This is approximately similar to the experimental measurements of Wille *et al.*

In summary, analyses presented in this appendix using a phenomenological modelling approach demonstrate that transient cell contractility during dynamic loading cannot be replicated using a classical Hill-type contractility model. Fading memory approaches improve the predictions of transient force generation, and fading memory effective strain rates appear require an asymmetric between loading and unloading contributions.

In summary, the thermodynamically consistent mechanistically based cross-bridge cycling model and SF formulation presented in the main paper provides a physical rationalisation of the apparent fading memory behaviour in the experimental results of Wille *et al.*

Bibliography

- Abercrombie, M. 1978. "Fibroblasts." *Journal of Clinical Pathology. Supplement (Royal College of Pathologists)* 12. BMJ Publishing Group: 1–6. <http://www.ncbi.nlm.nih.gov/pubmed/365883>.
- Alberts, Bruce, Alexander Johnson, Julian Lewis, Martin Raff, Keith Roberts, and Peter Walter. 2002. *Molecular Biology of the Cell*. Garland Science.
- Balestrini, Jenna L., and Kristen L. Billiar. 2009. "Magnitude and Duration of Stretch Modulate Fibroblast Remodeling." *Journal of Biomechanical Engineering* 131 (5). American Society of Mechanical Engineers: 051005. doi:10.1115/1.3049527.
- Chung, Man-Wei, Tatiana TSOUTSMAN, and Christopher SEMSARIAN. 2003. "Hypertrophic Cardiomyopathy: From Gene Defect to Clinical Disease." *Cell Research* 13 (1). Nature Publishing Group: 9–20. doi:10.1038/sj.cr.7290146.
- Curtin, N A, and R E Davies. 1975. "Very High Tension with Very Little ATP Breakdown by Active Skeletal Muscle." *Journal of Mechanochemistry & Cell Motility* 3 (2): 147–54. <http://www.ncbi.nlm.nih.gov/pubmed/1082485>.
- Deshpande, Vikram S., Robert M. McMeeking, and Anthony G. Evans. 2007. "A Model for the Contractility of the Cytoskeleton Including the Effects of Stress-Fibre Formation and Dissociation." *Proceedings of the Royal Society A: Mathematical, Physical and Engineering Sciences* 463 (2079): 787–815.
- Deshpande, Vikram S, Robert M McMeeking, and Anthony G Evans. 2006. "A Bio-Chemo-Mechanical Model for Cell Contractility." *Proceedings of the National Academy of Sciences of the United States of America* 103 (38): 14015–20.
- Dowling, Enda P., and J. Patrick McGarry. 2014. "Influence of Spreading and Contractility on Cell Detachment." *Annals of Biomedical Engineering* 42 (5): 1037–48. doi:10.1007/s10439-013-0965-5.
- Dowling, Enda P., William Ronan, and J. Patrick McGarry. 2013. "Computational Investigation of in Situ Chondrocyte Deformation and Actin Cytoskeleton Remodelling under Physiological Loading." *Acta Biomaterialia* 9 (4): 5943–55. doi:10.1016/j.actbio.2012.12.021.
- Dowling, Enda P, William Ronan, Gidon Ofek, Vikram S Deshpande, Robert M McMeeking, Kyriacos a Athanasiou, and J Patrick McGarry. 2012. "The Effect of Remodelling and Contractility of the Actin Cytoskeleton on the Shear Resistance of Single Cells: A Computational and Experimental Investigation." *Journal of the Royal Society, Interface / the Royal Society* 9 (77): 3469–79.
- Foolen, Jasper, Vikram S. Deshpande, Frans M.W. Kanters, and Frank P.T. Baaijens. 2012. "The Influence of Matrix Integrity on Stress-Fiber Remodeling in 3D." *Biomaterials* 33 (30). Elsevier: 7508–18. doi:10.1016/J.biomaterials.2012.06.103.
- Greaser, M. L. and Gergely, J. (1971) 'Reconstitution of troponin activity from three protein components.', *The Journal of biological chemistry*, 246(13), pp. 4226–33. Available at: <http://www.ncbi.nlm.nih.gov/pubmed/4253596>
- Hara, Fumihiko, Kanji Fukuda, Shigeki Asada, Masataka Matsukawa, and Chiaki Hamanishi. 2001. "Cyclic Tensile Stretch Inhibition of Nitric Oxide Release from Osteoblast-like Cells Is Both G Protein and Actin-Dependent." *Journal of Orthopaedic Research* 19 (1). No longer published by Elsevier: 126–31. doi:10.1016/S0736-0266(00)00011-5.
- Hill, Terrell L. 1974. "Theoretical Formalism for the Sliding Filament Model of Contraction of Striated Muscle Part I." *Progress in Biophysics and Molecular Biology* 28 (January). Pergamon: 267–340. doi:10.1016/0079-6107(74)90020-0.
- Hill, A. V. 1938. "The Heat of Shortening and the Dynamic Constants of Muscle." *Proceedings of the Royal Society B: Biological Sciences* 126 (843). The Royal Society: 136–95.

doi:10.1098/rspb.1938.0050.

- Hunter, P.J., A.D. McCulloch, and H.E.D.J. ter Keurs. 1998. “Modelling the Mechanical Properties of Cardiac Muscle.” *Progress in Biophysics and Molecular Biology* 69 (March): 289–331. doi:10.1016/S0079-6107(98)00013-3.
- Huxley, A. F., and R. M. Simmons. 1971. “Proposed Mechanism of Force Generation in Striated Muscle.” *Nature* 233 (5321). Nature Publishing Group: 533–38. doi:10.1038/233533a0.
- Huxley, A F. 1957. “Muscle Structure and Theories of Contraction.” *Progress in Biophysics and Biophysical Chemistry* 7: 255–318. <http://www.ncbi.nlm.nih.gov/pubmed/13485191>.
- Kaunas, Roland, Hsu, and Deguchi. 2010. “Sarcomeric Model of Stretch-Induced Stress Fiber Reorganization.” *Cell Health and Cytoskeleton* Volume 3 (December). Dove Press: 13. doi:10.2147/CHC.S14984.
- Kovács, Mihály, Judit Tóth, Csaba Hetényi, András Málnási-Csizmadia, and James R Sellers. 2004. “Mechanism of Blebbistatin Inhibition of Myosin II.” *The Journal of Biological Chemistry* 279 (34). American Society for Biochemistry and Molecular Biology: 35557–63. doi:10.1074/jbc.M405319200.
- Langanger, G, M Moeremans, G Daneels, A Sobieszek, M De Brabander, and J De Mey. 1986. “The Molecular Organization of Myosin in Stress Fibers of Cultured Cells.” *The Journal of Cell Biology* 102 (1). Rockefeller University Press: 200–209. doi:10.1083/JCB.102.1.200.
- Lucas, S M, R L Ruff, and M D Binder. 1987. “Specific Tension Measurements in Single Soleus and Medial Gastrocnemius Muscle Fibers of the Cat.” *Experimental Neurology* 95 (1): 142–54. <http://www.ncbi.nlm.nih.gov/pubmed/2947808>.
- Lymn, R W, and E W Taylor. 1971. “Mechanism of Adenosine Triphosphate Hydrolysis by Actomyosin.” *Biochemistry* 10 (25): 4617–24. <http://www.ncbi.nlm.nih.gov/pubmed/4258719>.
- McEvoy, E., V.S. Deshpande, and P. McGarry. 2017. “Free Energy Analysis of Cell Spreading.” *Journal of the Mechanical Behavior of Biomedical Materials* 74. doi:10.1016/j.jmbbm.2017.06.006.
- McGarry, J. P., J. Fu, M. T. Yang, C. S. Chen, R. M. McMeeking, A. G. Evans, and V. S. Deshpande. 2009. “Simulation of the Contractile Response of Cells on an Array of Micro-Posts.” *Philosophical Transactions. Series A, Mathematical, Physical, and Engineering Sciences* 367 (1902): 3477–97. doi:10.1098/rsta.2009.0097.
- McMahon, TA. 1984. *Muscles, Reflexes, and Locomotion*.
- Mitrossilis, Démosthène, Jonathan Fouchard, Axel Guiroy, Nicolas Desprat, Nicolas Rodriguez, Ben Fabry, and Atef Asnacios. 2009. “Single-Cell Response to Stiffness Exhibits Muscle-like Behavior.” *Proceedings of the National Academy of Sciences of the United States of America* 106 (43). National Academy of Sciences: 18243–48. doi:10.1073/pnas.0903994106.
- Nieponice, Alejandro, Timothy M. Maul, Joy M. Cumer, Lorenzo Soletti, and David A. Vorp. 2007. “Mechanical Stimulation Induces Morphological and Phenotypic Changes in Bone Marrow-Derived Progenitor Cells within a Three-Dimensional Fibrin Matrix.” *Journal of Biomedical Materials Research Part A* 81A (3). Wiley Subscription Services, Inc., A Wiley Company: 523–30. doi:10.1002/jbm.a.31041.
- Obbink-Huizer, Christine, Cees W. J. Oomens, Sandra Loerakker, Jasper Foolen, Carlijn V. C. Bouten, and Frank P. T. Baaijens. 2014. “Computational Model Predicts Cell Orientation in Response to a Range of Mechanical Stimuli.” *Biomechanics and Modeling in Mechanobiology* 13 (1). Springer Berlin Heidelberg: 227–36. doi:10.1007/s10237-013-0501-4.
- Offer, Gerald, and K.W. Ranatunga. 2013. “A Cross-Bridge Cycle with Two Tension-Generating Steps Simulates Skeletal Muscle Mechanics.” *Biophysical Journal* 105 (4). Cell Press: 928–

40. doi:10.1016/J.BPJ.2013.07.009.

- Pathak, Amit, Robert M. McMeeking, Anthony G. Evans, and Vikram S. Deshpande. 2011. “An Analysis of the Cooperative Mechano-Sensitive Feedback Between Intracellular Signaling, Focal Adhesion Development, and Stress Fiber Contractility.” *Journal of Applied Mechanics* 78 (4). American Society of Mechanical Engineers: 041001. doi:10.1115/1.4003705.
- Rastogi, Khushboo, Mohammed Shabeel Puliyakodan, Vikas Pandey, Sunil Nath, and Ravikrishnan Elangovan. 2016. “Maximum Limit to the Number of Myosin II Motors Participating in Processive Sliding of Actin.” *Scientific Reports* 6 (1). Nature Publishing Group: 32043. doi:10.1038/srep32043.
- Reynolds, N. H., and J. P. McGarry. 2015. “Single Cell Active Force Generation under Dynamic Loading - Part II: Active Modelling Insights.” *Acta Biomaterialia* 27. Acta Materialia Inc.: 251–63. doi:10.1016/j.actbio.2015.09.004.
- Reynolds, Noel H., W. Ronan, Enda P. Dowling, P. Owens, Robert M. McMeeking, and J. Patrick McGarry. 2014. “On the Role of the Actin Cytoskeleton and Nucleus in the Biomechanical Response of Spread Cells.” *Biomaterials* 35 (13). Elsevier Ltd: 4015–25. doi:10.1016/j.biomaterials.2014.01.056.
- Smith, C. W. and Marston, S. B. (1985) ‘Disassembly and reconstitution of the Ca²⁺-sensitive thin filaments of vascular smooth muscle.’, *FEBS letters*, 184(1), pp. 115–9. Available at: <http://www.ncbi.nlm.nih.gov/pubmed/3987897>
- Smith, D.A., and M.A. Geeves. 1995. “Strain-Dependent Cross-Bridge Cycle for Muscle.” *Biophysical Journal* 69 (2): 524–37.
- Vernerey, Franck J., and Mehdi Farsad. 2011. “A Constrained Mixture Approach to Mechano-Sensing and Force Generation in Contractile Cells.” *Journal of the Mechanical Behavior of Biomedical Materials* 4 (8). Elsevier: 1683–99.
- Vigliotti, A., W. Ronan, F. P T Baaijens, and V. S. Deshpande. 2015. “A Thermodynamically Motivated Model for Stress-Fiber Reorganization.” *Biomechanics and Modeling in Mechanobiology*. Springer Berlin Heidelberg.
- Weafer, P. P., N. H. Reynolds, S. P. Jarvis, and J. P. McGarry. 2015. “Single Cell Active Force Generation under Dynamic Loading - Part I: AFM Experiments.” *Acta Biomaterialia* 27. Acta Materialia Inc.: 236–50. doi:10.1016/j.actbio.2015.09.006.
- Weafer, P. P., W. Ronan, S. P. Jarvis, and J. P. McGarry. 2013. “Experimental and Computational Investigation of the Role of Stress Fiber Contractility in the Resistance of Osteoblasts to Compression.” *Bulletin of Mathematical Biology* 75 (8): 1284–1303. doi:10.1007/s11538-013-9812-y.
- Wille, Jeremiah J., Elliot L. Elson, and Ruth J. Okamoto. 2006. “Cellular and Matrix Mechanics of Bioartificial Tissues During Continuous Cyclic Stretch.” *Annals of Biomedical Engineering* 34 (11). Kluwer Academic Publishers-Plenum Publishers: 1678–90. doi:10.1007/s10439-006-9153-1.

CHAPTER 5

COMPRESSIBILITY AND ANISOTROPY OF THE VENTRICULAR MYOCARDIUM: EXPERIMENTAL ANALYSIS AND MICROSTRUCTURAL MODELLING



5.1. Introduction

Development of accurate models for tissue reorganisation and device implantation is of central importance in heart disease research, and requires a fundamental understanding of the structure and mechanics of ventricular myocardium. LeGrice *et al.* (1995) revealed the laminar structure of the myocardium and mapped the myofibre orientations throughout the ventricle wall, while nonlinear anisotropic tissue behaviour has been identified under biaxial and shear loading conditions (Demer and Yin 1983; Dokos *et al.* 2002; Sommer *et al.* 2015). Such investigations provide valuable insight into the role of the non-contractile tissue components in cardiac function, and motivated the development of a constitutive law for simulating the passive ventricular myocardium (Holzapfel and Ogden 2009).

Incompressibility is commonly assumed in the computational modelling of some soft tissues (primarily due to the fluid content within cells and interstitial components), though recent investigations have challenged such assumptions (Nolan and McGarry 2016; Yossef *et al.* 2017). The incompressible condition for myocardium is supported by a study from Vossoughi and Patel (1980). However, Ashikaga *et al.* (2008) revealed there are regional changes in the myocardial volume up to 10% during the cardiac cycle that cannot be fully accounted for by movement of blood through the vasculature. Recent computational investigations have also highlighted the need for further evidence (Göktepe *et al.* 2011; Soares *et al.* 2017). In Section 5.2 of this paper the compressibility of myocardial tissue is quantified through a joint experimental-computational investigation, revealing changes in volume of passive excised porcine myocardium tissue under both tensile and confined compression loading conditions. An appropriate nonlinear hyperelastic model is identified to capture the observed compressible mechanical behaviour of the myocardium. This compressible model is then combined with the well-established Holzapfel-Ogden model for the anisotropic contribution of myocardium fibres (Holzapfel and Ogden 2009), providing a full volumetric-isochoric-anisotropic hyperelastic model for the passive behaviour of the myocardium.

While an accurate continuum description of the myocardium is extremely useful in tissue- and organ-level simulations, the tissue microstructure must be considered in order to better understand the factors that contribute to observed tissue anisotropy and compressibility. Microstructural models have previously been developed to examine the structure and function of biological tissues. The work of Ahmadzadeh *et al.* (2015) investigated the volume reduction observed in tendons under tensile loading. Other studies have developed micromechanical models to understand cellular loading conditions in bone marrow (Vaughan *et al.* 2015) and cartilage (Dowling *et al.* 2013). However, to the best of our knowledge, such modelling approaches have yet to be applied

to the myocardium. In Section 5.3 we develop an RVE of the myocardial tissue to (i) parse the contribution of the solid and vascular tissue components to myocardium compressibility, and (ii) investigate the influence of micro-scale fibre alignment and dispersion on tissue-level mechanical behaviour.

5.2. Compressibility and continuum modelling of myocardium

In this section of this paper we examine the myocardium at the macro-scale. Previous histological studies have shown that the myocardium has a laminar architecture (LeGrice *et al.* 1995), composed primarily of cardiomyocytes that bind end to end forming myofibrillar structures. Parallel arrangements of myofibres are bound by endomysial collagen which, along with other collagenous components and elastin, form individual myolaminae (sheets). These sheets vary in orientation throughout the myocardium. This makes it possible to define a local right-hand orthogonal set of axes to define the myofibre (f) direction, the cross-fibre or sheet (s) direction, and the normal (n) direction to this plane. The anisotropic biaxial and isochoric shear behaviour of the myocardial tissue have been carefully characterised in previous experimental studies (Dokos *et al.* 2002; Sommer *et al.* 2015). Here we investigate the passive compressibility of the tissue. We then show that a compressible anisotropic framework accurately describes experimental data for porcine and human tissues.

5.2.1. Experimental methods

5.2.1.1. Tissue preparation

Tissue specimens are excised from porcine hearts, sourced from a certified abattoir (Brady's, Athenry, Ireland). The organs are stored at -80°C until required, and thawed in phosphate buffer solution at room temperature, in accordance with previous protocols (Nolan and McGarry 2016). The atria are removed, and a transmural base-apex cut is

taken between the posterior and anterior papillary muscles from the lateral left ventricular wall (Figure 5.1a) following the protocol of Dokos *et al.* (2002). Evans Blue dye is used to highlight the individual sheets, and 3mm sections are cut along the sheet axis. These are then cut on the face normal to the fibre-sheet plane with a circular punch (radius 3mm). The sample diameter and height is measured with an electronic Vernier callipers. As the myocardium exhibits local variations in the f and s directions, the aforementioned test specimen dimensions are chosen to be sufficiently small so as to avoid intra-specimen variations in fibre orientation (Sommer *et al.* 2015). A total of 13 samples are excised and tested.

5.2.1.2. Mechanical testing

The samples are rigidly bonded to a lower- and upper- platens using a thin layer of cyanoacrylate adhesive (Loctite, Dusseldorf, Germany), as shown in Figure 5.1b. The platens are attached to a uniaxial mechanical testing machine (Zwick Z2.5, Ulm, Germany). The lower-platen is fixed and the upper-platen is displaced in the positive normal, n , direction so that the specimen is deformed at a nominal strain rate of $= .01 \text{ s}^{-1}$ up to a stretch of 1.3. Two video-extensometer cameras (1.31 MPx, 25 fps; uEye, IDS, Obersulm, Germany; videoXtens software, Zwick, Ulm, Germany) are positioned so that sample deformation in two orthogonal planes is monitored. The recorded series of images from both orthogonal planes are used to reconstruct the 3D deformation of the specimen. Volume change during stretching is tracked using the quasi-3D methodology proposed by Nolan and McGarry (2016). A series of images from the orthogonal video-extensometer cameras are imported to and digitised in MATLAB (R2017b, Mathworks, Natick, MA, USA). The specimen is discretised into sections orthogonal to the n -axis, each of height h_i . The total volume V of the specimen at a given time-point during the experiment is computed as:

$$V = \pi \sum_{i=1}^{N-1} h_i \left(\frac{a_i + a_{i+1}}{2} \right) \left(\frac{b_i + b_{i+1}}{2} \right) \quad (5.1)$$

where the deformed section dimensions a_j and b_j at section i are determined from the digitised images of the specimen. Specimen volume is computed at 11 time-points (including the undeformed configuration) throughout the experiment for all 13 specimens.

To further investigate the volumetric deformation, confined compression testing is performed (Figure 5.1c). Specimens are prepared as previously described for the tensile experiment. Samples are placed into a rigid die of the same radius. Die walls are coated with a thin film of lubricant (Unilever petroleum jelly, London, UK) to minimise friction during specimen compression. A loading indenter attached to a mechanical testing machine (Zwick Z2.5, Ulm, Germany) compresses the specimen at a nominal axial strain rate of 0.01 s^{-1} . Due to the constraint on lateral deformation in the specimen, axial strain is equal to volumetric strain. The specimen is deformed to a volumetric strain of 0.1 and the nominal stress in the loading direction is plotted as a function of volumetric strain. A total of 13 specimens are tested.

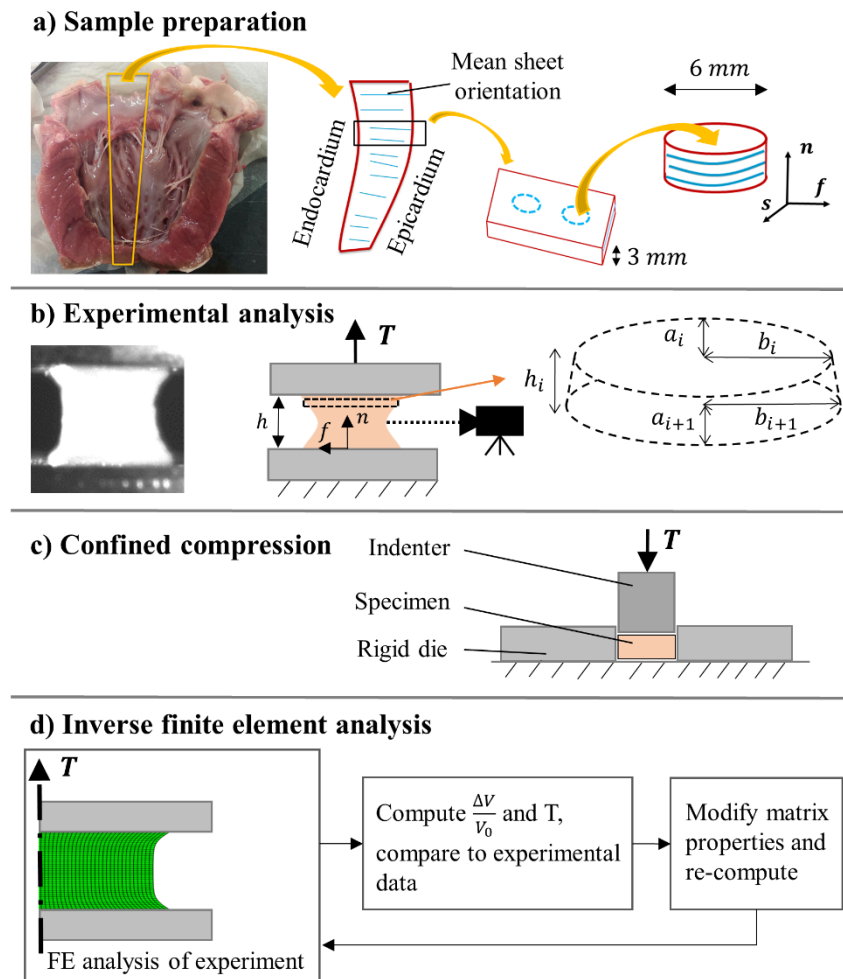


Figure 5.2: Overview of the compressibility study: a) specimen preparation from a porcine heart; b) sample is stretched between two platens and the volume change is determined; c) confined compression tests are performed to support the analysis; d) flowchart outlining the inverse FE scheme implemented to calibrate material parameters for the constitutive modelling. The experimental and simulated volume change $\Delta V/V_0$ and force T are compared.

5.2.2. Compressible constitutive law for the myocardium

Following the approach of Holzapfel and Ogden (2009), the mechanical behaviour of the myocardium is divided into an anisotropic component (to describe the muscle and collagen fibres) and an isotropic component (to describe the cell non-muscle components and elastin networks). The fibres are assumed not to contribute under shortening (compressive) loading conditions. When the specimen is stretched, as shown in Figure 5.1b, it results in a lateral shortening of the myofibre-sheet plane (on which the muscle

and collagen fibres are oriented). It is therefore assumed that the material behaviour is dominated by the isotropic component in the applied deformation.

All finite element simulations are performed using Abaqus/Standard (v6.14, DS Simulia, RI, USA). Constitutive equations are implemented via *user-defined material subroutines* (UMATs). The consistent tangent matrix is approximated numerically based on a forward difference perturbation of the deformation gradient matrix (Sun et al. 2008; Nolan *et al.* 2014). An inverse finite element (FE) scheme (Nolan and McGarry 2016) is implemented to identify a suitable constitutive model and to calibrate the associated material parameters (Figure 5.1d) using the stretch/stress and volume change data from the tensile stretching experiment (Figure 5.1b). A reduced polynomial Yeoh isotropic hyperelastic model (Yeoh 1993) is used to simulate the isotropic behaviour of the myocardium, where the stress tensor $\boldsymbol{\sigma}_{iso}$ is given as

$$\boldsymbol{\sigma}_{iso} = \sum_{i=1}^3 \kappa_i i (J - 1)^{2i-1} \mathbf{I} + \sum_{i=1}^3 \mu_i i (\bar{I}_1 - 3)^{i-1} \left(\bar{\mathbf{B}} - \frac{1}{3} \bar{I}_1 \mathbf{I} \right). \quad (5.2)$$

The first term on the right-hand side represents the hydrostatic stress contribution due to volumetric deformation, and the second term represents the deviatoric stress contribution due to isochoric deformation. The positive scalar J is the determinant of the deformation gradient \mathbf{F} , $\mathbf{B} = \mathbf{F}\mathbf{F}^T$ is the left Cauchy-Green tensor, with $\bar{\mathbf{B}} = J^{-\frac{2}{3}} \mathbf{B}$, and \mathbf{I} is the identity tensor. The first invariant I_1 is the trace of \mathbf{B} , with $\bar{I}_1 = J^{-\frac{2}{3}} I_1$, while κ_i and μ_i are volumetric and isochoric material parameters, respectively. At low strains μ_1 represents the initial shear modulus, which softens at moderate strains due to the negative value of μ_2 , and is followed by an inflection at high strains due to the positive constant μ_3 (Yeoh 1993).

The anisotropic behaviour of the myocardial tissue is well described by the Holzapfel and Ogden (2009) model, given as

$$\begin{aligned} \boldsymbol{\sigma}_{aniso} = & \sum_{m=f,s} 2a_m(I_{4m}-1) \exp[b_m(I_{4m}-1)^2] \mathbf{a}_m \otimes \mathbf{a}_m \\ & + a_{fs} I_{8fs} \exp(b_{fs} I_{8fs}^2) \mathbf{a}_f \otimes \mathbf{a}_s + \mathbf{a}_s \otimes \mathbf{a}_f, \end{aligned} \quad (5.3)$$

where the first term on the right-hand side represents the mechanical contribution in the myofibre (f) and sheet (s) directions, and the second is an orthotropic term accounting for the shear contribution in the f - s plane. I_{4f} , I_{4s} , and I_{8fs} are anisotropic invariants defined as $I_{4f} = \mathbf{a}_{0f} \cdot (\mathbf{C} \mathbf{a}_{0f})$, $I_{4s} = \mathbf{a}_{0s} \cdot (\mathbf{C} \mathbf{a}_{0s})$, and $I_{8fs} = \mathbf{a}_{0f} \cdot (\mathbf{C} \mathbf{a}_{0s})$. It has recently been shown that the full anisotropic invariants (e.g. I_{4f}) should be used in a compressible framework, as opposed to isochoric anisotropic invariants (e.g. \bar{I}_{4f}) (Nolan *et al.* 2014). The material tensor $\mathbf{C} = \mathbf{F}^T \mathbf{F}$ is the right Cauchy-Green tensor, while \mathbf{a}_{0m} ($m = f, s$) is a unit vector indicating the myofibre or sheet orientations, and \mathbf{a}_m is the same vector in the deformed configuration given by $\mathbf{a}_m = \mathbf{F} \mathbf{a}_{0m}$. The operator \otimes is the dyadic product of vectors resulting in a second-order structure tensor. a_m and b_m ($m = f, s, fs$) are anisotropic material parameters for each contribution. The total passive Cauchy stress $\boldsymbol{\sigma}_{tot}$ for the myocardial model is therefore:

$$\boldsymbol{\sigma}_{tot} = \boldsymbol{\sigma}_{iso} + \boldsymbol{\sigma}_{aniso}. \quad (5.4)$$

Initial simulations confirm that the horizontally aligned muscle and collagen fibres shorten under the applied experimental loading conditions, as shown in the Figures 5.1b and 1c. Therefore, anisotropic terms do not contribute to the material stress and the experimental data can be used to calibrate the isotropic component of the tissue model.

5.2.3. Experimental results and simulations

The experimentally measured nominal stress-stretch relationship for the tensile-stretching of porcine myocardium specimens is shown in Figure 5.2a. The observed relationship is nonlinear exhibiting both a concave and convex section with an inflection point about $\lambda \approx 1.15$. The six-parameter Yeoh model provides a good fit to the experimental data

($R^2 = .995$). Calibrated material properties are shown in Table 5.1 (porcine – isotropic). Specimen volume changes measured in the tensile-stretching experiments are shown in Figure 5.2b. Volume change increases with increasing applied stretch, reaching a value of $4.1 \pm 1.95\%$ at a stretch of 1.3. These data indicate that myocardial tissue shows compressibility. This could be the result of a volume increase in the porous extra-cellular matrix (ECM) and the vasculature. We do not expect any fluid to leave the system in such a tensile experiment when the volume is increasing. The Yeoh model also provides a reasonable fit to the volume change during the applied loading conditions ($R^2 = .951$).

Experimental results for confined compression of the myocardium are shown in Figure 5.2c. The nominal stress-volumetric strain relationship is highly nonlinear. Initially specimens exhibit little resistance to volume change, with a 5% volumetric strain occurring at a nominal stress of about 4 kPa. However, the resistance to volume change increases as the specimen is further compressed, with an applied nominal stress of 10% occurring at a nominal stress of about 49 kPa. Due to the confined nature of the experiment, and the proximity of the indenter to the compression rigid die wall, it is expected that the fluid loss in the system will not be significant. Using the Yeoh model (with parameters calibrated from the data in Figure 5.2a) a good fit to the nominal stress-volumetric strain relationship during confined compression is obtained ($R^2 = .985$). In summary, the following key points should be noted: (i) the experimental data presented in Figures 5.2b and 5.2c show that the myocardium undergoes significant volumetric strain under two distinctly different loading modes (positive volumetric strain during tensile stretching and negative volumetric strain during confined compression); (ii) a six-parameter compressible Yeoh hyperelastic material law can describe the material behaviour (including volume change) for both loading modes.

The compressible isotropic component of the myocardium constitutive law, equation 5.2, calibrated for porcine tissue in Figure 5.2a, is used in parallel with the anisotropic component of the model equation 5.3 to simulate the simple shear experiments of Dokos *et al.* (2002). The anisotropic parameters are calibrated to the experimental data using an inverse FE scheme whereby 6 modes of shear are simulated. While the material response to ns and nf shear is described by the isotropic terms (with parameters previously calibrated to the volumetric experiments), the stress state associated with sn , sf , fn , and fs shear modes is dominated by the anisotropic terms. As shown in Figure 5.3a this framework provides an accurate description of experimental porcine myocardium data, with the associated anisotropic material parameters reported in Table 5.1 (porcine). A detailed description of the individual modes of shear is provided in Section 5.3 of this paper.

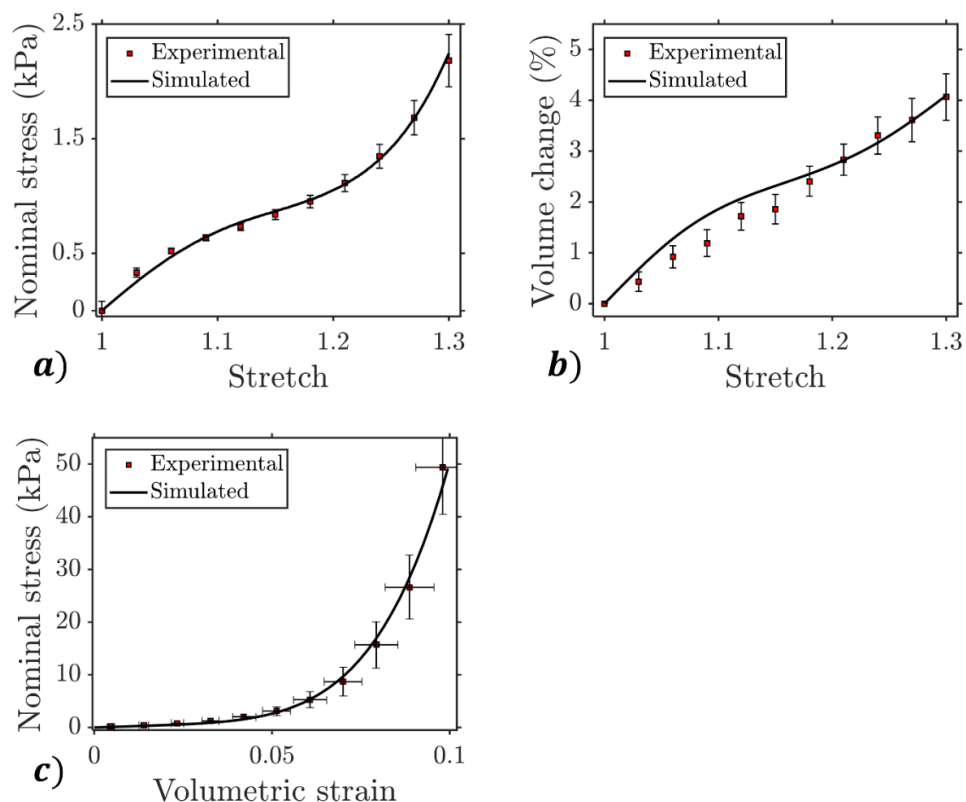


Figure 5.3: a) Experimental (mean \pm sem) and simulated nominal stress (kPa) during stretch of the myocardium specimens; b) experimental (mean \pm sem) and simulated volume change (%) during stretch. c) experimental (mean \pm sem) and simulated nominal stress (kPa) during confined compression.

	<i>Isotropic</i>						<i>Anisotropic</i>					
	μ_1 (kPa)	μ_2 (kPa)	μ_3 (kPa)	κ_1 (kPa)	κ_2 (kPa)	κ_3 (kPa)	a_f (kPa)	b_f (-)	a_s (kPa)	b_s (-)	a_{fs} (kPa)	b_{fs} (-)
<i>Porcine</i>	2.44	-6.04	14.56	18.23	145.8	1.6×10^6	28.21	20.06	2.15	29.8	.38	10.89
<i>Human</i>	.98	-.212	22.68	7.31	5.12	2.49×10^6	2.75	32.1	1.06	30.1	.175	5.02

Table 5.1: Isotropic and anisotropic parameters for porcine and human myocardium.

5.2.4. Modelling the behaviour of human tissue

The mechanical behaviour of human myocardial tissue under simple shear and biaxial loading was recently documented in a study by Sommer *et al.* (2015). The myocardium model presented in Section 5.2.2 is shown to describe the reported shear stress (Figure 5.3b), with the parameter set (determined via inverse FE) provided in Table 5.1 (human). In a biaxial test the relationship between the experimentally measured force and the material stress is complex, as has been highlighted recently by Nolan and McGarry (2016). Therefore, to simulate the reported biaxial data, an inverse finite element analysis scheme must be implemented whereby the experimental boundary conditions are applied. In the case of the experiments of Sommer *et al.* (2015), 25 x 25 x 2.3mm samples were excised, with the mean myofibre direction (MFD) and sheet direction (CFD) along the x and y axis, respectively. Five hooks were placed equidistant on each edge of the specimen. The material stretch was recorded by tracking markers located proximal to the sample centre. These conditions are replicated in a 3D axisymmetric finite element model, with the hook tension described by nodal displacements. As per the experiment the stretch is recorded at the marker positions, with the hook/nodal displacement adjusted accordingly to ensure an equibiaxial (1:1) 10% strain. The simulated strain non-uniformity in the tissue is shown in Figure 5.3c, and a reasonable description of the biaxial stress state is achieved (Figure 5.3d).

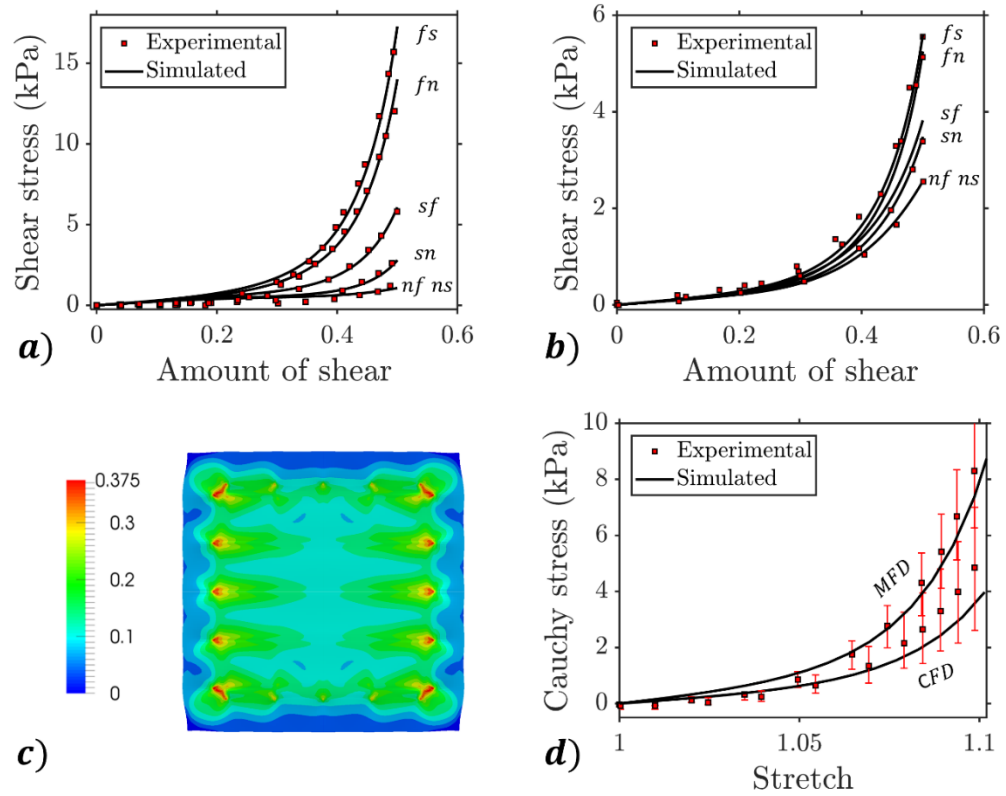


Figure 5.4: Experimental and simulated shear behavior for (a) porcine (Dokos *et al.* 2002) and (b) human myocardium (Sommer *et al.* 2015) ; (c) maximum principal strain in a simulated biaxial sample; (d) experimental and simulated biaxial behavior for human myocardium (Sommer *et al.* 2015), with stretch in the mean myofibre (MFD) and cross-fibre (CFD) directions.

While the aforementioned Holzapfel and Ogden (2009) model assumes that the anisotropic behaviour of the tissue is confined to tensile loading, the question of material anisotropy in compression is briefly discussed in Appendix 5.A.

5.3. Microstructural modelling

In this section a multifaceted microstructural model of the myocardium is developed to replicate the complex experimental behaviour shown in Figures 5.2 and 5.3. In the experimental analyses of Section 5.2 it is assumed that the tissue is unperfused, and therefore the empty vasculature may contribute to the recorded volumetric deformation. A representative volume element (RVE) is generated as motivated by histological studies, and experimental confined compression is simulated to assess this contribution. Additionally, several modes of simple shear are applied to the RVE to investigate the mechanical significance of fibre stiffness and arrangement on a micro-scale.

An RVE of the myocardium is created, comprised of discrete regions to describe cardiomyocytes, the extracellular matrix, and the vasculature. Several histological and SEM images were analysed to motivate a $2.7 \times 10^6 \mu\text{m}^3$ RVE cuboidal structure (Stoker *et al.* 1982; LeGrice *et al.* 1995; Yin *et al.* 1996; Hein *et al.* 2003), which is generated in Abaqus 6.14 with the following geometry: the cardiomyocytes are assumed to account for approximately 60% of the tissue volume, with a typical width of $15 \mu\text{m}$ and a cuboidal shape. Circular capillaries occupy approximately 5% of the volume, with a mean diameter of $5 \mu\text{m}$. The remainder of the RVE is accounted for by the extracellular matrix (ECM), which is largely composed of perimysial and endomysial collagen fibres (Figure 5.4). In this analysis the mechanical contribution of other cell phenotypes (such as cardiac fibroblasts) are not considered. A thick band of ECM separates individual myocardial sheets, with a typical thickness of $10 \mu\text{m}$.

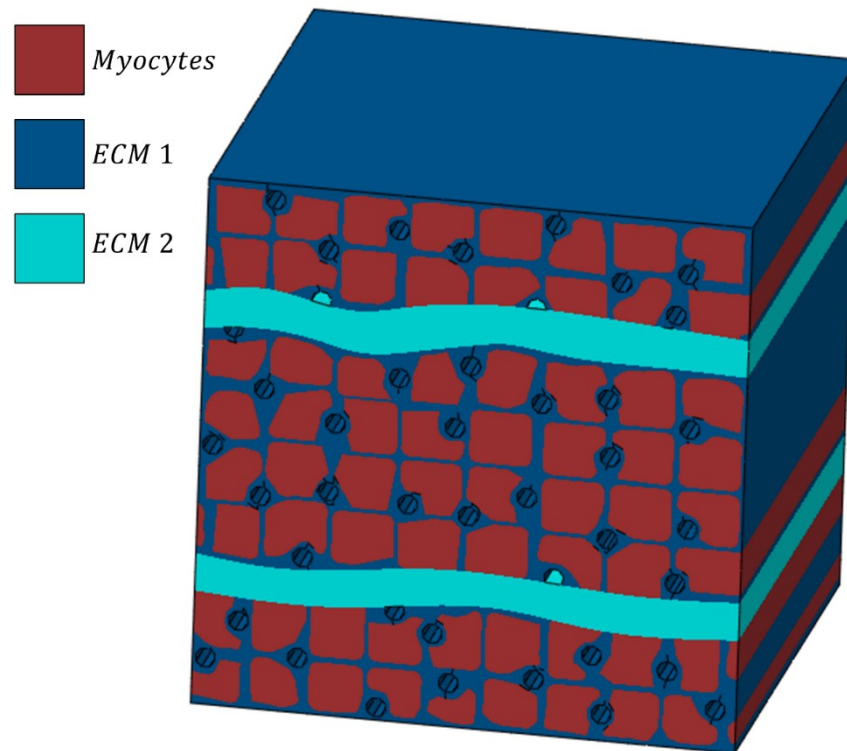


Figure 5.5: RVE of the myocardium with discrete regions for the cardiomyocytes, the matrix surrounding the cells (ECM 1), and the matrix surrounding the myocardial sheets (ECM 2). Capillaries are included as empty vessels.

5.3.1. RVE constituent materials

In order to investigate the influence of microstructural morphology and composition on tissue-level mechanical behaviour, we attempt to replicate the shear and confined compression data shown in Section 5.2 using a multi-component RVE (Figure 5.4). It should be noted that the continuum level sheet-fibre constitutive law of Holzapfel and Ogden is not used at the microstructure level. Rather, the architecture and distribution of collagen fibres and cells are explicitly represented, and a single fibre HGO formulation is used to represent the passive material behaviour of each component.

5.3.1.1. Fibre anisotropic contribution

Collagen and muscle fibres are represented by a hyperelastic model, proposed by Holzapfel *et al.* (2000), and recently modified for compressible materials by Nolan *et al.* (2014). The fibre stress is given by:

$$\sigma_{f,i} = \begin{cases} \frac{2}{J} k_1 (I_{4i} - 1) \exp[k_2 (I_{4i} - 1)^2], & I_{4i} > 1, \\ 0, & \text{otherwise,} \end{cases} \quad (5.5)$$

where $\sigma_{f,i}$ is the Cauchy stress of a single fibre family, I_{4i} is the anisotropic invariant defined by $I_{4i} = \mathbf{a}_{0i} \cdot (\mathbf{C} \mathbf{a}_{0i})$, and k_1 and k_2 are material constants. The fibres only contribute to the stress when in tension (i.e. $I_{4i} > 1$). The anisotropic stress tensor is given as

$$\boldsymbol{\sigma}_{aniso} = \sum_{i=1}^n \sigma_{f,i} \mathbf{a}_i \otimes \mathbf{a}_i, \quad (5.6)$$

where n is the number of fibre families, \mathbf{a}_{0i} is a unit vector indicating the myofibre or sheet orientations, and \mathbf{a}_i is the same vector in the deformed configuration given by $\mathbf{a}_i = \mathbf{F} \mathbf{a}_{0i}$.

5.3.1.2. Fibre dispersion

In order to account for dispersion of collagen fibres about a mean direction in the ECM, we implement a model adapted from the angular integration framework (Holzapfel and Ogden 2015), whereby the fibre directions are discretely modelled. This allows for an exclusion of the mechanical contribution of all fibres under compression. We consider that fibres can exist in a large number of discrete directions m in a 3D sphere at each integration point of a finite element model ($m = 240$ is found to provide a converged solution). This approach is adapted from the methodology of Ronan *et al.* (2012) for modelling cellular stress fibre formation. The probability density function for dispersion is described by a von Mises distribution (Li, Ogden, and Holzapfel 2016), where the distribution factor in a given direction is expressed as

$$\rho_j = \frac{4\sqrt{b}}{2\pi} \frac{\exp\left[2b(\mathbf{a}_{0,j} \cdot \mathbf{a}_{0,Mean})^2\right]}{\operatorname{erfi}(\sqrt{2b})}, \quad (5.7)$$

where b is a constant dispersion parameter, $erfi(x)$ denotes the imaginary error function, $\mathbf{a}_{0,Mean}$ is a unit vector indicating the mean fibre direction, and $\mathbf{a}_{0,j}$ is a unit vector indicating one of m directions. The distribution is normalized such that

$$\frac{1}{4\pi} \int_{\Omega} \rho(\mathbf{a}) d\Omega = 1, \quad (5.8)$$

where Ω is a unit sphere. The fibre stress, i.e. equation 5.5, is computed in all m directions.

The contribution of the dispersed fibres to the Cauchy stress tensor is then given as:

$$\boldsymbol{\sigma}_{aniso}^{disp} = \sum_{j=1}^m \rho_j \sigma_{f,j} \mathbf{a}_j \otimes \mathbf{a}_j. \quad (5.9)$$

This discrete dispersion model is validated against the generalized structure tensor (GST) model (Gasser *et al.* 2006). In the GST model fibres under compression are not necessarily excluded, as the tension condition is dependent only on stretch in the mean fibre direction. Applied ns shear of a unit cube is simulated for a single fibre family in the s - n plane, with the mean fibre direction rotated 60° from the s -axis. In the GST model the dispersion depends on parameter d . Three cases of dispersion are compared (i.e. slight dispersion [$b=10$, $d = 0.02$], intermediate dispersion [$b=1.5$, $d = 0.14$], and near isotropic dispersion [$b=0.1$, $d = 0.24$]). In all cases $k_1/\mu = 5$ and $k_2 = 0.01$ (Figure 5.5).

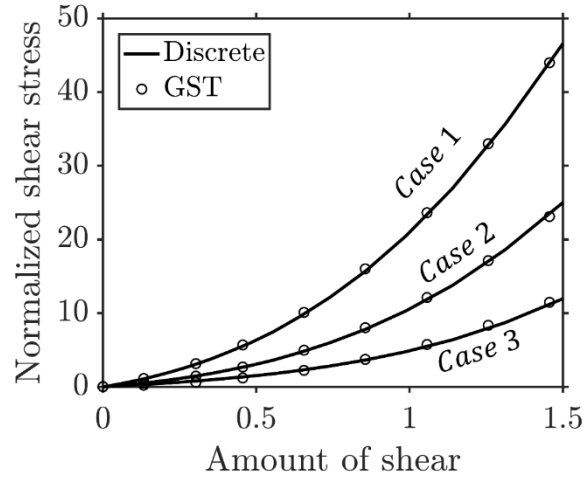


Figure 5.6: Discrete model (solid curve) and GST model (circles) for three cases of dispersion: Case 1 (slight dispersion) with $b=10$, $d = 0.02$; Case 2 (intermediate dispersion) with $b=1.5$, $d = 0.14$; Case 3 (near isotropic dispersion) with $b=0.1$, $d = 0.24$. The shear stress is normalized by the isotropic shear modulus μ , according to τ/μ .

5.3.1.3. Material isotropy

In all regions of the RVE we consider the presence of an underlying isotropic material described by a simple neo-Hookean hyperelastic model, with the Cauchy stress

$$\boldsymbol{\sigma}_{iso} = \kappa(J - 1)\mathbf{I} + \frac{\mu}{J} \left(\bar{\mathbf{B}} - \frac{1}{3} \bar{I}_1 \mathbf{I} \right). \quad (5.10)$$

The first term on the right-hand side represents the hydrostatic stress contribution due to volumetric deformation, and the second term represents the deviatoric stress contribution due to isochoric deformation, while κ and μ are the bulk modulus and shear modulus, respectively.

5.3.1.4. Physiological motivation for fibre alignments

The cardiomyocytes are described by a single fibre model in order to represent highly aligned myofibrils equation 5.6 in a nearly-incompressible isotropic cytoplasm equation 5.10. As the tissue is passive in the ex vivo experimental investigations considered in this study, active cellular contractility is not considered. Pope *et al.* (2008) investigated the organisation of collagen in the matrix surrounding the cardiomyocytes through extended volume confocal microscopy (EVCM). Thick perimysial collagen fibres were observed

to run parallel to the cells, and therefore contribute to the high stresses reported for tissue stretch in the fibre direction. These fibres are represented by the single fibre model described previously, i.e. equation 5.6. The orientation of the perimysial fibres that surround the myocardial sheets is more difficult to discern from EVCM. We investigate here the arrangement of these fibres through a dispersion model i.e. equation 5.9. The cardiomyocytes are bound together by endomysial collagen, and this is also described by fibre dispersion. The remaining constituents of the ECM are described by a compressible isotropic neo-Hookean model. Such a matrix (with embedded collagen fibres) has been shown to be compressible in several soft tissues (Yossef *et al.* 2017; Nolan and McGarry 2016; Böl *et al.* 2015), suggesting it is likely the source of non-vascular volume changes in the myocardium. The capillaries are modelled as empty inclusions. The relevant components of the Cauchy stress terms for each region are summarised in Table 5.2. As per Section 5.2, constitutive equations are implemented in the finite element software Abaqus through *user-defined material subroutines* (UMATs).

5.3.1.5. Boundary conditions and simulations

Periodic boundary conditions (PBCs) are applied to the model to ensure the deformation of opposing nodes remains continuous during the analysis, as per Dowling *et al.* (2013) and Vaughan and McCarthy (2011). The PBCs consist of a series of equation constraints, and can be expressed in terms of the nodal displacement. Detailed explanation on the implementation of PBCs can be found in Dowling *et al.* (2013). Confined compression in the normal (n) direction is simulated to a strain of 0.05, with deformation of s and f faces constrained in the s and f directions respectively (Figure 5.6a). Under such loading conditions all collagen and muscle fibres shorten and are, therefore, assumed not to contribute mechanically. Parametric studies are performed to determine values of shear and bulk moduli of the cells and ECM that yield a good agreement with experimental results. The elemental volumes of each region of the deformed RVE are computed to

parse the contribution of the vasculature to the total volume change. Confined compression in the fibre (f) and sheet (s) directions and resulting anisotropy is discussed briefly in Appendix 5.A. Six modes of shear were simulated on the RVE (Figure 5.6) with an applied shear strain of 0.5 in each case. Parametric analyses of fibre stiffness, dispersion, and fibre orientations of each region are performed to obtain a good agreement with experimental data. A mesh sensitivity study shows that a converged solution is obtained with 293,776 eight node hexahedral elements. Best-fit parameters are determined for: (i) porcine myocardium (Dokos *et al.* 2002), and (ii) human myocardium (Sommer *et al.* 2015).

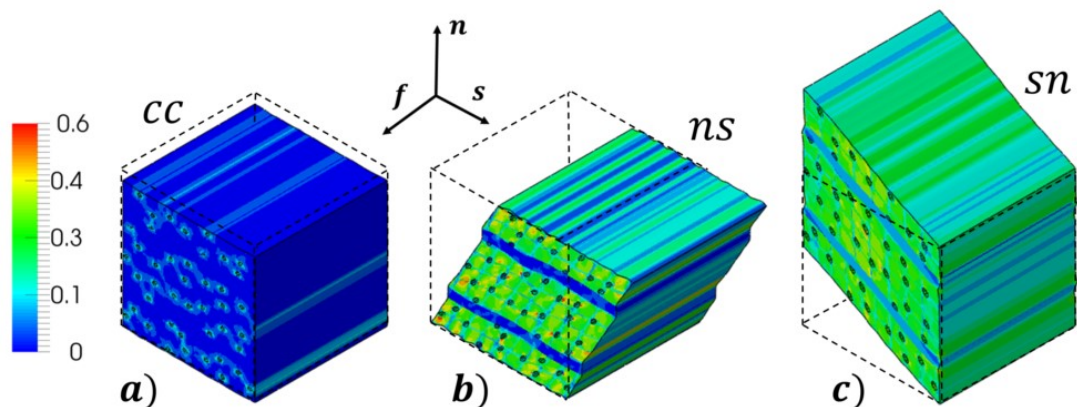


Figure 5.6: Maximum principal strain following loading of the RVE: (a) confined compression, cc; (b) shear in the ns plane; and (c) shear in the sn plane.

5.3.2. RVE results and discussion

In confined compression simulation all fibres shorten and therefore do not contribute mechanically. Under such loading the RVE stress state is governed by the isotropic elastic behaviour of the cells and the ECM. As the cardiomyocytes are considered nearly-incompressible, a high bulk modulus to shear modulus ratio was enforced in the cell regions of the RVE (Table 5.2). When the isotropic component of the ECM material is found to be slightly compressible (Table 5.2), a reasonable description of the experimental nominal stress-volumetric strain relationship is obtained (Figure 5.7a). As

shown in Figure 5.6a, the strain field throughout the RVE is non-uniform, with significant localised stress and strain concentrations in the material surrounding the capillaries. Figure 5.7b shows the simulated change in volume for each component of the RVE. At an applied confined compression strain of 0.05, the vascular volume decreases by 51.8%, the sheet matrix (ECM2) by 6.2%, the matrix surrounding the cells (ECM1) by 6.98%, and the cardiomyocytes by 0.5%. In summary, the vasculature is predicted to contribute about 42% of the total volume change during confined compression to a strain of 0.05, with the remaining volume change occurring primarily in the collagen ECM.

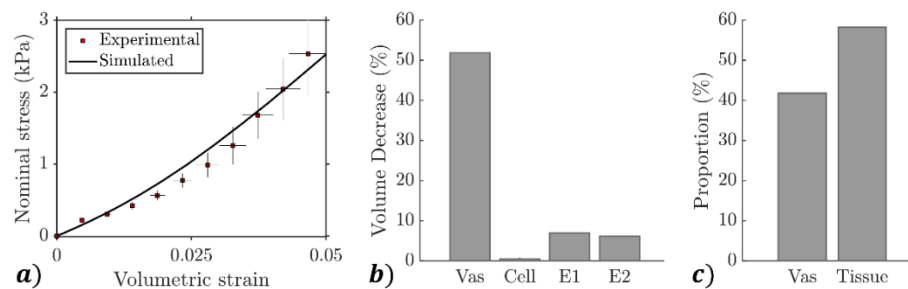


Figure 5.7: a) Experimental and simulated (from RVE) stress for confined compression; b) volume decrease of each region following compression (i.e. the vasculature, cells, ECM1 and ECM2); c) proportion that the vascular and solid components account for the total volume change.

We next apply six modes of shear deformation to the RVE to investigate the orientation and stiffness of collagen fibres in the ECM and myofibrils in the cells. A parametric study comprising of 140 simulations ($\sim 14e3$ CPU core hours) was performed in order to uncover fibre orientations and stiffness in each region of the RVE so that a good description of the experimental results of Dokos *et al.* (2002) is obtained. As shown in Figure 5.8a, the model parameters presented in Table 5.2 provide an accurate description of the multi-axial shear behaviour of porcine myocardium, i.e. $fs > fn \gg sf > sn > nf \cong ns$. Analyses uncover the key constituents contributing to the stress under each loading condition. Non-linearity in the ns and nf shear stress is dependent on dispersion of both the endomysial collagen surrounding the myocytes, and the perimysial collagen

surrounding the myolaminae (sheets). Correct trends are described only if the dispersion of perimysial fibres is included. The high stiffness response to sn and sf shear deformation is also primarily due to perimysial fibres, which have a dominant alignment in the sheet (s) direction. Myofibres in the cells and perimysial collagen fibres that run parallel to the cells provide a dominant contribution to the high stresses observed in fn and fs shear deformation. The difference in the fs and fn stress is caused by dispersion of the perimysial collagen fibres that surround the myolaminae.

A similar parameter study was performed for human myocardium data (Sommer *et al.* 2015), again achieving an excellent representation of the stress response to the six modes of simple shear (Figure 5.8b). Model parameters for human myocardium are presented in Table 5.2. There are some notable differences between the experimental observations for porcine and human tissue. The normal (n) and sheet (s) loading modes are observed to have a significantly stiffer response in the human tissue, while the fibre (f) loading modes are associated with a lower stress when compared to porcine data. These variances may be captured by alterations to the dispersion parameters and fibre stiffness, while dominant fibre orientations are similar to those determined for porcine tissue.

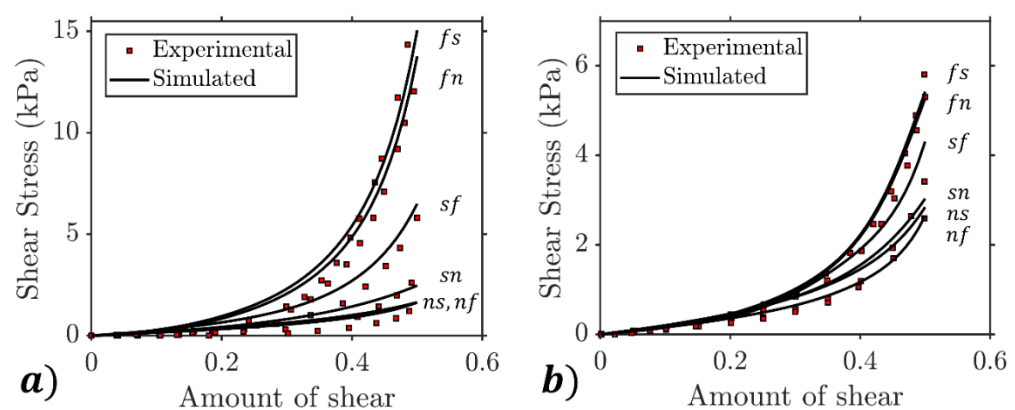


Figure 5.8: Simulated shear stress from RVE analyses of (a) porcine and (b) human tissue. Experimental data from (a) Dokos *et al.* [3] and (b) Sommer *et al.* [4] superimposed for reference.

<i>Cauchy Stress</i>		<i>Isotropic</i>		<i>Anisotropic</i>					<i>Dispersion</i>
<i>Porcine</i>		μ (kPa)	κ (kPa)	k_1 (kPa)	k_2	n	Ang (°)	Plane/Dir	b
<i>Cell</i>	Eq.(6),(10)	1.5	500	12	16	1	0.0	f	<i>N/A</i>
<i>ECM*</i> <i>(iso)</i>	Eq.(10)	1.0	40						
<i>ECM 1</i> <i>(peri)</i>	Eq.(6)			9.42	10.6	1	0.0	f	<i>N/A</i>
<i>ECM 1</i> <i>(endo)</i>	Eq.(9)			9.8	8.42	1	0.0	$n-s$	7.1
<i>ECM 2</i> <i>(peri)</i>	Eq.(9)			23	4.25	2	20.0	$s-f$	6.0
<i>Human</i>									
<i>Cell</i>	Eq.(6),(10)	1.5	500	5.3	12.4	1	0.0	f	<i>N/A</i>
<i>ECM*</i> <i>(iso)</i>	Eq.(10)	1.0	40						
<i>ECM 1</i> <i>(peri)</i>	Eq.(6)			5.2	10.1 3	1	0.0	f	<i>N/A</i>
<i>ECM 1</i> <i>(endo)</i>	Eq.(9)			12.25	8.85	1	0.0	$n-s$	7.1
<i>ECM 2</i> <i>(peri)</i>	Eq.(9)			42.0	16.2	2	31.25	$s-n$	20.6

Table 5.2: Cauchy stress terms and material parameters for RVE regions. *The isotropic component of ECM1 and ECM2 is equivalent, simply denoted as ECM (iso). In the cases where fibres are aligned in a plane, they are rotated from the first direction stated.

5.4. Concluding remarks

The compressibility of myocardial tissue is quantified through a joint experimental-computational investigation, where it is revealed that the passive tissue changes in volume under both tensile and confined compression loading conditions. We therefore suggest that the myocardium should be considered as a compressible material, and we show that both the volumetric and isochoric contributions to the isotropic component of the myocardium are highly nonlinear. The compressible isotropic hyperelastic component can be combined with the anisotropic component of the constitutive law proposed by Holzapfel and Ogden (2009) to provide a full description of the passive myocardium. The model describes the experimentally observed behaviour of porcine and human myocardial tissues. Previous studies have demonstrated there is no significant difference in the physiological mechanics of fresh and frozen/thawed arterial tissue (Adham *et al.* 1996; Stemper *et al.* 2007). However, such differences have not been specifically examined for myocardium and this may be a potential limitation of the study. Future studies are recommended to determine if freezing of samples has a significant influence on the passive mechanical behaviour of myocardial tissue. Investigation of the passive properties of freshly excised tissue would require inhibition of cross-bridge activity (Dokos *et al.* 2002; Sommer *et al.* 2015). In addition to our compressible anisotropic hyperelastic framework such studies may also consider porohyperelastic models (Ahmadzadeh *et al.* 2015; Simon *et al.* 1996) to investigate the volume change.

The change in vascular volume during the cardiac cycle has been well documented (Liu *et al.* 1992; van der Ploeg *et al.* 1993). Yin *et al.* (1996) monitored the blood volume of perfused myocardium under loading, and found the vascular volume changed by up to 40% during stretching. It was therefore important that we attempted to parse the contribution of the solid tissue and vasculature to myocardial compressibility. An RVE of the myocardium was developed for this purpose. In the regional geometry assessed

under confined compression a reduction in vascular volume accounts for 42% of the volume change, while the solid tissue components accounting for the remainder. An important outcome of this modelling insight is that even if the blood dynamics were to be explicitly included in an analysis, the solid tissue should still be considered compressible. In our investigation we assumed the vessels to be empty, but if filled with blood it is expected that the solid tissue would contribute a larger portion of the volume change. Future studies may attempt to determine if fluid is drained from the tissue during confined compression testing.

The RVE analyses also revealed the key constituents contributing to the stress under various modes of simple shear. The high stiffness reported for the fs and fn modes is due to stretching of the myofibres within the cells and the perimysial collagen that runs parallel to the cells. Dispersion of endomysial collagen and the perimysial fibres that surround the myolaminae dominate the RVE response to the ns and nf shear modes. The RVE developed in this study is based on published anatomical images (Stoker *et al.* 1982; LeGrice *et al.* 1995; Yin *et al.* 1996; Hein *et al.* 2003) and provides new insights into the relationship between the cell/ECM micro-architecture and the tissue level mechanical behaviour. Variations in the myocardium microstructure, e.g., collagen orientation, stiffness, cell size, ECM volume, or capillary volume, will have a significant influence on the mechanical behaviour. In future work, the sensitivity of the RVE to constituent geometry (e.g. cell size, capillary density) should be investigated. Further developments of our RVE approach should incorporate the following: active dynamic contractility (Reynolds and McGarry 2015) and remodelling (McEvoy *et al.* 2017) of cardiomyocytes; mechanical contribution of cell nuclei (Reynolds *et al.* 2014); fluid-structure-interaction modelling of blood flow dynamics in capillaries. Such developments would provide a deeper insight into the effective time dependent tissue volume changes during a cardiac cycle.

Appendix 5.A: Evidence of weak anisotropy in compression

Anisotropy in the myocardium under tensile loading conditions has been well characterized experimentally, as presented in the shear and biaxial data of Figure 5.3. This data can be accurately modelled through the constitutive framework proposed by Holzapfel and Ogden (2009). In this model the anisotropic terms only contribute when the associated invariant is in tension (e.g. $I_{4f} > 1$). This is controlled by a switching statement in the *user-defined material subroutine (UMAT)*.

In the experiment described in Section 5.2, columnar samples of myocardium are stretched in the normal (n) direction. The deformation is recorded, and the volume change during the stretch is calculated. The midplane sample dimensions (see Figure 5.A1a) can be used to approximate the tissue anisotropy in compression by considering the ellipticity (i.e. a/b). At a maximum stretch ($\lambda = 1.3$), an ellipticity of $1.038 \pm .0165$ is calculated. This suggests the myocardium exhibits weak anisotropy in compression, with the lowest contracture observed in the fibre direction.

The experiment is simulated using the properties outlined in Table 5.1. We now exclude the aforementioned switch statement and allow the anisotropic terms to contribute in both tension and compression. Ellipticity values of 1.101 and 1.036 are observed for porcine and human parameters, respectively (Figure 5.A1b). In both cases the material is observed to contract less in the fibre (f) direction than in the sheet (s) direction. To investigate the influence of the microstructure on tissue anisotropy in compression, confined compression in the f , s , and n directions is simulated with the model outlined in Section 5.3. Additionally, uniaxial tension is simulated in all three directions to highlight the anisotropy in tension.

Allowing for the mechanical contribution of fibres in compression (i.e. exclusion of switch statement) in the anisotropic modelling framework offers a possible means of

describing the weak tissue anisotropy in compression, though the parameters calibrated for fibres in tension do not necessarily represent the compressive behaviour (Figure 5.A1b). A computational study by Soares *et al.* (2017) has recently demonstrated a weak mechanical contribution of a single discrete fibre subjected to compression. In the current study our RVE simulations suggest that tissue-level anisotropy will result, in part, from the micro-structural arrangement of ECM and cells, even in the absence of a fibre contribution under compression. The simulated microstructural anisotropic stress under confined compression is presented in Figure 5.A1c, where clearly the tissue is slightly stiffer when compressed in the fibre (f) direction. Under tensile loading the tissue anisotropy is significantly more pronounced due to the additional contribution of complex fibre distributions (Figure 5.A1d).

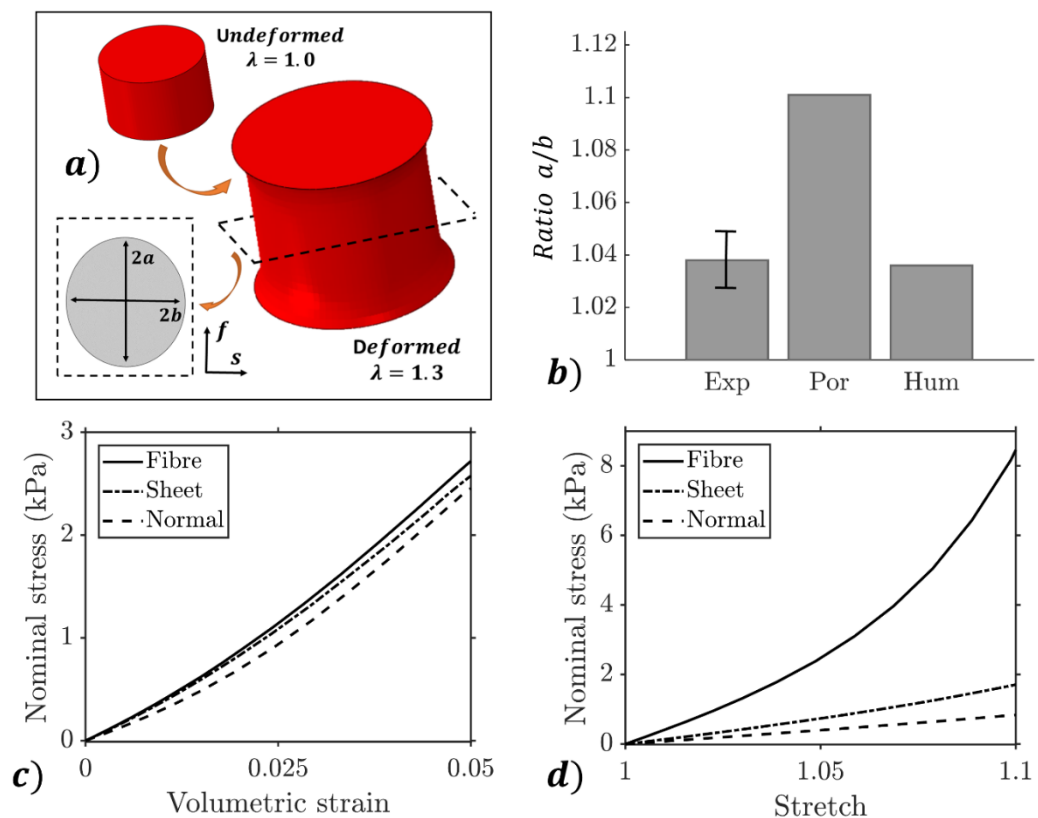


Figure 5.A1: a) Cross-section taken at midplane of simulated tensile experiment to measure ellipticity; b) experimental and simulated ellipticity with porcine and human material parameters; c) simulated nominal stress (kPa) vs volumetric strain for a simulated micro-model confined compression in f , s , and n directions; d) simulated nominal stress (kPa) vs stretch for the micro-model under tensile loading.

Bibliography

- Adham, M, J P Gournier, J P Favre, E De La Roche, C Ducerf, J Baulieux, X Barral, and M Pouyet. 1996. "Mechanical Characteristics of Fresh and Frozen Human Descending Thoracic Aorta." *The Journal of Surgical Research* 64 (1). Elsevier: 32–34. doi:10.1006/jsre.1996.0302.
- Ahmadzadeh, Hossein, Benjamin R. Freedman, Brianne K. Connizzo, Louis J. Soslowsky, and Vivek B. Shenoy. 2015. "Micromechanical Poroelastic Finite Element and Shear-Lag Models of Tendon Predict Large Strain Dependent Poisson's Ratios and Fluid Expulsion under Tensile Loading." *Acta Biomaterialia* 22. Acta Materialia Inc.: 83–91. doi:10.1016/j.actbio.2015.04.035.
- Ashikaga, Hiroshi, Benjamin a Coppola, Katrina G Yamazaki, Francisco J Villarreal, Jeffrey H Omens, and James W Covell. 2008. "Changes in Regional Myocardial Volume during the Cardiac Cycle: Implications for Transmural Blood Flow and Cardiac Structure." *American Journal of Physiology. Heart and Circulatory Physiology* 295: H610–18. doi:10.1152/ajpheart.00107.2008.
- Böl, Markus, Alexander E Ehret, Kay Leichsenring, and Michael Ernst. 2015. "Tissue-Scale Anisotropy and Compressibility of Tendon in Semi-Confined Compression Tests." *Journal of Biomechanics* 48 (6). Elsevier: 1092–98. doi:10.1016/j.jbiomech.2015.01.024.
- Demer, L L, and F C Yin. 1983. "Passive Biaxial Mechanical Properties of Isolated Canine Myocardium." *J Physiol* 339: 615–30.
- Dokos, Socrates, Bruce H Smaill, Alistair a Young, and Ian J LeGrice. 2002. "Shear Properties of Passive Ventricular Myocardium." *American Journal of Physiology. Heart and Circulatory Physiology* 283 (6): H2650–59. doi:10.1152/ajpheart.00111.2002.
- Dowling, Enda P., William Ronan, and J. Patrick McGarry. 2013. "Computational Investigation of in Situ Chondrocyte Deformation and Actin Cytoskeleton Remodelling under Physiological Loading." *Acta Biomaterialia* 9 (4): 5943–55. doi:10.1016/j.actbio.2012.12.021.
- Gasser, T. Christian, Ray W Ogden, and Gerhard A Holzapfel. 2006. "Hyperelastic Modelling of Arterial Layers with Distributed Collagen Fibre Orientations." *Journal of The Royal Society Interface* 3 (6). <http://rsif.royalsocietypublishing.org/content/3/6/15.short>.
- Göktepe, S., S. N. S. Acharya, J. Wong, and E. Kuhl. 2011. "Computational Modeling of Passive Myocardium." *International Journal for Numerical Methods in Biomedical Engineering* 27 (1). John Wiley & Sons, Ltd.: 1–12. doi:10.1002/cnm.1402.
- Hein, Stefan, Eyal Arnon, Sawa Kostin, Markus Schönburg, Albrecht Elsässer, Victoria Polyakova, Erwin P. Bauer, Wolf-Peter Klövekorn, and Jutta Schaper. 2003. "Progression From Compensated Hypertrophy to Failure in the Pressure-Overloaded Human Heart." *Circulation* 107 (7). <http://circ.ahajournals.org/content/107/7/984.full>.
- Holzapfel, Gerhard A., Thomas C. Gasser, and Ray W. Ogden. 2000. "A New Constitutive Framework for Arterial Wall Mechanics and a Comparative Study of Material Models." *Journal of Elasticity* 61 (1–3): 1–48. doi:10.1023/A:1010835316564.
- Holzapfel, Gerhard A., and Ray W. Ogden. 2015. "On the Tension–compression Switch in Soft Fibrous Solids." *European Journal of Mechanics - A/Solids* 49: 561–69. doi:10.1016/j.euromechsol.2014.09.005.
- Holzapfel, Gerhard A., and Ray W Ogden. 2009. "Constitutive Modelling of Passive Myocardium: A Structurally Based Framework for Material Characterization." *Philosophical Transactions. Series A, Mathematical, Physical, and Engineering Sciences* 367 (1902): 3445–75. doi:10.1098/rsta.2009.0091.
- LeGrice, I J, B H Smaill, L Z Chai, S G Edgar, J B Gavin, and P J Hunter. 1995. "Laminar Structure of the Heart: Ventricular Myocyte Arrangement and Connective Tissue

- Architecture in the Dog.” *Am J Physiol* 269 (2 Pt 2): H571-82. <http://www.ncbi.nlm.nih.gov/pubmed/7653621>.
- Li, Kewei, Ray W. Ogden, and Gerhard A. Holzapfel. 2016. “Computational Method for Excluding Fibers under Compression in Modeling Soft Fibrous Solids.” *European Journal of Mechanics - A/Solids* 57: 178–93. doi:10.1016/j.euromechsol.2015.11.003.
- Liu, Y H, R C Bahn, and E L Ritman. 1992. “Dynamic Intramyocardial Blood Volume: Evaluation with a Radiological Opaque Marker Method.” *The American Journal of Physiology* 263 (3 Pt 2): H963–67.
- McEvoy, E., V.S. Deshpande, and P. McGarry. 2017. “Free Energy Analysis of Cell Spreading.” *Journal of the Mechanical Behavior of Biomedical Materials* 74. doi:10.1016/j.jmbbm.2017.06.006.
- Nolan, D. R., and J. P. McGarry. 2016. “On the Compressibility of Arterial Tissue.” *Annals of Biomedical Engineering* 44 (4). Springer US: 993–1007. doi:10.1007/s10439-015-1417-1.
- Nolan, D.R., A.L. Gower, M. Destrade, R.W. Ogden, and J.P. McGarry. 2014. “A Robust Anisotropic Hyperelastic Formulation for the Modelling of Soft Tissue.” *Journal of the Mechanical Behavior of Biomedical Materials* 39. Elsevier: 48–60. doi:10.1016/j.jmbbm.2014.06.016.
- Nolan, D.R., and J.P. McGarry. 2016. “On the Correct Interpretation of Measured Force and Calculation of Material Stress in Biaxial Tests.” *Journal of the Mechanical Behavior of Biomedical Materials* 53. Elsevier: 187–99. doi:10.1016/j.jmbbm.2015.08.019.
- Pope, Adèle J., Gregory B. Sands, Bruce H. Smail, and Ian J. LeGrice. 2008. “Three-Dimensional Transmural Organization of Perimysial Collagen in the Heart.” *American Journal of Physiology - Heart and Circulatory Physiology* 295 (3). <http://ajpheart.physiology.org/content/295/3/H1243>.
- Reynolds, N. H., and J. P. McGarry. 2015. “Single Cell Active Force Generation under Dynamic Loading - Part II: Active Modelling Insights.” *Acta Biomaterialia* 27. Acta Materialia Inc.: 251–63. doi:10.1016/j.actbio.2015.09.004.
- Reynolds, Noel H., W. Ronan, Enda P. Dowling, P. Owens, Robert M. McMeeking, and J. Patrick McGarry. 2014. “On the Role of the Actin Cytoskeleton and Nucleus in the Biomechanical Response of Spread Cells.” *Biomaterials* 35 (13). Elsevier Ltd: 4015–25. doi:10.1016/j.biomaterials.2014.01.056.
- Ronan, William, Vikram S. Deshpande, Robert M. McMeeking, and J. Patrick McGarry. 2012. “Numerical Investigation of the Active Role of the Actin Cytoskeleton in the Compression Resistance of Cells.” *Journal of the Mechanical Behavior of Biomedical Materials* 14. Elsevier: 143–57. doi:10.1016/j.jmbbm.2012.05.016.
- Simon, B. R., M. V. Kaufmann, M. A. McAfee, and A. L. Baldwin. 1996. “Porohyperelastic Theory and Finite Element Models for Soft Tissues with Application to Arterial Mechanics.” In , 245–61. Springer, Dordrecht. doi:10.1007/978-94-015-8698-6_14.
- Soares, Joao S., David S. Li, Eric Lai, Joseph H. Gorman III, Robert C. Gorman, and Michael S. Sacks. 2017. “Modeling of Myocardium Compressibility and Its Impact in Computational Simulations of the Healthy and Infarcted Heart.” In , 493–501. Springer, Cham. doi:10.1007/978-3-319-59448-4_47.
- Soares, João S., Will Zhang, and Michael S. Sacks. 2017. “A Mathematical Model for the Determination of Forming Tissue Moduli in Needled-Nonwoven Scaffolds.” *Acta Biomaterialia* 51 (March). Elsevier: 220–36. doi:10.1016/J.ACTBIO.2016.12.038.
- Sommer, Gerhard, Andreas J. Schriefl, Michaela Andrä, Michael Sacherer, Christian Viertler, Heimo Wolinski, and Gerhard A. Holzapfel. 2015. “Biomechanical Properties and Microstructure of Human Ventricular Myocardium.” *Acta Biomaterialia* 24 (September): 172–92. doi:10.1016/j.actbio.2015.06.031.

- Stemper, Brian D, Narayan Yoganandan, Michael R Stineman, Thomas A Gennarelli, Jamie L Baisden, and Frank A Pintar. 2007. "Mechanics of Fresh, Refrigerated, and Frozen Arterial Tissue." *The Journal of Surgical Research* 139 (2). Elsevier: 236–42. doi:10.1016/j.jss.2006.09.001.
- Stoker, M E, a M Gerdes, and J F May. 1982. "Regional Differences in Capillary Density and Myocyte Size in the Normal Human Heart." *The Anatomical Record* 202 (2): 187–91. doi:10.1002/ar.1092020203.
- Sun, Wei, Elliot L Chaikof, and Marc E Levenston. 2008. "Numerical Approximation of Tangent Moduli for Finite Element Implementations of Nonlinear Hyperelastic Material Models." *Journal of Biomechanical Engineering* 130 (6): 061003. doi:10.1115/1.2979872.
- van der Ploeg, C. P., J. Dankelman, and J. A. Spaan. 1993. "Functional Distribution of Coronary Vascular Volume in Beating Goat Hearts." *American Journal of Physiology - Heart and Circulatory Physiology* 264 (3). <http://ajpheart.physiology.org/content/264/3/H770.short>.
- Vaughan, T. J., M. Voisin, G. L. Niebur, and L. M. McNamara. 2015. "Multiscale Modeling of Trabecular Bone Marrow: Understanding the Micromechanical Environment of Mesenchymal Stem Cells During Osteoporosis." *Journal of Biomechanical Engineering* 137 (1). American Society of Mechanical Engineers: 011003. doi:10.1115/1.4028986.
- Vaughan, T.J., and C.T. McCarthy. 2011. "Micromechanical Modelling of the Transverse Damage Behaviour in Fibre Reinforced Composites." *Composites Science and Technology* 71 (3): 388–96. doi:10.1016/j.compscitech.2010.12.006.
- Vossoughi, Jafar, and Dali J Patel. 1980. "Compressibility of the Myocardial Tissue." *Adv Bioeng*, 45–48.
- Yeoh, O. H. 1993. "Some Forms of the Strain Energy Function for Rubber." *Rubber Chemistry and Technology* 66 (5): 754–71. doi:10.5254/1.3538343.
- Yin, F C, C C Chan, and R M Judd. 1996. "Compressibility of Perfused Passive Myocardium." *The American Journal of Physiology* 271 (20): H1864–70.
- Yossef, Ofry Efraim, Mor Farajian, Ilan Gilad, Udi Willenz, Nimrod Gutman, and Zohar Yosibash. 2017. "Further Experimental Evidence of the Compressibility of Arteries." *Journal of the Mechanical Behavior of Biomedical Materials* 65: 177–89. doi:10.1016/j.jmbbm.2016.08.013.

CHAPTER 6

CONTRACTILITY AND REMODELLING OF THE LEFT VENTRICULAR MYOCARDIUM



6.1. Introduction

Heart failure is a global pandemic affecting over 25 million people worldwide. This inability of the heart to sufficiently perfuse the body may result from pathologies such as hypertension, increased ventricle blood volume, and tissue thinning and fibrosis post-infarction. In all cases, it may be viewed as a remodelling in response to an alteration in the mechanical environment. Heart failure often follows from cardiac hypertrophy, a medical condition whereby the cardiomyocytes in the tissue wall remodel (Chung *et al.* 2003). Such hypertrophy is typically categorised as concentric or eccentric. Concentric hypertrophy is where the tissue becomes thicker (often related to aortic stiffening and hypertension). The number of parallel myofibrils in the cardiomyocytes increases, and the cells themselves also swell in size (Izumo and Nadal-Ginard 1988; Chien *et al.* 1993; Sawada and Kawamura 1991). Consequently, the ventricle volume is reduced, so that an insufficient volume of blood is available for pumping during systole. With the onset of concentric hypertrophy, there is also an increased concentration of calcium in the tissue,

thought to be due to a reduced absorption rate (Balke and Shorofsky 1998). Eccentric hypertrophy is where the ventricle becomes thinner and longer, often onset by an increased diastolic blood volume. Cardiomyocytes undergo longitudinal cell growth and addition of sarcomeres in-series (Dorn *et al.* 2003). The contractility of this thin ventricle wall is dramatically reduced, and, consequently, the volume of blood ejected during systole is reduced, despite the fact that the enlarged ventricle can store an increased volume.

Significant advances have been made in the field of cardiac modelling over the past 20 years, from a detailed imaging of the tissue myofibre micro-structure (LeGrice *et al.* 1995), to development of finite element models of anatomically accurate patient specific geometries (Wang *et al.* 2013). However, current finite element approaches typically use phenomenological formulations to represent tissue contractility (Pezzuto *et al.* 2014; Baillargeon *et al.* 2014). More detailed phenomenological models have also been developed based on experimentation that uncovered “fading memory” type behaviour in cardiomyocytes (Bergel and Hunter 1979; Hunter *et al.* 1998). In this paper we develop a model of the contractile left ventricle, with active cell tension described by the thermodynamically motivated dynamic cross-bridge model proposed by McEvoy *et al.* (2018). Simulations uncover a mechanism by which changes to the mechanical environment result in altered actin-myosin cross-bridge cycling, in turn driving remodelling of myofibrils in the heart wall. Myofibrillar remodelling associated with concentric and eccentric hypertrophy is predicted to occur following periods of hypertension and volume overload, respectively. The link between cross-bridge thermodynamics and myofibril remodelling proposed in this study may significantly advance current understanding of cardiac disease onset.

6.2. Computational methodology

6.2.1. Passive mechanics

In addition to the high density of contractile cells in the ventricle wall, the myocardium contains a complex extracellular matrix (ECM) that supports the cells, and contributes significantly to the passive material behaviour. The ECM has a laminar architecture (Legrice *et al.* 1997), composed primarily of cardiomyocytes that bind together to form myofibre structures. Parallel arrangements of myofibres are bound by endomysial collagen which, along with other collagenous components and elastin, form individual myolaminae (sheets). These sheets vary in orientation throughout the ventricle wall. With this structure it is possible to define a local right-hand orthogonal set of axes to define the myofibre (f) direction, the cross-fibre or sheet (s) direction, and the normal (n) direction to this plane. The anisotropic biaxial and isochoric shear behaviour of the tissue has been well characterized (Dokos *et al.* 2002; Sommer *et al.* 2015), and is described by the Holzapfel and Ogden (2009) model, given as

$$\begin{aligned} \boldsymbol{\sigma}_{aniso} = & \sum_{m=f,s} 2a_m(I_{4m}-1) \exp[b_m(I_{4m}-1)^2] \mathbf{a}_m \otimes \mathbf{a}_m \\ & + a_{fs} I_{8fs} \exp(b_{fs} I_{8fs}^2) (\mathbf{a}_f \otimes \mathbf{a}_s + \mathbf{a}_s \otimes \mathbf{a}_f), \end{aligned} \quad (6.1)$$

where the first term on the right-hand side represents the mechanical contribution in the myofibre (f) and sheet (s) directions, and the second is an orthotropic term accounting for the shear contribution in the f - s plane. I_{4f} , I_{4s} , and I_{8fs} are anisotropic invariants defined as $I_{4f} = \mathbf{a}_{0f} \cdot (\mathbf{C} \mathbf{a}_{0f})$, $I_{4s} = \mathbf{a}_{0s} \cdot (\mathbf{C} \mathbf{a}_{0s})$, and $I_{8fs} = \mathbf{a}_{0f} \cdot (\mathbf{C} \mathbf{a}_{0s})$. Full anisotropic invariants (e.g. I_{4f}) should be used in a compressible framework, as opposed to isochoric anisotropic invariants (e.g. \bar{I}_{4f}) (Nolan *et al.* 2014). The material tensor $\mathbf{C} = \mathbf{F}^T \mathbf{F}$ is the right Cauchy-Green tensor, while \mathbf{a}_{0m} ($m = f, s$) is a unit vector indicating the myofibre or sheet orientations, and \mathbf{a}_m is the same vector in the deformed configuration given by $\mathbf{a}_m = \mathbf{F} \mathbf{a}_{0m}$. The operator \otimes is the dyadic product of vectors resulting in a second-order

structure tensor. a_m and b_m ($m = f, s, fs$) are anisotropic material parameters for each contribution.

A recent study by McEvoy *et al.* (2018) demonstrates that the myocardium is compressible, and the isotropic component of its mechanical behaviour is accurately described by a reduced polynomial Yeoh isotropic hyperelastic model (Yeoh 1993). The Cauchy stress tensor for the isotropic compressible component of the myocardium is given as

$$\boldsymbol{\sigma}_{iso} = \sum_{i=1}^3 \kappa_i i (J - 1)^{2i-1} \mathbf{I} + \sum_{i=1}^3 \mu_i i (\bar{I}_1 - 3)^{i-1} \left(\bar{\mathbf{B}} - \frac{1}{3} \bar{I}_1 \mathbf{I} \right), \quad (6.2)$$

where the first term on the right-hand side represents the hydrostatic stress contribution due to volumetric deformation, and the second term represents the deviatoric stress contribution due to isochoric deformation. The positive scalar J is the determinant of the deformation gradient \mathbf{F} , $\mathbf{B} = \mathbf{F}\mathbf{F}^T$ is the left Cauchy-Green tensor, with $\bar{\mathbf{B}} = J^{-\frac{2}{3}} \mathbf{B}$, and \mathbf{I} is the identity tensor. The first invariant I_1 is the trace of \mathbf{B} , with $\bar{I}_1 = J^{-\frac{2}{3}} I_1$, and κ_i, μ_i are volumetric and isotropic isochoric material parameters, respectively. The total passive Cauchy stress $\boldsymbol{\sigma}^{pas}$ follows as:

$$\boldsymbol{\sigma}^{pas} = \boldsymbol{\sigma}_{iso} + \boldsymbol{\sigma}_{aniso}. \quad (6.3)$$

6.2.2. Cross-bridge modelling

Myofibrils in cardiomyocytes are comprised of individual sarcomeric structures that actively generate tension via cross-bridge cycling. Here we summarise the key equations of the cross-bridge cycling framework introduced by McEvoy *et al.* (2018). We consider a 2-state model to account for the number of attached myosin heads (motivated by the model of Huxley (1957)). Within a sarcomere, there are a number of myosin heads m_{tot} available for attachment and subsequent cycling. The rate of myosin binding is given by:

$$\frac{d\hat{m}_a}{dt} = -k_d\hat{m}_a + k_a\hat{m}_d, \quad (6.4)$$

where $\hat{m}_a = m_a/m_{tot}$ is the (normalised) number of attached myosin heads, $\hat{m}_d = \hat{m}_{tot} - \hat{m}_a$ is the (normalised) number of unattached heads. The rate coefficients k_d and k_a are derived from the chemical potentials of the attached and unattached myosin heads under conditions of thermodynamic equilibrium, such that:

$$k_a = k_d \exp\left(\frac{\Delta\mu_{cb} - \phi_m + F\Delta_m}{k_B T}\right), \quad (6.5)$$

where $\Delta\mu_{cb} = \mu_a - \mu_d$ is the enthalpy difference between the attached and unattached myosin heads, k_B is the Boltzmann constant, and T is the absolute temperature. $F\Delta_m$ is the work term, with $F = \delta\phi_m/\delta\Delta_m$. The strain energy in the myosin tail is given by

$$\phi_m = \frac{1}{2}\kappa_m\Delta_m^2, \quad (6.6)$$

where κ_m is the tail stiffness (pN/nm), and Δ_m is the strain imposed on the tail. As myosin activity is inhibited during ventricular filling due to lack of calcium signalling, lengthening conditions in the sarcomere are not considered in the current study. Therefore, the strain imposed on the myosin tail only depends on isometric and shortening conditions, i.e.

$$\Delta_m = l_s + \Delta_m^s, \quad (6.7)$$

where l_s is strain induced in the myosin tail due to a tension generating stroke (caused by a change in configuration of the myosin head), and Δ_m^s is the offset in this strain caused by shortening of the sarcomere, given by

$$\Delta_m^s = L_{sarc} \dot{\epsilon}_n t_s, \quad (6.8)$$

where L_{sarc} is the length of a half sarcomere, $\dot{\epsilon}_n$ is the sarcomere strain rate, and t_s is the period of time the myosin head remains attached during a cycle. Clearly, at isometric

conditions ($\dot{\tilde{\epsilon}}_n = 0$) Δ_m depends only on the stroke distance. The total number of myosin heads available for binding m_{tot} depends on the overlap s between the actin and myosin filaments, with the availability being a maximum at the optimum overlap s_0 . A functional form for the overlap is given by a Cauchy-type distribution:

$$\hat{s} = \frac{1}{\varepsilon_s \pi \left(1 + \left(\frac{\tilde{\epsilon}_n - \tilde{\epsilon}_{ss}}{\varepsilon_s} \right)^2 \right)} s_0, \quad (6.9)$$

where $\tilde{\epsilon}_n$ is the internal nominal strain of a sarcomere, $\tilde{\epsilon}_{ss}$ is the sarcomere strain at an optimal overlap, and ε_s is a distribution parameter. The distribution is normalized by $s_0 = 1/(\pi \varepsilon_s)$, which corresponds to an optimal overlap at $\tilde{\epsilon}_n = \tilde{\epsilon}_{ss}$. Additionally, myosin attachment in the myofibril is inhibited by a troponin-tropomyosin complex which blocks the actin binding site. An action potential in the ventricle wall triggers release of calcium, which subsequently binds to troponin and unblocks the actin binding site. Calcium release is phenomenologically described by a signal that rapidly increases to a maximum followed by an exponential decay, given by:

$$\hat{C}_{Ca^{2+}} = \begin{cases} t/t_{max} & , t < t_{max} \\ \exp\left(-\frac{t-t_{max}}{\gamma_c}\right) & , t \geq t_{max} \end{cases} . \quad (6.10)$$

Here t is the time since the most recent signal is initiated (following blood filling), t_{max} is the time at which the signal is at a maximum, and γ_c is a constant that controls the decay rate of the signal. The form of the signal is motivated by the models of Hunter *et al.* (1998) and Wong *et al.* (2013). During IVR the signal is adjusted to ensure it reduces to zero at the end of the cardiac cycle. The availability of myosin heads depends both on the calcium signal and the overlap of the actin and myosin filaments. The number of available myosin heads follows as

$$m_{tot} = \hat{s} \hat{C}_{Ca^{2+}} m_0, \quad (6.11)$$

where m_0 is the total number of myosin heads in the sarcomere. The sarcomere tension is calculated as a function of the tension in the myosin tails and the total number of active heads:

$$T_s = \hat{m}_a \kappa_m \Delta_m. \quad (6.12)$$

6.2.3. Myofibril remodelling

Within cardiomyocytes in the ventricle wall, there is a high density of contractile myofibrils composed of actin-myosin sarcomeres. These myofibrils actively generate tension via cross-bridge cycling, as described in Section 6.2.2. A thermodynamically consistent model (Vigliotti *et al.* (2015)) is used in conjunction with the aforementioned cross-bridge model to uncover the relationship between actin-myosin tension generation and remodelling at the myofibril scale. Here we summarise key equations of the sarcomere remodelling framework.

Consider an existing myofibril in its ground state with a number of sarcomeres n^R along its length. Should a nominal material strain ε_n be applied to the cell (and directly translated to the fibre), it will cause a reduction in the overlap s between the actin and myosin filaments of an individual sarcomere. Such a reduced overlap is expected to initiate a remodelling process (due to the associated increase in the internal energy). The case of an applied stretch would result in the addition of sarcomeres in-series, with the opposite occurring for a compressive strain. Following remodelling, the internal strain within a sarcomere $\tilde{\varepsilon}_n$ would differ from an applied material strain, such that

$$\tilde{\varepsilon}_n = \frac{1 + \varepsilon_n}{\hat{n}} - 1, \quad (6.13)$$

where $\hat{n} = n/n^R$. The kinetic law for remodelling is given as

$$\dot{n} = \begin{cases} -\frac{1}{\hat{n}} \left(\frac{\hat{N}_u}{\hat{\eta}} \right)^2 \left[\psi(\tilde{\varepsilon}_n) - \frac{\delta\psi}{\delta\tilde{\varepsilon}_n} (1 + \tilde{\varepsilon}_n) \right] \frac{\alpha_n}{\mu_{b0}}, & \text{if } \frac{\delta\Psi}{\delta n} \leq 0 \\ -\frac{\hat{n}}{4} \left[\psi(\tilde{\varepsilon}_n) - \frac{\delta\psi}{\delta\tilde{\varepsilon}_n} (1 + \tilde{\varepsilon}_n) \right] \frac{\alpha_n}{\mu_{b0}}, & \text{otherwise,} \end{cases} \quad (6.14)$$

where \hat{N}_u is the (normalized) number of available cytoskeletal proteins, $\hat{\eta}$ is the concentration of myofibrils, and α_n is a rate constant. The internal energy of n^R sarcomeres ψ increases as the internal strain $\tilde{\varepsilon}_n$ changes, with a functional form given by

$$\psi = \mu_{b0} + \beta \mu_{b0} |\tilde{\varepsilon}_n|^p, \quad (6.15)$$

where μ_{b0} is the internal energy of n^R sarcomeres in their ground state, and β and p are non-dimensional constants that govern the sarcomere strain at an optimal overlap $\tilde{\varepsilon}_{ss}$, such that

$$(p-1)\tilde{\varepsilon}_{ss}^p + p\tilde{\varepsilon}_{ss}^{p-1} - \frac{1}{\beta} = 0. \quad (6.16)$$

The rate of change of the internal energy follows as

$$\frac{\delta\Psi}{\delta n} \dot{n} = \dot{n} \left[\psi(\tilde{\varepsilon}_n) - \frac{\delta\psi}{\delta\tilde{\varepsilon}_n} (1 + \tilde{\varepsilon}_n) \right]. \quad (6.17)$$

Formation and dissociation of myofibrils is governed by thermodynamic equilibrium of proteins available for binding (unbound), and those already bound in sarcomeres. The standard enthalpy μ_b of n^R sarcomeres within a myofibril is written as

$$\mu_b = \psi - \sigma_f [1 + \tilde{\varepsilon}_n] \Omega, \quad (6.18)$$

where Ω is the volume of n^R sarcomeres in a myofibril. σ_f is the fibre stress, given by

$$\sigma_f = \frac{T_s}{T_{s0}} \sigma_{iso}, \quad (6.19)$$

where T_s is the sarcomere tension (determined from equations 6.4-6.12), T_{s0} is the sarcomere tension computed at steady state isometric conditions, and σ_{iso} is the

maximum isometric stress. Unbound proteins are affected by an activation signal level, and tend to transform into their bound states more readily when such signalling is increased. The standard enthalpy μ_u of unbound SF proteins follows as

$$\mu_u = \mu_{u0} + \Delta\mu_{u0}\hat{C}_{SF}, \quad (6.20)$$

where μ_{u0} is the standard enthalpy of the unbound proteins in the absence of a signal \hat{C}_{SF} and $\Delta\mu_{u0}$ is the increase in the enthalpy of the unbound molecules at full activation ($\hat{C}_{SF} = 1$). Fibre formation is initiated by a biochemical or mechanical perturbation that triggers a signalling cascade within the cell. Due to the high cycling frequency in the ventricular wall, a constant SF formation signal is assumed in this analysis. For a detailed explanation of the signalling pathways, or more rigorous signal formulations, the reader is referred to Vigliotti *et al.* (2015) and Pathak *et al.* (2011). The rate of fibre formation/dissociation follows as

$$\dot{\hat{\eta}} = \frac{\hat{N}_u}{\hat{n}} \omega_n \exp\left[-\hat{n} \frac{\mu_{ab} - \mu_u}{k_B T}\right] - \hat{\eta} \omega_n \exp\left[-\hat{n} \frac{\mu_{ab} - \mu_b}{k_B T}\right] \quad (6.21)$$

where ω_n is the collision frequency of the unbound molecules, and μ_{ab} is an activation barrier. The (normalized) number of unbound cytoskeletal proteins may be calculated as

$$\hat{N}_u = 1 - \hat{\eta}\hat{n}, \quad (6.22)$$

where $\hat{\eta}\hat{n}$ determines the (normalized) number of bound cytoskeletal proteins. As the cardiomyocytes are oriented in the previously defined myofibre (f) direction, the Cauchy stress due to fibre contractility is given by

$$\boldsymbol{\sigma}^{act} = \hat{\eta} \sigma_f f_0 \mathbf{a}_f \otimes \mathbf{a}_f, \quad (6.23)$$

where f_0 is the volume fraction of cardiomyocytes in the heart wall. Finally, the total Cauchy stress may be calculated as a function of the active and passive contributions, such that

$$\boldsymbol{\sigma}^{tot} = \boldsymbol{\sigma}^{pas} + \boldsymbol{\sigma}^{act}. \quad (6.24)$$

6.2.4. Finite element modelling

In this section, development of a 3D finite element model of the left ventricle is described. A solid model of the generic heart is created by means of a truncated ellipsoid (Figure 6.1a), motivated by the passive ventricle models of Göktepe *et al.* (2011) and Rausch *et al.* (2011), and discretized with 7435 hexahedral elements. All simulations are performed using Abaqus/Standard (v2017, DS Simulia, RI, USA), and constitutive equations are implemented via *user-defined material subroutines* (UMATs). The consistent tangent matrix is approximated numerically based on a forward difference perturbation of the deformation gradient matrix (Nolan *et al.* 2014; Sun *et al.* 2008). As mentioned previously, a local right hand orthogonal set of axes may be established, denoting the myofibre (f), sheet (s), and normal (n) directions. The sheet direction is assumed to orient normal to the endocardial and epicardial ventricle walls, while the orientation of the myofibres varies transmurally by an angle θ . This angle changes from approximately -70° at the endocardium to 70° at the epicardium, with respect to the circumferential direction and rotated about the sheet axis (Figure 6.1b). For simplicity the wall thickness is discretized into five regions, with θ assumed to be uniform within each region, as are the myofibril concentration $\hat{\eta}$ and number of in-series sarcomeres \hat{n} .

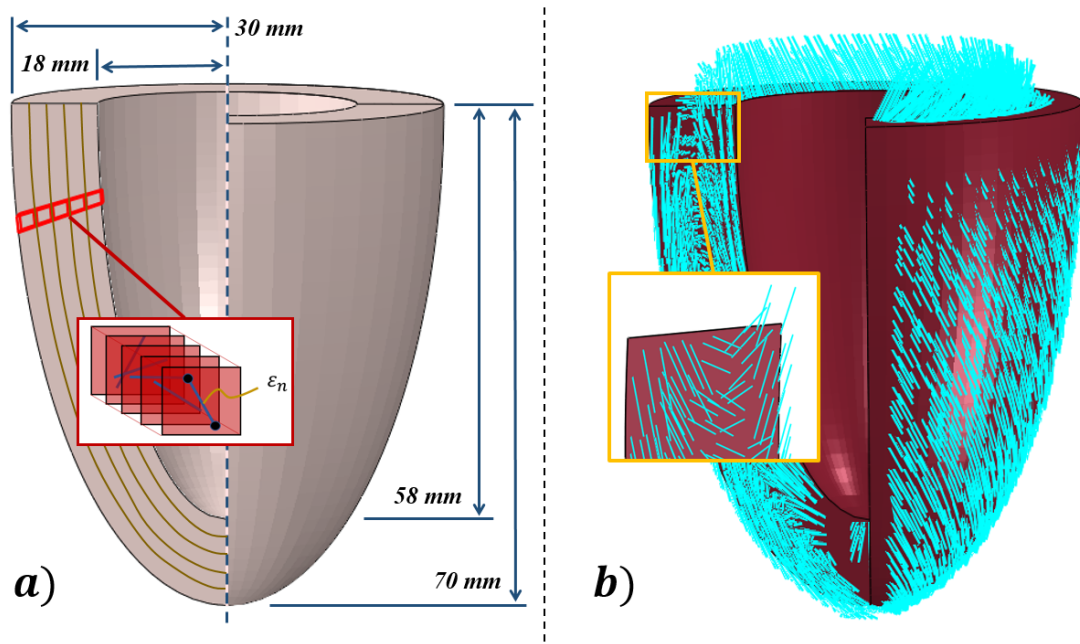


Figure 6.1: a) Geometry of an idealised left ventricle model with sub-model region highlighted in red; b) transmural variation of myofibre (f) direction

6.2.4.1. Simulation of physiological conditions

For a healthy physiological cardiac cycle, boundary conditions representative of the ventricular blood volume are applied (Figure 6.2a). The volume increases during filling, and remains fixed during isovolumetric contraction (IVC). At the beginning of systole, the calcium signal is initiated (as shown in Figure 6.2b). The active contractility of the cells in the myocardium then increase the pressure during IVC. The ejection phase is simulated through a reduction in the ventricular volume; a linear decrease is assumed.

An iterative multi-scale procedure is developed to determine the evolution of the myofibril concentration $\hat{\eta}$ and the number of in-series sarcomeres \hat{n} (within cells) in the heart wall such that a non-uniform steady state distribution is obtained, while also correctly predicting the ventricle pressure. Initially $\hat{\eta}$ and \hat{n} are assumed to be spatially uniform (estimated values are required for a Runge-Kutta solver scheme implemented within the UMAT). As described in Figure 6.3, the following steps then take place:

- (i) Cardiac cycle is simulated in the full ventricle model, with the local strain history stored.
- (ii) Strain field is applied to the submodel at a range of points through the myocardial thickness (with a large number of cycles simulated) until steady state values of $\hat{\eta}$ and \hat{n} are attained.
- (iii) Converged values for $\hat{\eta}$ and \hat{n} for each spatial location are then input to the ventricle model.
- (iv) Cardiac cycle is simulated again in the full ventricle, outputting the predicted pressure and strain field.
- (v) Procedure is repeated until (a) the correct pressure trend is computed and (b) $\hat{\eta}$ and \hat{n} change by $<1\%$ between iterations.

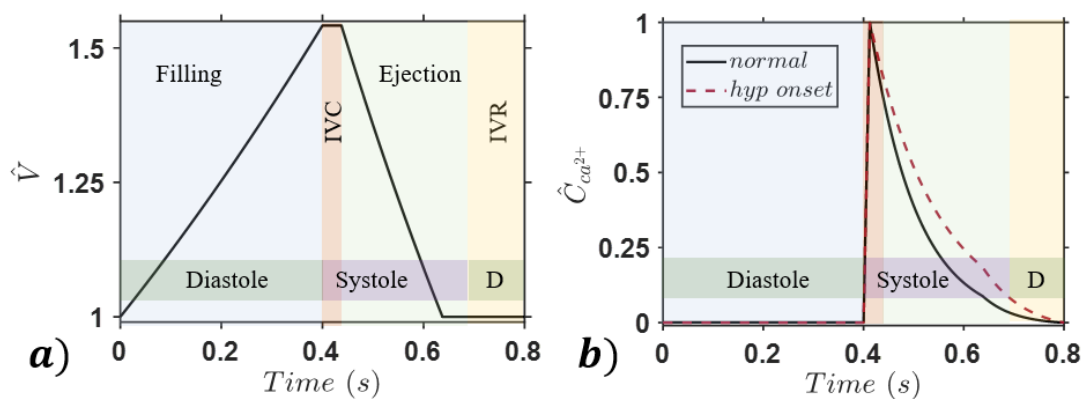


Figure 6.2: Applied boundary conditions for simulation of healthy cardiac cycle: a) volume ($\hat{V} = V/V_0$) of the ventricle; b) calcium signal to unblock actin binding sites. Durations are highlighted for blood filling, isovolumetric contraction (IVC), and blood ejection, and isovolumetric relaxation (IVR).

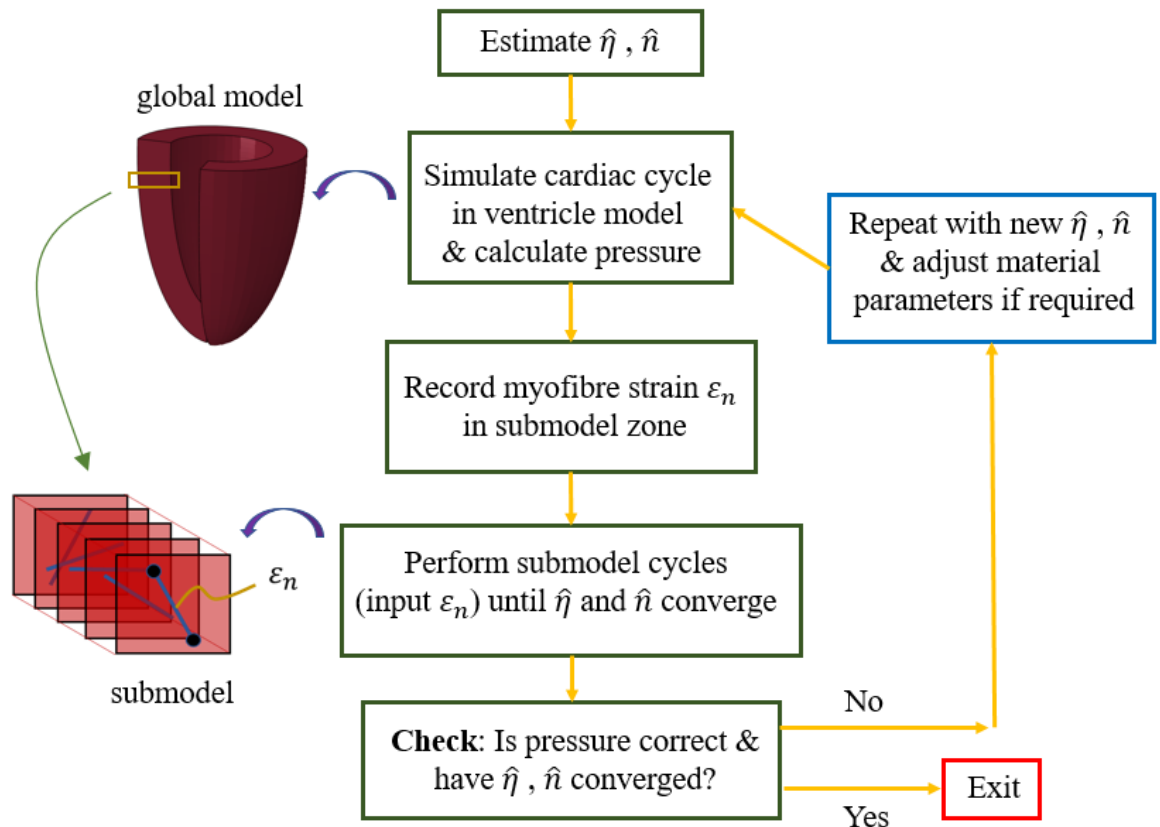


Figure 6.3: Flowchart of model calibration for physiological conditions.

6.2.4.2 Simulation of pathological conditions

Modified boundary conditions are implemented to simulate the biomechanical conditions that have been clinically observed to result in cardiac hypertrophy. We simulate the myocardium behaviour under such altered loading conditions in order to explore the link between alterations in cross-bridge cycling and myofibril remodelling in myocardial pathogenesis. $\hat{\eta}$ and \hat{n} are initially assumed to be the steady state non-uniform distributions determined under physiological loading. We simulate the change in these values due to altered boundary conditions. In summary, the following cases are examined:

- (i) Eccentric hypertrophy is reported to occur in response to an increase in ventricle blood volume during filling. This condition is simulated by increasing the applied volume during filling by 20%.

- (ii) Concentric hypertrophy is reported to occur in response to aortic hypertension (i.e. a higher pressure is required before the aortic valve can open). This condition is simulated by increasing the duration of IVC by 0.02 seconds, and allowing the pressure at IVC to increase to ~ 100 mmHg.
- (iii) With the onset of concentric hypertrophy, it has been reported that the calcium signal is prolonged (Balke and Shorofsky 1998). The effect of a longer signal is also examined by increasing the value of the signal decay constant γ_c (Figure 6.3b).

We examine the ability of the modelling framework to predict: (i) an increase in the number of in-series sarcomeres (\hat{n}) under eccentric hypertrophy boundary conditions (as reported by Dorn *et al.* (2003)); and (ii) an increase in the cross-sectional concentration of myofibrils ($\hat{\eta}$) under concentric hypertrophy boundary conditions (as reported by Chien *et al.* (1993) and Sawada and Kawamura (1991)). Predictions of alterations of \hat{n} and $\hat{\eta}$ within the myocardium are viewed as an initial step in cell remodelling. Subsequent events, including alterations in cell size and shape, and myocardium growth are not considered in the current study, but will be addressed in future developments of the thermodynamically motivated modelling framework.

6.2.5. Modelling parameters

Material constants for the passive anisotropic hyperelastic model are chosen as those previously calibrated to experimental data from human tissue by Mcevoy *et al.* (2018). The anisotropic constants are $a_f = 2.75 \text{ kPa}$, $b_f = 32.1$, $a_s = 1.06 \text{ kPa}$, $b_s = 30.1$, $a_{fs} = 0.175 \text{ kPa}$, and $b_{fs} = 5.02$. The isotropic constants for the compressible formulation are $\mu_1 = 0.98 \text{ kPa}$, $\kappa_1 = 7.31 \text{ kPa}$, $\mu_2 = -0.212 \text{ kPa}$, $\kappa_2 = 5.12 \text{ kPa}$, $\mu_3 = 22.68 \text{ kPa}$, and $\kappa_3 = 2.49e6 \text{ kPa}$. All simulations are reported for cells at a normal body temperature $T = 310 \text{ K}$. Cross-bridge parameters were fixed at those reported by

McEvoy *et al.* (2018). The stroke distance $l_s = 6.5 \text{ nm}$, the myosin tail stiffness $\kappa_m = 1.75 \text{ pN nm}^{-1}$, and parameters $k_t = 4 \text{ s}^{-1}$ and $\varepsilon_s = 0.225$. The cross-bridge enthalpy difference $\Delta\mu_{cb}$ was reduced to $9k_B T$, and the attached duty cycle time t_s increased to 0.005 s such that good agreement is achieved for myosin activity in cardiomyocytes with ranges predicted by Locher *et al.* (2009). In cardiomyocytes, the length of a half sarcomere L_{sarc} is taken to be 900 nm (Nguyen *et al.* 2017). The volume fraction of cells in the heart wall f_0 is 0.75 . The time of peak calcium signal (from initiation) t_{max} is 0.015 s , and the decay rate γ_c for physiological conditions is 0.091 , increased to 0.13 for simulation of a prolonged signal following hypertrophic onset. The parameters for the myofibril framework are confined to ranges reported by Vigliotti *et al.* (2015), with $\Omega = 10^{-71} \mu\text{m}^3$, $\beta = 1.2$, $p = 2$. The enthalpies of bound and unbound fibre proteins are $\mu_{u0} = \Delta\mu_{u0} = 5.5k_B T$, $\mu_{b0} = 9k_B T$, and $\mu_{ab} = 20k_B T$, and the remodelling rates $\omega_n = 2 \text{ Hz}$ and $\alpha_n = 1 \text{ mHz}$. The maximum isometric stress $\sigma_{iso} = 240 \text{ kPa}$ is consistent with a wide range of measurements on muscle fibres (Lucas *et al.* 1987).

6.3. Results

6.3.1. Predictions for physiological conditions

Simulations for a normal heart under physiological conditions were performed for the analysis described in Section 6.2.4. A converged solution was obtained for (i) the concentration of myofibrils $\hat{\eta}$ and the number of in-series sarcomeres \hat{n} , and (ii) the pressure in the ventricle during a cardiac cycle. The predicted ventricle pressure is shown in Figure 6.4a. During blood filling in diastole, the pressure reaches 10 mmHg . As the calcium signal is not yet in effect, the increase in the ventricle wall stress is purely due to deformation of the passive tissue constituents (via equations 6.1-6.3). At the beginning of IVC the pressure starts to climb rapidly. At this point, the initiated calcium signal (Figure 6.3b) results in unblocking of the actin binding sites (allowing for attachment of myosin).

The ensuing tension is not instantaneous, but develops due to the transients in the attachment/recruitment of myosin heads \hat{m}_a as shown in Figure 6.4b. Once the pressure reaches 80 mmHg (as highlighted by the blue marker in Figure 6.4a), ejection begins and the volume starts to decline. Although at this time the signal is also decreasing, \hat{m}_a continues to increase as it has not yet reached the upper limit set by the signal via equation 6.10 and 6.11 (even though the rate $d\hat{m}_a/dt$ is reducing). Thus the cardiomyocyte-generated tension continues to increase. Figure 6.4c shows the predicted overlap of the actin and myosin filaments, which is optimal at different times during the cardiac cycle. The overlap affects the total number of myosin heads available for binding (via equations 6.9 and 6.11). As more unattached heads become available, chemical equilibrium drives a higher attachment rate. The peak \hat{m}_a values (Figure 6.4b) therefore correspond closely to the occurrence of an optimal actin-myosin overlap. Thus it is clear how the pressure is predicted to increase from 80 mmHg to 120 mmHg during this time. Following this peak pressure, the decaying signal then significantly reduces m_{tot} in late systole (via equations 6.10 and 6.11). Chemical equilibrium requires fewer attached myosin heads, so \hat{m}_a decreases. Therefore, the cell tension also reduces until the tissue returns to its reference state.

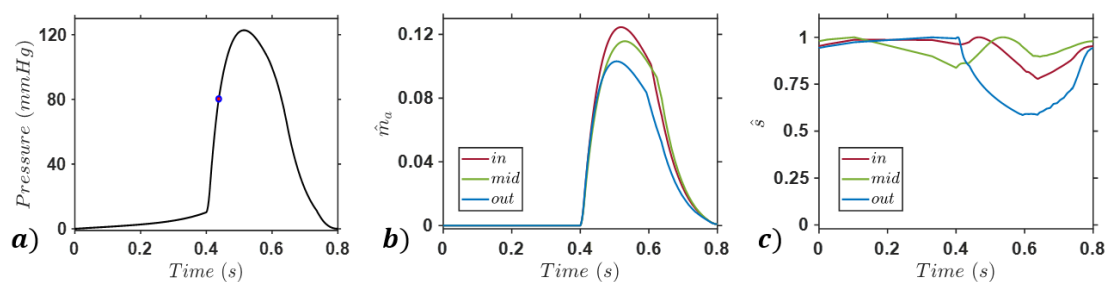


Figure 6.4: a) Predicted ventricular pressure over the course of a single cardiac cycle. b) Predicted number of active myosin heads \hat{m}_a and c) predicted overlap \hat{s} of the actin and myosin filaments over the course of a single cardiac cycle, at locations in the inner, middle, and outer ventricle wall.

The Cauchy stress in the myofibre (f) direction is shown in the contour plots of Figure 6.5a. As described, the stress at end diastole ($t = 0.4$ s) is due to deformation of the passive tissue constituents. This stress is highest at the centre of the tissue wall, where the myofibre orientation is effectively in the circumferential direction. Therefore (in comparison to other fibres in the wall) it receives the highest stretch at this location. The wall stress increases following onset of the calcium signal ($t=0.4$ s), and is highest at peak systole ($t = 0.505$ s). As the calcium signal decays and the myosin activity decreases, the myofibre stress is significantly reduced by the end of the systole ($t = 0.638$ s). Significant apical torqueing is observed over the course of the cardiac cycle due to the complex distribution of myofibres, as shown in Figure 6.1b. Such torqueing is physiological and has been reported clinically by Sengupta *et al.* (2008). The tissue volume is predicted to increase during ventricular filling (Figure 6.5b). The greatest increase in myocardium volume is computed near the outer wall. As the active cell tension develops during the isovolumetric contraction phase, a decrease in the volume of the myocardium tissue is computed at all locations. The highest reduction in myocardium volume (8% – 10% reduction) is predicted at the inner wall at peak systole ($t = 0.505$ s), with the highest myofibril stress also computed in this region. In contrast, at the outer wall the volume at peak systole reduces by less than 2%. These predicted patterns of spatially heterogeneous volume changes in the myocardium throughout the cardiac cycle are supported by the measurements of Ashikaga *et al.* (2008). Neglecting the volumetric behaviour of passive tissue deformation may result in incorrect predictions of the strain state in the myocardium, which could in turn lead to inaccurate predictions of cell contractility and remodelling.

The converged values for $\hat{\eta}$ and \hat{n} are shown in Table 6.1, reported for three regions in the ventricle wall: 1.2 mm from the inner wall (*inner*), 6.1 mm from the inner wall

(*middle*), and 1.2 mm from the outer wall (*outer*). The myofibril concentration ranges from 0.86 – 0.895, and the number of in-series sarcomeres from 0.757 – 0.77.

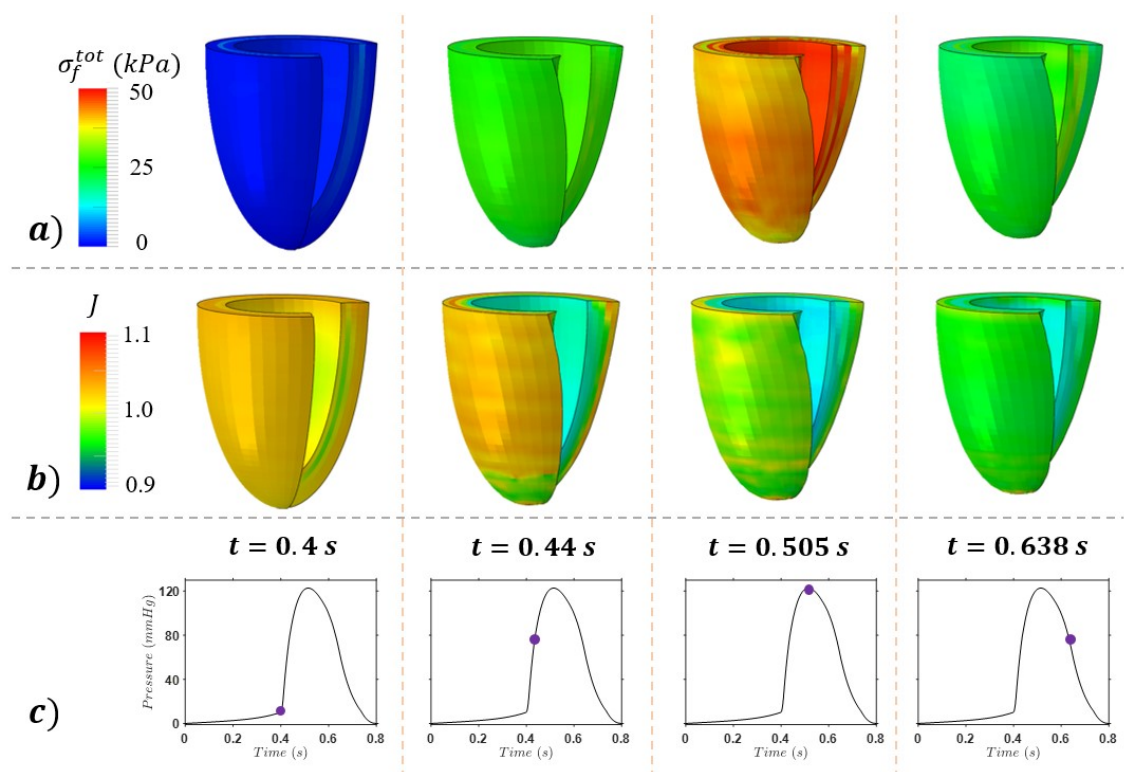


Figure 6.5: Predicted distributions of a) the Cauchy stress (active + passive) in the myofibre (f) direction, and b) elemental volume (J); c) Time-points for contours are shown on the predicted pressure curve over a single cardiac cycle: end diastole at $t = 0.4s$, peak IVC at $t = 0.44s$, systolic peak at $t = 0.505s$, and end systole at $t = 0.638s$).

6.3.2. Predictions for pathological conditions

Eccentric hypertrophy is reported to occur in the myocardium in response to an increase in the ventricle blood volume (volume overload). Following the application of such conditions, as described in Section 6.2.4, the number of in-series sarcomeres (\hat{n}) within cells in the heart wall is predicted to increase (Figure 6.6a). Recall that myofibrils remodel the number of in-series sarcomeres in order to reduce their free energy (by maximising active stress generated through cross-bridge cycling). An increase in the ventricle volume increases the strain within the myocardial wall. The higher wall strain increases the internal sarcomere strain $\tilde{\epsilon}_n$, and thus the difference between $\tilde{\epsilon}_n$ and $\tilde{\epsilon}_{ss}$ (optimal overlap strain). This reduces the actin-myosin overlap via equation 6.9 (Figure 6.6c). A reduction

in the overlap lowers the availability of myosin heads m_{tot} and therefore reduces the number of attached myosin heads (as described previously). This lowers the active contractility and thus increases the sarcomere free energy. The myofibril remodels such that additional sarcomeres \hat{n} are added in-series (via equations 6.14-6.16), increasing the overlap of the actin and myosin filaments. This in turn increases \hat{m}_a and the active tension, and reduces the free energy of individual sarcomeres. However, due to the constraint on the number of cytoskeletal proteins (equation 6.22), the parallel concentration of myofibrils $\hat{\eta}$ is lowered (Figure 6.6b) and the overall contractility of the myocardium is reduced (impairing the pumping ability of the heart).

Concentric hypertrophy is known to be concurrent with aortic hypertension (e.g. due to vessel stiffening (Cho *et al.* 2015) or device implantation (Gyöngyösi *et al.* 2017)). These conditions are applied by increasing the pressure required for the aortic valve to open, as described in Section 6.2.4. As shown in Figure 6.6b such conditions are predicted to result in an increase of the myofibril concentration $\hat{\eta}$. The increased time for which the valve remains closed allows the sarcomere to remain at isometric conditions (and not shortening conditions) for longer. The myosin tail strain is not offset by actin sliding (equations 6.6-6.8) and therefore a higher number of myosin heads attach (with an associated increase in the active fibre stress – see Figure 6.6d). Following the pathways proposed by McEvoy *et al.* (2018) for SF remodelling, this promotes an increase in the concentration of myofibrils via a reduction in the internal free energy of the sarcomeres (equation 6.18). Although the increase in peak fibre stress σ_f is not significant (as during IVC and early systole the calcium signalling dominates the myosin behaviour), it remains higher for longer due to the extended time the valve remains closed. At the outer wall the increase in $\hat{\eta}$ is less pronounced, as the tissue is less constrained and may still shorten on a level comparable with normal conditions (see Table 6.1). Interestingly, it has been observed that following onset of hypertrophy the calcium signal is extended (Balke and Shorofsky

1998). This is thought to be due to a reduced calcium absorption rate in the remodelling tissue. We therefore also examined the influence of a prolonged signal on myofibril remodelling (as described in Section 6.2.4). Such signalling is predicted to have a significant effect on the concentration $\hat{\eta}$ (Figure 6.6b). The longer signal allows for additional attachment of myosin heads, resulting in a higher fibre stress (Figure 6.6d) and therefore higher formation of myofibrils.

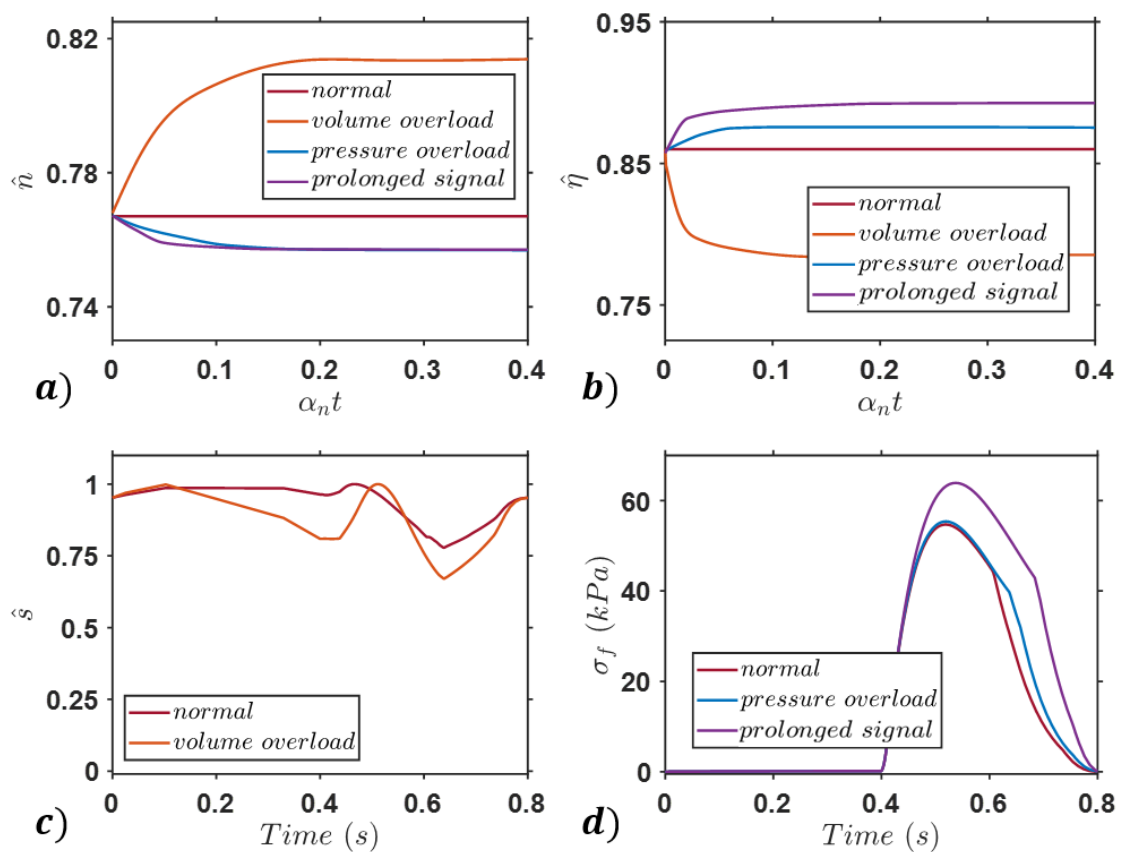


Figure 6.6: Remodelling of a) the number of in-series sarcomeres \hat{n} and b) the myofibril concentration $\hat{\eta}$ in response to altered loading conditions, as a function of normalised quantity $\alpha_n t$ (remodelling rate by time); For a single cardiac cycle: c) predicted overlap \hat{s} of the actin and myosin filaments, and d) the fibre stress σ_f (within the sarcomere). For these simulations \hat{n} and $\hat{\eta}$ are fixed at the healthy values. All values computed at the inner ventricular wall.

	<i>healthy</i>		<i>volume overload</i>		<i>pressure overload</i>		<i>prolonged signal</i>	
	\hat{n}	$\hat{\eta}$	\hat{n}	$\hat{\eta}$	\hat{n}	$\hat{\eta}$	\hat{n}	$\hat{\eta}$
<i>In</i>	.767	.86	.813	.785	.757	.875	.757	.892
<i>Mid</i>	.757	.895	.775	.857	.756	.897	.756	.908
<i>Out</i>	.77	.885	.783	.875	.776	.887	.776	.907

Table 6.1: Steady state number of in-series sarcomeres within myofibrils \hat{n} and myofibril concentration $\hat{\eta}$ in (i) healthy tissue, (ii) following volume overload, (iii) following pressure overload, (iv) following pressure overload and a prolonged calcium signal. Values are reported for three regions in the ventricle wall: 1.2 mm from the inner wall (*inner*), 6.1 mm from the inner wall (*middle*), and 1.2 mm from the outer wall (*outer*).

6.4. Concluding remarks

In this study we implement a thermodynamically motivated model for myofibrillar contractility, coupled with a compressible anisotropic hyperelastic framework, to simulate the behaviour of the ventricular myocardium during the cardiac cycle. Homeostatic concentrations of myofibrils and number of in-series sarcomeres are determined under healthy conditions. Simulation of the transient recruitment of myosin (following initiation of calcium signalling) results in correct patterns of ventricular pressure predicted over a cardiac cycle. This investigation constitutes the first incorporation of such fundamental sub-cellular thermodynamics into a contractile finite element heart model, which has widely been acknowledged as essential to the development of next-generation models (Baillargeon *et al.* 2014; Trayanova 2011; Chabiniok *et al.* 2016).

With an understanding of the processes driving normal cardiac contractility, deviations from homeostatic conditions were examined to provide insight into the mechanisms driving remodelling of the tissue. Eccentric hypertrophy, whereby the number of in-series sarcomeres increases in the myocardial wall, is associated with an increase in the

ventricular blood volume (Dorn *et al.* 2003). We demonstrate that such remodelling is initiated by a higher wall stretch associated with an increased venous return. This reduces the overlap \hat{s} of the actin and myosin filaments within individual sarcomeres. In order to reduce their free energy (i.e. maximise the potential fibre stress σ_f via increasing the availability of myosin heads), the myofibrils add additional sarcomeres \hat{n} in-series to reduce individual sarcomere strain $\tilde{\epsilon}_n$, thereby improving the overlap. Such remodelling of \hat{n} is consistent with observations following the onset of eccentric hypertrophy (Sawada and Kawamura 1991; Gerdes *et al.* 1992). Concentric hypertrophy (increase in parallel myofibril concentration) is typically associated with aortic hypertension. The tissue must generate a higher wall stress (therefore higher ventricle pressure) to overcome the pressure gradient across the aortic valve. The extended period of isometric conditions in the sarcomere allows for increased myosin binding, and therefore a higher fibre stress σ_f . Increases in the fibre stress reduce the enthalpy of the bound sarcomere proteins, thereby promoting a higher myofibril concentration. Increases in the parallel concentration of myofibrils is also consistent with previous literature (Chien *et al.* 1993; Izumo and Nadal-Ginard 1988; Sawada and Kawamura 1991). It is expected the computed trends will be similar in the analysis of a patient-specific geometry. Furthermore, with the onset of hypertrophy, calcium absorption is reduced (Balke and Shorofsky 1998; Bentivegna *et al.* 1991). The prolonged calcium signalling is predicted to further promote myofibrillar formation; via unblocking of more actin binding sites, additional myosin heads may attach. Calcium channel blockers have been shown to prevent the development of hypertrophy and are one of the main drug groups used in treatment (Gregor and Čurila 2015). The findings in this study provide insight into the mechanisms by which such treatment is effective.

Rodriguez *et al.* (1994) developed a framework for volumetric growth in a continuum mechanics setting. Through decomposition of the deformation gradient into an elastic and

growth component the material volume can be as altered as a function of a variable of interest (e.g. strain). In recent years with the advent of powerful computational modelling tools and facilities, such growth models have been integrated into full 3D models of the heart and used to simulate cardiac hypertrophy (Rausch *et al.* 2011), and the pathologies of diastolic and systolic heart failure (Genet *et al.* 2016). However, this phenomenological approach to simulating growth is simply motivated by measuring a change in stress from a pre-determined value, and does not consider the biophysical processes underlying cardiac modelling. In the current study, the cross-bridge and cell-level mechanisms that drive such remodelling are uncovered, and can further our understanding of how such phenomenological measures predict the onset of growth.

The imposed boundary conditions associated with hypertrophic remodelling are simplified relative to the true physiological conditions. While here we provide insight into the pathways leading to myofibrillar remodelling, more complex conditions should be simulated to obtain a deeper understating of the underlying mechanisms, such as: realistic patient geometries, fluid-structure interaction to motivate ventricle pressure and volume, modelling the action potential and more accurate calcium signalling, aortic modelling for realistic hypertensive boundary conditions and pulse wave interactions. Additionally, the next step is to extend the current framework to consider the role of free energy (McEvoy *et al.* 2017; McEvoy *et al.* 2018) in organ level growth, in response to the initiation of sub-cellular remodelling predicted in this study.

Bibliography

- Ashikaga, Hiroshi, Benjamin a Coppola, Katrina G Yamazaki, Francisco J Villarreal, Jeffrey H Omens, and James W Covell. 2008. "Changes in Regional Myocardial Volume during the Cardiac Cycle: Implications for Transmural Blood Flow and Cardiac Structure." *American Journal of Physiology. Heart and Circulatory Physiology* 295: H610–18. doi:10.1152/ajpheart.00107.2008.
- Baillargeon, Brian, Nuno Rebelo, David D. Fox, and Robert L. Taylor. 2014. "The Living Heart Project: A Robust and Integrative Simulator for Human Heart Function." *European Journal of Mechanics - A/Solids* 48: 38–47. doi:10.1016/j.euromechsol.2014.04.001.
- Balke, C, and Stephen R. Shorofsky. 1998. "Alterations in Calcium Handling in Cardiac Hypertrophy and Heart Failure." *Cardiovascular Research* 37 (2). Oxford University Press: 290–99. doi:10.1016/S0008-6363(97)00272-1.
- Bentivegna, L A, L W Ablin, Y Kihara, and J P Morgan. 1991. "Altered Calcium Handling in Left Ventricular Pressure-Overload Hypertrophy as Detected with Aequorin in the Isolated, Perfused Ferret Heart." *Circulation Research* 69 (6). American Heart Association, Inc.: 1538–45. doi:10.1161/01.RES.69.6.1538.
- Bergel, DA, and PJ Hunter. 1979. "The Mechanics of the Heart." In *Quantitative Cardiovascular Studies, Clinical and Research Applications of Engineering Principles*, edited by HHC Hwang, DR Gross, and DJ Patel, 151–213. University Park Press, Baltimore. https://scholar.google.com/scholar?hl=en&as_sdt=0%2C5&q=bergel+hunter+the+mechanics+of+the+heart+1979&btnG=.
- Chabiniok, Radomir, Vicky Y. Wang, Myrianthi Hadjicharalambous, Liya Asner, Jack Lee, Maxime Sermesant, Ellen Kuhl, *et al.* 2016. "Multiphysics and Multiscale Modelling, Data-model Fusion and Integration of Organ Physiology in the Clinic: Ventricular Cardiac Mechanics." *Interface Focus* 6 (2). Royal Society: 20150083. doi:10.1098/rsfs.2015.0083.
- Chien, KR, H Zhu, and KU Knowlton. 1993. "Transcriptional Regulation during Cardiac Growth and Development." *Annual Review Of*. <https://www.annualreviews.org/doi/pdf/10.1146/annurev.ph.55.030193.000453>.
- Cho, In-Jeong, Hyuk-Jae Chang, Hyung-Bok Park, Ran Heo, Sanghoon Shin, Chi Young Shim, Geu-Ru Hong, and Namsik Chung. 2015. "Aortic Calcification Is Associated with Arterial Stiffening, Left Ventricular Hypertrophy, and Diastolic Dysfunction in Elderly Male Patients with Hypertension." *Journal of Hypertension* 33 (8): 1633–41. doi:10.1097/HJH.0000000000000607.
- CHUNG, Man-Wei, Tatiana TSOUTSMAN, and Christopher SEMSARIAN. 2003. "Hypertrophic Cardiomyopathy: From Gene Defect to Clinical Disease." *Cell Research* 13 (1). Nature Publishing Group: 9–20. doi:10.1038/sj.cr.7290146.
- Dokos, Socrates, Bruce H Smaill, Alistair a Young, and Ian J LeGrice. 2002. "Shear Properties of Passive Ventricular Myocardium." *American Journal of Physiology. Heart and Circulatory Physiology* 283 (6): H2650–59. doi:10.1152/ajpheart.00111.2002.
- Dorn, Gerald W., Jeffrey Robbins, and Peter H. Sugden. 2003. "Phenotyping Hypertrophy." *Circulation Research* 92 (11).
- Genet, M., L. C. Lee, B. Baillargeon, J. M. Guccione, and E. Kuhl. 2016. "Modeling Pathologies of Diastolic and Systolic Heart Failure." *Annals of Biomedical Engineering* 44 (1). Springer US: 112–27. doi:10.1007/s10439-015-1351-2.
- Gerdes, AM, SE Kellerman, and JA Moore. 1992. "Structural Remodeling of Cardiac Myocytes in Patients with Ischemic Cardiomyopathy." *Circulation* 86 (2). <http://citeseerx.ist.psu.edu/viewdoc/download?doi=10.1.1.872.8939&rep=rep1&type=pdf>.
- Göktepe, S., S. N. S. Acharya, J. Wong, and E. Kuhl. 2011. "Computational Modeling of Passive Myocardium." *International Journal for Numerical Methods in Biomedical Engineering* 27

- (1). John Wiley & Sons, Ltd.: 1–12. doi:10.1002/cnm.1402.
- Gregor, Pavel, and Karol Čurila. 2015. “Medical Treatment of Hypertrophic Cardiomyopathy – What Do We Know about It Today?” *Cor et Vasa* 57 (3). Urban & Fischer: e219–24. doi:10.1016/J.CRVASA.2015.02.003.
- Gyöngyösi, Mariann, Noemi Pavo, Dominika Lukovic, Katrin Zlabinger, Andreas Spannbaauer, Denise Traxler, Georg Goliasch, *et al.* 2017. “Porcine Model of Progressive Cardiac Hypertrophy and Fibrosis with Secondary Postcapillary Pulmonary Hypertension.” *Journal of Translational Medicine* 15 (1). BioMed Central: 202. doi:10.1186/s12967-017-1299-0.
- Holzapfel, Gerhard A, and Ray W Ogden. 2009. “Constitutive Modelling of Passive Myocardium: A Structurally Based Framework for Material Characterization.” *Philosophical Transactions. Series A, Mathematical, Physical, and Engineering Sciences* 367 (1902): 3445–75. doi:10.1098/rsta.2009.0091.
- Hunter, P.J., A.D. McCulloch, and H.E.D.J. ter Keurs. 1998. “Modelling the Mechanical Properties of Cardiac Muscle.” *Progress in Biophysics and Molecular Biology* 69 (March): 289–331. doi:10.1016/S0079-6107(98)00013-3.
- Izumo, S, and B Nadal-Ginard. 1988. “Protooncogene Induction and Reprogramming of Cardiac Gene Expression Produced by Pressure Overload.” *Proceedings of The. <http://www.pnas.org/content/85/2/339.short>*.
- Legrice, I J, P J Hunter, and B H Smaill. 1997. “Laminar Structure of the Heart: A Mathematical Model.” *The American Journal of Physiology* 272: H2466–76.
- LeGrice, I J, B H Smaill, L Z Chai, S G Edgar, J B Gavin, and P J Hunter. 1995. “Laminar Structure of the Heart: Ventricular Myocyte Arrangement and Connective Tissue Architecture in the Dog.” *Am J Physiol* 269 (2 Pt 2): H571-82. <http://www.ncbi.nlm.nih.gov/pubmed/7653621>.
- Locher, Matthew R, Maria V Razumova, Julian E Stelzer, Holly S Norman, Jitandrakumar R Patel, and Richard L Moss. 2009. “Determination of Rate Constants for Turnover of Myosin Isoforms in Rat Myocardium: Implications for in Vivo Contractile Kinetics.” *American Journal of Physiology. Heart and Circulatory Physiology* 297 (1). American Physiological Society: H247-56. doi:10.1152/ajpheart.00922.2008.
- Lucas, S M, R L Ruff, and M D Binder. 1987. “Specific Tension Measurements in Single Soleus and Medial Gastrocnemius Muscle Fibers of the Cat.” *Experimental Neurology* 95 (1): 142–54. <http://www.ncbi.nlm.nih.gov/pubmed/2947808>.
- McEvoy, E., V.S. Deshpande, and P. McGarry. 2017. “Free Energy Analysis of Cell Spreading.” *Journal of the Mechanical Behavior of Biomedical Materials* 74. doi:10.1016/j.jmbbm.2017.06.006.
- McEvoy, Eoin, Vikram S. Deshpande, and Patrick McGarry. 2018. “Transient Active Force Generation and Stress Fibre Remodelling in Cells under Cyclic Loading.” *Biomechanics and Modeling in Mechanobiology* (in review).
- Mcevoy, Eoin, Gerhard A Holzapfel, and Patrick MCGarry. 2018. “Compressibility and Anisotropy of the Ventricular Myocardium: Experimental Analysis and Microstructural Modeling.” *Journal of Biomechanical Engineering*. doi:10.1115/1.4039947.
- McEvoy, Eoin, Siamak S. Shishvan, Vikram S. Deshpande, and Patrick McGarry. 2018. “Thermodynamic Modelling of the Statistics of Cell Spreading on Ligand Coated Elastic Substrates.” *Biophysical Journal* (In review).
- Nguyen, Nathalie, William Nguyen, Brynna Nguyenton, Phachareeya Ratchada, Guy Page, Paul E Miller, Andre Ghetti, and Najah Abi-Gerges. 2017. “Adult Human Primary Cardiomyocyte-Based Model for the Simultaneous Prediction of Drug-Induced Inotropic and Pro-Arrhythmia Risk.” *Frontiers in Physiology* 8. Frontiers Media SA: 1073. doi:10.3389/fphys.2017.01073.

- Nolan, D.R., A.L. Gower, M. Destrade, R.W. Ogden, and J.P. McGarry. 2014. "A Robust Anisotropic Hyperelastic Formulation for the Modelling of Soft Tissue." *Journal of the Mechanical Behavior of Biomedical Materials* 39. Elsevier: 48–60. doi:10.1016/j.jmbbm.2014.06.016.
- Pezzuto, S., D. Ambrosi, and A. Quarteroni. 2014. "An Orthotropic Active-Strain Model for the Myocardium Mechanics and Its Numerical Approximation." *European Journal of Mechanics, A/Solids* 48 (1). Elsevier Masson SAS: 83–96. doi:10.1016/j.euromechsol.2014.03.006.
- Rausch, M. K., A. Dam, S. Göktepe, O. J. Abilez, and E. Kuhl. 2011. "Computational Modeling of Growth: Systemic and Pulmonary Hypertension in the Heart." *Biomechanics and Modeling in Mechanobiology* 10 (6): 799–811. doi:10.1007/s10237-010-0275-x.
- Rodriguez, Edward K., Anne Hoger, and Andrew D. McCulloch. 1994. "Stress-Dependent Finite Growth in Soft Elastic Tissues." *Journal of Biomechanics* 27 (4): 455–67. doi:10.1016/0021-9290(94)90021-3.
- Sawada, K., and K Kawamura. 1991. "Architecture of Myocardial Cells in Human Cardiac Ventricles with Concentric and Eccentric Hypertrophy as Demonstrated by Quantitative Scanning Electron Microscopy." *Heart and Vessels*. <http://link.springer.com/article/10.1007/BF02058278>.
- Sengupta, Partho P., A. Jamil Tajik, Krishnaswamy Chandrasekaran, and Bijoy K. Khandheria. 2008. "Twist Mechanics of the Left Ventricle." *JACC: Cardiovascular Imaging* 1 (3).
- Sommer, Gerhard, Andreas J. Schriefl, Michaela Andrä, Michael Sacherer, Christian Viertler, Heimo Wolinski, and Gerhard A. Holzapfel. 2015. "Biomechanical Properties and Microstructure of Human Ventricular Myocardium." *Acta Biomaterialia* 24 (September): 172–92. doi:10.1016/j.actbio.2015.06.031.
- Sun, Wei, Elliot L Chaikof, and Marc E Levenston. 2008. "Numerical Approximation of Tangent Moduli for Finite Element Implementations of Nonlinear Hyperelastic Material Models." *Journal of Biomechanical Engineering* 130 (6): 061003. doi:10.1115/1.2979872.
- Trayanova, Natalia A. 2011. "Whole-Heart Modeling: Applications to Cardiac Electrophysiology and Electromechanics." *Circulation Research* 108 (1). NIH Public Access: 113–28. doi:10.1161/CIRCRESAHA.110.223610.
- Vigliotti, A., W. Ronan, F. P T Baaijens, and V. S. Deshpande. 2015. "A Thermodynamically Motivated Model for Stress-Fiber Reorganization." *Biomechanics and Modeling in Mechanobiology*. Springer Berlin Heidelberg. doi:10.1007/s10237-015-0722-9.
- Wang, Vicky Y, Corné Hoogendoorn, Alejandro F Frangi, B R Cowan, Peter J Hunter, Alistair A Young, and Martyn P Nash. 2013. "LNCS 7746 - Automated Personalised Human Left Ventricular FE Models to Investigate Heart Failure Mechanics." *LNCS 7746*: 307–16.
- Wong, J, S Göktepe, and E Kuhl. 2013. "Computational Modeling of Chemo-Electro-Mechanical Coupling: A Novel Implicit Monolithic Finite Element Approach." *International Journal for Numerical Methods in Biomedical Engineering* 29 (10). NIH Public Access: 1104–33. doi:10.1002/cnm.2565.
- Yeoh, O. H. 1993. "Some Forms of the Strain Energy Function for Rubber." *Rubber Chemistry and Technology* 66 (5): 754–71. doi:10.5254/1.3538343.

CHAPTER 7

CONCLUDING REMARKS



7.1. Summary of key contributions

Key contributions of this thesis to the field of biomechanics are summarized in this section.

Chapter 2:

Novel technical contributions

- A steady-state thermodynamically motivated model for stress fibre (SF) formation is developed and implemented within an Abaqus UMAT, with a non-local finite element scheme for global protein conservation.
- A framework for focal adhesion (FA) assembly is proposed, with formation governed by thermodynamic equilibrium of low and high affinity integrins on the cell surface. Traction mediated focal adhesion formation is predicted, with adhesion density limited by availability of ligands on the substrate surface.

Novel scientific insights

- It is demonstrated that cell spreading may be viewed as a competition between the increasing elastic strain energy associated with deformation of passive cell and substrate components, and the decreasing free energy associated with formation of stress fibres and focal adhesions.
- The hypothesis that cells tend to assume a low (or minimum) free energy configuration is explored by simulating a range of spread states and computing the associated system free energy. The stress fibre and focal adhesion distributions in predicted low free energy states are consistent with experimentally observed behaviour. Furthermore, analyses reveal that the total free energy is lower when cells spread on stiffer substrates.

Chapter 3:***Novel technical contributions***

- A modified form of the FA framework of Chapter 2 is developed to represent traction mediated adhesion complex formation in cells spreading within a statistical mechanics *ensemble*. A methodology is proposed to reduce the probability of cells assuming configurations that give rise to unphysical tractions.

Novel scientific insights

- As cells never truly achieve an equilibrium minimum free energy while alive, and spread cells exist in a perpetually fluctuating state, the energetic competition from Chapter 2 is extended to a statistical mechanics setting where it is demonstrated that spreading is motivated by the free energy associated with homeostasis.

- This framework provides new insights into the thermodynamics that motivate the highly coupled influence of surface collagen (ligand) density and substrate stiffness on cell spreading. Key experimental observations of Engler *et al.* (2003) are predicted, including (i) the increase in cell spread area (mean and SD) with increasing collagen density, (ii) a reduction in spread area when the collagen density is increased beyond a critical value, and (iii) the increase in the mean and SD of spread area with increasing substrate stiffness.

Chapter 4:

Novel technical contributions

- A model for transient SF contractility due to actin-myosin cross-bridge cycling is proposed and developed. The rate of cross-bridge formation (myosin binding) within SFs is governed by the chemical potentials of attached and unattached myosin heads. The model is shown to describe dynamic force generation in cells, and provides a mechanistic explanation for “fading memory” type formulations.

Novel scientific insights

- The cross-bridge cycling model is coupled with a thermodynamically motivated framework for SF remodelling to analyse the influence of transient force generation on cytoskeletal evolution. A direct link is established between (i) the influence of loading on nanoscale actin-myosin interactions, (ii) the consequential chemical potential imbalance between the attached and unattached myosin heads, (iii) the sarcomere stress due to cross-bridge cycling, and (iv) the concentration of SFs in the cell.

- Under long term cyclic loading, high applied strain rates are predicted to result in low SF formation, due to an offset in myosin tension caused by high shortening velocities. Low strain rates lead to high levels of SF formation, as cross-bridge conditions are consistently close to isometric.

Chapter 5:

Novel technical contributions

- An experiment is designed to measure the in-plane deformation of the myocardial tissue at orthogonal angles during a tensile stretch, and derive a 3D representation of the material volume change.
- A microstructural model of the myocardium is developed as motivated by experimental and SEM images, accounting discretely for the myocytes, capillaries, and ECM that connects the cells and surrounds the myolaminae.

Novel scientific insights

- In contrast with common assumptions, it is empirically demonstrated that the passive myocardial tissue is compressible, and changes in volume under both tensile and confined compression loading conditions. The volumetric material behaviour of the tissue is captured by a compressible isotropic hyperelastic model.
- To simulate the multi-axial passive behaviour of the myocardium, the compressible isotropic component is combined with the well-established Holzapfel and Ogden (2009) anisotropic model for myocardium. This framework is shown to describe the experimentally observed behaviour of porcine and human tissue under shear and biaxial loading conditions.

- Analyses are performed with the microstructural model to parse the contribution of vasculature and solid tissue to the material compressibility, as it is well-known the intra-myocardial blood volume changes over the course of a cardiac cycle. Simulations confirm that the solid tissue is compressible, and should be considered as such even if blood dynamics were to be explicitly included in an analysis.
- Analyses also reveal the key tissue constituents that contribute to the stress under several modes of shear loading. Dispersion of endomysial and perimysial collagen that surrounds the myolaminae contributes significantly to the stress in all loading modes, and the high stresses measured under loading in the myofibre direction are predominantly due to deformation of the myofibres and perimysial collagen oriented in the same direction.

Chapter 6:

Novel technical contributions

- A contractile model of left ventricle is developed, with the active cell tension described by an extension of the thermodynamically motivated cross-bridge model proposed in Chapter 4, and the passive tissue mechanics by the multi-axial hyperelastic framework developed in Chapter 5. Simulation of transient myosin recruitment is shown to predict correct patterns of ventricular pressure over a cardiac cycle.

Novel scientific insights

- A myofibril remodelling framework is coupled with the cross-bridge cycling model to investigate how deviations in the transient force generation drive restructuring of cellular myofibrils in the heart wall. Analyses reveal that pathological loading conditions can alter how actin and myosin interact within cellular sarcomeres. An imbalance between the internal free energy of myofibrils and that of unbound contractile proteins results from the consequent deviation in sarcomere stress, and onsets the remodelling process.
- Myofibril remodelling associated with concentric and eccentric hypertrophy is predicted to occur following periods of hypertension and volume overload, respectively.

7.2. Future perspectives

The work presented in this thesis has addressed several key topics in relation to contractility and remodelling of cells and tissue, as summarised in Section 7.1. These contributions have implications for related areas in biomechanics, and design of medical implants and diagnostic equipment. The current section provides a discussion of future perspectives.

In Chapters 2 and 3 a thermodynamic framework for cell spreading is proposed, and shown to predict a wide range of experimental behaviour. This novel approach to the modelling of spread cells offers a powerful computational tool to aid the design of devices and tissue engineered structures. In the current form, the framework could be used to inform experimentalists of ideal substrate ligand patterning to achieve optimal cell alignment (Ristori *et al.* 2016), contractility (Polacheck and Chen 2016), or device adhesion (Iulian *et al.* 2016). The statistical mechanics model may also prove useful in investigating the probabilistic nature of differentiation in cells constrained to fixed ligand patches (Kilian *et al.* 2010). A possible next step would be to progress the model to the simulation of 3D cell spreading, though the additional degrees of freedom would add significantly to computational cost. This would allow for optimisation of cell spreading in engineered hydrogels (Deng *et al.* 2017). Furthermore, the framework could be expanded to a temporal description of spreading by using dynamic forms of the stress fibre formulation, improving on current models of transient cell migration and durotaxis (González-Valverde and García-Aznar 2018).

The transient SF contractility model developed in Chapter 4 provides a new understanding of stress fibre force generation and remodelling. This constitutes an important progression from phenomenological steady state Hill-type models to describe the active contractility. In addition to providing a deeper insight into SF contractility in single cells under dynamic loading (Weafer *et al.* 2015; Reynolds and McGarry 2015),

this model could be implemented in the simulation of engineered tissue under long term loading to provide more accurate predictions of the evolving stress and strain state. Potential applications include engineering of heart valves (Loerakker *et al.* 2016), arterial tissue (L'Heureux *et al.* 2006), and tendon (Garvin *et al.* 2003).

Tissue incompressibility is commonly assumed in the modelling of cardiac myocardium (Holzapfel and Ogden 2009; Göktepe *et al.* 2011; Genet *et al.* 2016), despite evidence of dynamic changes in the intra-myocardial blood volume (Yin *et al.* 1996; Ashikaga *et al.* 2008). In Chapter 5 the tissue volume is shown to change significantly under loading. It is therefore suggested that future computational models of the myocardium consider the tissue to be compressible, thereby avoiding the need for a Lagrange multiplier to enforce a fixed material volume (Holzapfel *et al.* 2000). However, further work is required to investigate regional specific tissue compressibility (Novak *et al.* 1994), and to quantify the behaviour in freshly excised human tissue (Sommer *et al.* 2015).

Recent models of the contractile heart typically rely on strain based motivations for cellular tension generation (Baillargeon *et al.* 2014; Pezzuto *et al.* 2014). Implementation of thermodynamically motivated cross-bridge cycling formulations, as proposed in this thesis, will provide more accurate simulation of tissue force generation in future models. This is of particular importance in the study of device implantation, as phenomenologically motivated models can provide little insight to the effects of an altered mechanical environment on actin-myosin interactions (and the resulting tissue contractility).

Furthermore, the investigation of hypertrophic onset in Chapter 6 reveals the interactions between cross-bridge cycling and remodelling of myofibrils in the heart wall. This preliminary study uncovers how pathological loading conditions drives such remodelling, and interestingly, can also provide insight into the pathways by which treatment such as

calcium blockers (Gregor and Čurila 2015) prove useful in patient recovery. The next stage of this work should be to extend the current framework to consider the role of free energy in organ level growth, in response to the initiation of sub-cellular remodelling. This will provide the groundwork for the development of next generation computational clinical tools for use in the diagnosis of cardiac hypertrophy onset, design of patient treatment plans, and in the study of device driven remodelling.

Bibliography

- Ashikaga, Hiroshi, Benjamin a Coppola, Katrina G Yamazaki, Francisco J Villarreal, Jeffrey H Omens, and James W Covell. 2008. “Changes in Regional Myocardial Volume during the Cardiac Cycle: Implications for Transmural Blood Flow and Cardiac Structure.” *American Journal of Physiology. Heart and Circulatory Physiology* 295: H610–18. doi:10.1152/ajpheart.00107.2008.
- Baillargeon, Brian, Nuno Rebelo, David D. Fox, and Robert L. Taylor. 2014. “The Living Heart Project: A Robust and Integrative Simulator for Human Heart Function.” *European Journal of Mechanics - A/Solids* 48: 38–47. doi:10.1016/j.euromechsol.2014.04.001.
- Deng, Jie, Changsheng Zhao, Joachim P. Spatz, and Qiang Wei. 2017. “Nanopatterned Adhesive, Stretchable Hydrogel to Control Ligand Spacing and Regulate Cell Spreading and Migration.” *ACS Nano* 11 (8): 8282–91. doi:10.1021/acsnano.7b03449.
- Engler, A., M. Sheehan, H. L. Sweeney, and D. E. Discher. 2003. “Substrate Compliance vs Ligand Density in Cell on Gel Responses.” *European Cells and Materials* 6 (SUPPL. 1). Elsevier: 7–8. doi:10.1016/S0006-3495(04)74140-5.
- Garvin, Joanne, Jie Qi, Melissa Maloney, and Albert J. Banes. 2003. “Novel System for Engineering Bioartificial Tendons and Application of Mechanical Load.” *Tissue Engineering* 9 (5). Mary Ann Liebert, Inc. : 967–79. doi:10.1089/107632703322495619.
- Genet, M, LC Lee, B Baillargeon, and JM Guccione. 2016. “Modeling Pathologies of Diastolic and Systolic Heart Failure.” *Annals of Biomedical*. <http://link.springer.com/article/10.1007/s10439-015-1351-2>.
- Göktepe, S., S. N. S. Acharya, J. Wong, and E. Kuhl. 2011. “Computational Modeling of Passive Myocardium.” *International Journal for Numerical Methods in Biomedical Engineering* 27 (1). John Wiley & Sons, Ltd.: 1–12. doi:10.1002/cnm.1402.
- González-Valverde, Ismael, and José Manuel García-Aznar. 2018. “Mechanical Modeling of Collective Cell Migration: An Agent-Based and Continuum Material Approach.” *Computer Methods in Applied Mechanics and Engineering* 337 (August). North-Holland: 246–62. doi:10.1016/J.CMA.2018.03.036.
- Gregor, Pavel, and Karol Čurila. 2015. “Medical Treatment of Hypertrophic Cardiomyopathy – What Do We Know about It Today?” *Cor et Vasa* 57 (3). Urban & Fischer: e219–24. doi:10.1016/J.CRVASA.2015.02.003.
- Holzapfel, Gerhard A., Thomas C. Gasser, and Ray W. Ogden. 2000. “A New Constitutive Framework for Arterial Wall Mechanics and a Comparative Study of Material Models.” *Journal of Elasticity* 61 (1–3): 1–48. doi:10.1023/A:1010835316564.
- Holzapfel, Gerhard a, and Ray W Ogden. 2009. “Constitutive Modelling of Passive Myocardium: A Structurally Based Framework for Material Characterization.” *Philosophical Transactions. Series A, Mathematical, Physical, and Engineering Sciences* 367 (1902): 3445–75. doi:10.1098/rsta.2009.0091.
- Iulian, Antoniac, Sinescu Cosmin, and Antoniac Aurora. 2016. “Adhesion Aspects in Biomaterials and Medical Devices.” *Journal of Adhesion Science and Technology*, April. Taylor & Francis, 1–5. doi:10.1080/01694243.2016.1170959.

- Kilian, Kristopher A, Branimir Bugarija, Bruce T Lahn, and Milan Mrksich. 2010. "Geometric Cues for Directing the Differentiation of Mesenchymal Stem Cells." *Proceedings of the National Academy of Sciences of the United States of America* 107 (11). National Academy of Sciences: 4872–77. doi:10.1073/pnas.0903269107.
- L'Heureux, Nicolas, Nathalie Dusserre, Gerhardt Konig, Braden Victor, Paul Keire, Thomas N Wight, Nicolas A F Chronos, *et al.* 2006. "Human Tissue-Engineered Blood Vessels for Adult Arterial Revascularization." *Nature Medicine* 12 (3). NIH Public Access: 361–65. doi:10.1038/nm1364.
- Loerakker, Sandra, Tommaso Ristori, and Frank P T Baaijens. 2016. "A Computational Analysis of Cell-Mediated Compaction and Collagen Remodeling in Tissue-Engineered Heart Valves." *Journal of the Mechanical Behavior of Biomedical Materials* 58. Elsevier: 173–87. doi:10.1016/j.jmbbm.2015.10.001.
- Novak, V P, F C Yin, and J D Humphrey. 1994. "Regional Mechanical Properties of Passive Myocardium." *Journal of Biomechanics* 27 (4). Elsevier: 403–12. doi:10.1016/0021-9290(94)90016-7.
- Pezzuto, S., D. Ambrosi, and A. Quarteroni. 2014. "An Orthotropic Active-Strain Model for the Myocardium Mechanics and Its Numerical Approximation." *European Journal of Mechanics, A/Solids* 48 (1). Elsevier Masson SAS: 83–96. doi:10.1016/j.euromechsol.2014.03.006.
- Polacheck, William J, and Christopher S Chen. 2016. "Measuring Cell-Generated Forces: A Guide to the Available Tools." *Nature Methods* 13 (5). NIH Public Access: 415–23. doi:10.1038/nmeth.3834.
- Reynolds, N. H., and J. P. McGarry. 2015. "Single Cell Active Force Generation under Dynamic Loading - Part II: Active Modelling Insights." *Acta Biomaterialia* 27. Acta Materialia Inc.: 251–63. doi:10.1016/j.actbio.2015.09.004.
- Ristori, Tommaso, Andrea Vigliotti, Frank P.T. Baaijens, Sandra Loerakker, and Vikram S. Deshpande. 2016. "Prediction of Cell Alignment on Cyclically Strained Grooved Substrates." *Biophysical Journal* 111 (10). Cell Press: 2274–85. doi:10.1016/J.BPJ.2016.09.052.
- Sommer, Gerhard, Andreas J. Schriefl, Michaela Andrä, Michael Sacherer, Christian Viertler, Heimo Wolinski, and Gerhard A. Holzapfel. 2015. "Biomechanical Properties and Microstructure of Human Ventricular Myocardium." *Acta Biomaterialia* 24 (September): 172–92. doi:10.1016/j.actbio.2015.06.031.
- Weafer, P. P., N. H. Reynolds, S. P. Jarvis, and J. P. McGarry. 2015. "Single Cell Active Force Generation under Dynamic Loading - Part I: AFM Experiments." *Acta Biomaterialia* 27. Acta Materialia Inc.: 236–50. doi:10.1016/j.actbio.2015.09.006.
- Yin, F C, C C Chan, and R M Judd. 1996. "Compressibility of Perfused Passive Myocardium." *The American Journal of Physiology* 271 (20): H1864–70.